THE UNIVERSITY *of* EDINBURGH

Acoustic characterisation of ultrasound contrast agents at high frequency

Chao Sun

A thesis submitted for the degree of Doctor of Philosophy

The University of Edinburgh

December, 2012

To my grandparents

Abstract

This thesis aims to investigate the acoustic properties of ultrasound contrast agents (UCAs) at high ultrasound frequencies. In recent years, there has been increasing development in the use of high frequency ultrasound in the fields of preclinical, intravascular, ophthalmology and superficial tissue imaging. Although research studying the acoustic response of UCAs at low diagnostic ultrasonic frequencies has been well documented, quantitative information on the acoustical properties of UCAs at high ultrasonic frequencies is limited.

In this thesis, acoustical characterisation of three UCAs was performed using a preclinical ultrasound scanner (Vevo 770, VisualSonics Inc., Canada). Initially the acoustical characterisation of five high frequency transducers was measured using a membrane hydrophone with an active element of 0.2 mm in diameter to quantify the transmitting frequencies, pressures and spatial beam profiles of each of the transducers. Using these transducers and development of appropriate software, high frequency acoustical characterisation (speed and attenuation) of an agar-based tissue mimicking material (TMM) was performed using a broadband substitution technique. The results from this study showed that the acoustical attenuation of TMM varied nonlinearly with frequency and the speed of sound was approximately constant 1548m·s^{-1} in the frequency range 12-47MHz.

The acoustical properties of three commercially available lipid encapsulated UCAs including two clinical UCAs Definity (Lantheus Medical Imaging, USA) and SonoVue (Bracco, Italy) and one preclinical UCAs MicroMarker (untargeted) (VisualSonics, Canada) were studied using the software and techniques developed for TMM characterisation. Attenuation, contrast-to-tissue ratio (CTR) and subharmonic to fundamental ratio were measured at low acoustic pressures. The results showed that large off-resonance and resonant MBs predominantly contributed to the fundamental response and MBs which resonated at half of the driven

frequency predominantly contributed to subharmonic response. The effect of needle gauge, temperature and injection rate on the size distribution and acoustic properties of Definity and SonoVue was measured and was found to have significant impacts.

Acoustic characterisations of both TMM and UCAs in this thesis extend our understanding from low frequency to high frequency ultrasound and will enable the further development of ultrasound imaging techniques and UCAs design specifically for high frequency ultrasound applications.

Acknowledgments

I would like to gratefully appreciate the patient guidance, critical inspiration, continuous encouragement and writing corrections from my supervisors Dr. Carmel Moran, Dr. Vassilis Sboros, Dr. Mairead Butler. I thank Mr. Adrian Thomson for helping me familiar with the preclinical experimental environment, Prof. Norman McDicken, Dr. Xin Yang and Dr. David Thomas for useful discussions of my experiments, Mrs Irene Craig and Mr Tom Anderson for caring and creating an atmosphere that make me focus on my PhD study. Many thanks also to Dr. Stephen Pye, Ms. Anna Janeczko, Mr. Bill Ellis, Mr. Stan Loneskie, Mr. Ian Peaston from Medical Physics department in NHS Lothian for their help in making the tissue mimicking materials and moulds, Prof. Jim Ross, Mr. James Black, Mrs. Kathyrn Sangster, Mrs. Linda Norrie from Tissue injury group for lending me so many experimental tools, Dr. Jacinta Browne from Dublin Institute of Technology for giving me a chance of experiencing an optimistic life in Ireland and working in a lab with sunshine.

I shall also thank my good friends Luan Ying, Bai Jianing, Han Lei, Liu Jing and all the postgraduates of medical physics in Edinburgh.

Thanks to my parents for their support and understanding when I felt mostly needed.

Finally, I would like to acknowledge the funding from the China Scholarship Council (CSC) and the University of Edinburgh joint scholarship.

Declaration of originality

I declare that the submitted thesis and the research have been originated by myself, except where otherwise clearly stated and acknowledged, in Medical Physics, Centre for Cardiovascular Science, University of Edinburgh.

Chao Sun

December 2012

Contents

List of Figures

List of Tables

Chapter 1

Introduction to high frequency ultrasound and ultrasound contrast agents

1.1 AIM

Clinical diagnostic scanning usually occurs in the frequency range of 2-15 MHz (Hoskins 2002). The range of applications of high frequency ultrasound (>20MHz) in life sciences has been increasing in recent years, specifically in the emerging fields of preclinical imaging (Foster et al. 2000, Goertz et al. 2005, Maruvada et al. 2000), intravascular ultrasound imaging (IVUS) (Rhee 2007), superficial tissue imaging (Vogt et al. 2007) and ophthalmology (Silverman et al. 2008). The research of high frequency ultrasound starts from the manufacture and assessment of high frequency transducers (Sprague et al. 2011) and ultrasound systems (Foster et al. 2011). Ultrasound contrast agents (UCAs) are specifically useful in preclinical research for functional imaging of the microcirculation (Foster et al. 2011, Goertz et al. 2005, Needles et al. 2011). This PhD project aims to investigate the acoustic characterisation of lipid encapsulated UCAs over the high frequency range from 12 to 43 MHz using a preclinical ultrasound scanner (Vevo 770, VisualSonics Inc., Canada). In this chapter, the background of ultrasound and UCAs are reviewed mainly focusing on the principle, application and acoustic properties.

1.2 ULTRASOUND

1.2.1 Principles of ultrasound

Ultrasound is the transmission of mechanical vibration through a medium (gas, liquid or solid) with a frequency greater than the upper limit of human hearing 20 kHz

(McDicken 1991). In medical applications, ultrasound is often used to produce images of human tissue, which mainly comes from three aspects: (1) the reflection and refraction of the ultrasonic waves at large boundaries, (2) the scatter of the ultrasound wave from small particles, (3) the sound absorption by the bio-tissue (Hoskins 2002).

1.2.2 Properties of ultrasound transducer

Ultrasound transducer refers to the device manufactured of piezoelectric material that is capable of converting the energy between sound wave and electronic signal (Zagzebski 1996). An array transducer is most commonly used in clinical ultrasound due to the advantage in temporal resolution, adjustable focal length and bandwidth (Hoskins et al. 2010), although a single element transducer may be used in special applications, e.g., ophthalmology (Silverman 2009) and in research like studies of this thesis. Types of array transducers include linear-, curvilinear, phased- and annular- array, classified by the assembled shape of piezoelectric elements. Except annular array, all the other three types of transducer enable electronic beam steering across the imaging field without mechanical movement of the transducer (Zagzebski 1996).

1.2.3 Applications of ultrasound

Compared with other non-invasive medical imaging techniques in clinical diagnosis (e.g., computed tomography (CT), positron emission tomography (PET) and magnetic resonance imaging (MRI)), the popularity of ultrasound arises from its cost effective, portable advantage, providing high resolution and real-time images and most importantly the lack of ionizing radiation (Kips et al. 2008). Table 1.1 summaries the penetration and resolution of the discussed modalities. In addition to imaging, ultrasound can also be used in therapeutic medical tool and mainly applies high-intensity focused ultrasound (HIFU).

Table 1. 1: *Parameters of various clinical imaging modalities (Dobrucki and Sinusas 2005)*

Modality	Penetration	Spatial resolution	Temporal resolution
Ultrasound	mm-cm	50-500 μm	real time
CT	No limit	50-200 μm	min
PET	No limit	1-2 mm	10s-min
MRI	No limit	25-100 μm	min-hrs

1.2.3.1 The principal of imaging modes and techniques

Ultrasound imaging is widely used in medical diagnosis, such as cardiology, obstetrics, gynecology and abdominal imaging (Ali et al. 2008). It is predominantly a pulse-echo technique which is used in ultrasound imaging technique (Fish 1990). The speed of sound varies as it travels through different media. Media have an acoustic impedance that is equal to the product of the velocity and density of the material. The impedance mismatch between two adjacent media through which the sound propagates leads to the difference in amplitude of the reflected echoes. The amplitude of the echo determines the brightness of the pulse displayed on the screen. The distance between the reflection or scatter interfaces is determined by the time of arrival of the echoes from these interfaces to the scanner, assuming a speed of sound in soft tissue of 1540 $m \cdot s^{-1}$. Pulse-echo imaging basically functions in two modes: B-mode and M-mode.

Brightness modulation (B-mode) is the most commonly used ultrasound imaging mode. Two dimensional greyscale images in B-mode are generated by ultrasound beam scanning through the tissue. The brightness of each spot on the image indicates the amplitude of the echo and the position calculated from the time of arrival of the returning echo. **Motion mode (M-mode)** is primarily designed to show the rapid motion of heart valves or vessel wall along one ultrasound line. The sweeping lines indicating the movement of all the points at various depths down one scan line as a

function of time. Due to fixing on only one scanning line, M-mode improves the temporal resolution and hence is particularly useful in visualising fast-moving structures such as heart valves.

Doppler mode is used to display blood velocity within a pre-selected sample volume. The velocity is calculated using the Doppler effect, which calculates the shift in the observed frequency of a wave resulting from the motion of the wave source or scatterer (McDicken 1991). The mathematical expression of Doppler principle is:

$$f_D = \frac{2v\cos\theta}{c} f_0 \tag{1.1}$$

where f_D is the Doppler shift. f_0 and c are the frequency and speed of the incident ultrasonic wave. θ is the angle between the testing object (e.g., vessels) and the insonating ultrasound beam, *v is* the moving speed of the object, for example the velocity of blood fluid. Thus by measuring the Doppler shift, the velocity and the direction of the reflector or scatterer are monitored. Pulsed-wave (PW) Doppler, Colour Doppler and Power Doppler are three common used modes in a clinical ultrasound scanner.

PW Doppler ultrasound is used to depict the movement of blood within the selected sample volume – usually positioned within a blood vessel. The Doppler sample volume is aligned along the length of the vessel enabling the velocity of blood to be calculated using equation 1.1. On the graphic display of the PW-Doppler mode, there is a baseline indicating that there is no blood flow. If the fluid is moving away from the transducer, then there is a negative frequency shift and a positive frequency shift if blood moving towards transducer. **Colour Doppler** echoes are displayed with colours rather than grey scale brightness. The colours depict local flow in the *x-y* plane by estimating the mean Doppler frequency shift at a particular position. The brightness of the colour represents the intensity of the echoes (Martinoli et al. 1998). **Power Doppler** depicts the amplitude or power of Doppler signals rather than the frequency shift. The power is determined by the amount of

flow present and leads to advantages including: higher sensitivity to flow and better edge definition of the smaller vessels, but at the expense of directional and velocity information (Martinoli et al. 1998).

Ultrasonic elastographic technique measures the Young's modulus of tissue to help diagnose the lesion and tumour in the tissue as the malignant tumour is generally stiffer than the benign tissue (Ophir et al. 2002). Two underlying ultrasound approaches are generally used to measure the Young's modulus, E (Hoskins et al. 2010). The first method is strain technique, i.e., static method, E=stress/strain, where strain, the change in dimension of tissue (equal to the relative displacement dividing the original length) is measured after applying a known force, stress equals the quotient of the force and the cross-sectional area. The second method is shear-wave technique, i.e., dynamic method, $E=3\rho C_s^2$, ρ is the density, C_s is the measured speed of the shear wave after inducing shear waves in tissue.

1.2.3.2 Therapeutic ultrasound

Therapeutic ultrasound has been studied in the fields of **physiotherapy** (mainly in treating soft tissue injuries, accelerating wound healing and softening scar tissue), **bone healing** (mainly use low intensity ultrasound to enhance bone repair rate and reduce healing times), **enhancement of drug/gene uptake** (mainly in raising the penetration of pharmacologically active drugs through the skin/ increasing the transfer rate of genes to diseased tissues and organs) and **High Intensity Focused ultrasound (HIFU)** (ter Haar 2007). Among these ultrasound therapies, HIFU is a surgical tool by using high intensity focused ultrasound on diseased tissue (Kennedy 2005) and it is rapidly gaining clinical acceptance (ter Haar 2008). Compared with the low intensities (~0.1 $W \cdot cm^{-2}$) used in common ultrasound imaging, the high intensities applied in HIFU are up to 1000 $W \cdot cm^{-2}$ and show thermal ablation (coagulative necrosis) in the focal volume without damaging the surrounding tissue (ter Haar 2008). With the guidance of ultrasound or MRI, HIFU has been used clinically in treating uterine fibroids, the cancer of liver, kidney, breast, bladder and prostate (Kennedy et al. 2003).

1.2.4 Measurements of ultrasound parameters

The acoustic characterisation of ultrasound includes quantification of many parameters. In particular the speed of sound, attenuation and scattering are described here because: 1) the accurate knowledge of these parameters directly reflects the location of the object and its acoustic signature as discussed in the pulse echo imaging (section 1.2.2), 2) they are the parameters to be studied in this thesis.
The *speed of sound c* defines as

$$c = \sqrt{k/\rho} \tag{1.2}$$

where *k* is stiffness (Pa) of the medium the sound wave propagates, ρ is the density ($kg \cdot m^{-3}$) of the medium.

The *attenuation* is the reduction in ultrasound intensity as the wave passes through the medium. It is caused by absorption, scattering, beam divergence, reflection and refraction and increases with frequency (Fish 1990). The attenuation coefficient is the intensity decrease per unit path length at a specified frequency and expressed in $dB \cdot cm^{-1}$ (AIUM 1995).

The *scattering* describes the process in which part of the wave energy is redirected and appears separately to the original incident direction when a wave travels through a non-uniform medium (Hill 1986). Backscatter coefficient is the mean acoustic power backscattered into a unit solid angle per unit incident intensity per unit volume at a specified frequency and expressed in $cm^{-1} \cdot sr^{-1}$ (AIUM 1995).

1.2.5 High frequency ultrasound imaging and characteristics

With the development of high frequency ultrasound transducers, the well-established clinical imaging techniques can be transferred into application at high frequencies. Preclinical imaging is one of the most important applications for studying models of

the human disease like cancer (sizing tumour, quantifying tumour blood flow, contrast imaging, molecular imaging of angiogenesis) and cardiovascular disease (quantifying function of left ventricle, contrast perfusion imaging), and exploring developmental biology (evaluation of the development of embryo, role of mother and placenta during pregnancy) in small animals (Foster et al. 2011, Kagadis et al. 2010, Moran et al. 2012).

High frequency ultrasound has improved resolution compared to low frequency ultrasound. Spatial resolution is a parameter for assessing the imaging ability of a system by distinguishing closely spaced objects as distinct and visibly separate objects (González and Woods 2001). Specifically, the axial resolution/ lateral resolution/ elevation (azimuthal) resolution are defined as the smallest separation of a pair of targets at the same range on the beam axis/ in the scan plane/in the elevation plane (at the right angle of scan plane), which can be displayed as two separable images (Hoskins 2002). Both lateral resolution and elevation resolution approximate to half of the beam width (more details discussed in Chapter 2) on the scanning plane and elevation plane, respectively (Hoskins et al. 2010). Axial resolution approximates to half the pulse length (Hoskins et al. 2010).

One of the disadvantages of high frequency ultrasound is that the attenuation of the ultrasound beam increases and hence sacrifices penetration depth. To estimate the frequency dependence of attenuation $\alpha(f)$, a power law function is commonly used to fit the typical attenuation data and can be expressed as:

$$\alpha(f) = \alpha_0 f^n \tag{1.3}$$

α_0 and n are the material parameters characteristic of the sample. For tissues, the exponent n is generally in the range $1 \leq n \leq 2$. In particular, it was observed that n = 1.1 to 1.4 for fatty liver, n = 1.5 for spleen in the frequency range of 2-5 MHz (Narayana and Ophir 1984). Thus the choice of the transducer requires a balance between the depth of the object to be imaged and the resolution of the image quality.

1.3 ULTRASOUND CONTRAST AGENTS

1.3.1 Background and development

Ultrasonic contrast agents (UCAs) are gas-filled non-toxic microbubbles (MBs) designed to significantly enhance the diagnostic information in ultrasound clinical scans (Bouakaz and de Jong 2007). The ultrasound scatter from blood without the UCAs is much weaker than that from other tissue, typically 30 to 60 dB weaker at diagnostic frequencies (2 - 15 MHz) (Hoff 2001). The aim of introducing UCAs is to increase the backscatter of the ultrasound from the blood for several minutes and enhance the echo strength in grey scale or Doppler (Harvey et al. 2001). Figure 1.1 shows an improvement of endocardial definition after contrast administration by demonstrating a comparison of a four-chamber view of human heart pre and post contrast injection.

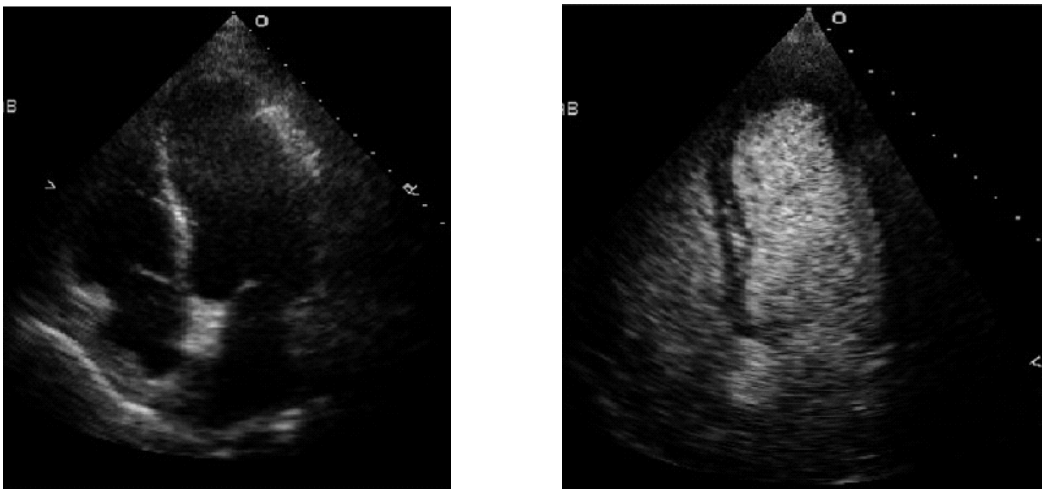

Figure 1. 1: *Examples of heart images in four-chamber view presenting poor endocardial definition at baseline (left panel) and improvement after contrast administration (right panel) (Kaufmann et al. 2007).*

The early publications of UCAs for medical ultrasound imaging dated back to the 1960s whereby saline was injected in the supravalvular position to observe the echoes from the aortic root and diagnose a defect on the aortic valve (Gramiak and

Shah 1968). Thereafter various classes of UCAs were developed such as free and encapsulated gas bubbles, colloidal suspensions, emulsions, and aqueous solutions (Ophir and Parker 1989). However, considering the instability of the free bubbles, toxicity of the colloidal suspensions and low scatter efficiency of emulsions and aqueous solutions, encapsulated bubbles proved to be the most promising approach for the manufacture of UCAs. The commercially available UCAs are reconstituted as a liquid containing encapsulated MBs with 1–7 μm in diameter, similar to the size of red blood cells (Cosgrove 2006).

Four transpulmonary UCAs are currently approved within European Countries: Levovist®, Optison®, SonoVue® and Luminity® (Claudon et al. 2008). Optical images of Definity (brand name of Luminity used in US market) after reconstitution and dilution are shown in Figure 1.2. The details of these commercial agents are described in Table 1.2.

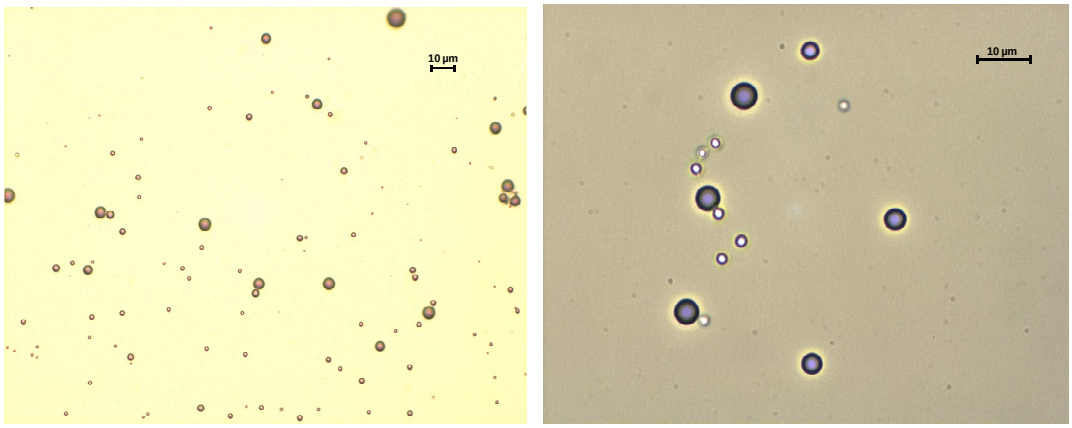

a. Definity bubble in 40× *b. Definity bubble in 100×*

Figure 1. 2: *Definity observed using an optical microscope (Olympus BH-2) and a digital camera system (Leica DC 300F) in a magnification of (a) 40 and (b) 100 times*

The encapsulated bubbles, performing as blood pool tracers, have overcome the instability and non-transpulmonary limitation of the free bubbles. By changing the surface tension of the MBs, e.g. choosing the type of gas and adjusting the material

component, thickness and structure of the shell, the stiffness and flexibility of the MBs can be controlled and can therefore influence their interaction with the ultrasound waves. On one side, the general requirement is to extend the duration of MBs *in vivo* by applying a pliable shell and including a low soluble gas of low diffusion, high density and stability. On the other side, fragility of MBs (collapse of MBs) and release and dissolution of the gas is helpful in assessment of tissue perfusion (Bruce et al. 2004). Additionally, fragility of the MB shell is also important for drug and gene delivery because the drug is generally encapsulated within the MBs and released after MBs collapse on the targeted tissue (Stride and Saffari 2003). Thus, MB composition determines the shell flexibility and fragility, the selection of which depends on the choice of application of UCAs.

Table 1. 2: *Clinical Ultrasound Contrast Agents licensed in Europe, information gathered from (Bristol-MyersSquibb 2006, Claudon et al. 2008, Correas et al. 2001, Piscaglia et al. 2011, Sboros 2008). Gas solubility and shell stiffness are noted as high (H) or low (L).*

Name	**Gas (solubility)**	**Shell (stiffness)**	**Size distribution**	**Applications**	**Manufacture**	**In production**
Levovist®	Air (H)	Galactose and palmitic acid as a surfactant (L)	99% < 10µm; mean diameter: 3µm	Heart, abdomen, vesico-ureteric reflux and transcranial	Schering, AG. (Germany)	No
Optison®	C_3F_8 (L)	Albumin (H)	95% < 10µm; Mean diameter: 4.5 µm	Cardiac wall motion studies	GE Healthcare Inc. (USA)	Yes
SonoVue®	SF_6 (L)	Phospholipids (L)	99% < 11µm; mean diameter: 2-3µm	Cardiac (endocardial border delineation), macrovascular (characterisation of focal lesions in liver and breast)	Bracco (Italy)	Yes
Luminity® (Definity)	C_3F_8 (L)	Phospholipids (L)	98% < 10µm; mean diameter: 1.1-3.3 µm	Left ventricular opacification	Lantheus Medical Imaging (USA)	Yes

1.3.2 Physics interactions of MBs with ultrasound waves

It has been shown that the magnitude of the peak negative pressure, which is incorporated in the Mechanical Index (MI), strongly influences MBs behaviour (Correas et al. 2001, Whittingham 2007). Since the degree of MB oscillation also depends on the properties of the MB itself, such as the shell characteristics, gas contained, size and concentration (Hoff 2001), the MI values should not be considered as definite thresholds but only as relative references.

The *Thermal Index* (TI) and *Mechanical Index* (MI) are standard indices for real-time display of mechanical and thermal acoustic output on diagnostic ultrasound equipment, which are used to quantify ultrasound bio-effects and safety. These indices were first prepared by the American Institute of Ultrasound in Medicine (AIUM) and National Electrical Manufacturers Association (NEMA) (Patton et al. 1994). TI is defined as the ratio of the total acoustic power to the power used to increase the temperature of tissue by 1°C under assumptions which relate with a simple tissue model and beam shapes (Duck et al. 1998). TI provides an estimate of the average increase in temperature that may occur in the region of the ultrasound scan and is generally displayed in three forms: TI for soft tissue (TIS), TI for bone (TIB) and TI for cranial bone (TIC)(BMUS 2009). MI is implemented as a safety parameter on ultrasound scanners to evaluate non-thermal ultrasonic bio-effects and is defined in Equation 1.4 (Apfel and Holland 1991)

$$\mathrm{MI} = \frac{P_{ra}}{\sqrt{f_{cn}}} \qquad (1.4)$$

where P_{ra} = peak rarefractional pressure (MPa), f_{cn} = transmitting central frequency (MHz). As an example, Table 1.3 listed the recommended MI and TI for general abdominal and peripheral vascular applications (BMUS 2009).

Table 1. 3: *Recommended MI, TI and exposure time for general abdominal and peripheral vascular applications, √ symbolizes no scanning times restricted, MI=0.3-0.7, there is a risk of capillary bleeding (BMUS 2009).*

Thermal Index value		**Mechanical Index value**	
0 - 1.0	> 1.0	0 - 0.3	> 0.7
√	Restrict time to 1.0<TIB≤1.5 : 120 min 1.5<TIB≤2.0 : 60 min 2.0<TIB≤2.5 : 15 min 2.5<TIB≤3.0 : 4 min 3.0<TIB≤4.0 : 1 min 4.0<TIB≤5.0 : 15 sec 5.0<TIB≤6.0 : 5 sec TIB>6: not recommended	√	Risk of cavitation with UCAs

The dynamic motion of MBs varies with the local acoustic field shown in Figure 1.3.

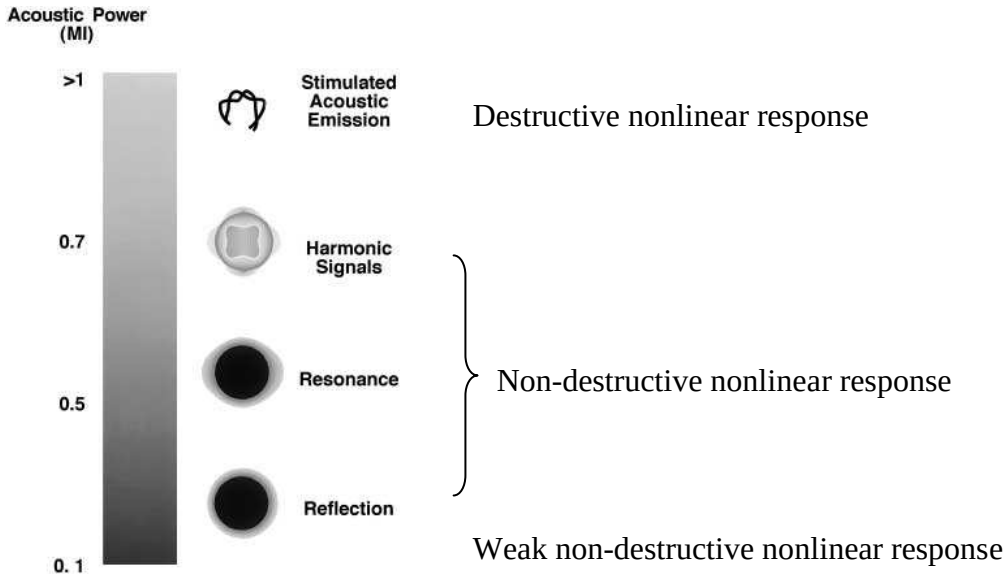

Figure 1. 3: *Response of MBs with MI range in the frequency range 1-9 MHz in response to a pressure range from 0.1 to 3MPa (Correas et al. 2001, Harvey et al. 2000)*

At low MI value (<0.1), MBs respond with linear oscillation (equal expansion and contraction) (Burns and Becher 2000) shown in Figure1.4.a. MBs act as efficient scatterers due to the large difference in impedance between the gas contained and the medium in which the MBs are suspended and also due to the bubbles oscillating in the acoustic field (Quaia 2007). Low MI imaging is appropriate for Doppler applications as well as for real-time contrast imaging because MBs experience a long lifetime (Correas et al. 2001).

In a non-destructive oscillating process when resonance occurs, MBs begin to oscillate at the same frequency as the insonation frequency and the acoustic pressure response producing maximum signal enhancement. The *resonant frequency* can be approximately calculated by Equation 1.5 (Ophir and Parker 1989)**.** The derivation of this equation adapts a linear theory of harmonic oscillators by assuming bubbles oscillate with small amplitude without considering the damping terms.

$$f_0 = \frac{1}{2\pi a}\sqrt{\frac{3\gamma P_0}{\rho_0}} \tag{1.5}$$

where f_0 = resonant frequency, a = bubble radius, P_0 = the ambient fluid pressure, ρ_0 = density, γ = adiabatic ideal gas constant. The predominant resonance frequency of clinical MBs occurs within the clinical frequency range 1-20MHz (Harvey et al. 2000).

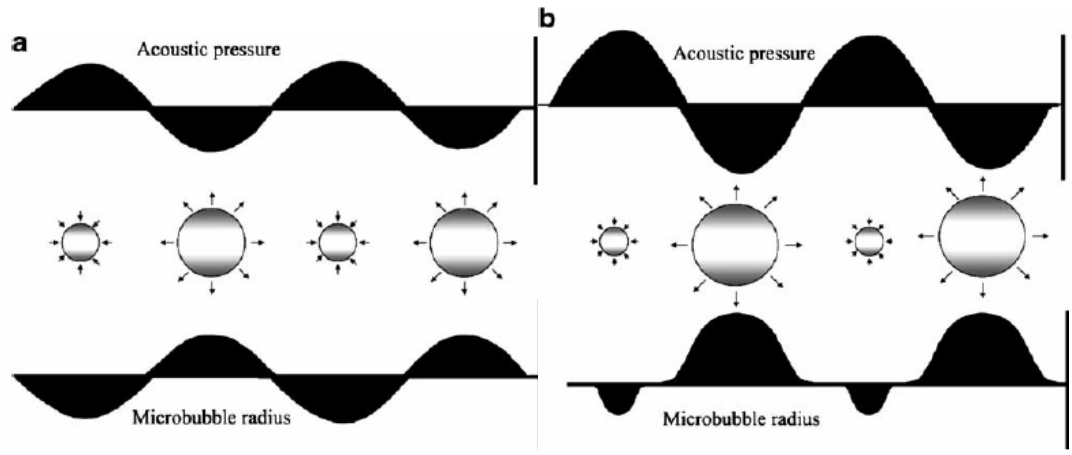

(a) Linear response *(b) Nonlinear response*

Figure 1. 4: *Diagram of the size variation of MBs with different insonation pressure (a) linear response of MB at low pressure, (b) asymmetry oscillation and nonlinear response of MB in response to high insonation pressure (Quaia 2007).*

When the MI increases, the pulsation of the MBs becomes nonlinear resulting in non-linear signal propagation. Figure 1.4.b illustrates the nonlinear oscillation of MBs. Their expansion during the negative cycle of the pressure exceeds the contraction during the positive part. At these pressures the nonlinear response at harmonic frequencies are different to that of the incident wave (fundamental frequency), the frequencies of which include the subharmonic (half of the fundamental frequency), ultraharmonic (1.5 times of the fundamental frequency), second harmonic and higher harmonics (Correas et al. 2001).

Using high MI (>1) values leads to the destruction of MBs (Whittingham 2007). The shell is broken and the gas rapidly diffuses into the surrounding medium. The sudden collapse of MBs produces a transient response, known as stimulated acoustic emission (SAE). SAE is a short-lived phenomenon due to the dissolution of the gas, but it provides the most sensitive detection of UCAs particularly when coupled with colour or power Doppler (Correas et al. 2001). Other applications of these characteristics of MBs are described in section 1.3.6.

1.3.3 Overview of MBs phenomena

Dynamic behaviour of encapsulated MBs has been summarized and categorized by Postema (Postema et al. 2004). There are a number of MB phenomena that have been observed by ultra-high speed cameras: oscillation, translation, coalescence and bounce, fragmentation, sonic cracking and jetting. *Oscillation* is the alternate expanding and contracting bubble response to an acoustic pulse. At low driving pressures, bubbles pulsate moderately. When acoustic amplitude increases, inertial (transient) cavitation occurs: a longer expansion phase of the MBs which is followed by a rapid contraction (collapse) (Postema 2004). MB *translation* has been attributed to primary and secondary radiation acoustic forces, the former of which is due to the pressure gradient across the bubble surface and the latter of which is due to the varying pressure fields generated by oscillating bubbles. When MBs translate towards each other, two or more bubbles can fuse. This phenomenon is named *coalescence*. If coalescence does not occur, the bubbles appear to effectively *bounce* off one another (Postema et al. 2004). Coalescence is mainly caused by the attracting molecular force (Van der Waals force) between the adjacent bubbles when they become close and thin shell surface of expanding bubble reaches a thickness threshold around 0.1μm at which point the two shells of bubbles merge to form a larger bubble (Duineveld 1997). *Fragmentation* is the fission of MBs into smaller bubbles. Sonic cracking is the process of gas escaping from MBs because of the ultrasound wave causing shell defects. *Jetting* is the asymmetrical collapse of a microbubble near a boundary resulting in a high speed jet projected through the bubble towards the boundary (Barnett 1998). The therapeutic potentials of these phenomena in drug and gene delivery have been considered (Postema et al. 2004) and discussed in section 1.3.6.

1.3.4 Theoretical modelling of UCAs

The behaviour of MBs when insonated by ultrasound can be investigated through two main tools: theoretical modelling and experiments. The theoretical modelling tool for studying MBs can be catalogued into two approaches (Leighton and

Dumbrell 2004): 1) a study of empirical acoustic scattering cross-sections, 2) dynamics of single MBs.

Acoustic scattering is a diffuse reflection as opposed to specular reflection. Scattering of ultrasound occurs when waves propagate through a non-uniform medium and part of the energy is forced to deviate from its original trajectory (Hill 1986). It is a function of the scattering cross-section σ. The average diameter of the UCAs is less than the capillary diameter 7 μm and thus the UCAs are much smaller than the wavelength of the high frequency ultrasound (e.g., frequency = 30 MHz, wavelength = 51 μm), not to mention the wavelength (200 μm -500μm) of the diagnostic ultrasound (assuming speed of sound is 1540 $m \cdot s^{-1}$). Thus, scattering from UCAs can be explained using Rayleigh scattering theory. Rayleigh scattering describes a linear scatterer (when MB driven at low pressure), the size of which is much smaller than the incident ultrasound pulse wavelength, σ is defined as (Morse and Ingard 1986):

$$\sigma = \left(\frac{4}{9}\pi R^2 (KR)^4\right)\left(\left(\frac{\kappa_s - \kappa}{\kappa}\right)^2 + \frac{1}{3}\left(\frac{3(\rho_s - \rho)}{2\rho_s - \rho}\right)^2\right) \tag{1.6}$$

i.e., rewritten in the format of $\sigma = A_R\left(\gamma_k^2 + \frac{1}{3}\gamma_p^2\right)$

where R is the radius of the scatterer (<< λ), λ is the wavelength, k=2π/λ is the wavenumber, κ_s and κ are the compressibility of the scatterer and the surrounding medium, ρ_s and ρ are the density of the scatterer and the surrounding medium. A_R is the amplitude term, γ_k^2 is the compressibility term and γ_p^2 is the density term.

The advantage of the first type of theoretical modelling tool is that it is simple to apply and the simulation of the scattering cross section can be directly related to the measurement of MB population. However, this class provides limited information of the fundamental physics of the response of individual MBs to the propagation of ultrasound.

The second type of studies the dynamic oscillation of single bubble based on the previous models. Rayleigh-Plesset-Noltingk-Neppiras-Poritsky (RPNNP) model (Leighton 1997) (Equation 1.7) is the basic motion equation for simulating UCAs and describing the radical oscillation of a free bubble in a viscous and incompressible fluid.

$$R\ddot{R}+\frac{3\dot{R}^2}{2}=\frac{1}{\rho_L}\left[\left(P_0+\frac{2\sigma}{R_0}-P_v\right)\left(\frac{R_0}{R}\right)^{3\kappa}+P_v-\frac{2\sigma}{R}-4\eta_L\frac{\dot{R}}{R}-P_0-P(t)\right] \qquad (1.7)$$

Parameters of MB:

R is the instantaneous radius of MB, $\dot{R}$ =dR/dt is the speed of MB wall, $\ddot{R}$ = d^2R/dt^2, R_0 is the rest radius, κ is the polytropic exponent of gas also the ratio of specific heat of gas.

Pressures:

($P_0 - P_v + 2\sigma/R_0$) is the pressure of the gas in the MB at equilibrium status, P_0 is the hydrostatic pressure at rest, P_v is the vapour pressure in the MB, $2\sigma/R_0$ is the Laplace pressure and σ is the surface tension, P(t) is the driving pressure.

Parameters of liquid:

η_L is the dynamic viscosity, ρ_L is the density.

In addition to the RPNNP equation, other motion models e.g., Herring, Trilling, Keller-Miksis equations were developed with consideration of the radiation damping (caused by compressive liquid) and thermal damping (caused by thermal conduction between the gas and liquid) (Doinikov and Bouakaz 2011).

Based on the RPNNP model, models for encapsulation of the MBs were explored using two methods (Doinikov and Bouakaz 2011): 1) adding phenomenological terms of empirical observations or ad hoc assumptions from encapsulated bubbles to RPNNP equation (e.g., de Jong model) and 2) rigorous derivation from RPNNP equation incorporating assumptions of encapsulated bubbles (e.g., Church model).

Solving these differential equations yields the bubble radius as a function of time. The scattered pressure P(r) at distance r can be calculated using Equation 1.8 (Vokurka 1985),

$$P(r) = \frac{\rho R}{r}\left(R\ddot{R} + 2\dot{R}^2\right) \tag{1.8}$$

where ρ is the density of the liquid, R is the radius of the MBs, $\dot{R}$ = dR/dt is the speed of MB wall, $\ddot{R}$ = d^2R/dt^2.

1.3.5 Experimental study of UCAs

Optical and acoustic methods are the two main experimental tools to study UCAs. Results obtained from these experimental methods can be inserted into theoretical models, such as Equation 1.7, and can be used to inform the model optimizations of single bubbles.

Optical experiments using high-speed camera capture the radial oscillation of individual MBs and the acoustic and frequency response can be calculated. Two such systems were built: Brandaris128 in Erasmus MC (Chin et al. 2003) and the other in the Centre for Ultrasound Molecular Imaging and Therapeutics, University of Pittsburgh (Chen et al. 2012). Based on a design of rotating mirror camera, both systems have a maximal frame rate of 25 Mega-frames per second and can save 128 frames in a single run, while the camera in Pittsburgh shows a higher resolution (1392×1040 pixels) than the one in Erasmus (500×292 pixels).

The limitation of the theoretical models and the corresponding experimental results are that only the wall dynamics and the radiated pressure field of bubble are calculated and no key propagation characteristics e.g., speed of sound, backscatter and attenuation are determined. From the description of pulse echo imaging, the travel time of the received signals depends on the accurate knowledge of the speed of sound through the medium through which the ultrasound wave is travelling. The interpretation of the amplitude of the received signal is compromised without the correct information of attenuation (Leighton and Dumbrell 2004). Acoustic

backscatter measurement is a direct measurement of the efficiency of the UCAs to scatter ultrasound back to the transducer (Hoff 2001).

The physical properties of the MBs and their response to ultrasound are not fully understood and still attract continuing research. These properties are generally divided into three aspects (Sboros 2008): the effect of the ultrasonic pulse (frequency, phase, acoustic pressure, pulse duration), the MB composition (shell, gas, MBs dispersions), and the MBs environment (the liquid environment, the presence of a wall, tube and other MBs). All these factors impact the oscillation of the MBs, and further determine their scattering and effectiveness for contrast enhanced imaging. The published work does not present a comprehensive description of the behaviour of MBs in the ultrasound field due to the usage of varying UCAs (both in-house and commercial compositions) under varied experimental conditions. This thesis is predominantly experimental and focuses on the bulk acoustic characterisation of UCAs.

1.3.6 Techniques and applications of UCAs

1.3.6.1 Techniques of contrast imaging

It is assumed that after injection of UCAs, the MBs mix freely with the blood and thus highlight the presence of blood within the body. The key to enhancing the signal to noise of the contrast-enhanced image is to separate the signal from UCAs and the surrounding tissue to study the blood flow pattern of the lesion. The techniques behind contrast applications are generally classified based on the pulse transmission and signal processing (Quaia 2007) and can be categorized under two mechanisms: 1) at low insonation pressure, the nonlinear response from MB oscillations without destruction; 2) at high pressure, the nonlinear response from the disruption of MBs (Claudon et al. 2008). The second technique also known as high MI imaging or intermittent imaging or stimulated acoustic emission is generally applied in perfusion studies (Hoskins et al. 2010). It used high power multi-pulses to disrupt MBs then observed the subsequent refilling of MBs in tissue under low MI values (Chomas et

al. 2001). As an example of perfusion, Figure 1.5 shows a variation in backscatter signal in a selected ROI within the myocardium after infusion of SonoVue using a pulse-inversion imaging technique. The principle of pulse-inversion technique is shown in Figure 1.7. The sharp decline in amplitude represents the disruption of microbubbles after a high MI insonation. The following curve shows the reperfusion of the microbubbles under a low MI value and its oscillatory variation represents the movement of the heart.

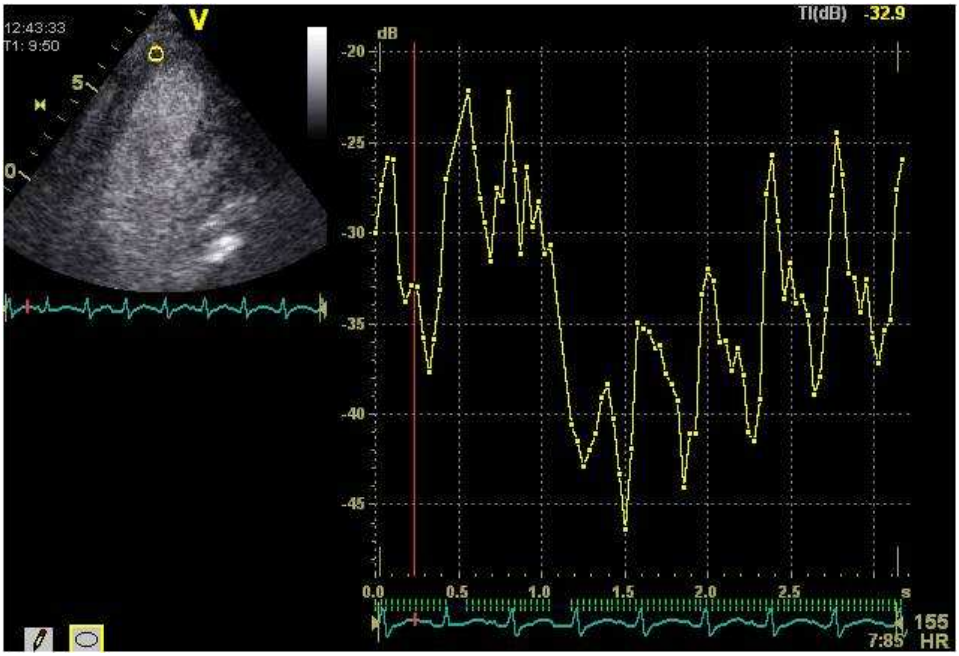

Figure 1. 5: *Example of clinical contrast perfusion study of apical two-chamber view of left ventricle. Image courtesy of Dr Stephen Glen, Sterling Royal Infirmary, Scotland.*

More imaging techniques focus on the nonlinear properties of MBs when insonated using non-destructive low-pressure ultrasound pulses. Table 1.4 lists the typical methods of grey scale imaging of contrast microbubbles employed by ultrasound researchers. Although contrast has been used to rescue failed Doppler examinations in detecting renal arteries and hepatic arteries (Leen 2001, Sidhu et al. 2006), methods for Doppler imaging are not included due to the limitations in blooming artefact (an artefact caused by the abnormal increase in flow signal strength displaying as the grey signal changing to colour in the region of no significant blood flow (Forsberg et al. 1994)) and signal saturation (Quaia 2007).

Second harmonic imaging utilises the nonlinear properties of the MBs at higher insonating pressure (0.1<MI<0.5 (Correas et al. 2001)) and multi-cycle pulse (Qin et al. 2009) to separate the blood signal from the surrounding tissue (de Jong et al. 2000). However, with increasing insonating pressure the second harmonic component of tissue increases accordingly. The tissue harmonic signal is caused by the nonlinear propagation of the sound wave through tissue in terms of the distortion of the waveform. Specifically, the compression part of the signal becomes tall and narrow while the rarefaction part becomes short and wide shown in Figure 1.6 (Duck 2002). The distorted compression part of the wave is in response to the harmonic components in the spectrum (Hoskins et al. 2010). Subharmonic imaging is introduced since the subharmonic component is a unique property of MBs, i.e., tissue does not generate subharmonics, but compromises resolution especially in the clinical frequency range (de Jong et al. 2000). More detailed description of the generation of subharmonics is given in Chapter 6.

Table 1. 4: *Summary of non-destructive contrast ultrasound techniques (Quaia 2007). Micro-flow imaging is used to observe the slow perfusion within an organ by summing the intensity of multi-consecutive frames and comparing their differences (Quaia 2007).*

Harmonic imaging	Phase modulation	Amplitude modulation	Phase and amplitude modulation	Coded imaging
- 2nd harmonic - Subharmonic - Ultra-harmonic	-Pulse inversion -Micro-flow imaging - Coherent contrast imaging	Power modulation	Cadence contrast pulse sequencing	-Chirp excitation -Coded harmonic

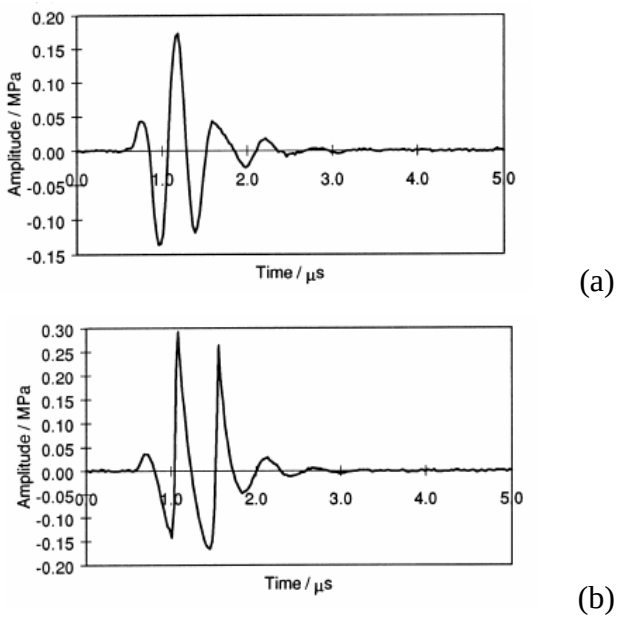

Figure 1. 6: *An example of nonlinear propagation of 2.25 MHz pulse through water (a) the waveform at the transducer and (b) the distorted waveform after propagating 0.6m (Humphrey 2000).*

Pulse inversion technique shown in Figure 1.7 is a typical phase modulation method in which two successive pulses of opposite phase at low pressure are transmitted and the two received signals are summed. At low pressure, the linearity of the tissue leads to the cancellation of the two signals whereas the nonlinear components from MBs can be saved to discriminate the signal from the tissue (Burns et al. 2000).

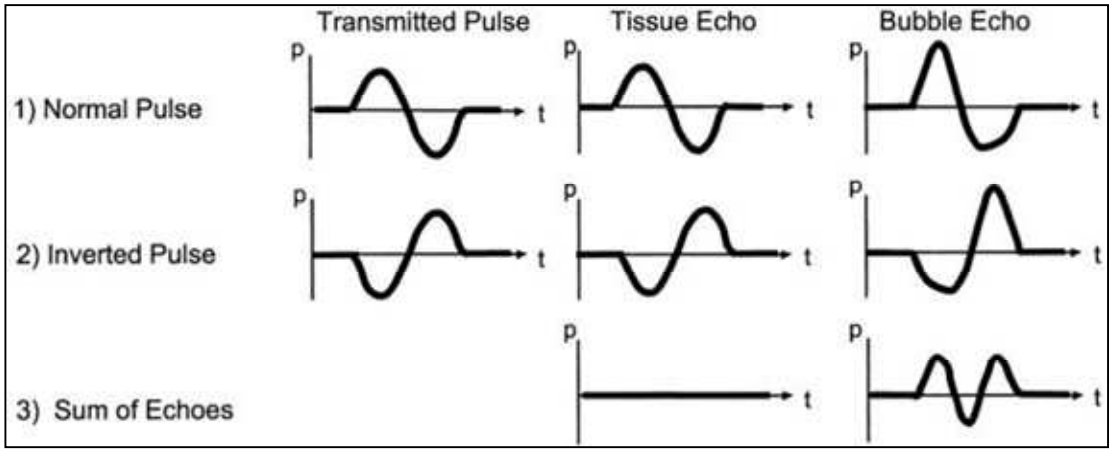

Figure 1. 7: *Basic principle of pulse inversion imaging (Burns et al. 2000)*

Similarly using the linearity of the tissue and the nonlinear response of MBs to ultrasound at low pressure, other modulations like amplitude or a combination of phase and amplitude modulation (Cadence contrast pulse sequencing shown in Figure 1.8) improve the sensitivity of detection of MBs (Quaia and Whittingham 2005). Chirp excitation represents one type of coded transmission pulses which improves the signal to noise ratio and increases the sensitivity at low transmission amplitude (Quaia and Whittingham 2005). This method transmits a chirp signal (frequency and amplitude of the signal varied with time) and employs a matched filter as a reference signal to compare and integrate with the received signals, the output of which signify the chirp signal and compress the non-chirp noise (Quaia and Whittingham 2005).

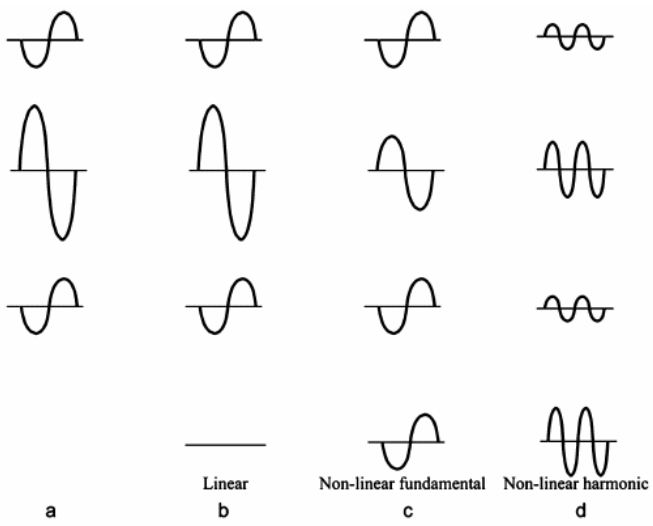

Figure 1. 8: *Basic principle of Cadence contrast pulse sequencing (Quaia and Whittingham 2005), (a) the transmitting three pulses include two pulses for which the amplitude is half of the other one with inverse phase, the sum of the resultant pulses through (b) a linear system, and through (c) and (d) a nonlinear system in terms of fundamental and harmonic components*

1.3.6.2 Applications of imaging

UCAs for medical imaging has been applied in the fields of heart (Edler and Lindström 2004), liver (Leen et al. 2006), kidney (Bertolotto et al. 2008), pancreas (Badea et al. 2009), blunt abdominal trauma (Catalano et al. 2009). Recommendations on clinical practice have been reviewed extensively by European Federation of Societies for Ultrasound in Medicine and Biology (EFUMB) (Claudon et al. 2008, Claudon et al. 2012, Piscaglia et al. 2011). Echocardiography and ultrasound of focal liver disease have been reported to evolve most with contrast-enhanced ultrasound (CEUS).

Heart

Echocardiography has been routinely used in bedside clinical diagnosis for the evaluation of myocardial function, cardiac anatomy and blood flow, because the relative blood volume fraction of myocardium primarily consists of capillaries, arterioles and venules (Kaufmann et al. 2007). For the patients who have difficulty with transthoracic ultrasound imaging due to obesity, recent thoracic surgery and lung disease, the evolvement of UCAs improves the sensitivity for microvasculature imaging and echocardiography, which is referred as myocardial contrast echocardiography (MCE). Left ventricular cavity opacification (LVO) has been approved clinically for increasing endocardial border delineation and detecting wall motion abnormalities operated at MI (0.4-0.5) (Kaufmann et al. 2007). Quantification of myocardial blood volume and flow rate employs the principle of perfusion by insonating high MI to disrupt the MBs (Wei et al. 1998). Figure 1.9 shows an example of a perfusion curve. The plateau of Video intensity (A) of the perfusion curve represents the blood volume in the measured region. The replenishing rate (β) of MBs into the microvasculature after the destruction of MBs represents the myocardial blood flow.

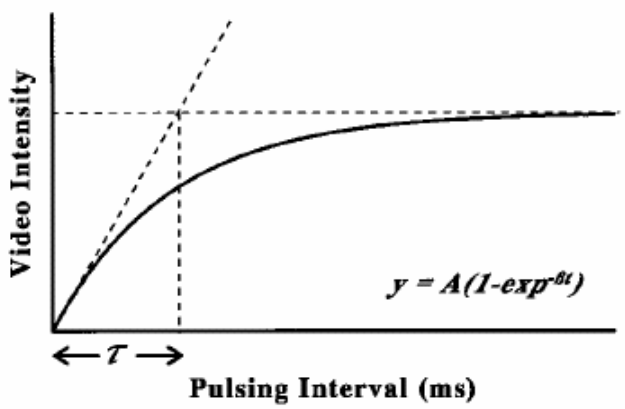

Figure 1. 9: *An example of perfusion curve as pulse interval (x axis) versus video intensity (y axis), dash line is the model prediction and solid line is the experimental observation. The function is used to derive the blood volume A and replenishing rate β (Wei et al. 1998)*

Liver

The liver imaging for lesion characterisation is of most advanced areas in the development of CEUS (Claudon et al. 2008). The appearance and flow of UCAs post-injection follow the blood supply of the liver and this process is divided into 3 phases: arterial, portal venous (PV) and later phases. Table 1.5 shows the time for visualizing these 3 phases, in which arterial phase is for acquiring the vascular pattern, PV and late phase is notably important for identifying the property of the focal lesion. Hypo-enhancing image is generally regarded as malignant lesions because here the wash out of UCAs is slower than the normal liver tissue shown in Figure 1.10. Iso- or hyper-enhancing image is mostly from the benign lesions. Low MI technique is recommended for CEUS for liver imaging in the clinical practice. More details of characterizing the lesions in response of the phases can be found in (Claudon et al. 2008, Claudon et al. 2012).

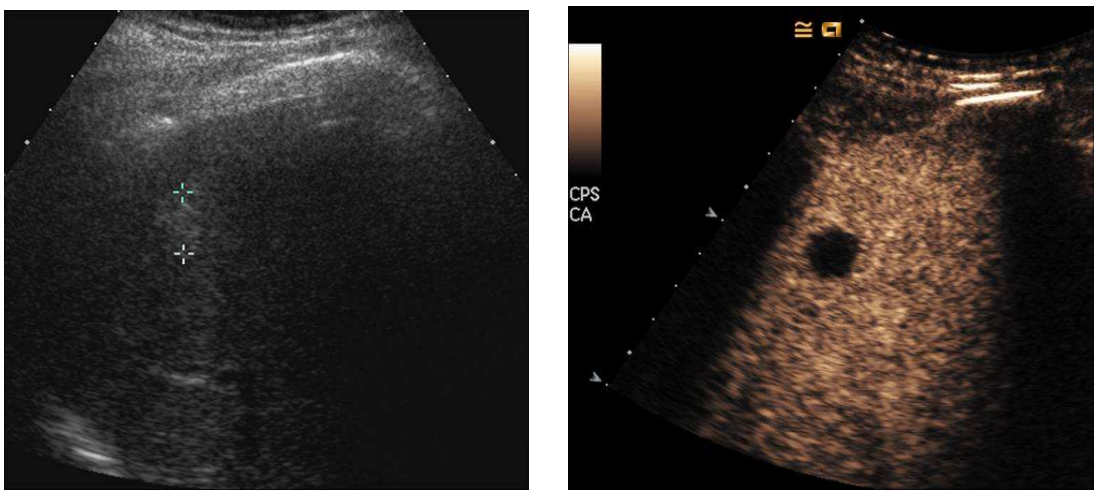

Figure 1. 10: *Left image with an echogenic liver metastasis (between callipers) acquired in fundamental imaging, Right image acquired 1 min 24 secs after bolus injection of SonoVue (portal-venous stage). Images courtesy of Dr Paul Sidhu, King's College Hospital, London, UK.*

Table 1. 5: *Hepatic vascular phases in CEUS (visualization post injection time) (Claudon et al. 2012). The onset of each phase time may vary due to the difference in individual global haemo-dynamic situation*

Phase	**Visualization post-injection time (seconds)**	
	Start	End
Arterial	10 - 20	30 - 45
Portal-venous (PV)	30 - 45	120
Late	>120	Bubble disappear (≈ 240 - 360)

Therapy applications

Another important area of research is in the area of drug and gene delivery and targeting of UCAs. Drugs and genes can be incorporated into UCAs by tailoring the physical properties of MBs and coating materials (Unger et al. 2001). As vehicles,

MBs may load drugs either outside or inside (Unger et al. 2002). Outside, drugs may be attached to the membrane surrounding, or imbedded within, the membrane or bound non-covalently to the surface of the MBs. Inside, drugs may enter into the MBs or some drugs e.g. hydrophobic drugs can form a oil layer (i.e. film) around MBs then the entire is stabilized by a membrane (Unger et al. 2002). Targeted UCAs allows attachment of the microbubbles to specific markers of disease by choosing an appropriate attachment strategy 1) electrostatic or intrinsic properties of shell components (Lindner 2002); 2) ligands (monoclonal antibody, carbohydrate ligand, covalent or avidin-biotin pair, long polymer spacer arm between the MB membrane and ligand) (Liu et al. 2006). Triggered by ultrasound, the cavitation of MBs releases the carried drugs or genes on the targeted site of the lesion and increases the permeability of the tissue (known as sonoporation). Preclinical studies have been performed using these techniques to improve cancer treatment (Frenkel 2008) and thrombolysis (Takeuchi et al. 1999).

The reviews of the fundamental and subharmonic response of UCAs at high frequency are included in the introduction section of Chapter 5 and 6, respectively.

1.4 THESIS OUTLINE

This thesis describes the experimental set-up and methods employed to quantify the acoustic characterisation of lipid encapsulated UCAs at high frequencies. The structure of thesis is briefly outlined below.

Chapter 1 introduced the background of ultrasound, UCAs and the interaction between UCAs and ultrasound.

Chapter 2 describes the acoustic characterisation of the preclinical Vevo770 scanner used in this thesis. The pressure in response to the power output, transmitting frequency and spatial beam profile of each of the five high frequency transducers are quantified using a membrane hydrophone (Precision Acoustics Ltd., Dorchester, UK).

Chapter 3 presents the experimental set-up and develops MATLAB codes based on a broadband substitution technique to calculate the speed and the attenuation of sound in an agar-based tissue mimicking material (TMM) over the frequency range 12-47MHz.

Chapter 4 studies the acoustical properties of three commercially available lipid encapsulated UCAs including two clinical UCAs Definity (Lantheus Medical Imaging, USA) and SonoVue (Bracco, Italy) and one preclinical UCA MicroMarker (untargeted) (VisualSonics, Canada) using the software and techniques developed for TMM characterisation. The attenuation and normalized backscatter power are investigated as a function of concentration and pressure, respectively.

Chapter 5 presents the influence of size distribution on the fundamental response (attenuation and contrast-to-tissue ratio (CTR)) of the three lipid UCAs (Definity, SonoVue and MicroMarker) in the frequency range 12-43 MHz.

Chapter 6 presents the theoretical simulation of single MBs using BUBBLESIM toolbox and investigates the influence of incident parameters (pressure, frequency and number of cycle) on the subharmonic response of three UCAs (Definity, SonoVue and MicroMarker). Incorporating the measured size distribution curve, the simulation result is compared with the experimental data of subharmonics of MBs at 25MHz (transducer 710B).

Chapter 7 investigates the effect of needle gauge, injection rate and temperature on the size distribution and acoustic properties of Definity and SonoVue in the frequency range 17-31 MHz. Statistical comparison is made for the two cases: the *in vitro* (19G needle gauge, 3ml/min injection rate, room temperature) and *in vivo* (27G and 30G needle gauge, 0.85ml/min injection rate, body temperature).

Chapter 8 summarizes the conclusions from each chapter and discusses future research.

Chapter 2

Characterisation of high frequency ultrasound transducers

2.1 AIM

The aim of this chapter is to characterise the high frequency transducers and to discuss the suitable parameter settings for the subsequent experiments. Specifically, 1) introduce the background of the Vevo 770 scanner and the procedure of raw data acquisition and analysis, 2) plot the beam profile of each transducer, 3) confirm the sensitive frequency range of each of the 5 transducers and 4) study the influence of the insonation power and pulse length (number of cycles) on the propagation of ultrasound through water in the high frequency range.

2.2 INTRODUCTION

The Vevo 770 scanner from VisualSonics Inc. is a high resolution, high-frequency ultrasound scanner (Figure 2.1). It operates within the frequency range from 25 to 55 MHz and supports seven ultrasound imaging modes: B-Mode, M-Mode, 3D-Mode, PW (Pulse Wave) Doppler Mode, Tissue Doppler Mode, Power Doppler Mode and Digital RF-Mode (VisualSonics 2006). The key advantages are its open architecture which allows comprehensive measurement and offline data analysis and an additional server connection is available for rapid remote access of files, images and measurements, which is beneficial to operator and researcher. The Vevo software outputs measurement and data for post-imaging analysis, and also exports image data for viewing in other applications, for storage or for use in presentations and publications (VisualSonics 2006).

2.2.1 Transducers

VisualSonics 700-Series RMV (real-time microvisualization) transducers are developed for high-resolution ultrasound imaging for small animal (preclinical) research. They feature a light and ergonomic design with maximum frame rates up to 200 frames per second (depending on the selection of RMV transducer, the field of view and sector size set for image acquisition) (VisualSonics 2006). Figure 2.2 shows the structure of the transducer. As a high frequency transducer, the 700-series scanhead is a single element transducer which functions as both the source and receiving transducer. The component is immersed in a coupling liquid (deionised and degassed water) within the transducer assembly. When the probe starts to operate, the transducer element is mechanically oscillated to allow the sweeping of the ultrasound beam across the plane of interrogation.

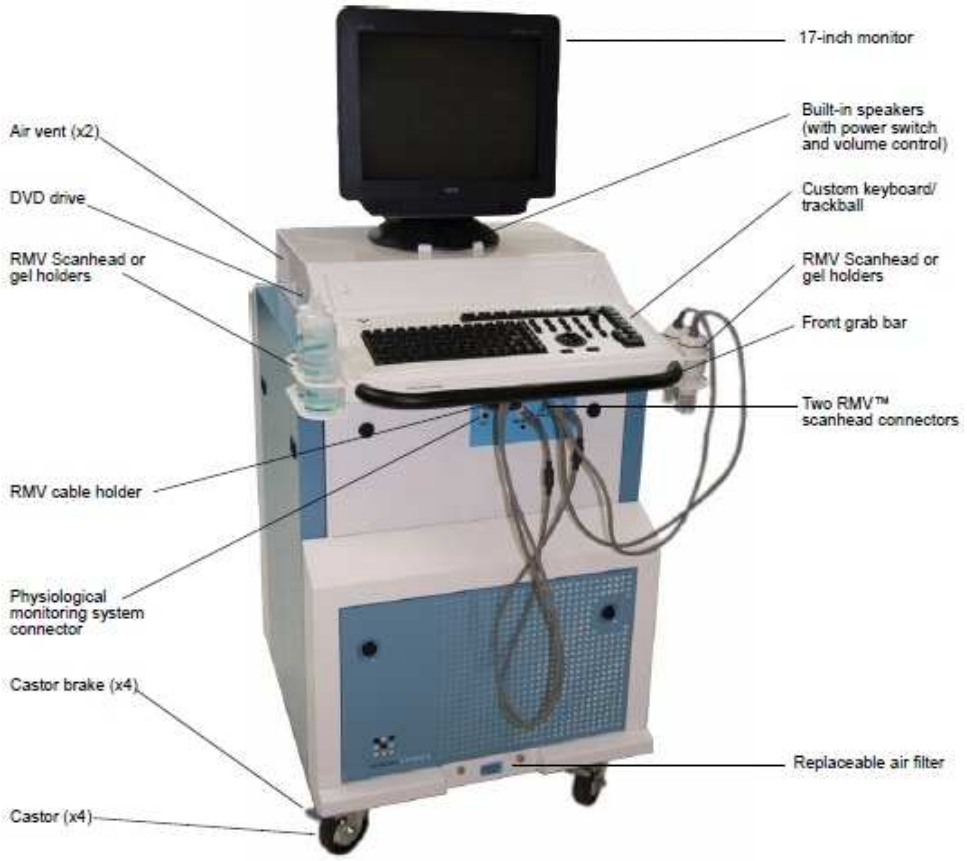

Figure 2. 1: *Front View of the Vevo 770 scanner (VisualSonics 2006)*

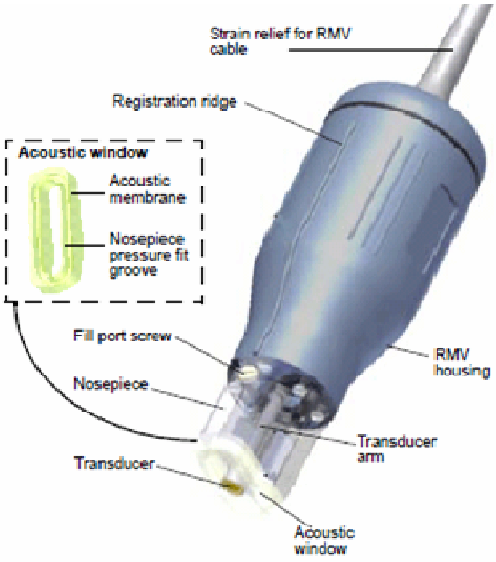

Figure 2. 2: *The structure diagram of RMV scanhead (VisualSonics 2006)*

Table 2.1 lists the main parameters of the transducers used for the experiments in this thesis. The five transducers from left to right in Figure 2.3 are 710B, 707B, 704, 711 and 708, the central frequency of which increase from 25 MHz to 55 MHz. For each of the transducers the physical size of acoustic window decreases with increasing frequency.

Table 2. 1: *Parameters of five transducers available for study as given by the manufacturer*

Model RMV	Central Frequency (MHz)	Focal Length (mm)	Axial Resolution (μm)	Lateral Resolution (μm)	Field of View (mm)
710B	25	15	70	140	20.0
707B	30	12.7	55	115	20
704	40	6	40	80	14.6
711	55	6	30	90	8.5
708	55	4.5	30	70	10.7

(a) 710B *(b) 707B* *(c) 704* *(d) 711* *(e) 708*

Figure 2. 3: *Front view of the transducers in Table 2.1*

2.2.2 RF mode

Digital radio-frequency (RF) mode is the main research mode of the scanner and able to provide the operator with the ability to acquire, digitize and export the raw RF data from pre-selected region of interest (ROI) for spectral analysis (VisualSonics 2006). The RF data has been used extensively to understand the properties of biological media in medical ultrasound (Insana et al. 1990, Lizzi et al. 1983). This mode is typically useful to study the frequency content of the returning echo. Figure 2.4 is a typical screen capture of the RF mode. In the process of scanning, the single element transducer sweeps back and forth to generate a real-time B-mode image shown in the right upper corner and zoomed in on a ROI shown in the bottom left corner of the screen. The red vertical lines in this zoomed window are individual lines of acquisition. For this case, 10 lines are chosen and these are evenly distributed throughout the ROI. The signal of the yellow line in the zoomed image is displayed in the time domain (red line) and frequency domain (blue line) in the box at the bottom right corner of Figure 2.4.

During scanning, a number of parameters can be set through the software interface, including the transmitting power and number of cycles of the transmission signal, overall gain values, the size of ROI and the format of output data. The output format of the RF data includes the number of lines (1-100), number of frames (1-1000) and number of acquisitions (1-20) per line. Only the RF data in the pre-selected ROI is saved. The A/D converter sampling frequency is 420 MHz (VisualSonics 2006), which defines the spectral resolution of the data.

Each raw RF data file is saved in two types: *.rdi (including sampling information e.g., number of frame, line, acquisitions per line, etc.) and *.rdb (including the binary data in ROI) (VisualSonics 2006). The RF data can be downloaded from the scanner and analysis is performed off-line using MATLAB software (MATLAB 2009a, The MathWorks Inc., Natick, MA, USA).

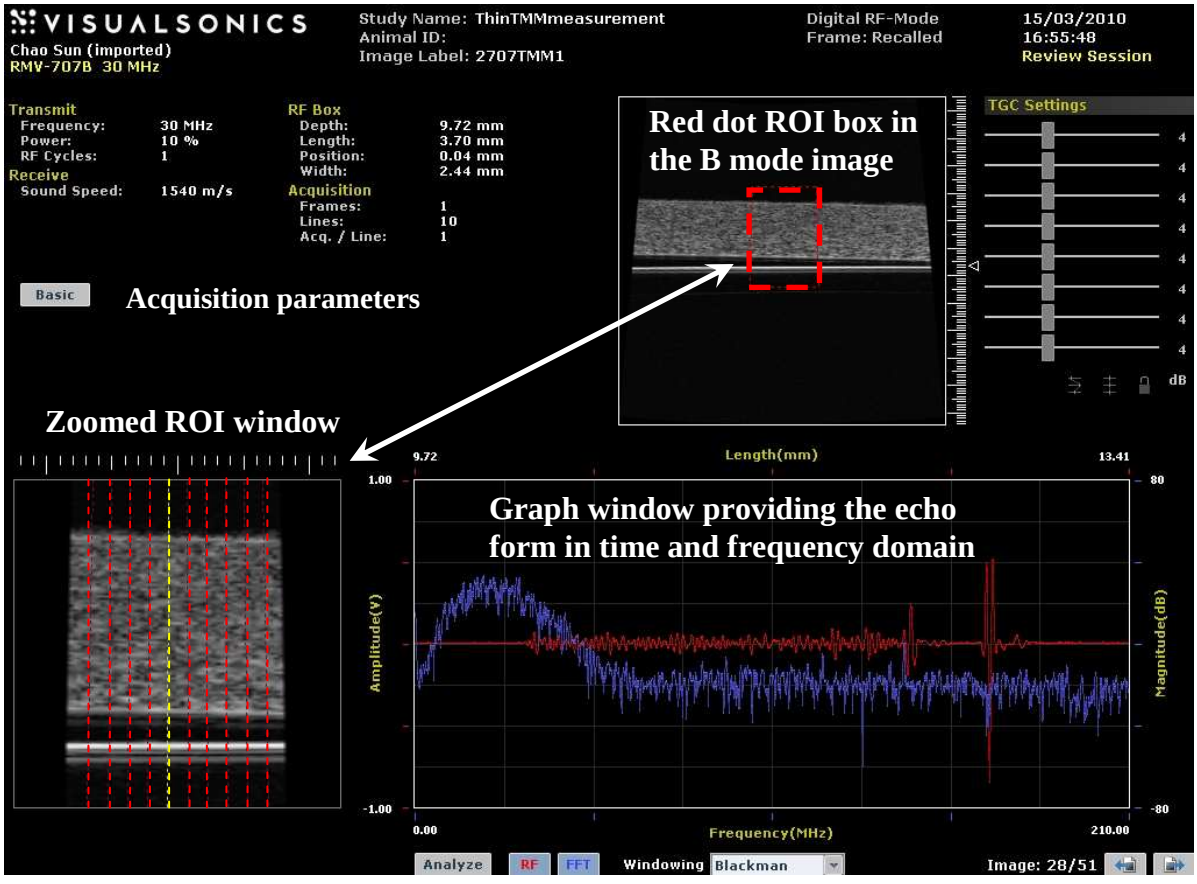

Figure 2. 4: *The screen view of RF mode*

2.3 METHODOLOGY

The beam profiles of five Vevo 770 transducers in M-mode and PW-Doppler mode were measured. In M-mode, the transducer repetitively transmits a single beam down one line thus generating data from one scan line. In addition the received bandwidth was characterised using a reflector.

2.3.1 The measurement of transmitted acoustic pressure using hydrophone

The apparatus were assembled as shown schematically in Figure 2.5. The ultrasound wave transmitted by the transducer was received by a membrane hydrophone and recorded by an oscilloscope (TDS2024B, Tektronix, Beaverton, Oregon, USA). The membrane hydrophone has a 0.2 mm diameter active element made of Polyvinylidene Fluoride (PVDF) (Precision Acoustics Ltd., Dorchester, UK) and was immersed in a water tank (inner diameter: 30cm, height: 15cm) containing air saturated distilled water. The hydrophone was calibrated in the frequency range 2-60 MHz by the National Physical Laboratory in combination with a submersible preamplifier, DC coupler and a 50 Ω 'in-line' shunt. The sensitivity for the above frequency range is provided as a certificate issued by National Physical Laboratory and is attached in Appendix 1. A best-fit curve to this data allows the sensitivity of the hydrophone at frequencies in between data points to be approximated.

A 3D-positioning system (VisualSonics Inc., Toronto, Canada) includes bench-mounted adjustable rail system (x - y direction) and a fully adjustable RMV transducer stand (z direction) to control the position of the hydrophone and the transducer with a step size of 0.1 mm. A physiological monitoring unit (VisualSonics Inc., Toronto, Canada) was used to measure the temperature of the water in real time. All the measurements were performed at $21 \pm 1\ ^{o}C$.

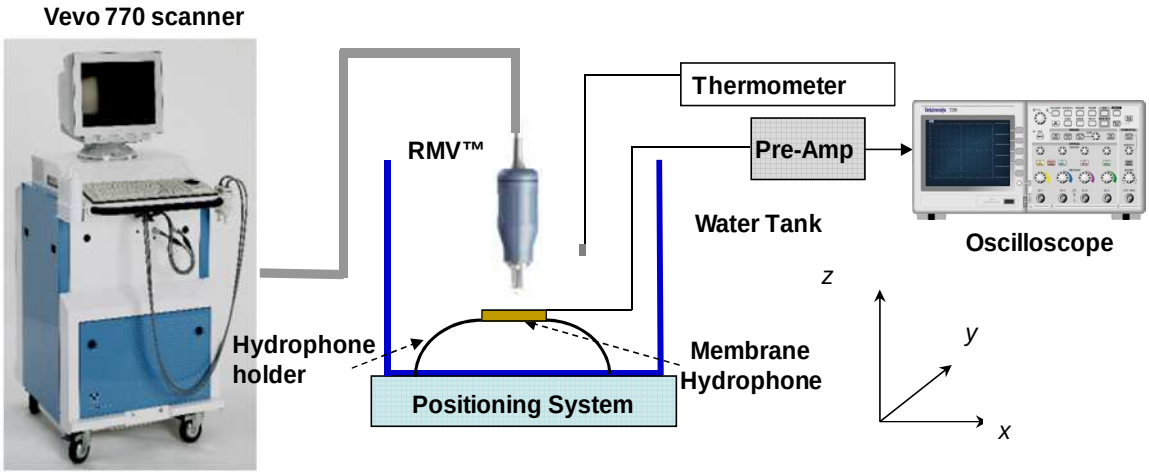

Figure 2. 5: *Schematic of experimental setup used to acquire the beam profile*

Figure 2.6 shows the schematic of the typical ultrasonic field of a transducer. Characterisation of the acoustic output from the transducers involved three sets of measurements.

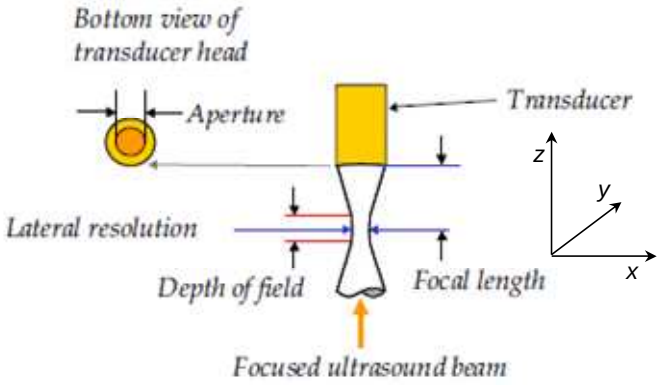

Figure 2. 6: *The schematic of the ultrasonic field from a transducer (VisualSonics 2006)*

Firstly, the signals on *y*-axis of the focal plane were recorded to plot the beam profile and calculate the 3dB beamwidth. This is assumed that the beam profile is symmetrical in the *x* and *y* directions because the shape of the transducer head is concave. The beam profile describes the spatial distribution of acoustic pressure in the ultrasound field generated by an ultrasonic transducer. By moving the

hydrophone across the ultrasonic beam in a direction normal to the propagation direction, the shape of the beam can be determined (Preston 1991). Specifically, for each transducer, the maximum acoustic signal output (an example shown on the screen of the oscilloscope in Figure 2.7) was found and its position was determined to be the focus by adjusting the position of the hydrophone near the nominal focal position after connecting devices as shown in Figure 2.5. Using the positioning system the transducer was then moved in incremental steps of 0.1mm in the y-direction (5 measurements on either side of focal position) and the signal amplitude of peak positive (P^+) and peak negative (P^-) were obtained at each position. The beam profile was plotted by connecting the 11 measurements after converting the measured amplitude to pressure using the sensitivity of hydrophone in Appendix 1. The 3dB beamwidth (approximately the half-power beamwidth, HPBW) (Van Trees 2002) is a standard measure of the width of the beam. It is defined to be the point from the beam profile where

$$|P|^2 = 0.5 \text{ or } |P| = 1/\sqrt{2} \tag{2.1}$$

where P is the peak of pressure.

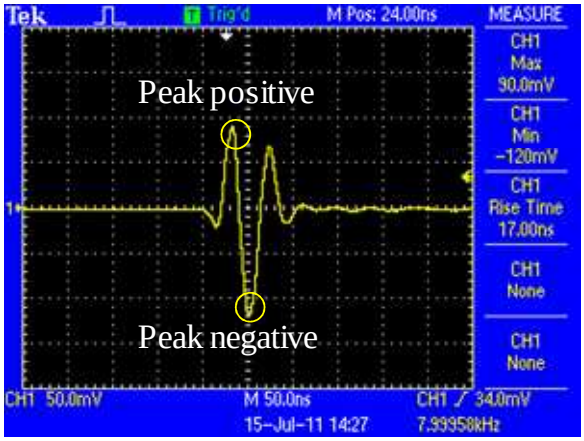

Figure 2. 7: *The screen capture of signal displayed on the oscilloscope*

Secondly, the acoustic pulses were recorded at different depth on the *z*-axis with a distance interval of 5mm in the similar manner as performed on the focal plane.

Thirdly, the acoustic pulses were measured at different insonation powers from 3% to 100% on the nominal focal position.

2.3.2 The measurement of the reflected signal

Figure 2.8 shows a schematic diagram of the experimental set-up. The 3dB bandwidth represents the frequency range over which the converting efficiency between electrical energy and sound energy is more than half of its maximum (Hoskins 2010). It was calculated from the frequency spectra obtained from the reflected signal from a polished polymethylpentene (TPX) reflector (Boedeker Plastics, Texas, USA) placed at the focus of the transducer. This reflector was recommended by VisualSonics as providing a suitable reference material, the magnitude of which would not saturate the received electronics. The TPX reflector was placed and scanned in a water bath of air-free distilled water.

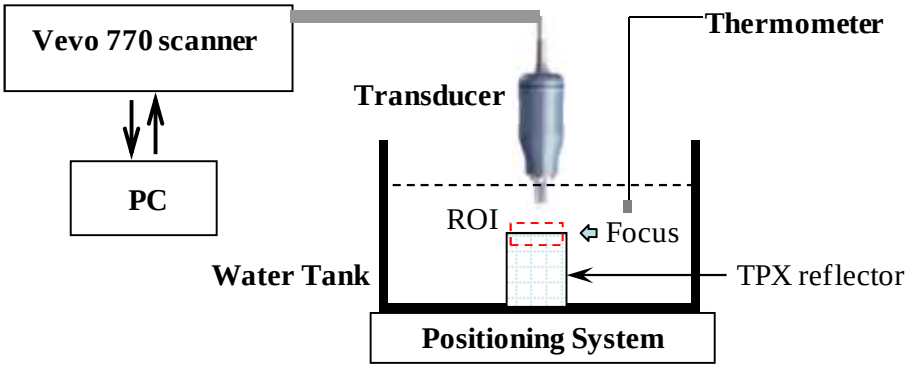

Figure 2. 8: *The experimental set-up used to measure the 3dB bandwidth of the transducer*

2.4 RESULTS

2.4.1 Beam Profile and 3dB beamwidth

Figure 2.9 and Figure 2.10 show examples of beam profiles of transducer 707B in M-mode and PW-Doppler mode. The beam profiles for the other transducers were

similar so they are not included. From these two figures, the acoustic pressure of peak positive (P^+) and peak negative ($|P^-|$) decrease away from the focus (in the centre) to the adjacent horizontal displacement. Based on the beam profiles of transducer shown in Figures 2.9 - 2.10, their 3dB beamwidths were calculated and listed in Table 2.2. The 3dB beamwidth of other transducers are included in Appendix 2.

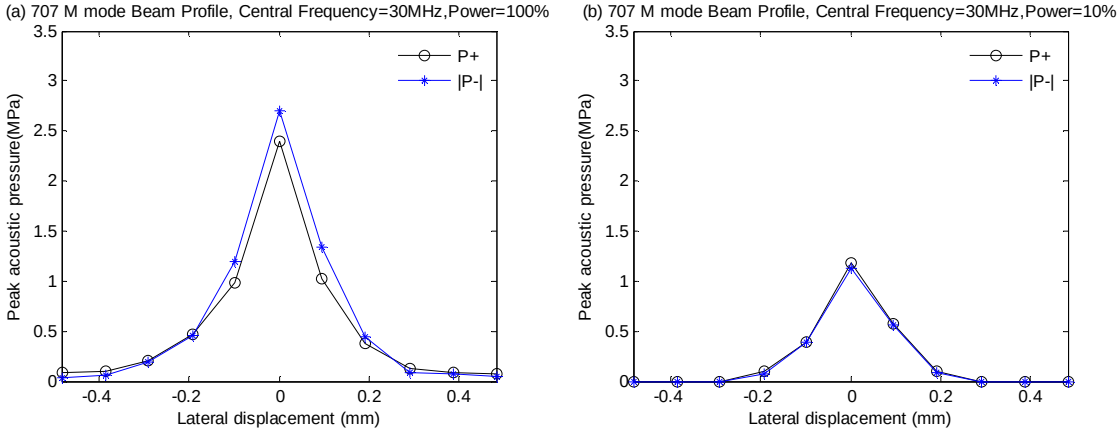

Figure 2. 9: *The beam profile of transducer 707B in M mode at 30 MHz-frequency, (a) 100% power and (b) 10% power.*

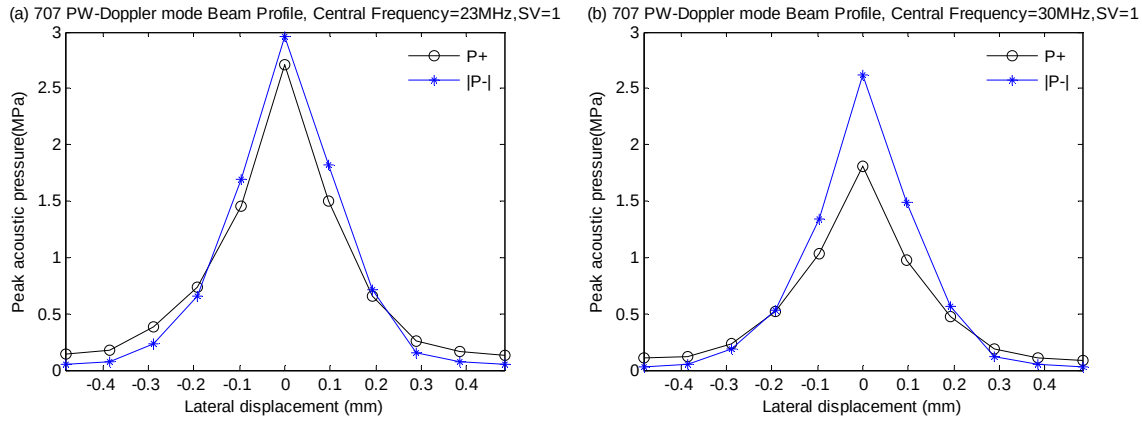

Figure 2. 10: *The beam profile of transducer 707B in PW-Doppler mode at frequency (a) 23 MHz and (b) 30 MHz and 100% power when the sample volume (SV) is 1 cycle.*

Table 2. 2: *Examples of the 3dB beamwidths of transducer 707B calculating from the beam profiles shown in Figures 2.9-10 and the full dataset is included in Appendix 2.*

Transducer 707B	M-mode		PW-Doppler mode	
	f=30MHz, Power=100%	*f*=30MHz, Power=10%	*f*=23MHz, SV=1	*f*=30MHz, SV=1
Peak positive	0.12	0.12	0.14	0.15
Peak negative	0.13	0.13	0.16	0.14

The contour maps of Figures 2.11 - 2.15 present the beam profile (in *y* direction with a step of 0.1mm in Figure 2.6) measured at different depths (*z* direction with a step of 5mm in Figure 2.6) for each transducer. The beam profile at the focal length is shown in Figure 2.9 (data from transducer 707B as an example). From these figures, the spatial distribution of the ultrasound energy during insonation is determined. The highest acoustic pressure appears in the focal zone. The depth close to the origin indicates the field near to the transducer and vice versa.

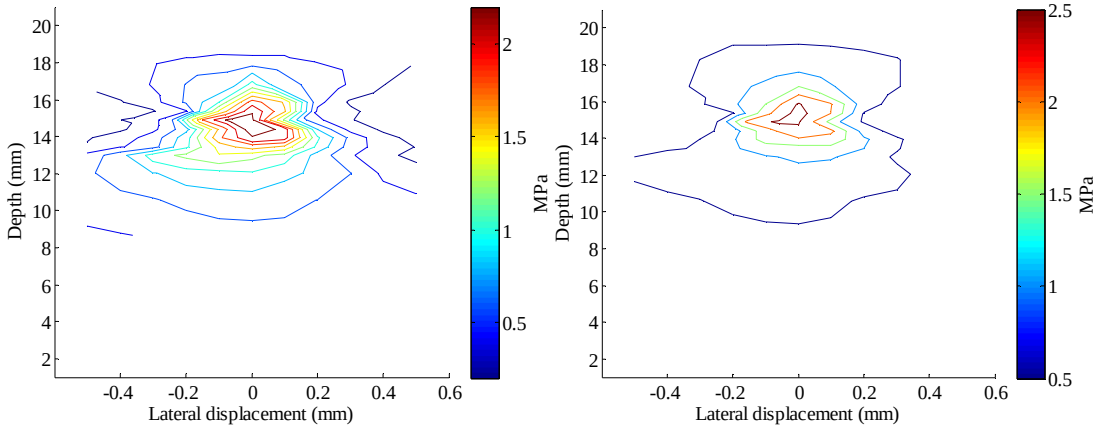

(a) *(b)*

Figure 2. 11: *The acoustic pressure of (a) peak positive and (b) peak negative from transducer 710B (focal length=15mm) measured at different depths*

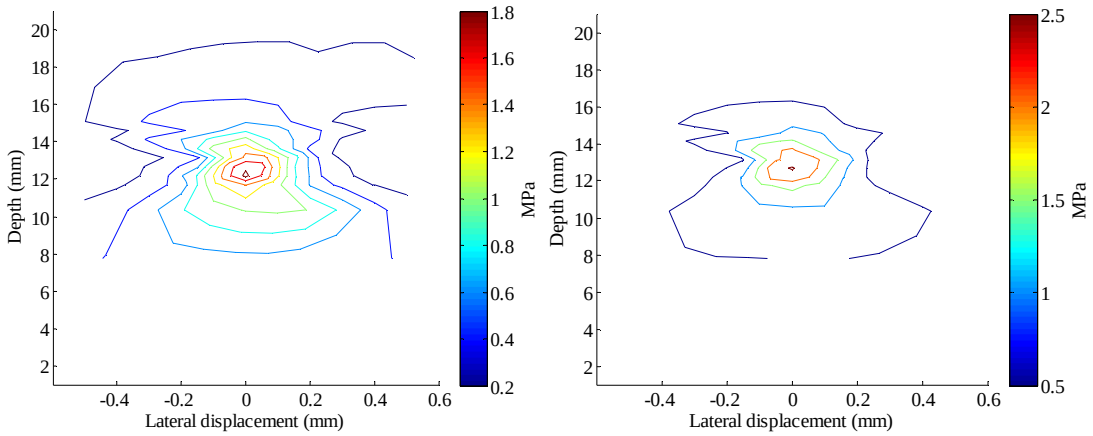

(a) *(b)*

Figure 2. 12: *The acoustic pressure of (a) peak positive and (b) peak negative from transducer 707B (focal length=12.7mm) measured at different depths*

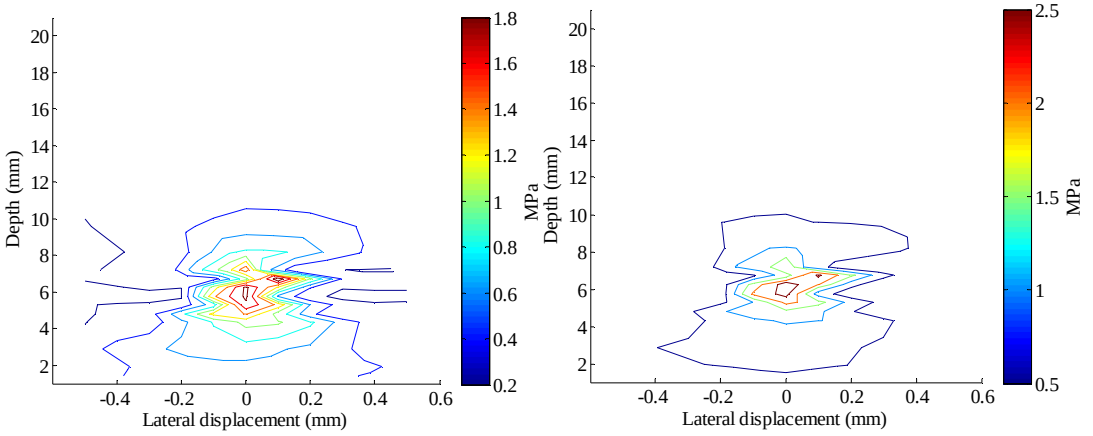

(a) *(b)*

Figure 2. 13: *The acoustic pressure of (a) peak positive and (b) peak negative from transducer 704 (focal length=6mm) measured at different depths*

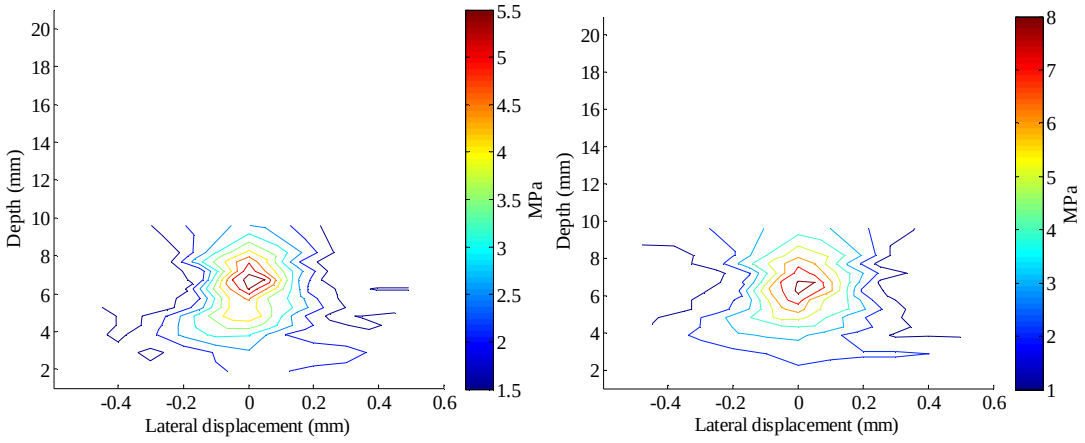

(a) *(b)*

Figure 2. 14: *The acoustic pressure of (a) peak positive and (b) peak negative from transducer 711(focal length=6mm) measured at different depths*

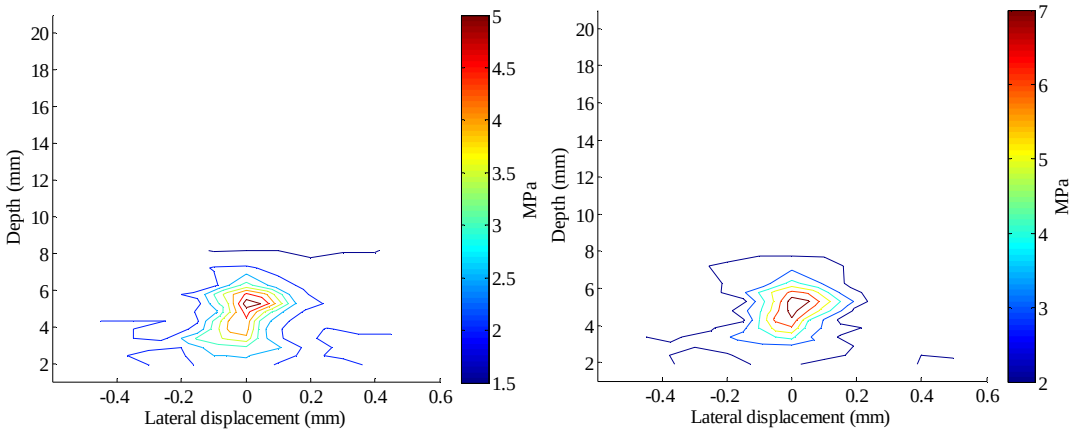

(a) *(b)*

Figure 2. 15: *The acoustic pressure of (a) peak positive and (b) peak negative from transducer 708 (focal length=4.5mm) measured at different depths*

2.4.2 Measurement of the 3dB bandwidth

The frequency dependence of the acoustic characterisation of the tissue mimicking material (TMM) in Chapter 3 and ultrasound contrast agents (Chapters 4-7) are the core of the research in this thesis. The frequency bandwidth of the signal from each of the transducers was measured to understand the energy distribution of each transducer in the frequency domain. Figure 2.16 shows the RF signal reflected from

the TPX reflector in (a) time domain and (b) frequency domain. The frequency spectrum is the FFT of the signal from the time domain and normalized to the peak of its spectrum. This is an example acquired from transducer 707B.

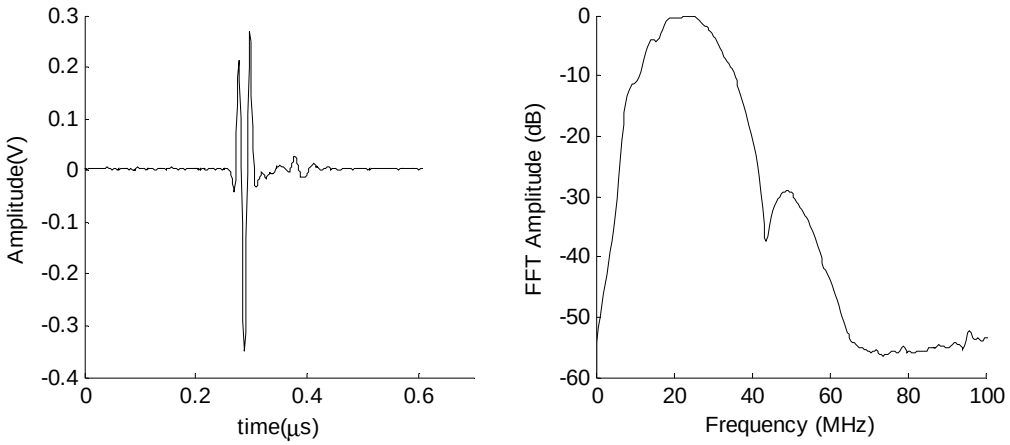

(a) *(b)*

Figure 2. 16: *The RF signal (a) in time domain and (b) frequency domain from transducer 707B (centre frequency 30MHz – manufacturer's literature) reflected from the TPX reflector through the water path in response to 30MHz, 10%- power, 1 cycle pulse.*

The measured 3dB bandwidth of each of the transducers at 10% power setting was calculated from their spectra and is presented in Table 2.3. This is the power setting and frequency range used in Chapter 3 for TMM characterisation.

Table 2. 3: *The 3dB bandwidth of the transducers at 10% power output*

Transducer model	710B	707B	704	711
Measured 3dB band width (MHz)	12 - 25	17 - 31	20 - 40	27 - 47

From Table 2.3, it can be seen that the measured 3dB bandwidths appear to be downshifted in frequency with respect to the nominal centre frequencies of the transducers (see Table 2.1). However, when a long cycle transmitting pulse was set in Engineering mode (mode allows more settings of parameters than default

settings), the peak of the corresponding spectrum appeared at the nominal central frequency. Figure 2.17 shows the signals of four different numbers of cycles received by transducer 707B under Engineering mode and Figure 2.18 presents the corresponding frequency spectra. The longer the transmitting signal, the narrower the main lobe of spectrum.

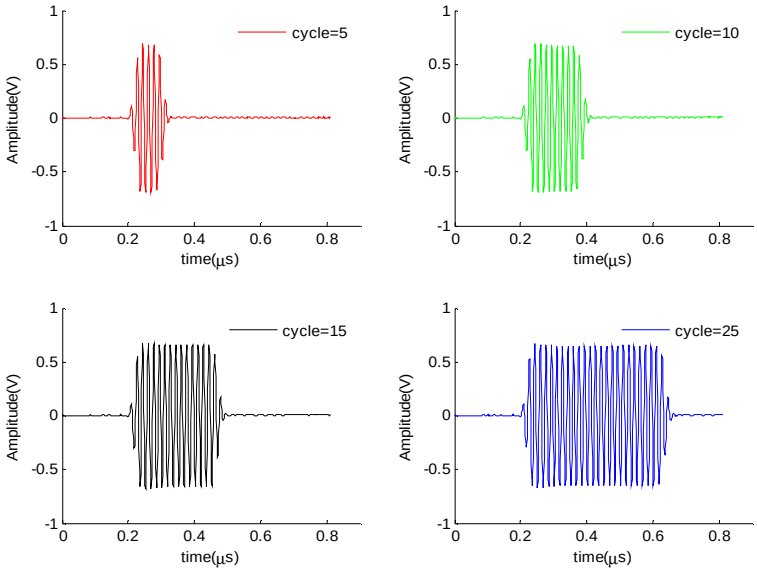

Figure 2. 17: *The RF signals from the scanner reflected by the TPX reflector through the water path at time domain in response to 30MHz, 10%- power, 5/ 10/ 15/ 25 cycle pulse transmitted by transducer 707B*

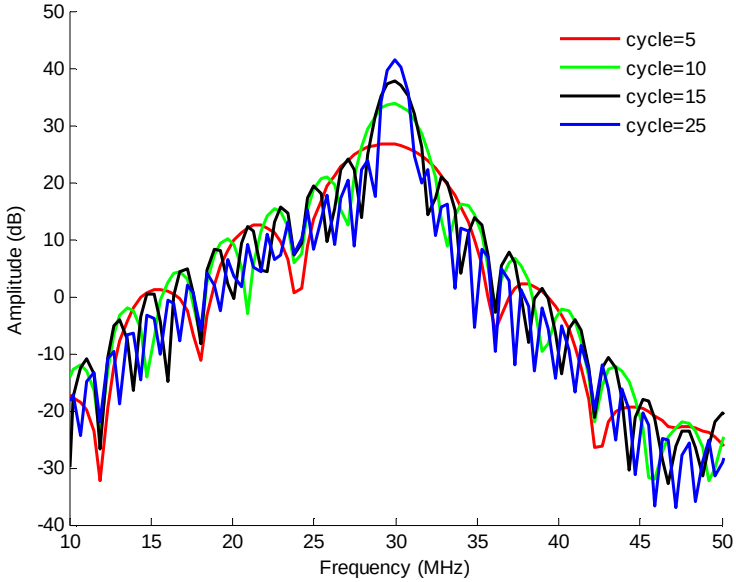

Figure 2. 18: *The spectra of the RF signals in response of the signal in Figure 2.17*

There are 16 power settings accessible in RF mode encompassing 3%, 4%, 5%, 6%, 8%, 10%, 13%, 16%, 20%, 25%, 32%, 40%, 50%, 63%, 79% and 100%. Appendix 3 listed the amplitude of the peak positive signal and peak negative signal at the power settings measured by the hydrophone. The calibrated peak negative pressure (PNP) and MI values are required for experiments in Chapters 3-7.

Figure 2.19 shows the PNP dependent centre frequency of the spectra from the signals received by (a) hydrophone and (b) scanner, examples of these spectra acquired by transducer 710B are shown in Figures 2.20 - 2.21. It can be seen that for each transducer, except transducer 704, with increasing PNP, the centre frequency shifts to lower frequencies. However, the fluctuation, e.g., frequency upshifts to higher frequencies from results of transducer 704, is likely to be caused by the variation in spectra around peak region.

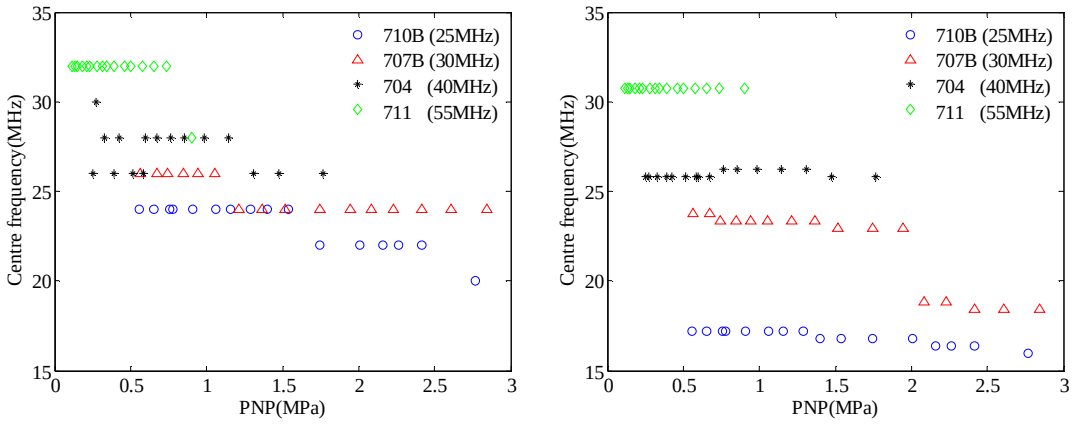

Figure 2. 19: *The variation in centre frequency at a series of PNP, signals received by (a) hydrophone and (b) scanner.*

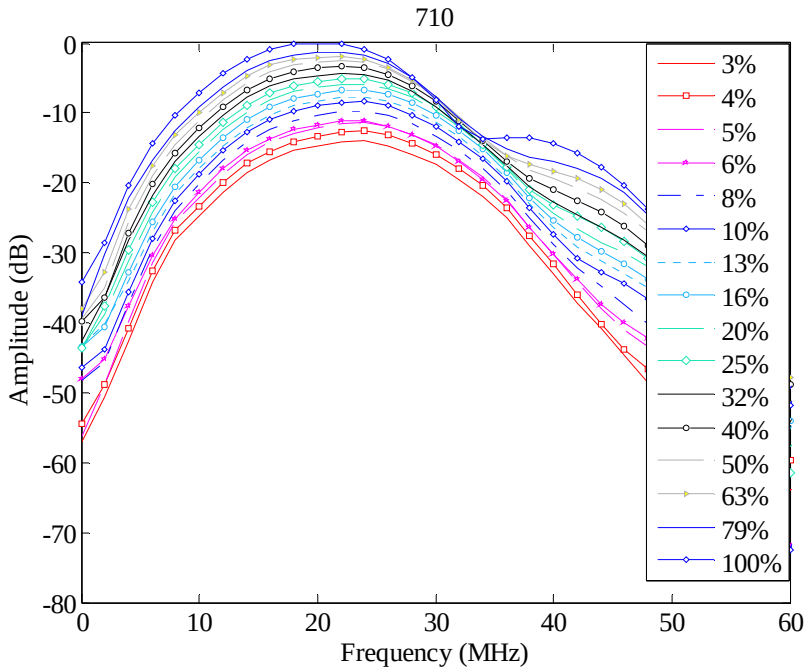

Figure 2. 20: *The spectra of the signals received by the hydrophone at a series of power setting from transducer 710B (central frequency: 25 MHz)*

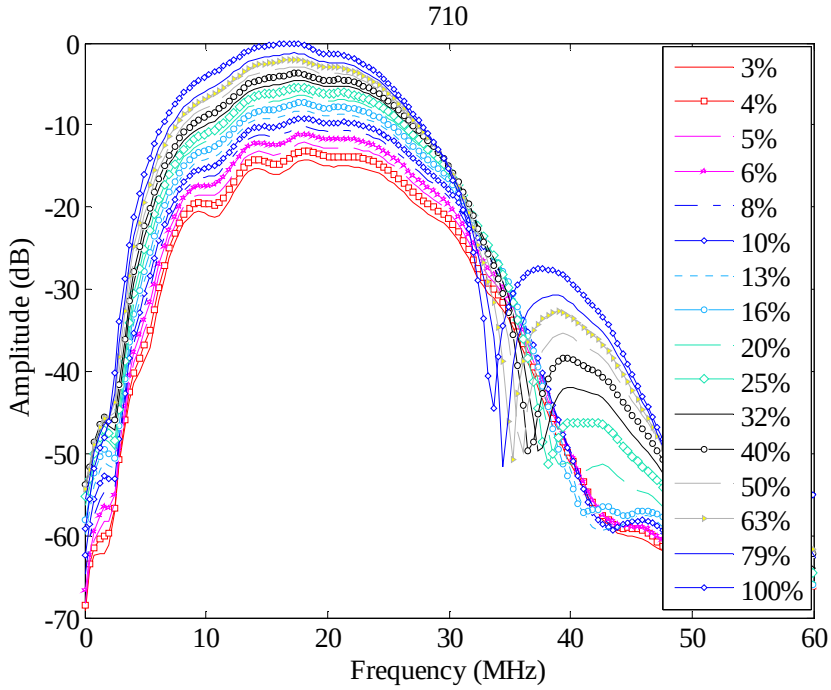

Figure 2. 21: *The spectra of the RF signals from the pulse-echo measurement at a series of power setting from transducer 710B (central frequency: 25 MHz)*

2.4.3 Linearity of the system

In Figure 2.22, the amplitude of peak negative signal (value read from the raw RF data in mV) received by the transducer at the sixteen power settings were plotted against the peak negative pressure values (calibrated data in Appendix 3 in MPa) acquired by the hydrophone at the same power settings for transducers 710B, 707B, 704 and 711. The goodness of fit by R^2 is shown to be greater than 0.99 for the entire linear function fitting of all the curves. This linear relationship demonstrates insignificant nonlinearity of scanner itself.

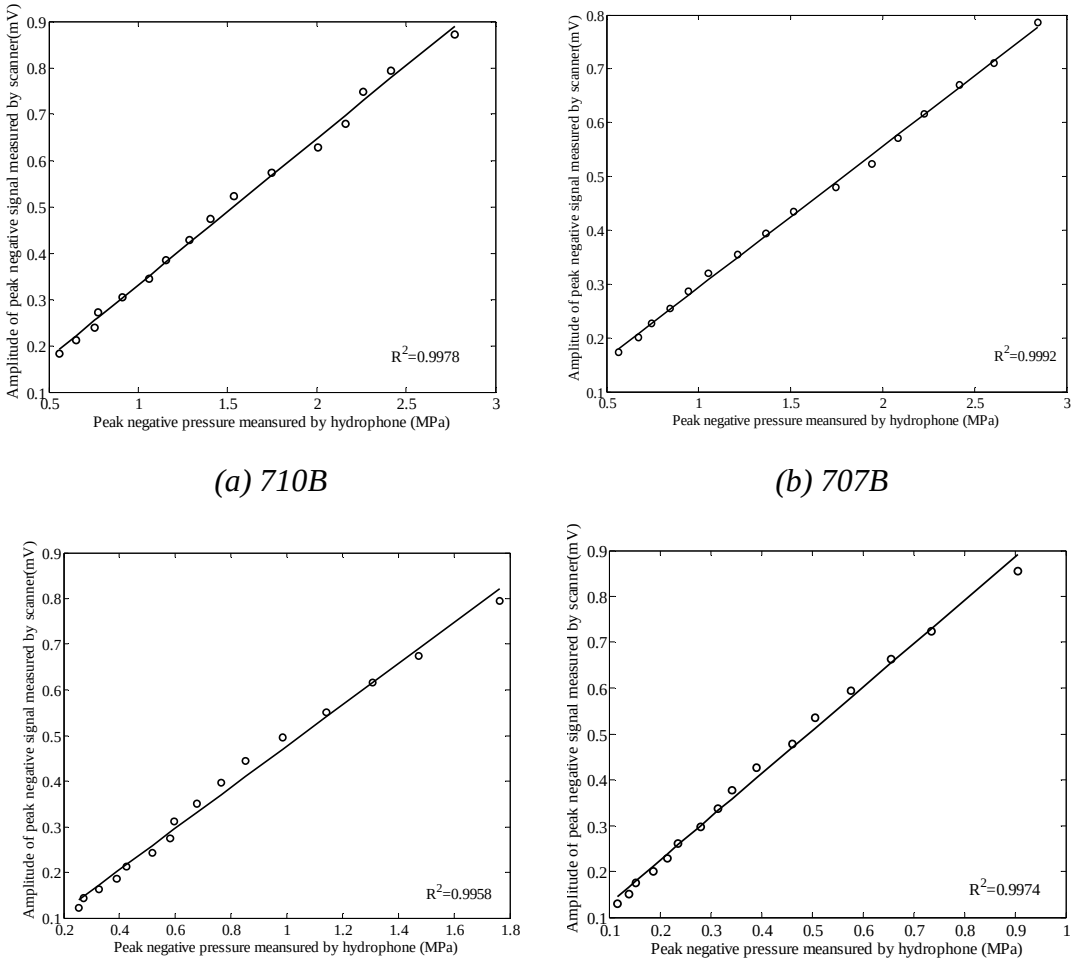

(a) 710B *(b) 707B*

(c) 704 *(d) 711*

Figure 2. 22*: The comparison of signals received by each transducer and the hydrophone at different power settings*

2.5 DISCUSSION

This chapter measured the acoustic parameters of each transducer of the high frequency ultrasound scanner Vevo770 including: beam profile, 3dB bandwidth, characteristics of short and long transmitting pulses in time/frequency domain and peak negative pressures at different power settings. These datasets will be referred in the later chapters. Specifically, low power single cycle pulses are used in Chapter 3 to measure the acoustical properties of TMM; low power short cycle pulses are used in Chapter 4 and 5 to measure the attenuation and backscatter of lipid shelled microbubbles (MBs); long cycle pulses for analyzing the subharmonic components of MBs are used in Chapter 6 and 7. The discussion focuses on the impacts of these signatures on the underlying selections of experimental parameters in the following chapters.

2.5.1 Beam Profile

Figure 2.9 shows the beam profiles of transducer 707B in M-mode at positions of maximum pressure amplitude. Overall uncertainties of acoustic output measurements are mainly attributed to the uncertainties in hydrophone sensitivity calibration. The acoustic pressure decreased when the power output was reduced from 100% to 10%. At low power output (10%) the output acoustic pressure was approximately 1MPa or above. At lower frequencies at these acoustic pressures commercial UCAs have been shown to rupture (if frequency=1MHz, then MI > 1 (Correas et al. 2001)). However, considering the high frequency range is far from the resonant frequency of these MBs, their behaviour will be studied in the following chapters.

2.5.2 Focal position and focal zone

Figures 2.11 – 2.15 show the spatial distribution of acoustic pressure. The maximum signal in the water was determined to be the position of the focus of the transducer. Curved transducers and lenses are two main methods for changing the directivity of

transducers as shown in Figure 2.23 (Wells 1977). Wells (Wells 1977) summarized the work of (O'Neil 1949) and (Fry and Dunn 1962) and showed that

1) in Figure 2.23.a. the intensity at the centre of the curvature I_R and the average intensity at the radiating surface I_0 has an approximate relationship as

$$I_R/I_0 = (kh)^2 = (2\pi h/\lambda)^2 \quad (2.2)$$

2) in Figure 2.23.b

$$F \approx R/(1-1/n) \quad (2.3)$$

where n is the refractive index $n=c_1/c_2$, c_1 is the velocity in the lens and c_2 is the velocity in the medium. The speed of sound in the propagating medium is included in the both equations ($\lambda = v \cdot t$). Generally ultrasound scanners use the speed of sound in tissue 1540 $m \cdot s^{-1}$. However, the experiment used distilled water, the acoustic velocity of which is 1480 $m \cdot s^{-1}$ at 19.3^oC (Bilaniuk and Wong 1993). The discrepancy between the speeds of sound is the main reason for the shift (± 0.5 mm from the nominal focal position) in position of maximum signal. Thus, the nominal focal position is close to the measured focal zone and used in the following experimental work.

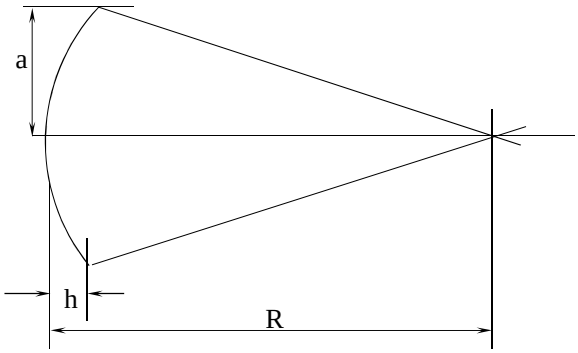

(a) The schematic geometry of a curved transducer (self-focusing radiator)

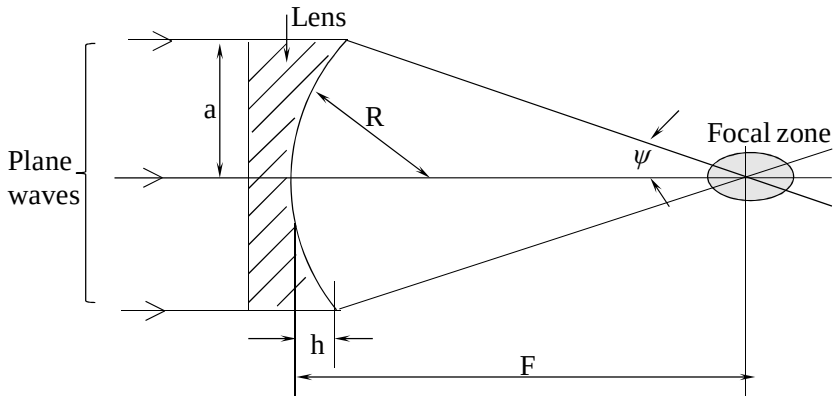

(b) The schematic geometry of a lens system

Figure 2. 23: *The schematic geometry of (a) a self-focusing radiator and (b) a lens system (Wells 1977)*

2.5.3 3dB bandwidth

The sensitive frequency range of the transducer was measured as the 3dB bandwidth of the spectrum from a single cycle pulse. The signature of frequency spectrum is determined by the insonation signal driven by the transducer and the properties of the propagation medium. In Chapter 3-7 where the frequency dependence of attenuation and the normalized backscatter are investigated for both TMM and UCAs, these calculations are performed over the 3dB frequency bandwidth of the transducers. Although the transducers function as both transmitter and receiver, the 3dB bandwidth instead of 6dB bandwidth is calculated. This is because 3dB bandwidth of each transducer is relatively narrow in which the energy mostly focuses and provides good signal to noise ratio. The overlapping frequency ranges of the five transducers enable the entire frequency bandwidth of 12 - 47 MHz (at 10% power) and 12 - 43 MHz (at 3% power) to be available for the study.

2.5.4 Characteristics of short and long transmitting pulses

Comparing the spectra of the short and long cycle signals in Figure 2.16 - 2.18, it was found that the peak of the spectrum from the long cycle signal occurs at the

nominal transmitting frequency of the signal. However, the peak of the broadband spectrum from a single cycle signal shifts to a lower frequency than the nominal transmitting frequency. The reason of this frequency shift of peak spectrum may be attributed to the variation of the waveform of the short cycle signal during propagation that increases nonlinearity of high frequency ultrasound. The density of the water varies with the propagation of the longitudinal wave in the underwater environment shown in Figure 2.24. Specifically, in the compression region (peak positive range) the density and the pressure are elevated, in the rarefaction region (peak negative range) these variables decrease with respect to the background (Zagzebski 1996). The speed of sound is related to the density, thus the speed during the compressed cycle of the wave is higher than the value in the expansion cycle. If the waveform of the pulse distorts during the propagation like shown in Figure 1.6, this distortion generates more harmonics during the wave propagation. Additionally, the ultrasound propagating through the water is known to be nonlinear and the attenuation increases with frequency with a relationship of f^2 (Pinkerton 1949). The nonlinearity may be more significant for the high frequency ultrasound due to the increasingly nonlinear loss of attenuation.

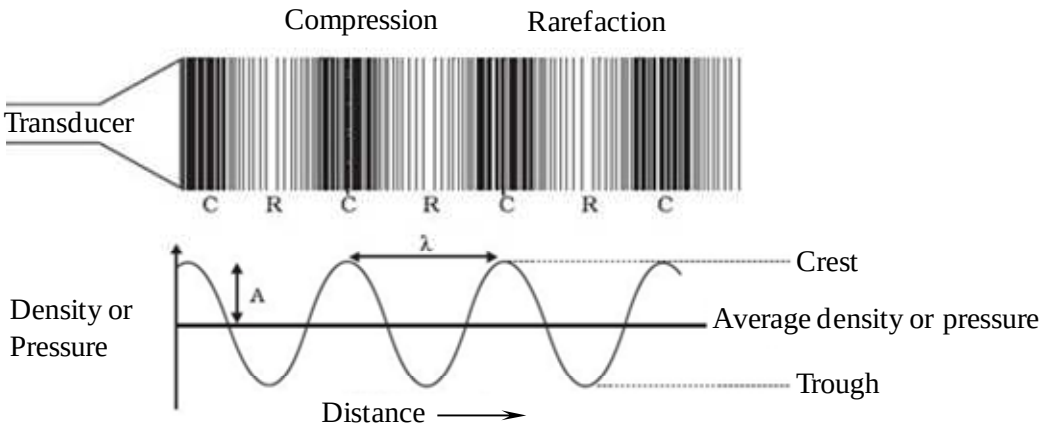

Figure 2. 24: The variation of pressure and density of the medium with the propagation of the sound wave (Zagzebski 1996)

2.5.5 Characteristics of transmitting signal of different powers

Figure 2.19 presents the frequency spectra of the signals received by the hydrophone and scanner at a series of power settings. At high power the frequency spectra shifts towards a lower frequency range indicating the nonlinear effect at high power is more prominent than at low power. With respect to the analysis above, high insonation pressure intensifies the distortion of the signal leading to nonlinearity by increasing the difference in the speed of sound between the compressed medium and the rarefied medium. The differences between the frequency measured from the spectra obtained from the signal from the TPX reflector to those obtained from the hydrophone may be due to the double transit time of the ultrasound pulse through water experienced by the TPX reflector measurements.

2.6 CONCLUSIONS

This chapter describes the acoustic characterisation of the high frequency ultrasound scanner Vevo770 using five different transducers covering the range of 25 - 55MHz. This includes:

1. The beam profile (the spatial distribution of the magnitude of pressure amplitude (positive and negative)) measurement using a 0.2mm membrane hydrophone.

2. The 3dB frequency bandwidth measurement for each of the transducers at 1 cycle at 10% power output confirming the sensitive frequency range of the transducer.

3. The impact of the acoustic pressure on the measured centre frequency of each of the transducers.

The objectivity of these measurements establishes the settings with which this set-up will be operated in the following chapters. Furthermore, an initial understanding of the limitations of the system is useful for all the future work.

Chapter 3

The acoustic speed and attenuation of a tissue-mimicking material at high frequencies

3.1 AIM

The aim of this chapter is to characterise the speed of sound and attenuation of the IEC agar-based tissue mimicking material (TMM) over the frequency range 10 to 47 MHz. Measurements were made using two independent systems, both employing broadband substitution techniques. The experimental method and MATLAB codes developed for TMM characterisation are fundamental for the calculations of ultrasound contrast agents in Chapters 4-7. Additionally, this TMM performed as a reference material for calculating contrast to tissue ratio in Chapters 5 and 7. The work in chapter 3 has been published in Ultrasound in Medicine in Biology, 2012 and is included as in Appendix of this thesis.

3.2 INTRODUCTION

Ultrasound phantoms are passive devices which simulate the acoustic properties of the human body and enable the performance assessment of an ultrasound system (AIUM 1995). In practice, variations of speed, impedance, scattering, absorption and attenuation affect the appearance of the pulse echo signal and provide information about the tissue structure. Thus, the knowledge of these parameters and their variation with frequency, temperature, amplitude, age and pathology is important for us to understand and make the most efficient use of present and potential ultrasonic diagnostic techniques (Hill 1986).

The phantoms are designed based on the specific function of the ultrasound scanner they are to test, e.g. TMM for measuring the attenuation and speed of sound of ultrasound scanners, blood mimicking fluid (BMF) and vessel mimicking tube (VMT) (Teirlinck et al. 1998) and string phantom for Doppler imaging (Culjat et al. 2010). In addition to the evaluation of attenuation, other parameters like thermal conductivity, diffusivity tolerating high temperature for high-intensity focused ultrasound (HIFU) (e.g. hydrogel based TMM (King et al. 2007)) and elastic and mechanical properties (stiffness and stress relaxation) for elasticity imaging (Elastography) (e.g. gelatine gels TMM (Hall et al. 1997)) can also be tested.

The purpose of a Tissue Mimicking Material (TMM) is to closely mimic the speed of sound, attenuation and backscatter properties of soft tissue in order to evaluate new signal or image-processing algorithms (Kofler and Madsen 2001, MacGillivray et al. 2010) and to provide a reproducible method of assessing the image quality of diagnostic ultrasound (Browne et al. 2004, Shaw and Hekkenberg 2007). Various base materials have been used to produce either commercial or in-house TMM including agar, gelatine, n-propanol and oil (Duck 1990), urethane rubber, Zerdine®, condensed milk (Browne et al. 2003), magnesium silicate, open cell foam, polyacrylamide gel, polyurethane, polyvinyl alcohol (PVA), silicone polymer and organics (Culjat et al. 2010). Table 3.1 lists the different TMMs and their respective properties that are of interest in this chapter.

Table 3. 1: *The speed of sound, attenuation and pros and cons of TMM (Culjat et al. 2010)*

Material	**Speed of sound (V) ($m \cdot s^{-1}$)**	**Attenuation (α) ($dB \cdot cm^{-1}$)**	**Advantage**	**Disadvantage**
Agarose-based	1498-1600+	0.04-1.40	Widely used and well documented	delicate structure
Gelatin-based	1520-1650	0.12-1.5	high stability near-room temperature	instability with temperature variations, scatter uniformity
Magnesium silicate-based	1458-1520	0.85	temperature stability(0-100^{o}C)	Incapability of sculpture or mould
Oil Gel-based	1480-1580	0.4-1.8	V and α increases linearly with the propylene glycol	High V and low α for ethylene glycol-based TMM
Open Cell Foam-based	1540	0.46	Convenience for manufacturing inhomogeneous phantoms	High temperature dependence of α
Polyarcrylimide Gel-based	1540	0.7dB/cm @5MHz	Acceptable V and impedance for mimicking soft tissue	Low α, highly toxic
Polyuerethane	1468	0.13	α increases linearly with temperature and frequency	Complexity of manufacture
Polyvinyl Alcohol-based	1520-1610	0.07-0.35	High structure rigidity, indefinite longevity, low cost, simple ingredients	Difficulty in controlling freeze-thaw cycle
Tofu	1059	0.75	Low cost	Low nonlinear parameter

To our knowledge there is no commercially available TMM for the quality assessment of high frequency ultrasound scanners (Moran et al. 2011). In addition, compared to low frequencies, there is little work to date that evaluates TMM at such frequencies. One gelatine-based tissue mimicking material with spherical glass scatterers has been characterised from 2 to 60 MHz (Bridal et al. 1996), the attenuation of which depended nonlinearly on the frequency. The propagation speed and attenuation coefficient of a phantom tissue-like polymethylpentene was reported in the frequency range 20-70 MHz (Madsen et al. 2011). However at the same time, there is increasing demand for the development of a tissue mimicking phantom which is characteristic of both human and animal model tissue properties at high frequencies.

The IEC agar-based TMM characterised in this chapter was developed as part of an International Electromechanical Commission project (IEC 2001, Zeqiri and Hodnett 2010). The base ingredients of this TMM are water and glycerol. Agar is added to increase stiffness and its concentration, together with the glycerol, determines the speed of sound. Powders incorporating Al_2O_3 and SiC in different sizes are added to adjust the attenuation and scattering properties (Teirlinck 1997). It has been widely used, for example in flow phantom design (Ramnarine et al. 2001), in oesophagus phantoms (Inglis et al. 2006) and in breast phantoms (Cannon et al. 2011). The acoustic properties of this agar-based TMM and their temperature and frequency dependence have previously been investigated over the frequency range 2.25 to 15 MHz at an ambient temperature range of 10 to 35 ^{o}C (Browne et al. 2003) and at an ultrasound frequency range 17 - 23 MHz over a temperature range of 22 ^{o}C to 37 ^{o}C (Brewin et al. 2008). These authors showed that the speed of sound remained relatively constant with increasing frequency but that it increased with an increase in temperature while attenuation was shown to decrease with temperature. This TMM also showed acoustical stability over 2 years (Brewin et al. 2008) and exhibited a linear response of acoustic attenuation in the low frequency range 2-7 MHz (Browne et al. 2003), 6-15 MHz (Inglis et al. 2006) and 17-23 MHz (Brewin et al. 2008).

3.3 MATERIALS AND METHODS

3.3.1 Manufacture of TMM

The agar-based TMM used in this study was prepared following the method of Ramnarine et al.(Ramnarine et al. 2001), Browne et al. (Browne et al. 2003) and Brewin et al. (Brewin et al. 2008) using the ingredients described in Table 3.2. Due to the short focal length of the high frequency transducers (Table 2.1) thin slices of TMM were manufactured. These were made by pouring a small volume of prepared TMM liquid at 46^{o}C into PVC cylinder rings (inner diameter 4.8cm, 2mm height). Prior to pouring the TMM into the rings, a stretched layer of 14 – 16 μm thick Saran Wrap (SC Johnson Inc., Racine, USA) was glued to one rim of the ring. The TMM-filled ring was then left on a flat surface to set. Once the TMM was cooled to room temperature, before the upper layer of Saran Wrap was stuck to the upper rim of the ring, approximately 0.2 ml of TMM preserving liquid (mixture of glycerol, water and disinfectant) was placed on the TMM and spread over the surface to moisten it and ensure good acoustic coupling between the TMM and Saran Wrap. Enclosure of the TMM samples in Saran Wrap ensured that the glycerol did not leach from the TMM into the surrounding water-bath during measurements. Twelve TMM slices which varied in thickness between 2mm and 4mm were produced and were allowed to cool overnight. These TMM samples will be referred to as TMM test cells (Figure 3.1). To account for the effect of the Saran Wrap, water test cells of the same dimensions were also produced, in which the TMM was replaced by distilled water. Two batches of TMM were manufactured following the same protocol to assess the reproducibility of the process.

Table 3. 2: *Ingredients of the agar based tissue-mimicking material (TMM)*

Ingredients	**Weight concentration**	**Order Code and Manufacturer / Distributor Details**
Water	82.97%	
Glycerol 99% (pure)	11.21%	(G7757) Sigma-Aldrich Company Ltd. The Old Brickyard, New Road, Gillingham, Dorset, UK
Merck Agar-Agar technical (111925)	3%	(53648 5K) VWR International Ltd. Hunter Boulevard, Magna Park, Lutterworth, Leics, UK
3µm Al_2O_3 Powder	0.95%	Logitech Ltd. Erskine Road, Old Kilpatrick, Glasgow, Scotland
0.3µm Al_2O_3 Powder	0.88%	Logitech Ltd. Erskine Road, Old Kilpatrick, Glasgow, Scotland
400 grain SiC Powder	0.53%	Logitech Ltd. Erskine Road, Old Kilpatrick, Glasgow, Scotland
10% solution of Benzalkonium chloride ($C_6H_5CH_2N(CH_3)_2RCl$)	0.46%	(09621) (50%solution, diluted in-house to 10%) Sigma-Aldrich Company Ltd. The Old Brickyard, New Road, Gillingham, Dorset, UK

Figure 3. 1: *TMM test cells*

3.3.2 Experimental set-up

Measurement of the speed of sound and attenuation of the TMM were performed based on a broadband reflection substitution technique (AIUM 1995) using a Vevo770 pre-clinical ultrasound scanner (VisualSonics Inc., Toronto, Canada) and a scanning acoustic macroscope (SAM) system developed in-house in Dublin Institute of Technology (Cannon et al. 2011). Using the broadband substitution technique, short duration, wideband transmitting pulses were used to acquire the data on the position and magnitude of the received sound pulse with and without the sample between a pulse-echo transducer and a specular reflector (AIUM 1995). As described below the thickness of each sample at each acquisition was also calculated for measurements made using the Vevo 770 scanner.

Figure 3.2 shows a schematic diagram of the experimental set-up. The TMM test cell was placed and scanned in a water bath of air-free and distilled water and a TPX reflector was mounted beneath the test cell as a reference reflector. Modelling clay (Plasticine, Flair, UK) was used to secure the position of the reflector and to offset the position of the TMM test cell from the reference reflector. A 3D-positioning system (VisualSonics Inc., Toronto, Canada) with a step size of 0.1 mm was used to adjust the position of the transducer and the test cell. The tank containing the TMM test cell was seated on a bench-mounted adjustable 2D (X, Y) rail system. The transducer was mounted on a Z positioning system. A physiological monitoring unit (VisualSonics Inc., Toronto, Canada) was used to measure the temperature of the water in real time. All the measurements were performed at $21\ ^{o}C \pm 1\ ^{o}C$.

A Vevo770 pre-clinical ultrasound scanner and four transducers driven at 10% output power were used for the acoustic measurements. The corresponding peak negative pressures at focal position are in Appendix 3 as described in Chapter 2. The nominal centre frequencies, focal lengths and the measured 3dB bandwidth of each of the transducers are given in Table 2.1 and 2.2. The Vevo770 scanner was operated in RF mode. It was not possible to capture the RF data from the complete image frames so regions corresponding to the site of the relevant echoes were pre-selected.

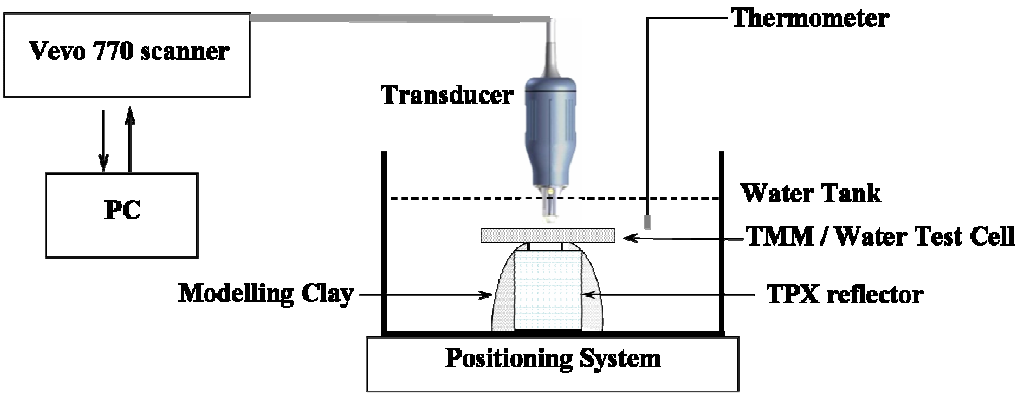

Figure 3. 2: *Schematic diagram of the experimental set-up of Vevo 770 scanner*

3.3.3 Measurement of speed of sound and thickness of TMM

The thickness of TMM and the speed of sound were calculated from the return time intervals of the pulse echoes from the front and rear surfaces of the TMM test cell and from the surface of the TPX reflector. Equations 3.1, 3.2 and 3.3 were used to derive the speed of sound (Equation 3.4) and the thickness (Equation 3.5) of the TMM. Figure 3.3 illustrates these time intervals schematically. The symbols in equations 3.1-3.5 are defined in Table 3.3. The recorded temperature enabled the identification of the corresponding speed of sound in the water (Bilaniuk and Wong 1993).

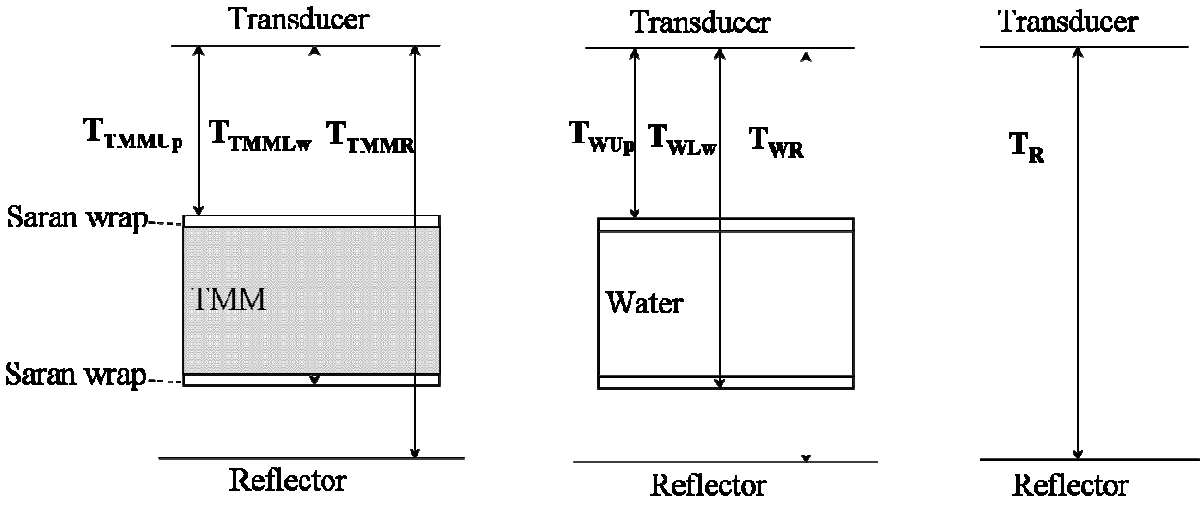

(a) *(b)* *(c)*

Figure 3. 3: *Diagram of the experiment and time intervals involved in calculations (not to scale) (a) TMM test cell, (b) Water test cell, (c) Water only. Definition of symbols can be found in Table 3.3.*

Table 3. 3: *Definitions of the symbols involved in Equations 3.1 – 3.5*

T_{TMMUp}	Time required for ultrasound pulse to travel from the transducer to the upper surface of the Saran wrap of the TMM test cell
T_{TMMLw}	Time required for ultrasound pulse to travel from the transducer to the lower surface of the Saran wrap through the TMM test cell
T_{TMMR}	Time interval between the transducer and surface of the TPX reflector through the TMM test cell
T_{WUp}	Time required for ultrasound pulse to travel from the transducer to the upper surface of the Saran wrap of the water test cell
T_{WLw}	Time required for ultrasound pulse to travel from the transducer to the lower surface of the Saran wrap through the water test cell
T_{WR}	Time interval between the transducer and surface of the TPX reflector through the water test cell
T_R	Time interval between the transducer and surface of the TPX reflector through the water only
D_{TR}	Distance between the transducer and TPX reflector
Vw	Speed of sound in water
V_{TMM}	Speed of sound in TMM
Vs	Speed of sound in Saran wrap
d_{TMM}	Thickness of TMM in the TMM test cell

In the experiment, the distance D_{TR} between the transducer and TPX reflector was fixed (Figure 3.3. a, 3.3.b and 3.3. c) and was equal to

$D_{TR} = (T_{TMMUp} + T_{TMMR} - T_{TMMLw}) \times Vw + [T_{TMMLw} - T_{TMMUp} - (T_R - T_{WR})] \times V_{TMM} + (T_R - T_{WR}) \times Vs$ (3. 1)

$D_{TR} = (T_{WUp} + T_{WR} - T_{WLw}) \times Vw + [T_{WLw} - T_{WUp} - (T_R - T_{WR})] \times Vw + (T_R - T_{WR}) \times Vs$ (3. 2)

$D_{TR} = T_R \times Vw$ (3. 3)

After re-arrangement of the equations, the speed of sound V_{TMM} and the thickness d_{TMM} of TMM in the TMM test cell are given by:

$$V_{TMM} = \left(1 + \frac{T_{WR} - T_{TMMR}}{T_{TMMLw} - T_{TMMUp} + T_{WR} - T_R}\right) V_W \quad (3. 4)$$

$$d_{TMM} = V_{TMM} \times [T_{TMMLw} - T_{TMMUp} - (T_R - T_{WR})] \quad (3. 5)$$

For each measurement each TMM test cell sample was submerged in the water tank for a period of approximately 10 minutes for each measurement. The speed of sound of slice of TMM without the Saran Wrap was measured by transducer 710B over 50 minutes as a comparison to show the effects of glycerol leaching from the TMM.

3.3.4 Measurement of attenuation

The attenuation was calculated by subtraction of the frequency spectra of the RF signals from the reflector with the TMM test cell from that with the water test cell in the path. The attenuation of TMM relative to water α in the unit of $dB \cdot cm^{-1}$ was calculated using Equation 3.6:

$$\alpha(x, y, f) = -\frac{20}{2d_{TMM}} [\log_{10} A(x, y, f) - \log_{10} A_0(x, y, f)] \quad (3. 6)$$

where $A(x, y, f)$ is the magnitude of the spectrum of the signal from the reflector with the TMM test cell in place (Fig 3.3.a), $A_0(x, y, f)$ is the magnitude of the spectrum of

the signal from the reflector with the water test cell in place (Fig3.3.b), and d_{TMM} is the thickness of TMM in the TMM test cell.

The attenuation of air-free distilled water is proportional to f^2 over the range 7.5 – 67.5 MHz (Pinkerton 1949). The attenuation in distilled water α_w at 20 ^oC is 2.17×10^{-3} dB·cm^{-1} ·MHz^{-2} (Duck 1990) .

The attenuation was calculated over the 3 dB bandwidth of each transducer. A polynomial curve fit was applied to the data using Equation 3.7, because the attenuation of water has been shown to be proportional to f^2 and the attenuation of TMM has been shown to vary linearly with frequency at low frequency range. Higher order terms, such as f^3 were excluded as their coefficients proved to be very small (10^{-5}) compared with that of the lower order terms.

$$\alpha_{TMM} = \alpha + \alpha_w = af + bf^2 \qquad (3.7)$$

where α_{TMM} is the absolute attenuation of TMM, f is the frequency, and a and b are the coefficients of the polynomial function.

3.3.5 Acquisition and analysis of acoustical data

Twelve TMM test cells were measured at 3 independent positions by each transducer. For each TMM test cell, the raw RF data of 5 lines (5 positions) from 500 consecutive frames in 3 independent measurements were saved to the scanner and later transferred onto a PC and analysed using MATLAB. The angular separation between adjacent RF acquisition lines was approximately 0.3^o and so the lines were assumed to be parallel and perpendicular to the TPX reflector. The water test cell was scanned in a similar manner. For each position the mean and standard deviation of the thickness, speed of sound and attenuation were calculated.

3.3.6 The speed of sound and attenuation using the SAM system

The SAM system (Figure 3.4) used a broadband immersion transducer as both a transmitter and a receiver, which had frequency centred at 50 MHz with 1.27 cm focal length (V390-SU/RM; Olympus NDT Inc., Waltham, MA, USA). The measured 3dB bandwidth of the transducer used in the SAM system was 10 – 33MHz. For the SAM system, the same technique was employed for measuring the 3dB bandwidth as was used for the Vevo770, but the reflector was a glass slide. A pulser-receiver (Model 5052PR; Panametrics, Waltham, MA, USA) with in-house software developed in LabView (National Instruments, National Instruments Corporation, Austin, TX, USA) (Cannon et al. 2011) manipulated the transmitting and receiving signals. The transmitted ultrasound pulses were perpendicular to the surface of a glass slide at the focal plane of the transducer. A computer with a data acquisition card (PCI–5144; National Instruments) then acquired and saved the reflected, digitised (250 MS s^{-1}) signals (Digitiser: National Instruments, Model PCI-5114). Finally, the data was output to MATLAB for further calculations. A plastic washer of height 1.6 mm was attached on the glass slide to form a space between the test cell and reflector. All acoustic measurements were performed in air saturated water at 20 $^{o}C \pm 1\ ^{o}C$.

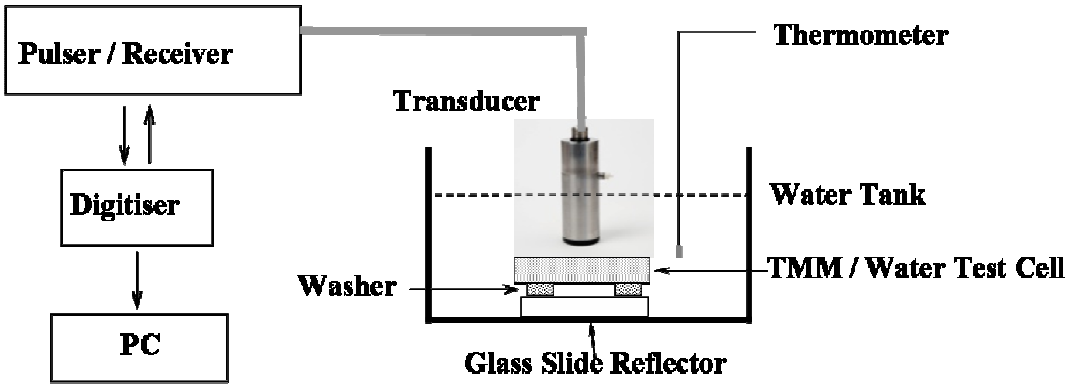

Figure 3. 4: *Schematic diagram of the SAM system*

The experimental process of sample and reference measurements were similar to those employed using the Vevo770 scanner. However, when using the SAM system,

the complete RF signal from each line was collected. For the measurements of one TMM test cell, 10 independent positions were scanned and 10 consecutive pulses at each position were recorded for data analysis. The attenuation was calculated using Equation 3.6. The speed of sound of the TMM measured by the SAM system required a known thickness of TMM that was previously acquired from measurements using the Vevo 770 scanner. The speed of sound of the TMM, V_{TMM}, was calculated using Equation 3.8 (AIUM 1995):

$$V_{TMM} = \frac{V_W}{1 + \Delta t \frac{V_W}{2d_{TMM}}} \tag{3. 8}$$

where d_{TMM} is the known thickness of the TMM test cell measured by Vevo770 scanner, V_w is the speed of sound in water and Δt is the measured time shift between T_{TMMR} and T_{WR}.

3.4 RESULTS

3.4.1 Speed of sound and thickness

The mean thickness values of each of the twelve TMM test cells measured by all the Vevo770 transducers are listed in Table 3.4 and show a maximum variation of 0.06 mm.

Table 3. 4: *The mean and standard deviation (in brackets) of the thickness of 12 TMM test cells measured by Vevo770 scanner*

Samples	**1**	**2**	**3**	**4**	**5**	**6**
Thickness (mm)	2.63 (0.02)	2.67 (0.04)	2.72 (0.03)	2.54 (0.02)	2.68 (0.02)	3.03 (0.03)
Samples	**7**	**8**	**9**	**10**	**11**	**12**
Thickness (mm)	3.17 (0.03)	2.55 (0.03)	2.96 (0.03)	2.47 (0.02)	2.75 (0.02)	2.72 (0.06)

Table 3.5 shows the measured TMM speed of sound and standard deviation. The mean values were found to be 1547.4 ± 1.4 $m \cdot s^{-1}$ and 1548.0 ± 6.1 $m \cdot s^{-1}$ measured by the Vevo 770 scanner and SAM system, respectively. Both results show good consistency and do not vary significantly over the frequency range 10 - 47 MHz. The acoustical properties from a second batch of 6 TMM test cells were also measured by the Vevo 770 scanner. The measured speed of sound was 1544.4 ± 1.0 $m \cdot s^{-1}$.

Figure 3.5 shows a typical time shift between T_{WR} and T_{TMMR} and the amplitude reduction of the reflected signal through the water test cell and TMM test cell in time domain. The two curves in Figure 3.6 show the corresponding spectra, the difference of which in the 3dB bandwidth is the attenuation as a function of frequency.

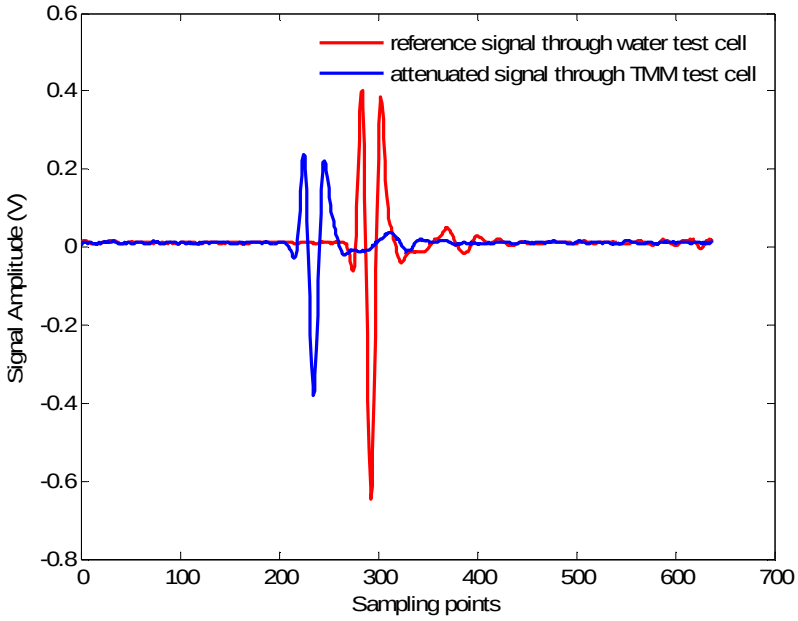

Figure 3. 5: *The signals reflected from the TPX reflector through the water test cell (reference) and through the TMM test cell in time domain*

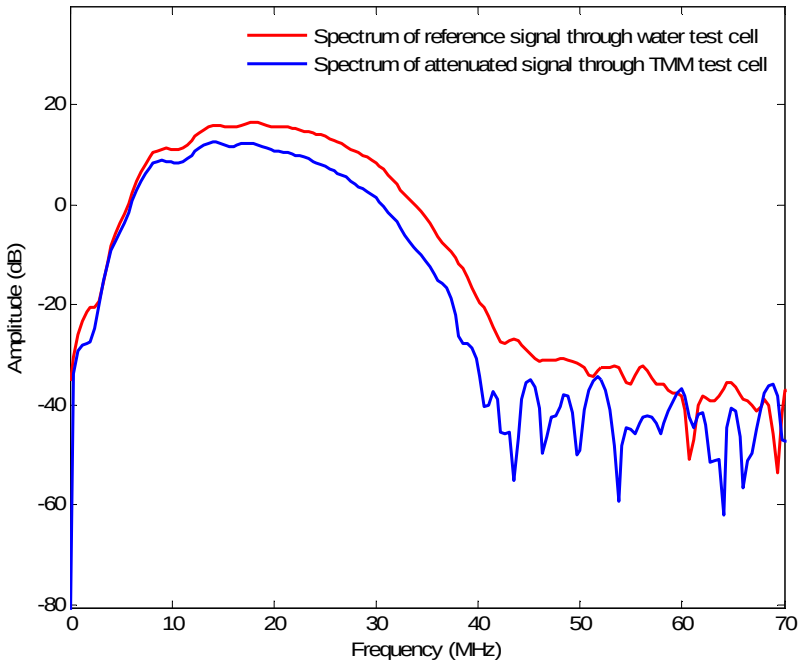

Figure 3. 6: *The frequency spectra of the signals reflected from the TPX reflector through the water test cell (reference) and through the TMM test cell*

Table 3. 5: *The mean and standard deviation (in brackets) of speed of sound ($m \cdot s^{-1}$) of 12 TMM test cells measured by the four transducers of Vevo770 scanner and SAM system (standard deviation was calculated from the averaged results of 15 positions on each TMM test cell)*

Transducer / Sample	710B	707B	704	711	SAM
1	1547.8 (0.5)	1547.6 (0.8)	1546.6 (4.1)	1546.9 (1.4)	1553.5 (2.7)
2	1548.3 (0.6)	1548.4 (0.9)	1547.9 (3.0)	1547.9 (2.0)	1552.1 (2.5)
3	1544.1 (1.5)	1545.7 (0.2)	1543.5 (0.4)	1547.2 (0.5)	1553.6 (2.4)
4	1547.4 (1.1)	1546.6 (1.1)	1548.3 (1.6)	1547.9 (1.0)	1554.8 (2.5)
5	1546.6 (1.6)	1547.0 (0.6)	1545.9 (2.0)	1546.6 (1.1)	1548.6 (5.6)
6	1546.1 (0.4)	1545.8 (0.5)	1546.7 (1.5)	1546.4 (0.3)	1549.5 (2.8)
7	1547.2 (0.4)	1547.0 (0.4)	1545.2 (1.5)	1547.4 (1.6)	1550.2 (2.5)
8	1547.8 (0.7)	1547.9 (0.6)	1547.3 (1.7)	1548.8 (0.5)	1539.6 (5.3)
9	1547.5 (0.5)	1547.8 (0.4)	1545.0 (1.3)	1548.3 (0.7)	1539.3 (3.3)
10	1547.4 (0.2)	1549.0 (1.0)	1547.6 (1.8)	1548.1 (1.4)	1542.6 (3.3)
11	1548.4 (0.5)	1550.2 (0.8)	1546.7 (2.7)	1548.1 (1.5)	1546.7 (3.0)
12	1548.4 (0.6)	1551.2 (0.8)	1549.4 (2.0)	1548.7 (2.3)	1545.9 (3.3)

Figure 3.7 shows the speed of sound results over 50 minutes of the unsealed TMM slice measured by transducer 710B over 50 minutes. The TMM sample was submerged in the water tank about 10 minutes for each measurement. The initial speed of sound is less than 1540 $m \cdot s^{-1}$and the value decreases about 15$m \cdot s^{-1}$ in the first 10 minutes.

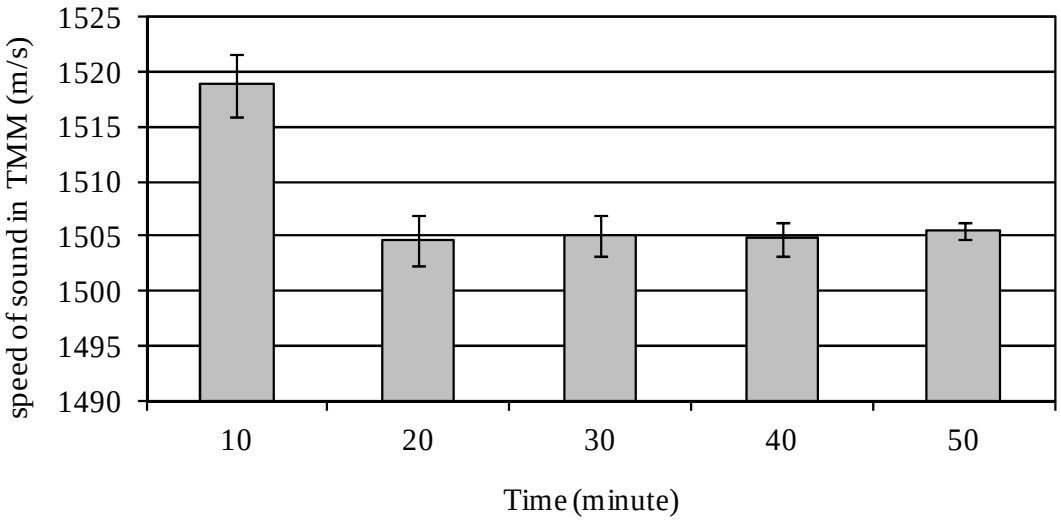

Figure 3. 7: *Variation in the speed of sound ($m \cdot s^{-1}$) with time (minute) for unsealed TMM samples*

3.4.2 Attenuation as a function of frequency

Figure 3.8 shows the attenuation of the two batches of TMM and demonstrates that the absolute attenuation in TMM increases with increasing frequency. When the previous TMM attenuation values measured by other groups (Brewin et al. 2008, Browne et al. 2003, Inglis et al. 2006) were compensated for the attenuation of water, the polynomial function $0.40\,f + 0.0076\,f^2$ was calculated to be the best-fit of all the relevant attenuation versus frequency data available for this TMM from 2 to 47MHz. This fitting curve is shown in Figure 3.9 with the previous attenuation results at the lower frequencies. The mean attenuation and standard deviation obtained with each transducer and for both batches of TMM are presented in Figure 3.10. The polynomial function fitting all the attenuation curves from batch 1 and batch 2, measured by transducers 710B, 707B, 704, 711 and the SAM system are listed in Table 3.6 and their goodness of fit by R^2 are shown to be greater than 0.99 for all fits.

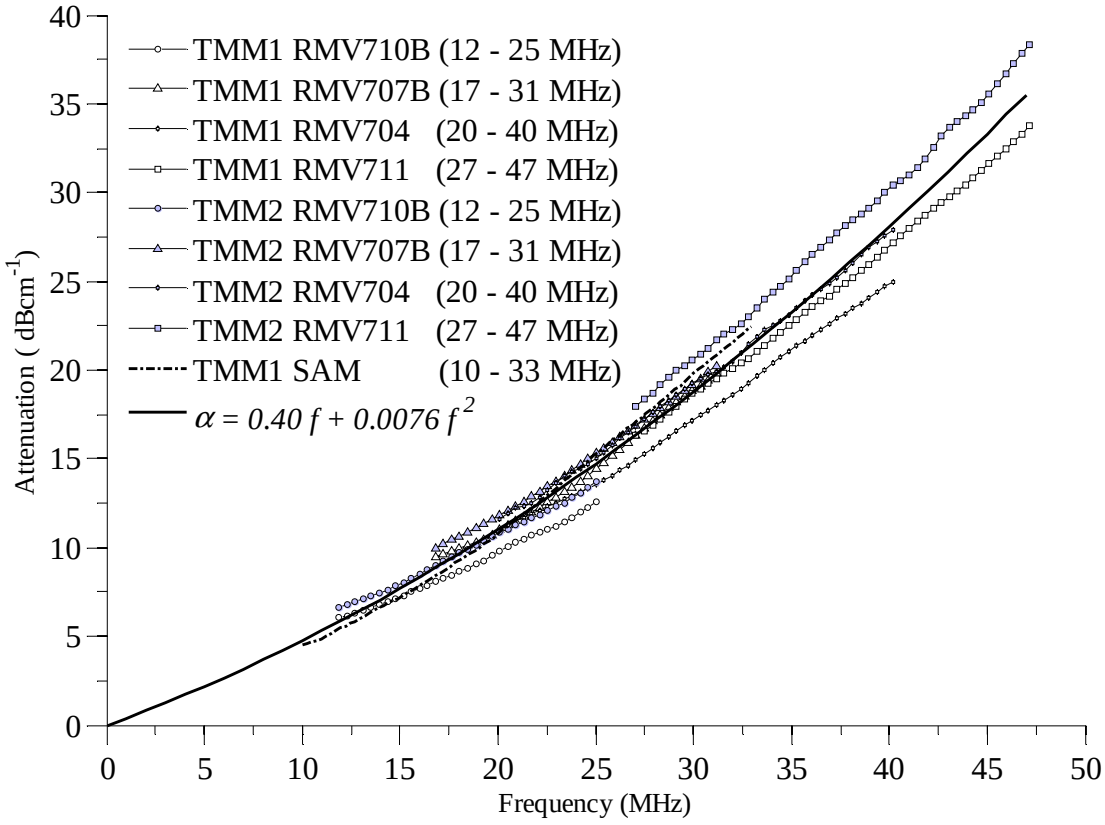

Figure 3. 8: *Attenuation of two batches of TMM as a function of frequency in the frequency range of 10-47 MHz measured by the Vevo770 scanner and SAM system, TMM1 is the first batch and TMM2 is the second batch.*

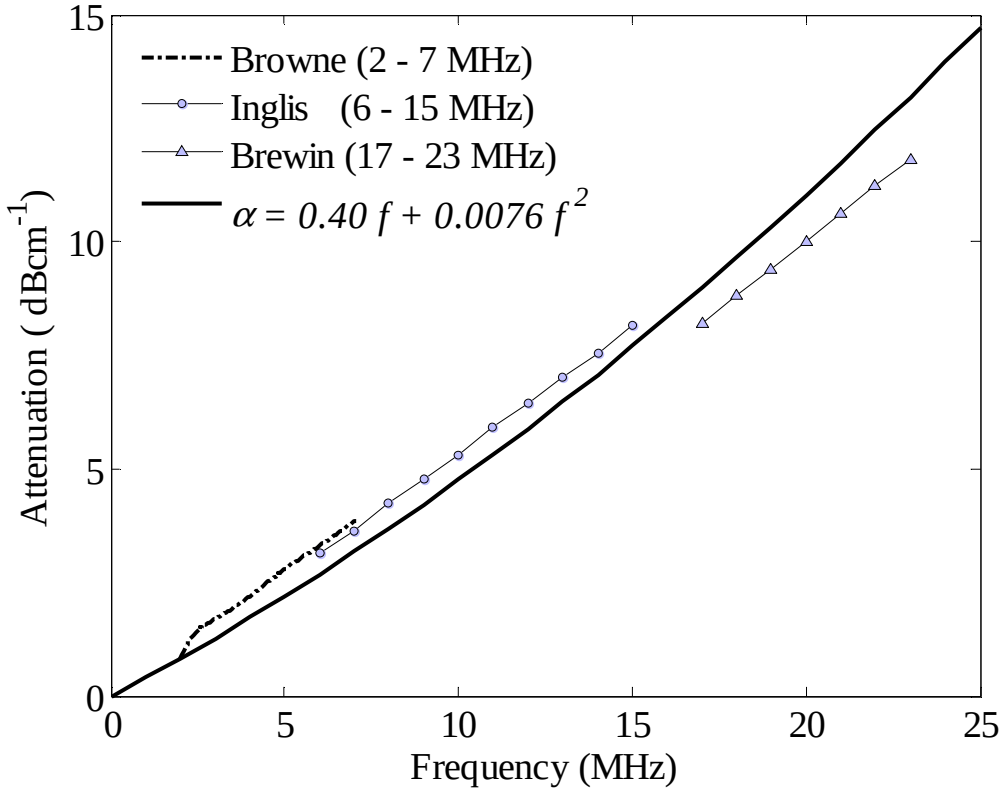

Figure 3. 9: *The polynomial curve-fit of the entire attenuation data set (both batches of TMM measured using four high frequency transducers and SAM system and the attenuation (compensated for attenuation of water) of TMM in 2-7 MHz (Browne et al. 2003), 6-15 MHz (Inglis et al. 2006) and 17-23 MHz (Brewin et al. 2008)).*

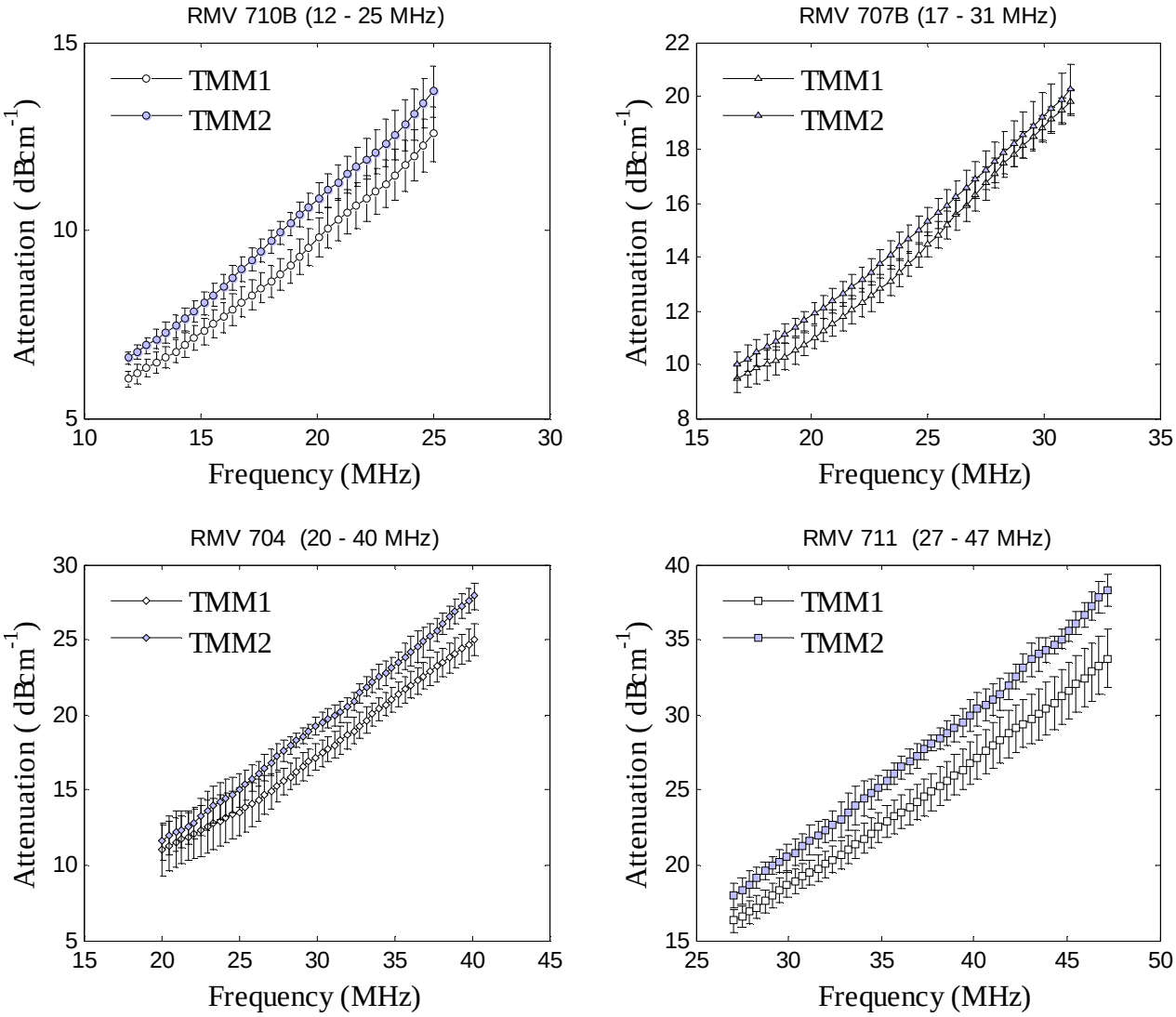

Figure 3. 10: *Mean and standard deviation attenuation values of the two batches of TMM as a function of frequency measured by transducers 710B, 707B, 704 and 711.*

Table 3. 6: *The polynomial fit ($\alpha = a f + b f^2$) of the attenuation of the two batches of TMM measured by Vevo 770 scanner and the SAM system*

Transducer	710B	707B	704	711	Combination	SAM
Batch 1	0.47 f + 0.00090 f^2	0.40 f + 0.0074 f^2	0.43 f + 0.0048 f^2	0.45 f + 0.0055 f^2	0.39 f + 0.0069 f^2	0.32 f + 0.011 f^2
Batch 2	0.53 f + 0.00030 f^2	0.50 f + 0.0048 f^2	0.46 f + 0.0059 f^2	0.48 f + 0.0069 f^2	0.39 f + 0.0088 f^2	

3.5 DISCUSSION

This chapter reports for the first time acoustical measurements of the IEC agar-based TMM at ultrasound frequencies higher than those routinely used in clinical practice but at frequencies commonly used for preclinical imaging. We did not attempt to separate the attenuation into the separate components of absorption and scattering but measured the overall attenuation of the TMM.

3.5.1 Sources of error

The sources of error were discussed for the measurement of thickness, speed of sound and attenuation respectively. For speed of sound and thickness, initially the reason for choosing the sealed test sample was explained. Secondly, the influence of variation in speed of sound in water and variation in the thickness of TMM were discussed because these two quantities were used to calculate the speed of sound shown in Equation 3.4 and Equation 3.8, respectively. For the attenuation measurement, there were four reflections as well as a double passage through the materials to take into consideration. The discussion detailing the magnitude of the uncertainty is most likely to be due to large uncertainties in the magnitude of the four reflections and their values and resultant influences were shown in section 3.5.1.2.

3.5.1.1 Measurement of thickness and speed of sound

In this study, the thickness of the TMM test cells was calculated using the RF data rather than by using mechanical callipers as the thin slices of TMM used in this study were easily compressed by the callipers. The small variation in the measured thickness at different sites on individual TMM slices is likely due to slight variations in the flatness of surface of TMM.

There are generally two approaches to test the thickness and speed of sound of a compressible and irregular shaped object using ultrasound. The first is to test the unsealed object in its preserving liquid that requires a known speed of sound of the preserving liquid over the relevant ultrasound frequency range. The second is to test the sealed object in water, since the acoustic properties of water have been extensively investigated across a wide ultrasound frequency range. Figure 3.7 shows the variation in speed of sound without wrapping or sealing. Brewin (Brewin et al. 2008) also quantified the glycerol leaching time by testing TMM with three thicknesses and showed that the speed of sound of a 7mm-thick TMM (the thinnest one) dropped from 1545 $m \cdot s^{-1}$ to 1525 $m \cdot s^{-1}$ in 40 minutes. The TMM samples in this experiment were approximate 2 mm, thus the thin piece increases the molecule interchange between the glycerol and water resulting in a faster reduction in speed of sound with time in water-bath.

The method described in this chapter adopted the second approach of testing the sealed object in water. This method of measuring the speed of sound in the TMM is relative and based on the published data of absolute speed of sound values in water (Bilaniuk and Wong 1993) and described by AIUM (AIUM 1995). However Lubbers and Graaff (Lubbers and Graaff 1998) have suggested that the speed of sound measurements in water made by Del Grosso and Mader (Del Grosso and Mader 1972) give more reproducible results. The discrepancy of speed of sound in pure water between the work of Del Grosso and Mader (Del Grosso and Mader 1972) and Bilaniuk and Wong (Bilaniuk and Wong 1993) between19 ^{o}C - 22 ^{o}C is smaller than

0.02 $m \cdot s^{-1}$ and therefore is smaller than the experimental error associated with this study.

The measured mean speed of sound in TMM in this study is comparable to the previously measured value of the speed of sound in TMM at lower frequencies. The thickness d_{TMM} used in the calculations of the SAM system was a mean thickness measured by the Vevo 770 scanner over 15 sites. Unlike the measurements made using the Vevo 770 when individual thickness measurements were used for each sampling position, a mean slice thickness was used in the measurement of the SAM system. This mean slice thickness value may contribute to the variation in speed of sound measurements measured by the SAM system.

3.5.1.2 Measurement of attenuation

The reflections from the TMM test cell interfaces contributed to the uncertainty on the attenuation measurements. Based on the calculations of transmission coefficients of TMM and water,
the amplitude transmission coefficient from water to TMM:

$$T_{W \to TMM} = \frac{2Z_{TMM}}{Z_W + Z_{TMM}} \tag{3.9}$$

the amplitude transmission coefficient from TMM to water:

$$T_{TMM \to W} = \frac{2Z_W}{Z_W + Z_{TMM}} \tag{3.10}$$

where the impedance of water is $Z_W = \rho_{water} c_{water}$, the speed of sound in water c_{water} = 1482.36 $m \cdot s^{-1}$ at 20°C, the density of water ρ_{water} =1.00286×10^3 $kg \cdot m^{-3}$ (Kaye and Laby 1995). The impedance of TMM is $Z_{TMM} = \rho_{TMM} c_{TMM,}$ the measured speed of sound in TMM c_{TMM} =1547.4 $m \cdot s^{-1}$, the density of TMM ρ_{TMM}= (1.07±0.03) ×10^3 $kg \cdot m^{-3}$ (Brewin et al 2008). The total amplitude transmission coefficient back and forth is

$$T_{total} = \left(\frac{4 Z_{TMM} Z_W}{(Z_{TMM} + Z_W)^2} \right)^2 = 0.9942 \qquad (3.11)$$

Consequently the transmission loss is constant and frequency invariant. However its influence on the measured attenuation of TMM does vary with frequency. The intensity transmission loss in the unit of $dB \cdot cm^{-1} \cdot MHz^{-1}$ is

$$\frac{20 \log_{10}(T_{total})}{f \cdot 2d} \qquad (3.12)$$

where f is the frequency, d is the thickness of TMM in cm. For a TMM sample of thickness 0.274cm, a theoretical uncertainty due to the four water-TMM boundaries was calculated to be less than 0.008 $dB \cdot cm^{-1} \cdot MHz^{-1}$ over the frequency range 12 - 47 MHz and so laid within experimental error of the attenuation measurements.

In addition, we have also quantified the uncertainties in the attenuation measurements due to the Saran Wrap interfaces on the test cells. We performed two substitution technique experiments using similar methods to those described previously. In the first experiment, the frequency spectra from the TPX reflector with a TMM test cell in the ultrasound path was subtracted from the frequency spectra with the same TMM test cell uncovered i.e. without Saran Wrap. In the second substitution experiment the frequency spectra from the TPX reflector with and without a water test cell (water encased in Saran Wrap) were subtracted. The difference between these two spectra was due to the difference in reflection coefficients at the Saran Wrap interfaces in these experiments. The maximum difference in these spectra was found to be less than 0.11 $dB \cdot cm^{-1} \cdot MHz^{-1}$, which is comparable to the standard deviation of the absolute attenuation value of ultrasound through TMM as shown in Figure 3.10.

3.5.2 The assessment of the usefulness of the TMM

3.5.2.1 TMM as a phantom for standard assessment at high frequencies

In this chapter the acoustical properites of an IEC agar-based TMM were measured from 21 - 47MHz to determine if such material has potential to be function as a suitable tissue mimic at high frequencies. We have shown that by combining all the data obtained from each of the transducers and the SAM system and including data at lower frequencies by other authors, a polynomial fit was applied to all the published data on this TMM from 2 – 47 MHz. The polynomial fit was found to be of the form $0.40\ f + 0.0076\ f^2$ and agreed well with the earlier measurements in the frequency range of 2 – 7 MHz (Browne et al. 2003) and 6 - 15 MHz (Inglis et al. 2006) and 17 - 23 MHz (Brewin et al. 2008). Moreover from Table 3.5, it can be seen that the coefficients of the linear terms varied between 0.4 $dB \cdot cm^{-1} \cdot MHz^{-1}$ and 0.5 $dB \cdot cm^{-1} \cdot MHz^{-1}$ for the four Vevo 770 transducers. The coefficients of quadratic term are not negligible showing the nonlinear frequency dependence of the TMM attenuation. However, at frequencies less than 15MHz, this polynomial approximated a linear fit to the data in the form of $0.47\ f + 0.32$.

In Figure 3.10 for all transducers, the attenuation of the second batch of TMM was shown to be higher than the first batch. The transducers 710B, 707B and 704 demonstrated differences in mean attenuation of less than 3 $dB \cdot cm^{-1}$. Note that the difference in mean attenuation between the two batches of TMM was found to be largest for the 711 transducer (highest frequency probe, 3dB bandwidth: 27-47MHz) with a maximum difference of 5 $dB \cdot cm^{-1}$ at higher frequencies. This large discrepancy may be attributed to the increasing nonlinearity of TMM at higher frequencies. From the phantom manufacture point of view, the variation between batches can be relatively easy to see in the high frequency range thus challenges the phantom production of comparable acoustic properties at high frequencies.

3.5.2.2 TMM for mimicking the properties of bio-tissue at high frequencies

As a primary step towards phantom manufacture at high frequencies, the TMM discussed in this chapter shows good reproducibility at high frequency and is consistent with the results from low-frequency acoustical characterisation results.

However, manufacturing the phantom that mimics the properties of tissue at high frequencies require acoustic data of bio-tissue at high frequencies. Published data on the acoustic properties of human and animal tissue at high frequency ultrasound (20 - 70 MHz) is limited and concentrated in the region of vascular tissues (Lockwood et al. 1991, Saijo et al. 1998), blood (Treeby et al.), skin tissues (Huang et al. 2007, Moran et al. 1995) and bovine tissue (Maruvada et al. 2000). Once data is published on the acoustical properties of soft tissue at high frequencies, the proportion of ingredients of TMM can be adjusted accordingly to approach these specific values.

3.6 CONCLUSION

The measured speeds of sound of an IEC agar-based TMM measured by the Vevo 770 scanner and SAM system were found to be 1547.4 ± 1.4 $m \cdot s^{-1}$ and 1548.0 ± 6.1 $m \cdot s^{-1}$. These values are consistent with the results in earlier studies by Browne et al. (Browne et al. 2003) over the range 2.25 - 15 MHz and Brewin et al. (Brewin et al. 2008) over the range 17 – 23 MHz. The attenuation in agar-based TMM was shown to increase with increasing frequency and is comparable to previous results when it extrapolates to the low frequency range. However at higher frequencies, the relationship between attenuation and frequency was shown to be non-linear. A unifying polynomial function $0.40\, f + 0.0076\, f^2$ was derived both based on the data generated in this study and on previously published data and was shown to be able to estimate the attenuation of this agar-based TMM in the frequency range 2 – 47 MHz. This characterisation of the TMM at frequencies greater than 20 MHz allows this IEC agar-based TMM to be potentially used in high frequency applications.

Furthermore, this work aids to develop the MATLAB codes that will be used for characterising the contrast agents and enable us to confidently use the TMM as a reference material.

Chapter 4

Development of the methodology for the acoustic characterisation of microbubbles

4.1 AIM

This chapter aims to develop a reproducible experimental set-up and methodology to explore appropriate experimental parameters for studying the acoustic properties of ultrasound contrast agents (UCAs) over the frequency range 12 to 43 MHz. After introducing the background information of commercial UCAs used in this thesis, the influence of concentration, pressure and insonation time are discussed.

4.2 INTRODUCTION

This thesis employed 3 commercially available UCAs: two clinical UCAs Definity (Lantheus Medical Imaging, USA) and SonoVue (Bracco Group, Italy) and one preclinical UCA MicroMarker (untargeted) (Visualsonics, Canada). Their parameters are listed in Table 4.1.

Table 4. 1: *The parameters of UCAs, *Definity (Lantheus Medical Imaging 2011), † SonoVue (Gorce et al. 2000, Schneider 1999), ‡MicroMarker (Visualsonics 2012).*

Name	**Gas**	**Shell**	**Mean diameter**	**Maximum concentration after reconstitution**	**Bolus dose recommended**
* Definity® (Luminity)	C_3F_8	Phospholipids	1.1-3.3 μm	1.2×10^{10} microspheres/ ml	10 μL/kg
†SonoVue®	SF_6	Phospholipids	2-3μm	$2\text{-}5\times10^{8}$ MBs/ml	2/2.4ml
‡MicroMarker™ untargeted contrast agent	C_4F_{10} / N_2	Polyethylene glycol, Phospholipids and fatty acid	2.3-2.9 μm	2×10^{9} microspheres/ ml	1×10^{7} bubbles/50μL

The magnitude of the backscattered spectrum is determined by the size, shape, number density and the elastic properties of the scatter materials (Insana et al. 1990). For sparsely and randomly distributed small spherical scatterers (e.g., air bubbles in water or fog droplets in air (Morse and Ingard 1986)), the diameter of which is much smaller than the wavelength and their relative incoherent backscattered intensity (De Jong 1993) at a distance r approximates to:

$$\frac{I_S}{I_0}=\frac{1}{9}nV\frac{k^4R^6\left(\gamma_k+\gamma_\rho\right)^2}{r^2} \qquad (4.\ 1)$$

Where I_s is the backscattered intensity, I_0 is the incident intensity, n is the concentration, i.e., number of scatterers per unit volume, V is the occupied volume, k is the wave number, R is the radius of the spherical scatter, γ_k is the compressibility

term, γ_ρ is the density term, r is the distance. From Equation 4.1, relative backscatter intensity has a linear relationship with the number of scatterers and it is proportional to diameter to the 6th power, which is equivalent to the square of the volume of the scatterer. Consequently, the variation in size distribution has a larger impact on the backscatter than concentration. Equation 4.1 is applicable only for sparsely populated linear scatterers. For a high concentration of scatterers, the magnitude of the scatter signal is not only dependent on the individual scatterer but also influenced by the interaction between the scatterers referred as multiple scattering (Stride and Saffari 2005).

One aim of this chapter is to determine the concentration range where the attenuation and backscatter are linearly proportional to the number of MBs. It is this linear range of concentrations which contributes to linear scattering models for modelling studies which generally assume homogeneously and randomly distributed scatterers and no multi-scattering (Marsh et al. 1998). For *in vitro* experiments performed in this linear concentration range, a linear relationship with the interested parameters (e.g., attenuation or backscatter intensity) is ensured and the occurrence of multiple scattering and shadow is avoided. Additionally, this linear range of concentration (dose) is also important in *in vivo* experiments, as the measured changes in the amplitude of received signals are directly proportional to the variations in haemodynamic properties (Stapleton et al. 2009). For this thesis, one concentration in this linear range is experimentally selected to ensure adequate signals with sufficient signal to noise ratio (SNR) for the following experiments.

The magnitude of acoustic pressure influences the oscillation of the microbubbles (MBs) and determines the amplitude and the spectral content of the received echoes. There is a balance that the pressure has to be sufficiently high to provide adequate SNR, and at the same time not destroy the MBs. Dissolution can occur when MBs enter into a solution and includes three types: non-destructive diffusion (static), transient diffusion (acoustically driven) and destruction (rapid fragmentation) depending on the driving pressure and bubble size (Bouakaz et al. 2005, Porter et al. 2006, Smith et al. 2007).

This chapter starts with the introduction of the preparation of UCAs (4.3), and the measurement of the size distribution (4.4). The acquisition format of the RF data is discussed in section 4.5. Acoustic measurements were measured at a series of concentrations of MBs to identify an appropriate range of concentration (4.6.1), in which the attenuation (4.6.2) and backscatter (4.6.3) vary linearly with number of MBs. Choosing one concentration in this range, the variation in attenuation and normalized backscatter power with incident pressure (4.7) and time (4.8) were measured to determine how the operating ultrasound parameters change the acoustic properties of MBs. As this chapter aims to develop method and experimental parameters, for each experiment the microbubble suspensions were tested only once unless otherwise stated. One measurement includes three continuous data acquisitions using one microbubble suspension.

In this chapter, since the results from the first experiments dictate the parameters selected in the later experiments the methods, results and discussions are compiled together for each experiment. No separated sections are set for results.

4.3 RECONSTITUTION OF UCAS

Definity contains 1.5ml clear liquid per vial and is recommended to be stored at 4^{o}C. The contrast agent is activated by rapid shaking for 45 seconds by a CAPMIX machine (ESPE, Seefeld, Germany).

SonoVue is kept at room temperature and is reconstituted by injecting 5ml sodium chloride solution 9mg/ml (0.9%) into 25mg lyophilized powder then hand shaking vigorously for 20 seconds.

MicroMarker (untargeted) is preserved at room temperature and is reconstituted by injecting 0.7 ml sodium chloride solution 9mg/ml (0.9%) into MicroMarker vial then gently agitating by hand for 1 minute.

After agitation, all MBs were left for 20 minutes for the surface bubbles on the suspension to disappear and to allow temperature of Definity to reach room temperature. Two 19G needles were inserted into the vial of Definity and MicroMarker, one of which was connected to a 1ml syringe. The needle and syringe were used to draw-up the contrast agent while the other 19G needle was used to vent the vial. SonoVue was withdrawn from the vial using the syringe incorporated in the SonoVue contrast reconstitution kit. The MBs were transferred into 0.2ml PCR tube (Eppendorf, UK) for storage and to enable smaller quantities to be extracted using pipettes (Gilson, USA). The specific volume of extraction depends on the concentration required. The activated MBs in the vial were resuspended by gently inverting the vial for 10 seconds before measurements. The activated UCAs may be used up to 12 hours for Definity (Lantheus Medical Imaging 2011) , 6 hours for SonoVue (Bracco 2011) and 3 hours for MicroMarker (Visualsonics). All the experiments of UCAs were completed within these time limits.

4.4 SIZE DISTRIBUTION OF UCAS

The size distribution of MBs was measured by a laser diffraction particle analyser named Mastersizer 2000 Hydro MU (Malvern Instruments Ltd**,** Malvern, UK). Optical microscope is also a common tool of sizing MBs (Sennoga et al. 2012) but not applied in this study because the sizing the interested small MBs(< 2 μm) in Chapters 5-6 is limited by the resolution of microscope.

The Malvern Mastersizer 2000 software (version 5.4) (Malvern Instruments Ltd**,** Malvern, UK) controlled the measurement, data generation and exportation of the data, and also allowed further calculation of curve fitting after data acquisition. The measurement used a standard operating procedure (SOP). A SOP was a pre-defined program in the software and consisted of laser alignment, background measurement, sample measurement and result output. The original measurement and output result

was volume based. Each sizing process defined in SOP consists of three measurements with 10 second-delay from one sample, then outputs one averaged size distribution curve automatically.

The sizing performed by the Mastersizer 2000 is based on optical technology and detects the laser diffraction pattern from the scattering solution, then employs Mie scattering theory and based on an assumption of spherical particle generated a size distribution curve. Mie theory is a solution to Maxwell's equation for modelling the scattering of generally spherical (both absorbing and non-absorbing) particles (Boliren and Huffman 1983). It has no particle geometric size limitation, so it is widely used in particle sizing.

Obscuration, refractive index (RI), absorption (imaginary RI) and residual are the most critical parameters for measurements. *Obscuration* is a quantity indicating the loss of light energy after introducing the test sample, the value of which determines the appropriate concentration of sample required ensuring sufficient sample present for sizing. As the size distribution of microbubble ranges from less than 1 μm to 10 μm, the obscuration recommended is larger than 10% (Malvern Instruments Ltd. 1999). *Refractive index (RI)* and *absorption (ABS) value* are quantitative measurements of the energy change of light transmitted through the sample medium. The RI and ABS function as coefficients in Mie model to fit the measured diffraction data set. *Residual* is the difference between the measured data and fitting curve. A value under 1% indicates a good fit (Malvern Instruments Ltd. 1999). If the residual is larger than 1%, RI and absorption values are not properly pre-defined in SOP and require adjustment to make the best fit of the measured data.

RI and absorption values of the contrast agents under test are unknown. Guan and Matula have previously shown that the intensity of the scattered optical signal showed little difference between free bubble and encapsulated thin shelled bubble (thickness of the shell < 30 nm) (Guan and Matula 2004). The shell thickness of SonoVue was reported to be 4 nm (Hoff 2001) and 2.5 nm (Chetty et al. 2008). The shell of Definity is a phospholipid monolayer and its thickness ranged between 1 to 2

nm (Goertz et al. 2007). Hence, the RI of the core gas was applied to the SOP and the resultant residual satisfied the requirements of being <1%. RI of the gas of SonoVue SF_6 was 1.00064 (Obriot et al. 1993) and approximately agreed with 1.0007 applied in the measurement of (Sennoga et al. 2012). The values of RI are listed in Table 4.2.

Table 4. 2: *The RI and absorption of contrast agent samples, glass beads and water * (Bideau-Mehu et al. 1996)*

	Water (Dispersant)	Glass bead	Definity	SonoVue	MicroMarker
RI	1.33	1.52	1.0012*	1.0007	1.001

Sennoga et al (2012) suggested that the absorption value for SonoVue was 0.01. This value produced residuals less than 1% and was used for all the UCAs sizing experiments.

4.4.1 Calibration using standard glass microspheres

Before sizing MBs, glass microspheres (QAS2002, Malvern instrument Ltd., Whitehouse scientific, UK) with known size 15-120 μm (nom), weight 2.5g (nom) were used to calibrate Mastersizer.

The size distribution of QAS 2002 glass microspheres ranges from 15 – 120 μm shown in Figure 4.1. Dv10, Dv50 and Dv90 give the size of particle below which 10%, 50% and 90% of the sample population lies respectively. The values of Dv10, Dv50 and Dv90 of the mean measured data are 29.274 μm, 46.48 μm and 73.384 μm. Table 4.3 lists the median values and limits provided by the manufacturer. These comparisons of the measured particle size distribution with the reference size range from the manufacture clearly show that Mastersizer passed the general calibration.

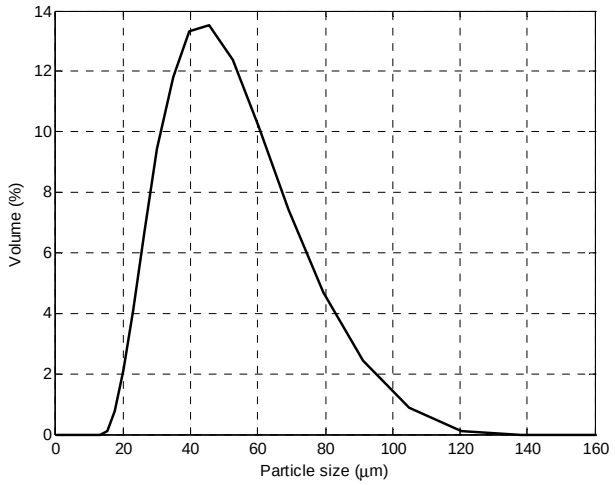

Figure 4. 1: *The size distribution of QAS 2002 glass microspheres*

Table 4. 3: *Standard percentile of the glass microspheres QAS 2002*

	Dv10 (μm)	Dv50 (μm)	Dv90 (μm)
Lower limit	26.72	45.40	72.38
Median values	28.43	46.8	77
Upper limit	30.14	48.20	81.62

As the diameter of the UCAs used in the following experiments is less than 15μm, a compensated performance verification certificate was issued from the manufacturer using latex beads of three diameters (nominal 0.3 μm, 1 μm and 9 μm) given in Appendix 4. All the above data certify Mastersizer 2000 functions properly particularly in the size range below 10 μm, i.e., the diameter range of MBs.

4.4.2 Sizing the microbubble suspensions

The SOP was initially built by inputting the RI of different UCAs in Table 4.2. Within the Mastersizer software, a general-purpose model with an assumption of irregular particle shape was used to fit the measured data and obtain the size

distribution curve. Although lipid MB are generally assumed to be spherical, the assumption of irregular particle shape was chosen due to the considerations: 1) automatic over-weighting factor on the detectors receiving small particles in spherical model 2) the surface roughness of shell leading to the light loss (Sennoga et al. 2012), and 3) possible dissolutions of MBs causing a buckling state (non-spherical geometry) (Marmottant et al. 2005).

MBs were added gradually until the required obscuration level was reached. Once the measurement was complete, the volume based size distribution curves were generated automatically. Using Mastersizer software, number based size distribution curves were derived from the volume based size distribution. Each sizing experiment took no more than 2 minutes and the total time of the UCAs sizing measurement was within the life time for UCAs as recommended by the manufacturer.

Figure 4.2 shows the size distribution curve of (a) Definity, (b) SonoVue and (c) MicroMarker. For each contrast agent, the left panel shows the volume-based size distribution and the right panel shows the number density size distribution. Although the total volume of the bubbles larger than 4 μm is greater than those less than 4 μm, the number of bubbles larger than 4 μm is much less than bubbles smaller than 4 μm.

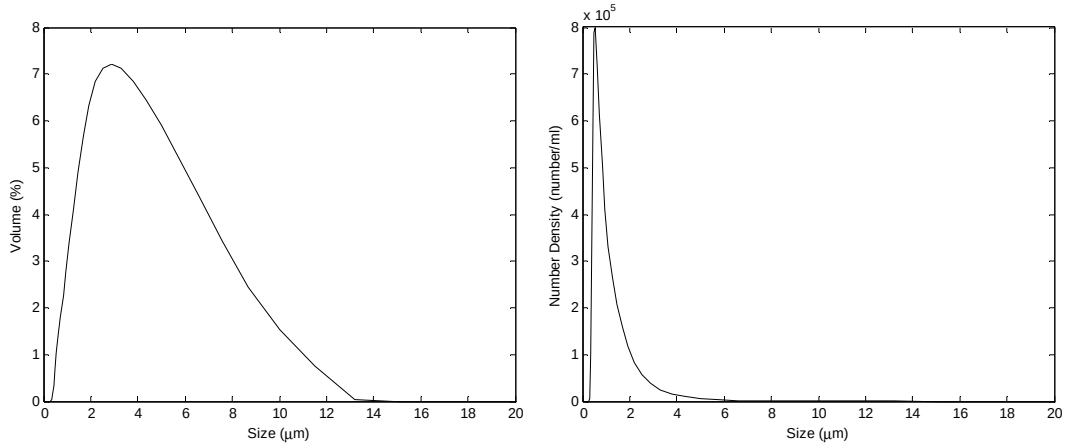

(a) Definity

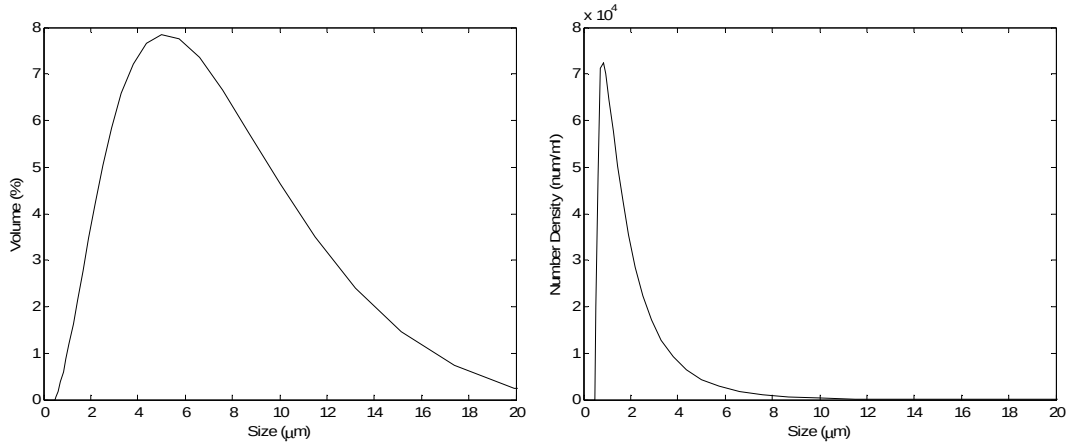

(b) SonoVue

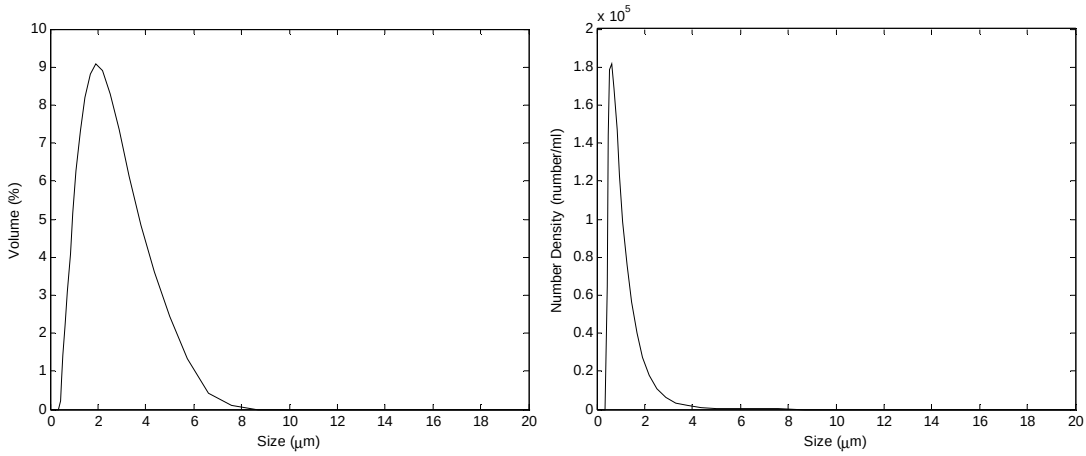

(c) MicroMarker

Figure 4. 2: *The native size distribution of microbubble: (a) Definity, (b) SonoVue and (c) MicroMarker. For each contrast agent, the left panel shows the volume-based size distribution. The right panel shows the number density size distribution.*

4.5 THE ACQUISITION OF RF DATA

Before introducing the experimental method of measuring the acoustic properties of the MBs, the RF data acquisition will be introduced first. Goertz stated that the time interval between adjacent measurements should be sufficiently long to allow independent sampling of signals (Goertz 2002). Based on the backscattered signal from the MB suspension, the acquired RF data was analysed to determine 1) whether the RF data samples are independent. This was determined using an autocorrelation function and 2) whether the magnitude of the data acquired at different lines (different spatial positions) is of statistical equivalence using one-way ANOVA.

The RF data from a pre-selected region of interest (ROI) was exported for analysis. The size of ROI was kept as small as possible to ensure that the pressure within the ROI was approximately the same and to ensure that attenuation within the ROI would be kept to a minimum. In these studies, the width of ROI is 1.5 ± 0.2mm and minimum length is 1 ± 0.2mm for each transducer.

Pulse repetition frequency (PRF) and frame rate were unable to be adjusted in RF mode. However, the time required for digitising and saving selected RF signals indirectly controlled the PRF and frame rate by setting the number of frames, lines and acquisition/line in ROI. The maximal number of frames, lines and number of acquisitions are 1000, 100 and 20. 20000 is the upper limit of the product of these three quantities, i.e., no more than 20000 signals were able to be saved per capture.

In this experiment, for RF data acquisition, the number of frames, lines and acquisitions/line were set at 100, 3 and 1. It took 4 seconds to save these 300 signals and approximate 13 ms between each acquisition. Three measurements of 100 frames, each frame comprising 3 lines of RF data, i.e. 100 samplings × 9 groups (lines) were acquired. As an example, for each acquisition the magnitude of the backscattered signal over 3dB bandwidth of the spectra of 9 groups using Definity measured by transducer 710B (centred at 25 MHz, 3dB bandwidth: 12-25MHz) was calculated.

The autocorrelation function of the 900 samplings (100 samplings × 9 lines) is shown in Figure 4.3. An autocorrelation of 1 indicates a perfect correlation and the value of 0 means uncorrelated between the samplings. Within 50 samplings, the autocorrelation value approximates to 0 in Figure 4.3 and shows that the data saved in the defined format is independent. Thus each measurement acquires backscattered echo from fresh MBs which have not been insonated and no interference occur between the adjacent acquisitions.

The box plot in Figure 4.4 shows the magnitude of the backscattered signal obtained from the 9 lines. The median (red line in the middle of the box) and the 25th and 75th percentile (top and bottom line of the box) of the samplings of each of the 9 lines are approximate the same (± 2dB). Symbol of + represents point beyond the whiskers. From the statistical analysis, the significance (P value) of the data between the 9 lines was calculated to be 0.62 indicating that there is no significant difference between the 9 lines, i.e., the RF data acquired at different positions (3 lines) is the statistically equivalent resulting from the homogeneous MB suspension under the same insonation. Consequently for the remainder of this chapter, the RF data was acquired in this format (100 frames ×3 lines×1 acquisition) and repeated 3 times.

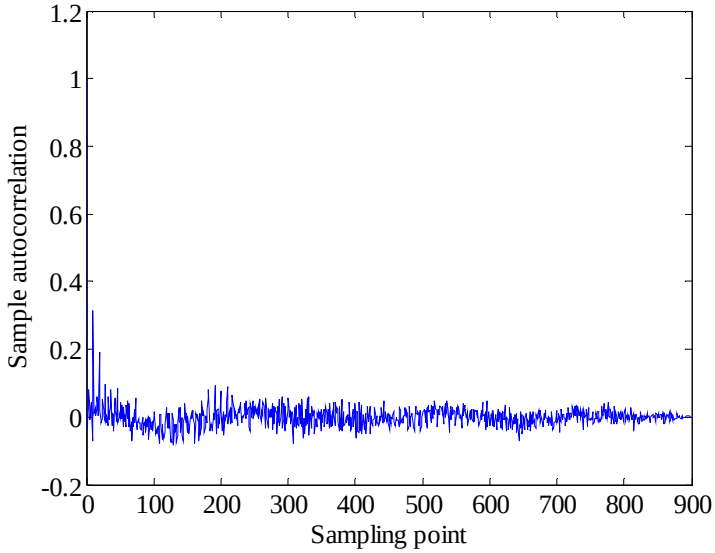

Figure 4. 3: *The autocorrelation function of the backscatter spectra of the 900 samplings*

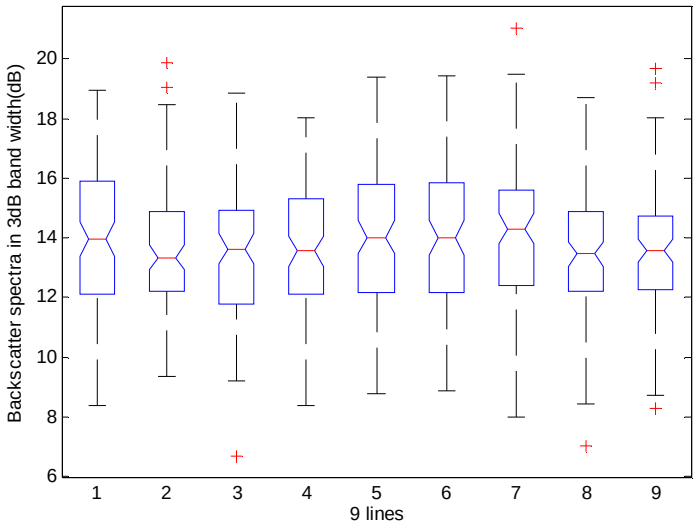

Figure 4. 4: *The comparison of the magnitude of the backscatter spectra at 9 lines. The three lines of the box represent the 25th, 50th (median) and 75th percentile sequentially and the symbol + represents point beyond the whiskers.*

4.6 THE VARIATION IN ATTENUATION AND NORMALIZED BACKSCATTER POWER AS A FUNCTION OF CONCENTRATION

The acoustic properties, including attenuation and normalized backscatter power of the microbubble suspensions, were measured using the substitution method described in Chapter 3. Due to the limited volume (0.7 ml per vial) and cost (10 times higher than SonoVue) of MicroMarker, the acoustical data of MicroMarker was measured only by transducers 707B and 704 (section 4.6.2).

4.6.1 Determination of tested concentration of MBs

This section described the reasons for choosing a series of tested concentrations of MBs. Figure 4.5 shows the B-mode image from (a) low concentration 0.1×10^{6}

mbs/ml to (c) high concentration 10×10^6 mbs/ml. The white horizontal line in each figure is the upper surface of the reflector. The white triangle symbol beside the scale indicates the focal position. Two horizontal figures are from the same tank of MBs and the only differences are the position of ROI and Gain values. The three figures on the left panel are used to show the influence of concentration on attenuation. With increasing concentration, the brightness of the signal from the reflector gradually reduces due to the attenuation. The three figures on the right panel are used to show the impact of concentration on backscattered signals from MBs. As a result of increasing concentration, the amplitude of backscatter signals increases first because of the increasing number of MBs then declines due to the attenuation in the path.

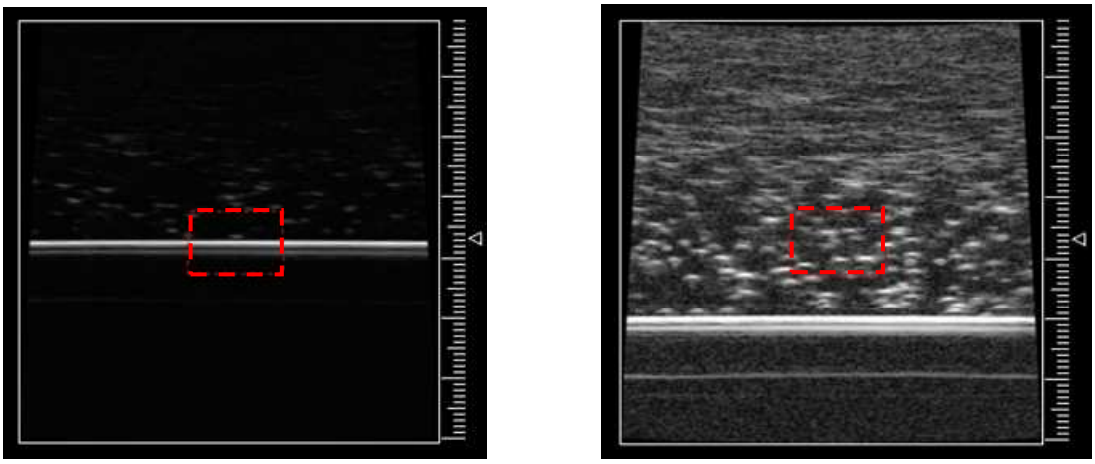

(a) Low concentration (0.1×10^6 mbs/ml) (Gain: -2dB (left), 23dB (right))

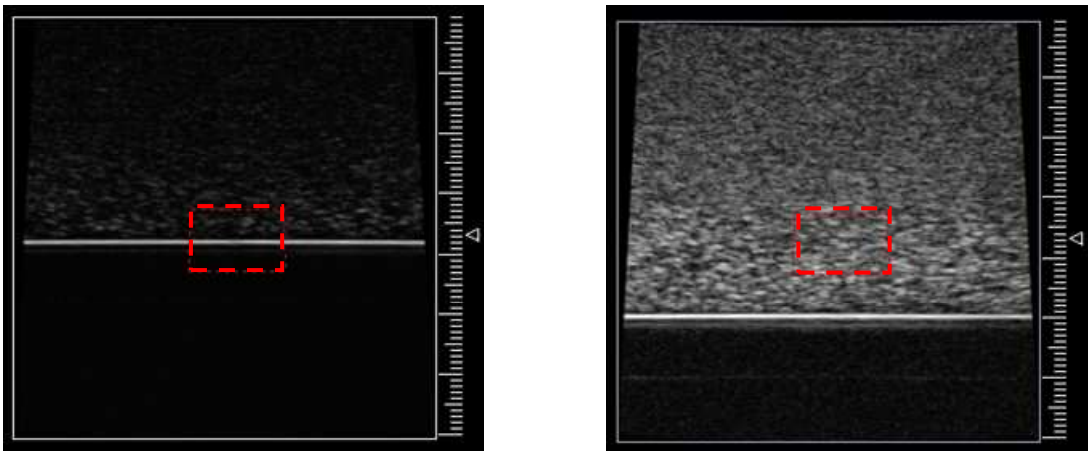

(b) Medium concentration (0.8×10^6 mbs/ml) (Gain: -2dB (left), 18dB (right))

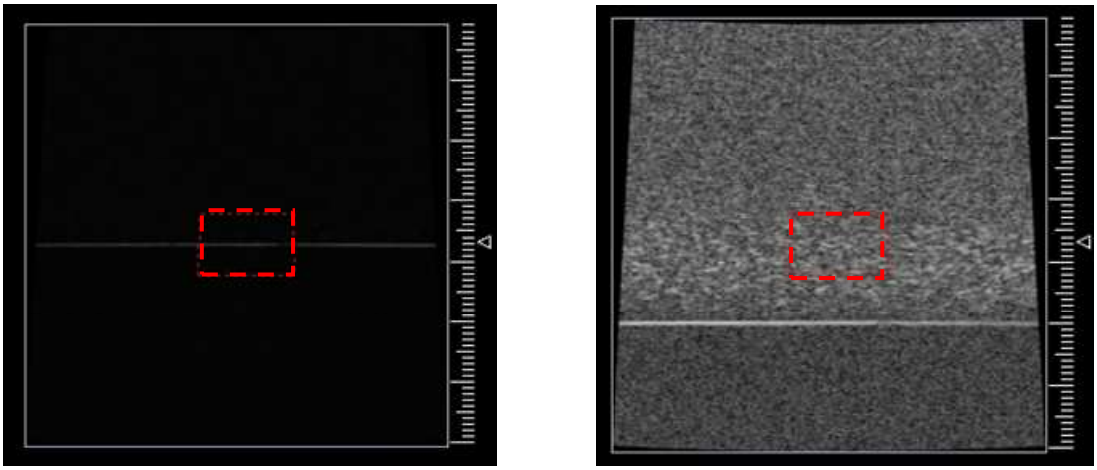

(c) High concentration (10× 10^6 mbs/ml) (Gain: -2dB (left), 31dB (right))

Figure 4. 5: *Examples of B-mode image of reflected signal from reflector and backscatter signals from microbubble suspension at (a) low, (b) medium and (c) high concentration acquired by transducer 707B, white triangle indicates the focus (12.7mm in this case) on the right scale (accuracy: 0.1mm), ROI size (red box): 1mm×1.5mm.*

The recommended concentrations of Definity, SonoVue and MicroMarker, in a unit of mbs/ml, for practical applications (shown in the last column of Table 4.5) are calculated based on the physiological parameters of human and mice (Janssen and Smits 2002) shown in Table 4.4, the maximum number of MBs within the vial after reconstitution and the recommended dosing regime from the manufacturer shown in Table 4.5. A series of test concentrations were chosen around these recommended concentrations and listed in Table 4.6. MBs were diluted in air saturated distilled water for the measurement.

Table 4. 4: *Physiological parameters of human and mice*

Human		**Mice**	
Weight	Blood volume	Weight	Blood volume
70 kg	5 L	0.03 kg	2ml

Table 4. 5: *The maximum concentration from manufacturer, recommended bolus dose and *their corresponding concentration in a unit of mbs/ml using the parameters of human (Table 4.4) for calculating the concentration of Definity and SonoVue, and the parameters of mice (Table 4.4) for calculating the concentration of MicroMarker*

Name	Maximum concentration after reconstitution	Bolus dose recommended	Calculated concentration*
Definity® (Luminity)	1.2×10^{10} microspheres/ ml	10 μL/kg	1.6×10^{6} mbs/ml
SonoVue®	$2\text{-}5\times10^{8}$ microspheres /ml	2/2.4ml	0.2×10^{6} mbs/ml
MicroMarker™ untargeted contrast agent	2×10^{9} microspheres/ ml	1×10^{7} bubbles/50μL	4.9×10^{6} mbs/ml

Table 4. 6: *The tested concentration and dilution rate of Definity, SonoVue and MicroMarker*

Definity ($\times10^{6}$ mbs/ml)	0.01	0.075	0.15	0.3	0.6	1.2	1.6	2.4
Dilution rate	1:320000	1:160000	1:80000	1:40000	1:20000	1:10000	1:7500	1:5000

SonoVue ($\times10^{6}$ mbs/ml)	0.1	0.2	0.4	0.8	1.6	4.9	6.4	10
Dilution rate	1:5000	1:2500	1:1250	1:625	1:312.5	1:102	1:78	1:50

MicroMarker ($\times10^{6}$ mbs/ml)	0.1	0.2	0.4	0.8	1.6	4.9	6.4	10
Dilution rate	1:20000	1:10000	1:5000	1:2500	1:1250	1:408	1:312.5	1:200

4.6.2 The concentration dependent attenuation measurement

The experimental apparatus for measuring attenuation were assembled as shown in Figure 4.6. A water tank (7cm-diameter, 4cm-height) was placed on a magnetic stirrer (RCT basic, IKA, US) with a magnetic bar (3mm-OD, 1cm-length) for ensuring a homogeneous suspension. A transducer was placed perpendicular to the TPX reflector which was positioned at the bottom of the tank, and the transmitting power was set at 10%-power, the corresponding peak negative pressures are given in Appendix 3. MBs, at a known concentration, were diluted into the water tank and stirred for one minute at a speed of 430 rpm before measurement. The schematic position of the ROI and the focus for the attenuation measurement are shown in Figure 4.7 and its corresponding figures from the scanner are presented in Figure 4.8.

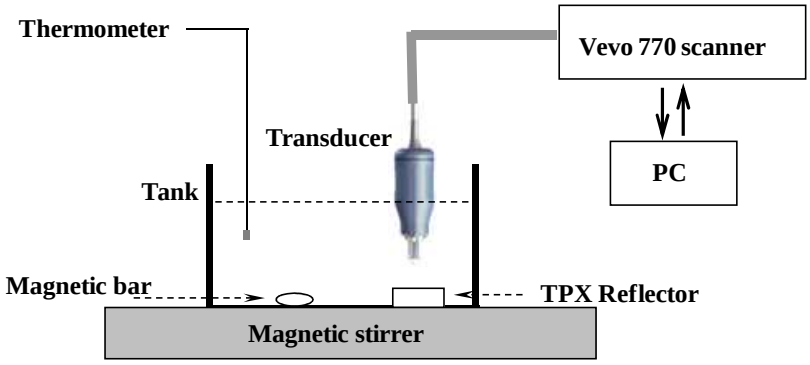

Figure 4. 6: *Schematic of experimental set-up*

The attenuation is measured as the amplitude reduction of the ultrasound signal, which has propagated through the diluted microbubble suspension, compared to the same signal propagated through the reference water medium. The attenuation coefficient was calculated by subtraction of the frequency spectra of the RF signals from the TPX reflector through the microbubble suspension from the RF signals from the TPX reflector through water. The attenuation coefficient α in the unit of dB•cm^{-1} was calculated using the Equation 4.2

$$\alpha = -\frac{10}{2d}\log_{10}\left(\frac{I(d)}{I(0)}\right) \qquad (4.\ 2)$$

where I(0) is the magnitude of the power spectrum of the signal from the reflector with the water in the tank (Figure 4.7.a), I(d) is the magnitude of the power spectrum of the signal from the reflector with the MBs in the tank (Figure 4.7.b), and d is the distance from the transducer to the upper surface of the TPX reflector. D is the distance reading from the RF raw data of the scanner which assumes speed of sound is 1540 $m \cdot s^{-1}$. The speed of sound V_{water} is from the published data (Bilaniuk and Wong 1993) at a specific temperature. The actual distance d between transducer and reflector is calculated by $d = (D/1540) \times V_{water}$.

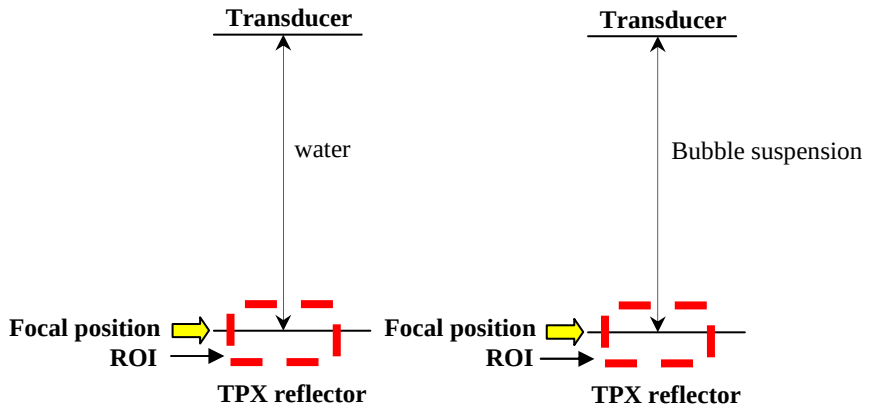

(a) Water in the tank *(b) Microbubble suspension in the tank*

Figure 4. 7: *Schematic of attenuation measurement showing the position of focus and ROI*

At each concentration, the attenuation of the contrast agent suspensions was integrated and averaged over the 3dB bandwidth of the transducers.

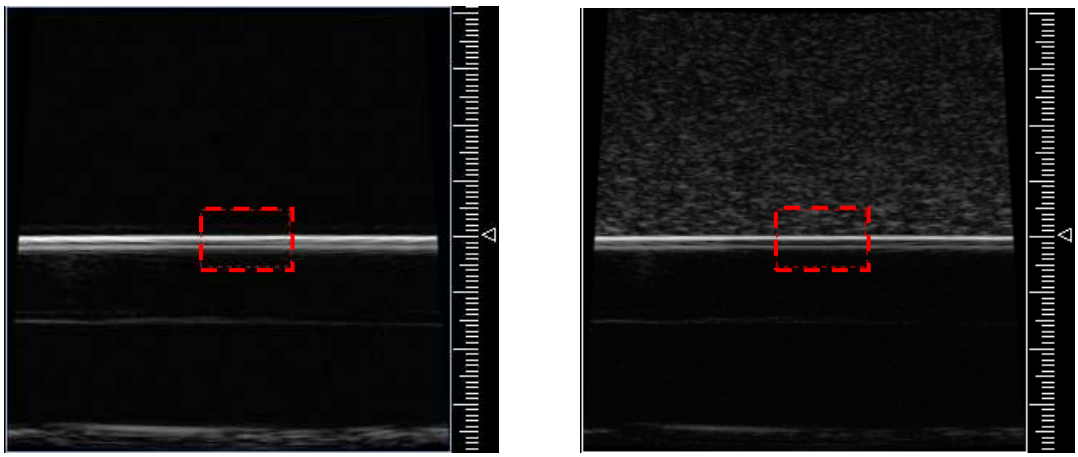

(a) Water in the tank *(b) Microbubble suspension in the tank*

Figure 4. 8: *The screen capture of the attenuation measurement corresponding to Figure 4.7. Examples acquired by transducer 710B, the red box is ROI (size: 1.2mm×1.7mm) and white triangle on the right side of scale indicates the position of the focus (15 mm in this case)*

The attenuation (Figure 4.9 - 4.12) of ultrasound through suspensions of Definity, SonoVue and MicroMarker (only measured by transducer 707B and 704) increase with increasing concentration measured by transducers 710B, 707B, 704 and 711 at 10% power. The inset in each figure shows the attenuation data as a function of concentration up to 10×10^6 MBs/ml. Attenuation varies linearly with concentration (at concentrations less than 3×10^6 mbs/ml) with R^2 shown to be greater than 0.99 for all fits.

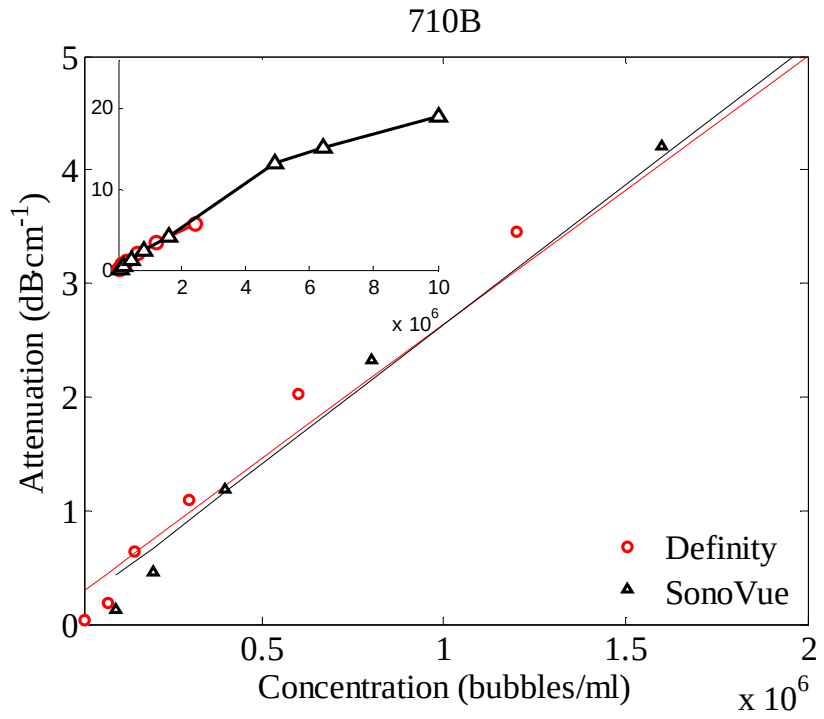

Figure 4. 9: *Attenuation of Definity and SonoVue as a function of concentration measured by transducer 710B (3dB bandwidth: 12-25 MHz)*

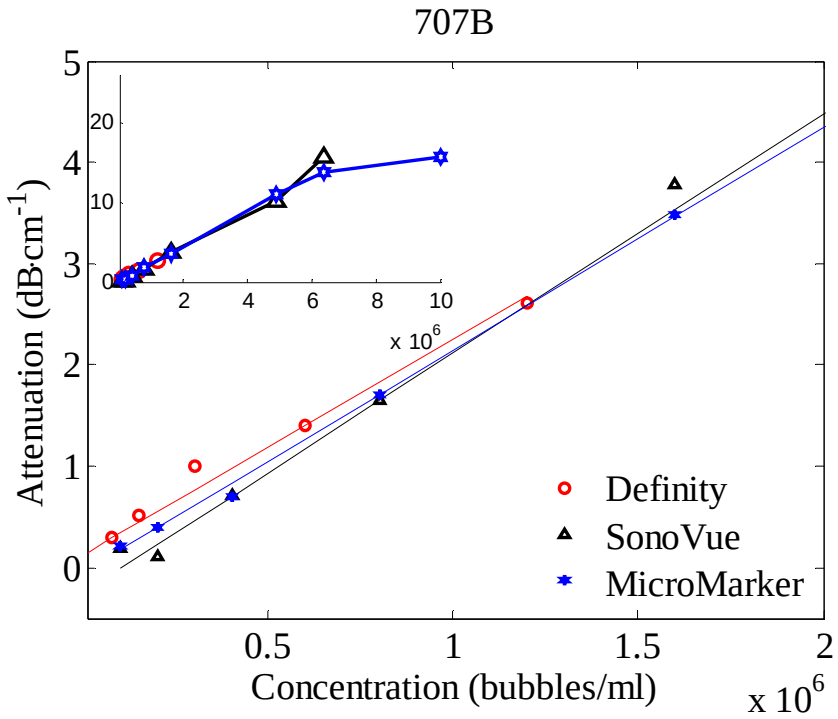

Figure 4. 10: *Attenuation of Definity, SonoVue and MicroMarker as a function of concentration measured by transducer 707B (3dB bandwidth: 17-31MHz)*

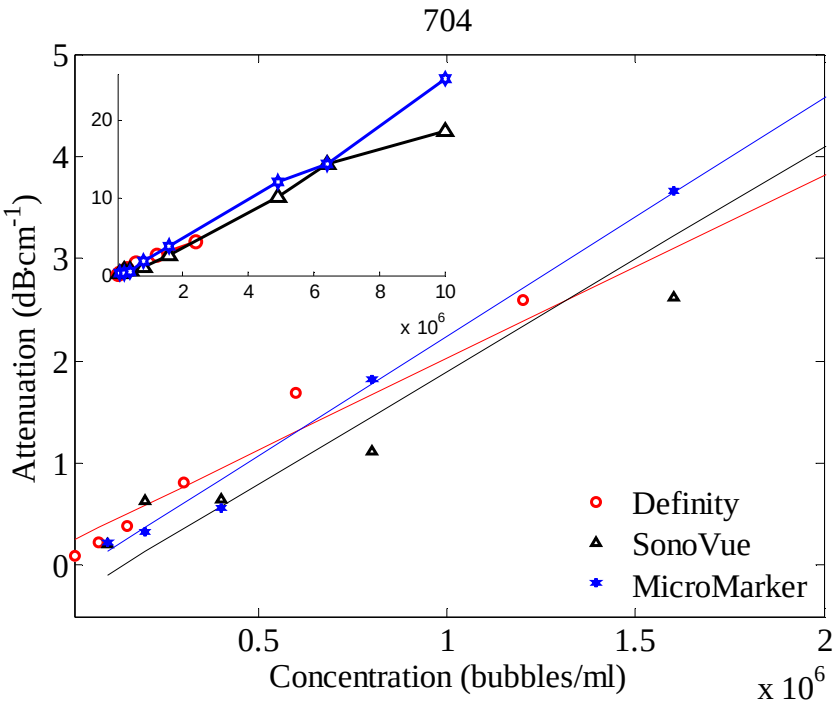

Figure 4. 11: *Attenuation of Definity, SonoVue and MicroMarker as a function of concentration measured by transducer 704 (3dB bandwidth: 18-32MHz)*

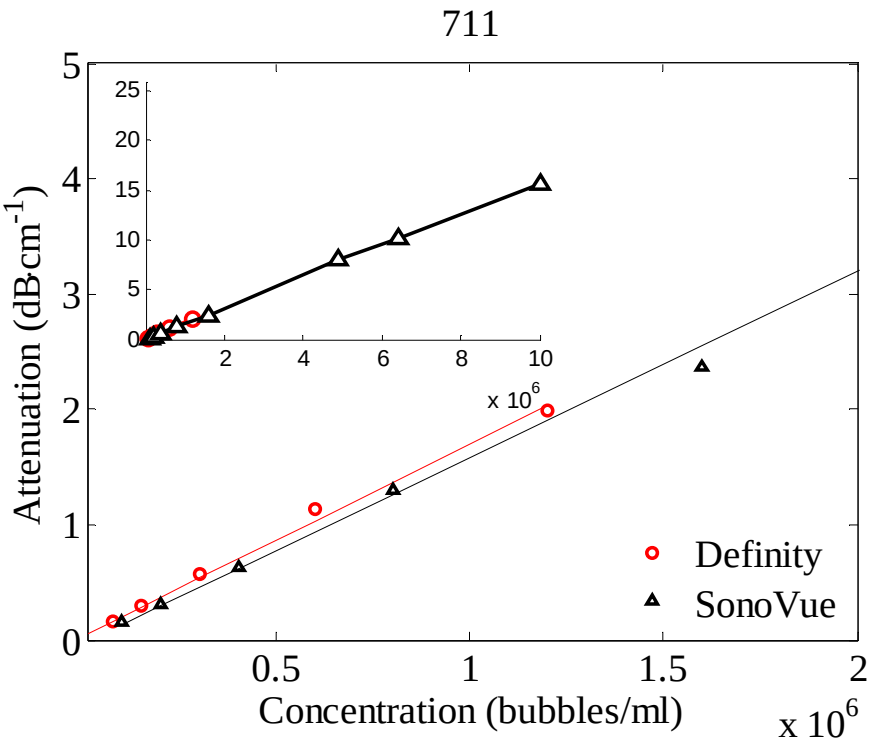

Figure 4. 12: *Attenuation of Definity and SonoVue as a function of concentration measured by transducer 711 (3dB bandwidth: 27-47MHz)*

4.6.3 The concentration dependence of normalized backscatter power

The normalised backscatter power (NBS) was calculated by normalizing backscatter power to a reference measurement to make the measurement independent of transducer properties. Previous groups have analysed six methods of processing the integrated backscatter signal in time and frequency domain and no significant difference was shown using myocardial tissue data (Rijsterborgh et al. 1993). The study regarded the integration of the backscattered spectrum over the 6dB bandwidth of the transducer as a gold standard. Other published calculations of the backscatter power include the root mean square (RMS) backscatter acoustic pressure (Pa) (Butler et al. 2008) and mean backscatter power (dB) over the sampling points (Moran et al. 2002).

The calculation of NBS in this chapter is based on the 'gold standard' from (Rijsterborgh et al. 1993) and normalized the mean squared acoustic power of the backscattered signal from the diluted microbubble suspension to the reflected signal from the reflector at the focus of the transducer in the microbubble suspension (Equation 4.3).

$$NBS = \frac{Backscattered\ \ Power\ \ Spectrum_{Bubble}}{Reflected\ \ Power\ \ Spectrum_{reference}} \qquad (4.3)$$

To avoid saturation of the amplifier electronics, the gain settings for the reference measurement were lower than that of diluted microbubble suspension backscatter measurements. This difference in gain settings was taken into consideration in the subsequent calculations.

For each concentration, the NBS of the contrast agent suspension was integrated and averaged over the 3dB bandwidth of the power spectra.

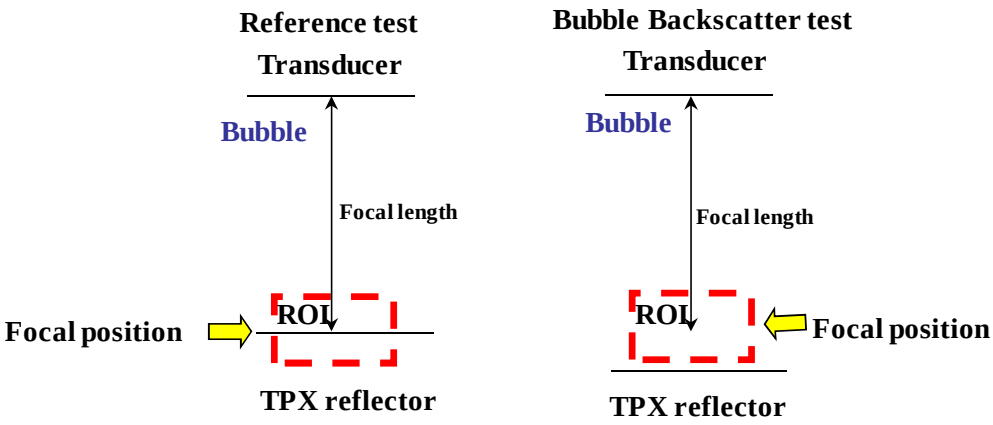

Figure 4. 13: *Schematic of normalized backscatter power measurement*

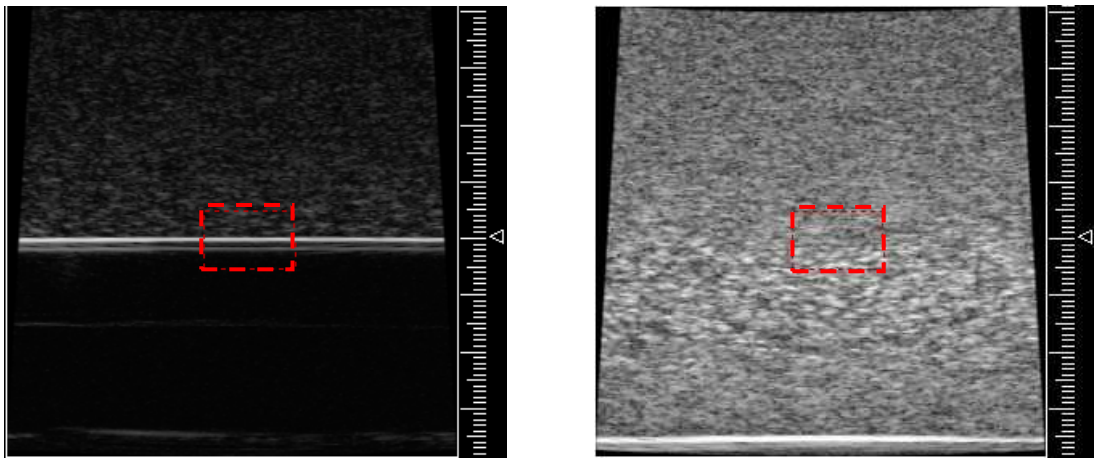

(a) Reference (Gain=-2dB) *(b) Backscattered signal from MBs (Gain= 23 dB)*

Figure 4. 14: *The screen capture of the NBS measurement corresponding to Figure 4.13 The red box is ROI and white triangle on the right side of scale indicates the position of the focus. Examples acquired by transducer 710B, the red box is ROI (size: 1.2mm×1.7mm) and white triangle on the right side of scale indicates the position of the focus (15 mm in this case)*

Figure 4.15 - 4.18 show NBS of ultrasound through suspensions of Definity, SonoVue and MicroMarker increase with increasing concentration measured by transducers 710B, 707B, 704 and 711 at 10% output power. NBS approximates a

linear relationship with concentrations (at concentrations less than 3×10^6 mbs/ml) with R^2 shown to be greater than 0.99 for all fits.

The insonating frequency of the testing transducers is much higher than the published resonance frequency of Definity (8 - 12 MHz) (Goertz et al. 2007) and SonoVue (1 - 3 MHz) (Gorce et al. 2000). In the same range of microbubble concentrations, the three UCAs produce comparable attenuation and normalized backscatter power responses. The transducer 711 that transmits the highest frequency ultrasound (3dB bandwidth 27-47MHz, the furthest from the resonance frequency) shows the lowest backscattered power and attenuation in Figure 4.18. The largest difference in normalized backscatter power between Definity and SonoVue is from the result of transducer 711.

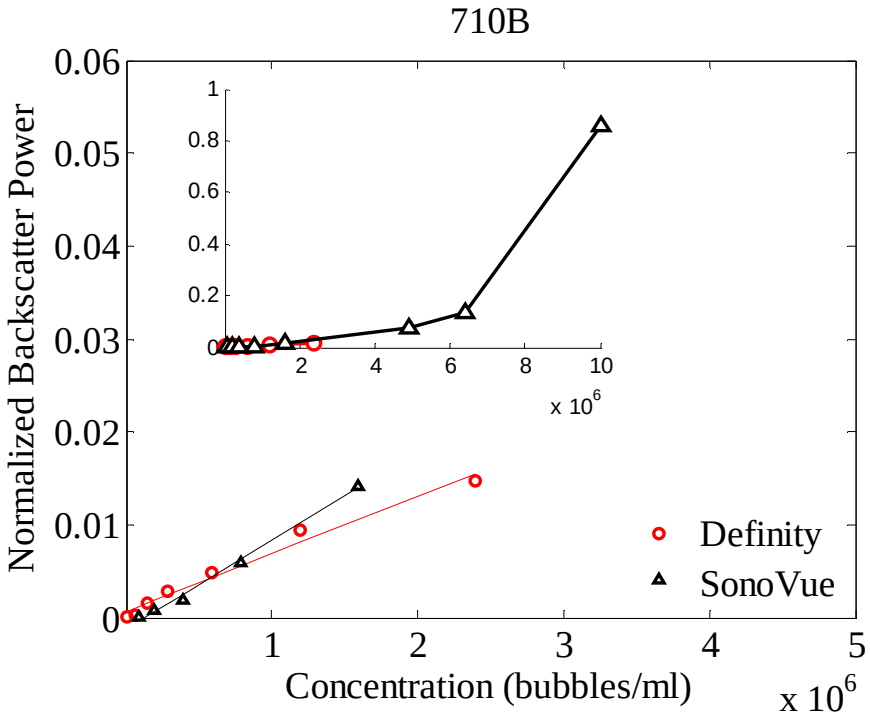

Figure 4. 15: *Normalized backscatter power of Definity and SonoVue varied with concentration measured by transducer 710B (3dB bandwidth: 12-25 MHz)*

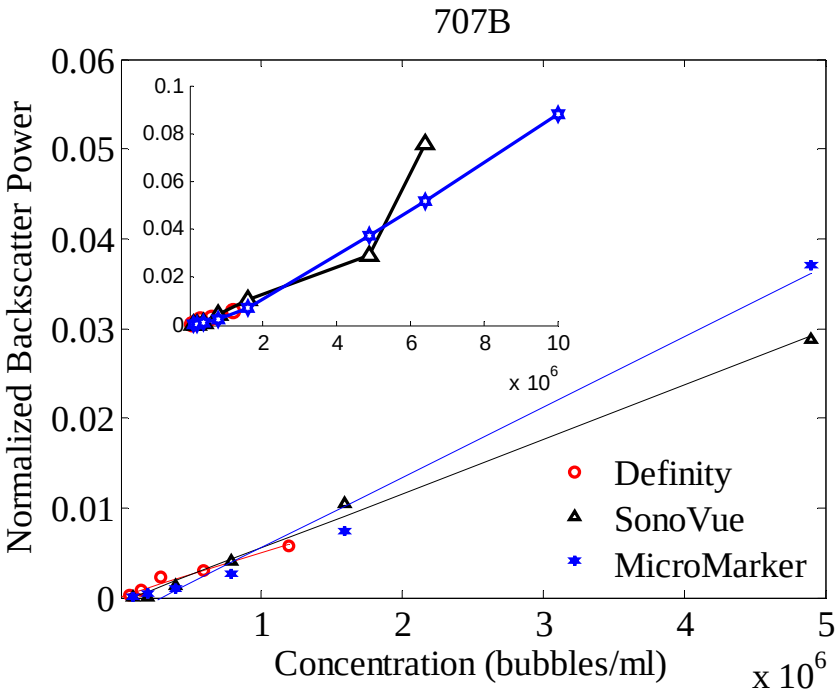

Figure 4. 16: *Norma*lized backscatter power of Definity, SonoVue and MicroMarker varied with concentration measured *by transducer 707B (3dB bandwidth: 17-31MHz)*

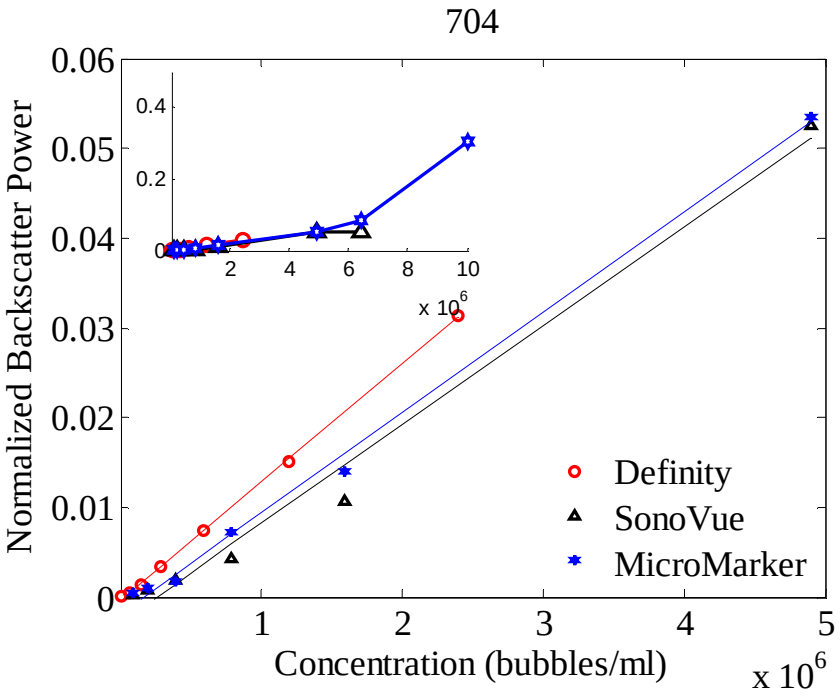

Figure 4. 17: *Normalized backscatter power of Definity, SonoVue and MicroMarker varied with concentration measured by transducer 704 (3dB bandwidth: 18-32MHz)*

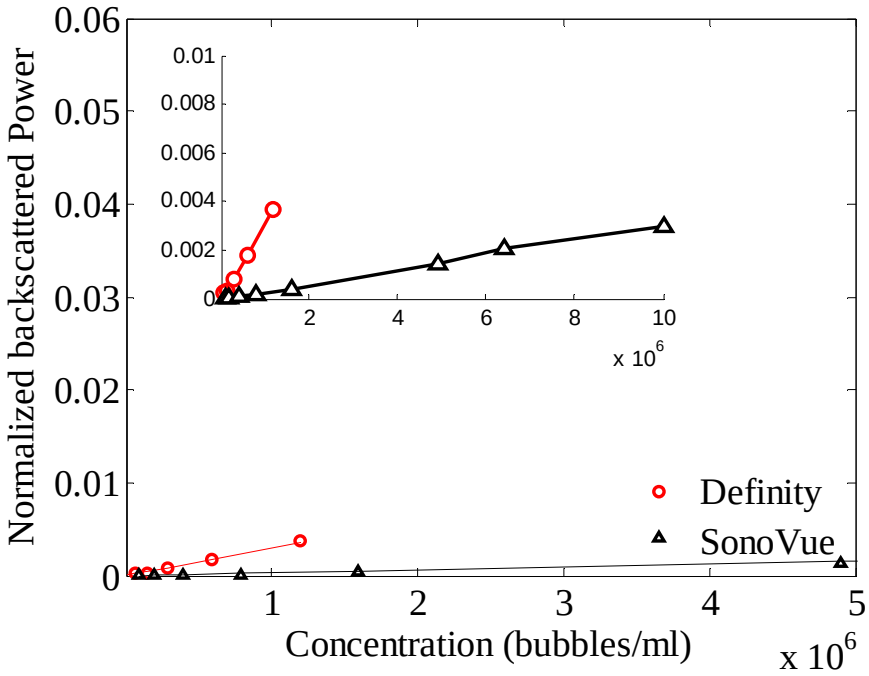

Figure 4. 18: *Normalized backscatter power of Definity and SonoVue varied with concentration measured by transducer 711 (3dB bandwidth: 27-47MHz)*

In summary, any concentration of tested MBs below 3×10^6 mbs/ml can be regarded as a suitable concentration for future experiments, as the attenuation and NBS demonstrate a linear relationship with the number of MBs. In this chapter, concentrations of 0.8×10^6 mbs/ml and 1.6×10^6 mbs/ml are used in the following experiments and 0.8×10^6 mbs/ml is used in Chapters 5-7.

4.7 THE PRESSURE DEPENDENCE OF ATTENUATION AND NBS

The acoustic pressure determines the amplitude of oscillation of MBs. Specifically, at low incident pressure, in a non-destructive environment the contrast microbubble can exhibit a prolonged enhancement period. At high incident pressure, the MBs are forced to collapse and produce a rapid and short enhancement. Some perfusion studies rely upon the interplay of two different acoustic pressure pulse transmission,

i.e., power modulation. Moreover drug-delivery studies use high pressures to cause the shells of drug- or gene-loaded MBs to collapse releasing a high gene- or drug-load to specific sites (Unger et al. 2001). Therefore it is important to assess MB behaviour at a range of acoustic pressures. A large number of studies is available at lower frequencies relevant for human diagnostic equipment, but not at the frequencies investigated here.

In this section, the attenuation and NBS of Definity and SonoVue suspensions were measured at transmitted powers from low (3%) to high (100%) using a concentration of 1.6×10^{6} mbs/ml, which was determined from Section 4.7 as a mid-point concentration at which attenuation and backscatter varied linearly as a function of concentration. In this experiment for each power, the attenuation and NBS of the microbubble suspensions was integrated and averaged over the 3dB bandwidth of the power spectra, respectively. Only transducer 707B was used because 707B shows the widest range of pressure (peak negative values (PNP) listed in Appendix 3) among the four tested transducers and its central frequency 30 MHz was in the middle of the frequency range of all the transducers. The experiment was completed once in one tank of MBs using one-cycle pulse over a period of 30 minutes. This pressure dependence experiment aimed to understand the trend of how attenuation and NBS varied with pressure and estimate a suitable pressure range for studies described in chapter 5 to measure the attenuation and contrast to tissue ratio under a non-destructive experimental environment.

Figure 4.19 shows the signal reflected from the TPX reflector through the water and microbubble suspension in the time domain and frequency domain. The difference of the spectra in Figure 4.19 (b) is the attenuation as a function of frequency over twice the distance between the transducer and the TPX reflector.

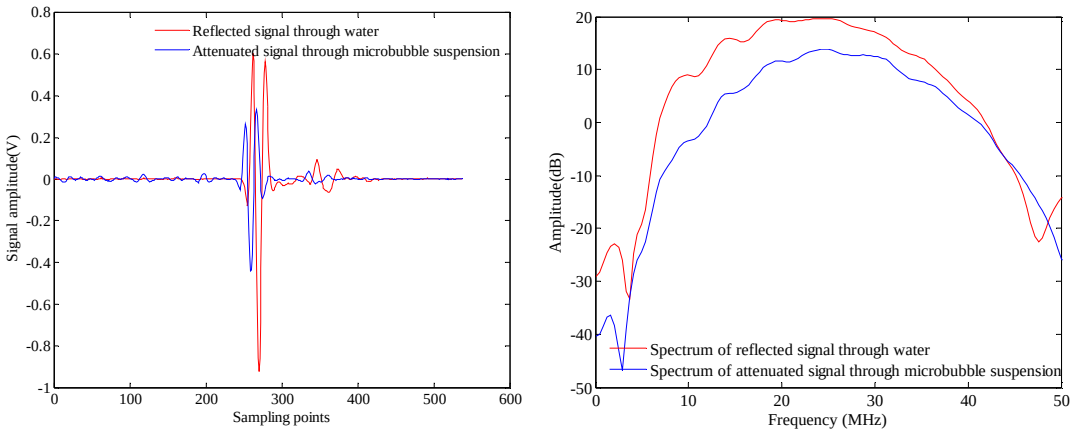

(a) *(b)*

Figure 4. 19: *The reflected ultrasound signals and their associated spectra reflected from the TPX reflector through the water (reference) and through the microbubble suspension in (a) time domain and (b) frequency domain*

From Figure 4.20, it can be seen that the attenuation decreases with increasing power settings. However, for powers below 8% power setting (the first 5 points on the PNP-axis), the attenuation curves of Definity and SonoVue stay approximately horizontal indicating a weak relationship between attenuation and pressure below 0.95 MPa (8%-power of transducer 707B).

The NBS is up to 8 dB higher at 3% power (the first PNP) than the 100% power (the last PNP) for Definity shown in Figure 4.21 (a) compared to a difference of 5dB for SonoVue in Figure 4.21 (b). At higher transmitting power, MBs oscillate in larger amplitude producing larger backscatter cross section, but also have a high possibility to be driven to diffuse and disrupt, thus the total number of scattering particles may reduce and the size distribution may change. For this reason, both the attenuation and NBS decrease with increasing power.

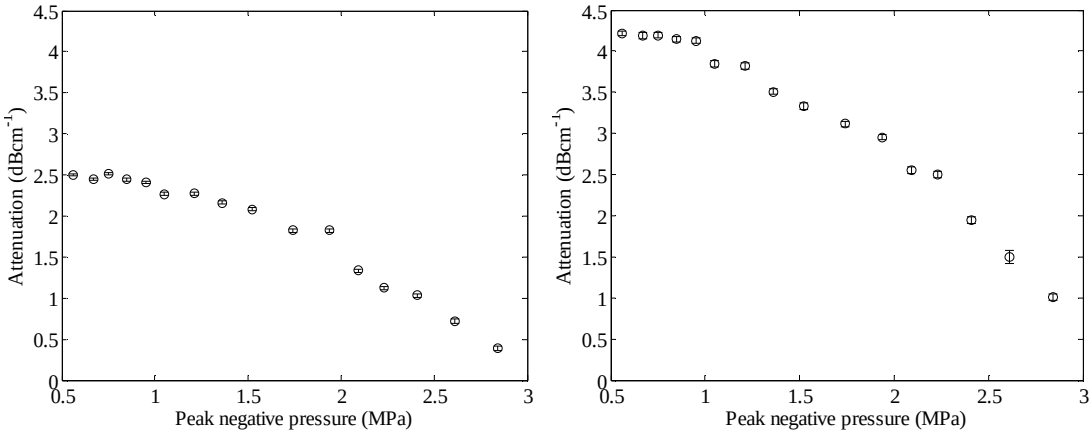

(a) Definity *(b) SonoVue*

Figure 4. 20: *The variation in the mean attenuation of (a) Definity and (b) SonoVue with PNP measured by transducer 707B*

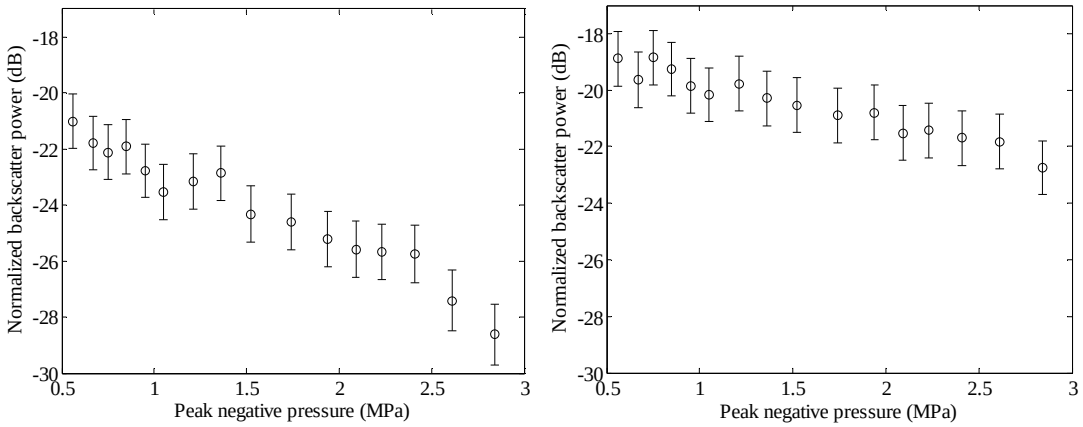

(a) Definity *(b) SonoVue*

Figure 4. 21: *The variation in the NBS of (a) Definity and (b) SonoVue with PNP measured by transducer 707B*

Note that the experiment in Figure 4.20-4.21 was completed in one tank of MBs in 30 minutes. Over this period of time, the natural diffusion of MBs may alter the acoustic response and the destruction of MBs may accumulate in the sequent measurements. Time and the different pressures may be additional factors to be considered, so the influence of time is further discussed in section 4.9 using one pressure per experiment. Additionally, the relationship between attenuation and

pressure could be further investigated by fast-time pressure dependent measurements as previously described (Tang et al. 2005). However, because of the long time-interval limitation of manual operation in setting varying pressure during the experiment, this work can not be accomplished using this scanner.

4.8 THE VARIATION OF ATTENUATION AND BACKSCATTER WITH TIME

The behaviour of the MBs over time is also of interest, as this may reveal the occurrence of acoustic driven diffusion and rapid fragmentation at various pressures. This section includes two experiments. The first one is the attenuation measurements obtained by transducer 707B at four power settings 4%, 10%, 50% and 100% acquired over a period of 15 minutes intermittent scanning. The second experiment is measurements of normalized backscatter intensity using 4 transducers 710B, 707B, 704 and 711 over 30 minutes intermittent and continuous scanning.

In the first experiment, the attenuation measurements were obtained 4 times intermittently by transducer 707B over 15 minutes with 5-minute interval between scans. Four power settings 4%, 10%, 50% and 100% were used in each independent test. In Figure 4.22, the frequency dependent attenuation curves at 4%-power are stable over 15 minute because the attenuation curves overlap, whereas the attenuation curves at other power settings drop gradually at sequential time points showing attenuation decreases with time. Higher power gives a more pronounced decrease of attenuation for each UCA seen from one column of Figure 4.22. The attenuation of Definity measured at 10%, 50% and 100% presents similar values around 3.5-3.75dB·cm^{-1} at 17MHz while the general trend of attenuation with frequency is steeper at 100% power than that at 10% power setting. However, for SonoVue, the attenuation curve of the initial measurement drops with increasing power.

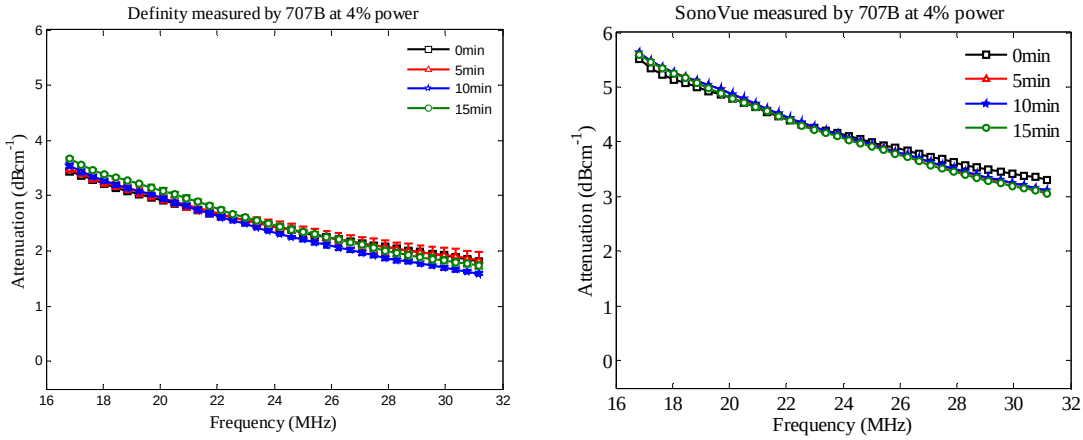
Definity measured by 707B at 4% power
SonoVue measured by 707B at 4% power
0min
5min
10min
15min
Attenuation (dBcm-1)
Frequency (MHz)

(a) 4%

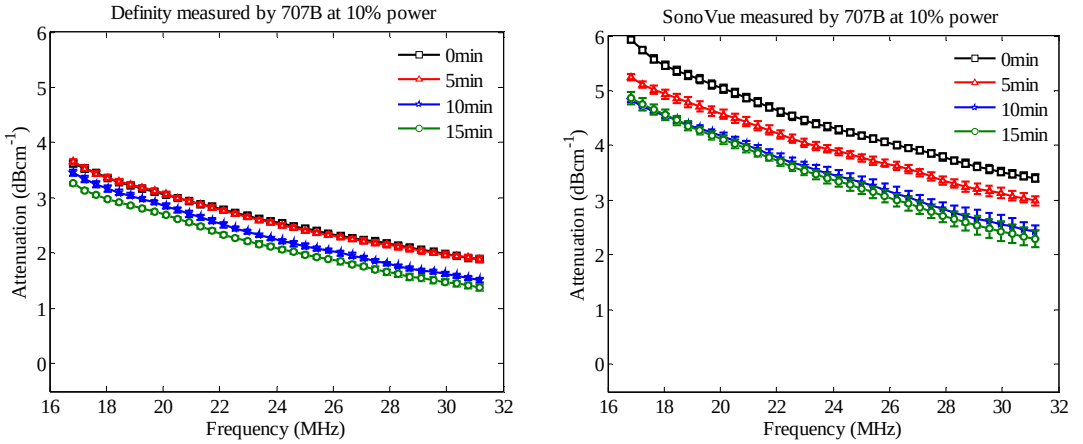
Definity measured by 707B at 10% power
SonoVue measured by 707B at 10% power
0min
5min
10min
15min
Attenuation (dBcm-1)
Frequency (MHz)

(b) 10%

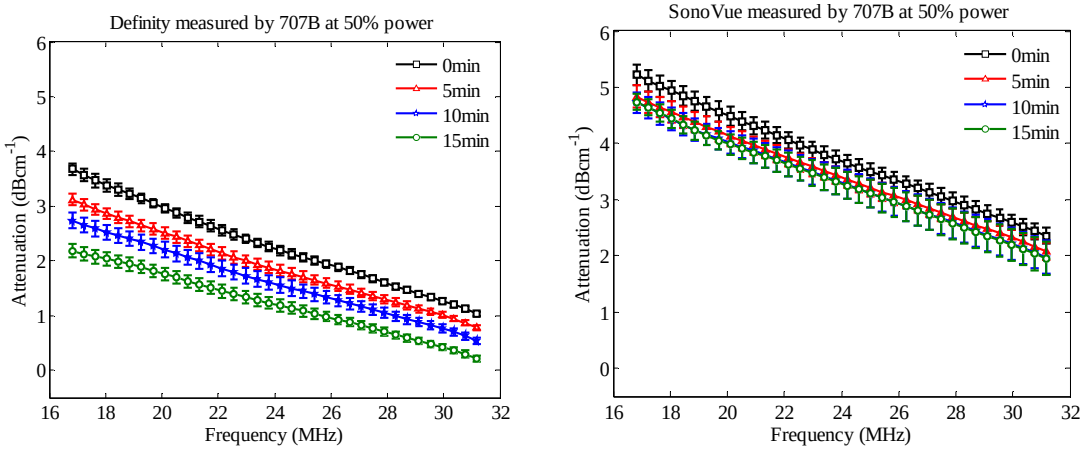
Definity measured by 707B at 50% power
SonoVue measured by 707B at 50% power
0min
5min
10min
15min
Attenuation (dBcm-1)
Frequency (MHz)

(c) 50%

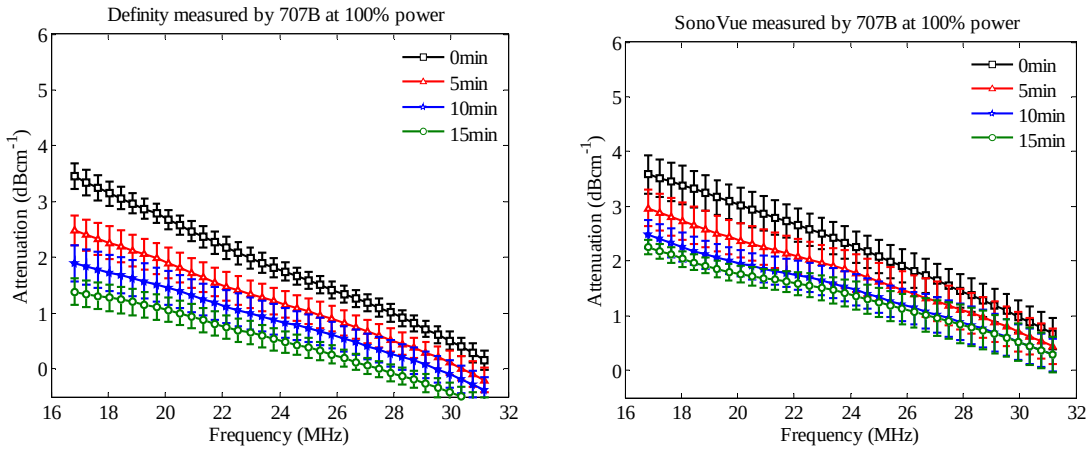

(d) 100%

Figure 4. 22: *The attenuation of ultrasound through Definity (left panel) and SonoVue (right panel) measured suspensions by transducer 707B at the power setting (a) 4%, (b) 10%, (c)50% and (d) 100% for 15 minutes*

The second experiment studied the influence of continuous insonation over 30 minute by calculating the normalized backscatter intensity at a low pressure (10% transmitted power). A flow chart in Figure 4.23 shows this process. The **continuous scan** was defined as a process of obtaining data from one tank of Definity (or SonoVue) microbubble suspensions at a concentration of 0.8×10^6 mbs/ml every 2 minutes for 30 minutes using transducers 710B, 707B, 704 and 711. Between the adjacent data acquisition every 2 minute, the scanner continued to transmit ultrasound. As control groups, the **intermittent scan** using a new tank of microbubble suspensions were acquired for 30 minutes with 2-minute interval for Definity and 4-minute interval for SonoVue. The reason of choosing 4-minute interval for SonoVue is based on the previous results of Definity as no obvious difference between the intermittent and continuous scan is found from Definity result measured by transducer 704 and 711, 4-minute interval was applied to reduce the time exposure to ultrasound in the intermittent scan. The microbubble suspensions were stirred continuously over the entire measurements.

The backscatter intensity was normalized to the initial value of each group. NBS is not calculated because it requires the data of attenuated signal from the reflector, the

measurement of which extends the exposure time to ultrasound. In this way, the ultrasound exposure time can be reduced. An exponent function of $y = a \cdot e^{-bx} + c$ (Smith et al. 2007) was fitted to the result and the correlation coefficient R^2 was calculated.

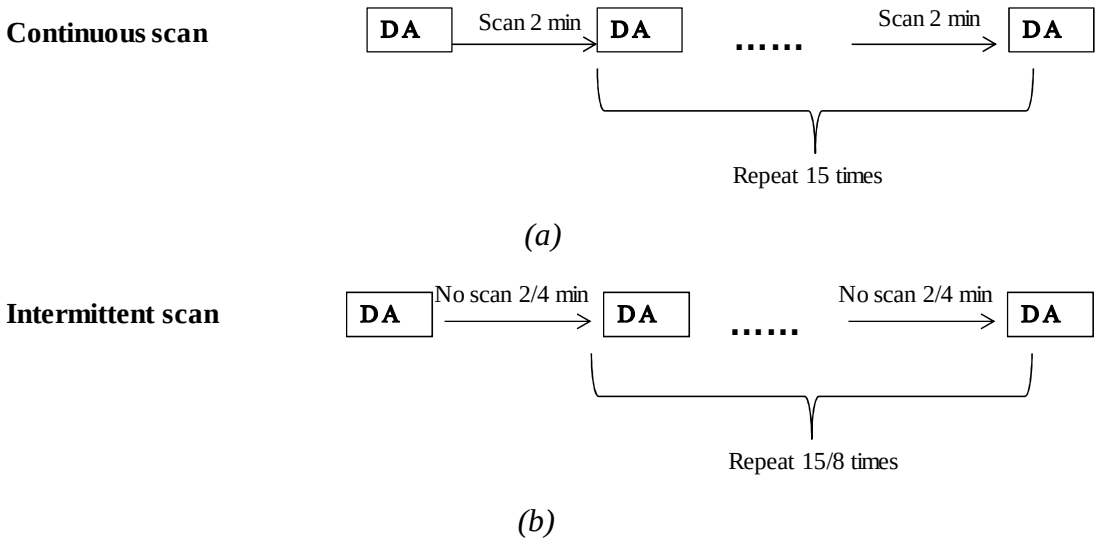

Figure 4. 23: *Flow chart of continuous scan and intermittent scan, DA indicates data acquisition. For intermittent scan, the time interval between measurements is 2 minutes for Definity and 4 minutes for SonoVue leading to different times of measurements in 30 minutes*

The influence of continuous insonation was studied at 10% transmitting power using Definity and SonoVue shown in Figure 4.24. The attenuation from intermittent scans decreases with time. The correlation coefficient R^2 of an exponent function of $y = a \cdot e^{-bx} + c$ were larger than 0.97 for all fittings.

The normalized backscatter intensities of continuous and intermittent scan overlap at 1 because of self-normalization. This does not mean that the absolute values of the first backscatter measurement are the same. This presentation format only focuses on the comparison of varied trend in backscatter with time.

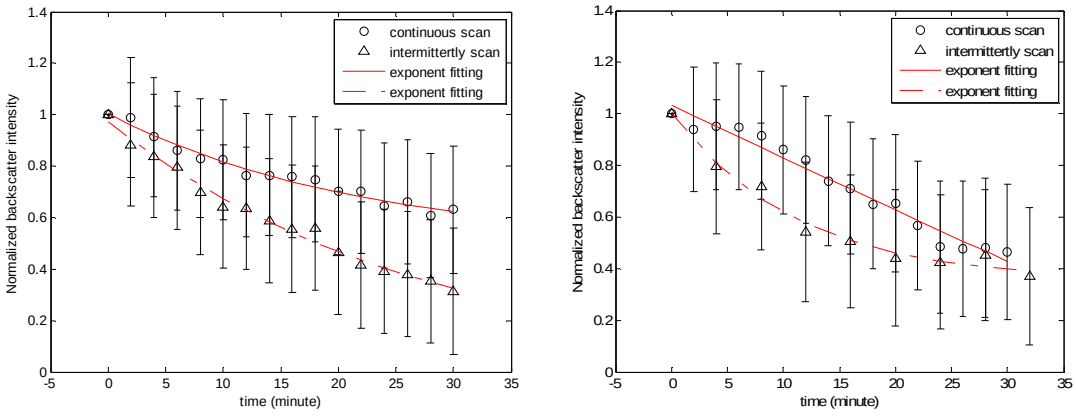

(a) 710B (3dB bandwidth: 12-25MHz)

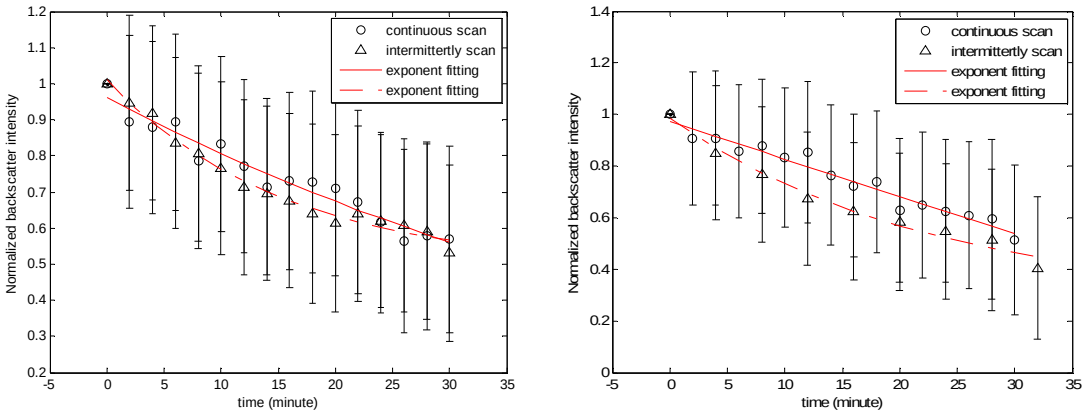

(b) 707B (3dB bandwidth: 30MHz)

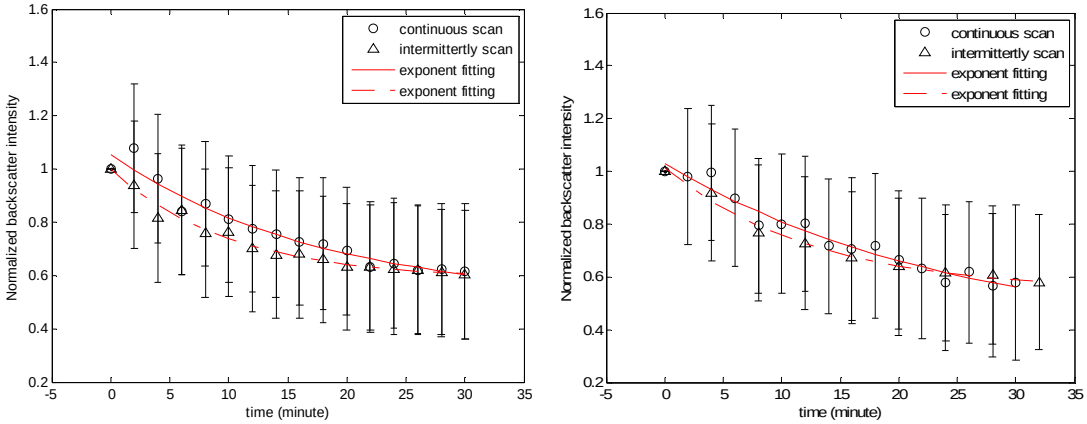

(c) 704 (3dB bandwidth: 20-40MHz)

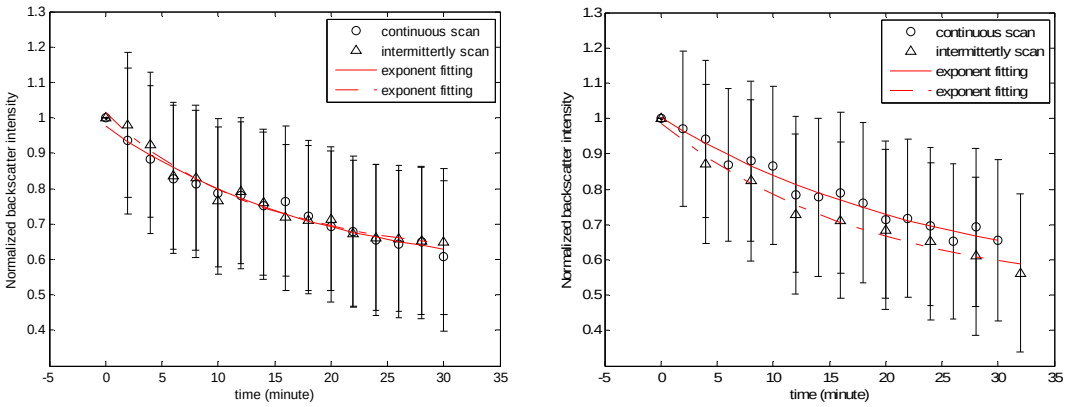

(d) 711 (3dB bandwidth: 27-47MHz)

Figure 4. 24: *Normalized backscatter intensity of Definity (left panel) and SonoVue (right panel) measured by 710B (a), 707B (b), 704 (c) and 711 (d)*

In Figure 4.24, the largest difference between the continuous scan and intermittent scan is from transducer 710B (Figure 4.24 (a)). The reasons include the transmitting peak negative pressure of 710B at 10% power setting is higher than two transducers 704 and 711 and its 3dB bandwidth is closest to the resonant frequency of Definity and SonoVue compared with other transducers. One interesting point is the curve of intermittent scan is steeper than the curve of continuous scan. The only difference between continuous and intermittent scan is the exposure time to ultrasound. On one side, the intermittent scan always drives fresh MBs into the insonation plane and reflects the natural lifetime of MBs with time if the insonation is non-destructive. On the other side, the receiving signals from continuous scan come from MBs of various stages: fresh, oscillated and disrupted. To some extent, the difference between the two curves is an indicator as to whether the insonation pressure destroys MBs. For this case, the large difference of the two curves indicates the pressure from transducer 710B may disrupt MBs. The possible reason of the low gradient from continuous scan compared to the intermittent scan may be due to the low backscatter signal from the initial measurement and further continuous destruction. Other possible reasons may be attributed to gas release from the encapsulated bubbles (de Jong et al. 2009). It is known that theoretically free small bubbles resonate at high

frequency, though they survive very short periods of time (few microseconds). Figure 4.25 shows the simulation of the resonance frequency of free and encapsulated MBs using the equation and parameters of encapsulated SonoVue bubbles (Goertz et al. 2007, Gorce et al. 2000). The detailed equation and parameters can be found in Chapter 5. Continuous scanning exerted energy on the bubble more frequently and was able to capture the echo from free bubbles. Thus, the continuous scan may produce higher backscatter than the intermittent scan. When the insonating frequency is removed from the resonance frequency of the MBs and transmitting pressure is low (case for transducer 704 and 711), little gas leases from the MBs producing no significant changes on the backscatter curves.

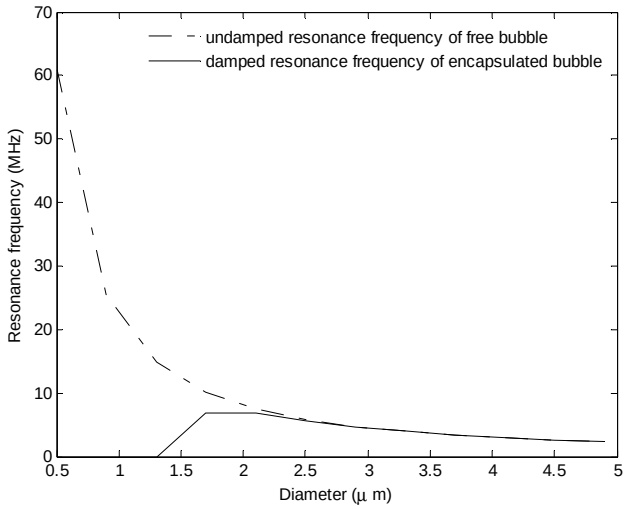

Figure 4. 25: *The simulation of the resonance frequency of free MB and encapsulated SonoVue MBs*

4.9 DISCUSSION

The reconstitution and sizing process of UCAs detailed in this chapter are used in the experiments of the following chapters 5-7.

Through the concentration dependent experiment of attenuation and NBS, a linear range was found to ensure the attenuation varied linearly with number of MBs and

NBS varied linearly with the number of MBs. Within this range, a concentration of 0.8×10^6 mbs/ml is determined to be used in the following chapters.

The variation in attenuation and NBS measured with increasing power showed that the MBs might be disrupted at high power, but the accumulated influence of higher power and time cannot be excluded because the experiments were completed in one sample. Thus, independent MB attenuation measuring at 4%, 10%, 50% and 100% - transmitting power over 15 minutes were made and only the power as low as 4% showed a stable attenuation curve. Additionally, the continuous and intermittent experiments measured at 10% power over 30 minutes also suggested possible MB destruction. All these indicate lower powers less than 4%, e.g. 3% would be suitable for prospective non-destructive experiments.

4.10 CONCLUSION

This chapter provides a set of preparations for measuring UCAs in the following experiments: UCA reconstitutions, size distribution measurement, and format of RF data acquisition. More importantly, the concentration of 0.8×10^6 mbs/ml and PNP in response to 3% power (minimal power out of the scanner) are determined to be used in the non-destructive acoustic experiments for chapters 5-7.

Chapter 5

The attenuation and contrast to tissue ratio of three phospholipids contrast agents from 12 to 43 MHz

5.1. AIM

The aim of this chapter is to compare the fundamental acoustic performance of Definity, SonoVue and MicroMarker as a function of size over the frequency range 12 - 43 MHz at 20 ± 1^{o}C. The values of measured attenuation are compared with those published previously and guide the choice of shell properties for computer simulation in the high frequency range. Based on the estimated resonant diameter from these simulation results, by a process of decantation, two subpopulations of the native microbubbles (MBs) are formed with differing size distributions. The analysis addresses the questions: 1. how the variation in size distribution and concentration alter the fundamental acoustic response at high ultrasound frequencies and 2. the potential impacts of size distribution on the improvement of the preclinical applications. The subsequent subharmonic responses of these subpopulations are discussed in Chapter 6.

5.2. INTRODUCTION

In previous *in vivo* studies, the backscatter response and the duration of enhancement of Definity were characterised in mice at 40 MHz using 3.5 MPa peak negative pressure (Sirsi et al. 2010) and it was found that large Definity MBs (4-5 and 6-8 μm diameter) had longer persistence and stronger contrast enhancement than small MBs (1-2 μm diameter). It also concluded that the dissolution of the gas core was the dominant mechanism of contrast decay and that this mechanism was larger than the filtration and removal of the UCAs by macrophages in the lung, liver and spleen. The

concentration dependent attenuation and backscatter properties of Defintiy at 30 MHz were investigated both *in vivo* and *in vitro* and the results suggested that doses between 10 and 60 μL ·kg^{-1} produced a linear increase in peak enhancement and these doses were recommended for quantitative contrast flow studies in mice (Stapleton et al. 2009).

For *in vitro* experiments studying the fundamental acoustic response of UCAs, the attenuation of UCAs has been previously studied: Definity ((Goertz et al. 2007) over 12-29 MHz and (Faez et al. 2011) over 5-15 MHz), SonoVue ((Gorce et al. 2000) over 0.8-10MHz) and MicroMarker ((Huo et al. 2010) over 18-25 MHz). Data based on these results are used to calculate the shell properties (listed in Table 5.2) and support the simulation study of MBs dynamics. Mean backscatter power and attenuation of surfactant encapsulated Sonazoid (Nycomed; Oslo, Norway), Definity, SonoVue and albumin shelled Optison (Mallinckrodt; Hennef, Germany) were measured at 30 MHz as a function of concentration and time (Moran et al. 2005, Moran et al. 2002). The concentration range of 10^4 to 10^6 MBs·ml^{-1} was found to present a linear relationship with mean backscatter power.

The literature has demonstrated that alteration of the MBs size distribution effectively changes the fundamental (Sirsi et al. 2010) and harmonic response (Cheung et al. 2008, Goertz et al. 2003) at high ultrasound frequencies. However, little work has been done on investigating the acoustic response of selective size distributions of MBs. Between the UCAs measured by various experiment set-ups, differences in shell, gas and size distribution of MBs exists and the differences in experimental methods cannot be excluded as having an effect on the acoustic response. Consequently, it is not clear which factor or factors predominantly influence the fundamental and subharmonic performance of MBs at high frequency. This chapter aims to address the effect of size distribution on the fundamental response of different-sized subpopulations and the following Chapter 6 studies the subharmonic response from these subpopulations.

5.3 MATERIALS AND METHODS

5.3.1 UCAs preparation

Reconstitution and sizing of UCAs were described in chapter 4 and referred as 'native MB population'. As the pre-reconstitution temperature of Definity influences the acoustic properties (Helfield et al. 2012), Definity was left 15 minutes at room temperature before activation. Based on the maximum concentration (Table 4.1) from the manufacturer's published literature, MBs in different dilutions (Table 5.1) were diluted in air saturated distilled water to reach the same concentration of 0.8×10^{6} MBs·ml^{-1} and stirred for one minute at a speed of 430 rpm before measurement. This concentration lies in the range of concentrations in which attenuation of Definity, SonoVue and MicroMarker varies linearly as shown in Chapter 4.

Table 5. 1: *The dilution of Definity, SonoVue and MicroMarker*

Name	Definity	SonoVue	MicroMarker
Dilution	1:15000	1:625	1:2500

5.3.2 Microbubble size distribution manipulation by decantation

The MBs were sub-divided into 2 subpopulations, referred to as large MBs and small MBs. This was achieved using the method of decantation that has been shown to be a simple method to alter the size distribution of MBs (Goertz et al. 2007, Gorce et al. 2000). The boundary between large and small MBs derives from the considerations of separating the MB population into MBs resonating above the lower limit of the testing frequency, i.e., 12 MHz. Applying de Jong's model, the simulation of scattering cross-section $\sigma_s(r, f)$ in Equation 5.1 (Equation 1 in (de Jong et al. 1992)) and resonance frequency f_{res} in Equation 5.2 (Equation 7 in (Goertz et al. 2007)) can

be used to determine the boundary of dividing the MBs population. The shell properties of the three UCAs used in the simulation are listed in Table 5.2.

$$\sigma_s(r, f) = \frac{4\pi r^2}{\left[\left(\frac{f_0(r)}{f}\right)^2 - 1\right]^2 + \delta_{total}(r, f)^2} \tag{5.1}$$

The resonance frequency corresponds to the MBs oscillating to a maximum scattering cross-section.

$$f_{res} = f_0\sqrt{1 - \frac{(\delta_{vis} + \delta_{sh})^2}{2}} \tag{5.2}$$

where $f_0(r) = \frac{1}{2\pi}\sqrt{\frac{3\gamma P_0}{\rho r^2} + \frac{2S_p}{\rho r^3}}$ is the resonance frequency of encapsulated bubble, the total damping δ_{total} consists of radiation, viscosity and shell friction damping

$$\delta_{total} = \delta_{rad} + \delta_{vis} + \delta_{sh}, \quad \delta_{total} = \frac{\omega r}{c} + \frac{4\mu_l}{\omega\rho r^2} + \frac{S_f}{4\pi\omega\rho r^3}$$

Ultrasound parameters:

$\omega = 2\pi f$, *f is the* driven frequency

Bubble parameters:

r: radius of bubble, S_f is shell friction = $48\pi\mu_s \in$, S_p is shell stiffness = $6Gs\in$, μ_s : shell viscosity, Gs: shell elastic modulus, $\in$ is the thickness of the shell,
γ is the polytropic exponent (Definity: 1.06 (Goertz et al. 2007), SonoVue: 1.095 (Marmottant et al. 2005) and MicroMarker: 1.045 (Helfield et al. 2012)).

Environment parameters:

ρ is the liquid density, c is the speed of sound in the transmitting medium, μ_l is the liquid viscosity.

Table 5. 2: *The shell stiffness S_p and friction S_f of the three UCAs*

UCAs	Frequency range	S_p ($N \cdot m^{-1}$)	S_f ($\times 10^{-6}$ $kg \cdot s^{-1}$)	Reference
Definity	12 – 28 MHz	1.71±0.24	0.015±0.015	(Goertz et al. 2007)
SonoVue	0.8 – 3 MHz	1.1	0.27	(Gorce et al. 2000)
MicroMarker	18 – 25 MHz	10.3*	0.15*	(Helfield et al. 2012)

* Shell elasticity χ = 5.15 $N \cdot m^{-1}$and shell viscosity $\kappa_s = 3 \times 10^{-9}$ $kg \cdot s^{-1}$ (Helfield et al. 2012) referred from (Huo et al. 2010), $S_p = 2\ \chi$, $S_f = 16\pi\ \kappa_s$ (Doinikov and Bouakaz 2011)

The resonance frequencies of Definity, SonoVue and MicroMarker as a function of MB diameter are plotted in Figure 5.1. The critical size, defined as the size below which the encapsulated MBs would never resonant (Khismatullin 2004), when insonated at 12 MHz are found to be 0.5μm for Definity, 1.5 μm for SonoVue and 1 μm for Micromarker. Above the critical size MBs with less than 1.7 μm-diameter (Definity) and 3.1 μm-diameter (MicroMarker) resonate at frequencies higher than 12 MHz, while no SonoVue MBs were found to resonate within this frequency range. A boundary of 2μm diameter was chosen as a compromise to divide the populations of Definity and SonoVue into large and small MBs. The reason is that below this diameter includes the Definity MBs capable of resonating above 12 MHz and SonoVue MBs approximately giving the peak of acoustic response. MicroMarker was not decanted for comparison due to over 80% MBs of its native population their diameters are less than 3.1 μm which are supposed to resonate above 12 MHz.

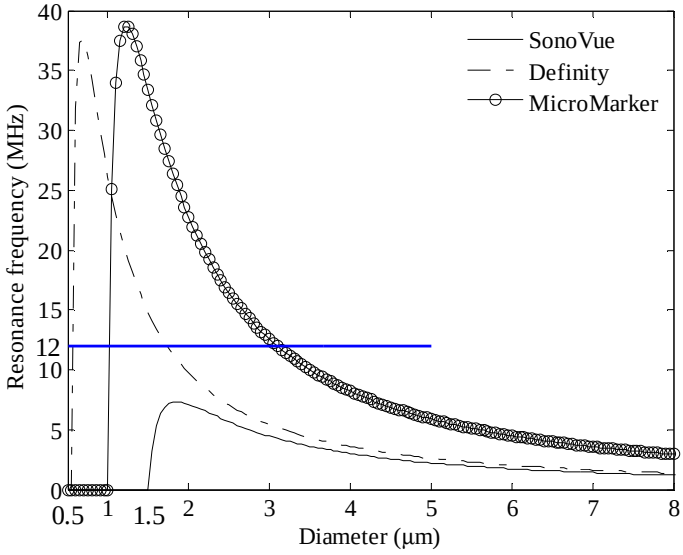

Figure 5. 1: *The resonance frequency as a function of diameter for Definity, SonoVue and MicroMarker (derived from Equation 7 in (Goertz et al. 2007) using de Jong's model). The shell parameters of the three UCAs used in the simulation of resonance frequency are listed in Table 5.2.The blue line at 12MHz is the lower end of the testing frequency range in this study*

The estimated decantation time for acquiring MBs of a specific diameter is based upon Stokes' equation (Equation 5.3) (Equation 12 in (Goertz et al. 2007)), the principal of which is based upon the varying times of different-sized MBs floating a certain height. The height is determined by the required volume and the shape of the container used for decantation.

$$t \cong \frac{9d\mu_l}{2r^2 g\rho_l} \tag{5.3}$$

where t is the floating time, d is the distance of rising, μ_l is the viscosity of liquid, r is the radius of bubble, g is the gravitational force and ρ_l is the density of liquid.

In this study 0.5ml Definity and 2ml SonoVue decanted MBs were selected to ensure the measurement of one UCA coming from the same vial at the required concentration, which corresponds to target rising height of 1.1cm for Definity and

1.6cm SonoVue using the original inverted vials as decanting containers. Figure 5.2 shows the varying time for MBs of diameter between 0.8 and 8 μm to float a 1.1 and 1.6 cm – in water. It can be seen that a period of approximately 1-hour for Definity and 2-hour for SonoVue is sufficient for MBs larger than 2μm to float the rising height.

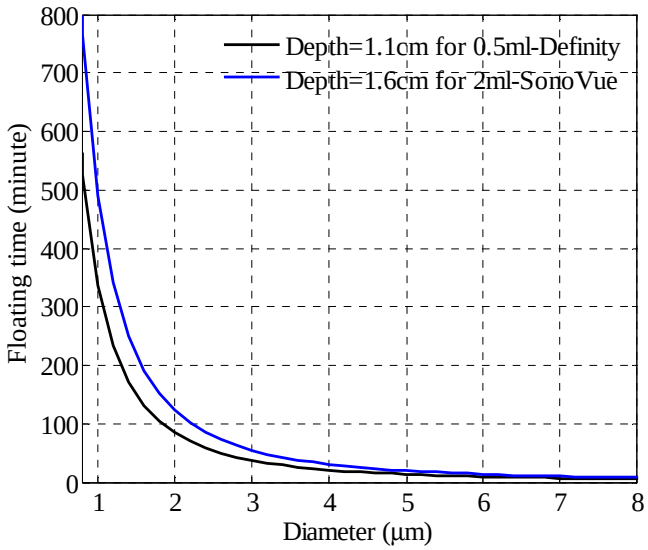

Figure 5. 2: *The time for MBs in a diameter of 0.8-8 μm to float a 1.1 cm and 1.6cm-distance using Stokes' equation*

Consequently 0.5ml of 1-hour decanted Definity and 2ml of 2-hour decanted SonoVue MBs were acquired in this study. For a detailed process of handling decantation, the original vials with reconstituted UCAs were inverted and stood at room temperature. After the certain period of time (1 hour for Definity and 2 hour for SonoVue), two 19G needles were inserted into the vial and the position of vial was kept inverted during this process. One needle was fully inserted for venting the gas. The head of the other needle was just inserted into the rubber stopper of vial allowing extraction of the required volume (0.5ml for Definity and 2ml for SonoVue). By collection of the decanted volume of UCAs allows separation of the MBs that are less than 2μm-diameter. MBs less than 2μm in diameter will be called **'small MBs'**. The remainder will be called **'large MBs'** and are from the native solution after removal of the small MBs. The detailed manipulation of decantation is given in

(Goertz et al. 2007). Same dilution was employed in each subpopulation pre- and post-decantation for the acoustic measurements.

The size distribution of Definity, SonoVue and MicroMarker MBs was measured by a Mastersizer 2000 Hydro MU and followed the protocol in Chapter 4. Mastersizer does not output the concentration directly, but the value can be calculated using the measured volume based size distribution data and assuming that the MBs are spherical. Based on a known volume of the suspension, the concentration can be acquired by calculating the total number of MBs from the measured volume and the volume of individual MBs at the measured diameter.

5.3.3 The measurement of attenuation and contrast to tissue ratio

The measurement of the attenuation was detailed in Chapter 4. The backscatter capacity of UCAs were evaluated using the contrast to tissue ratio (CTR) defined in Equation 5.4, which was calculated by normalizing the mean squared acoustic power of the backscattered signal from the MB suspension to the mean squared acoustic power of the backscattered signal of a tissue mimicking material (TMM) (Sun et al. 2012) placed at the focus of the transducer as shown in Figure 5.3. The backscattered power was calculated from the power spectra of the signal in frequency domain and integrated over the 3dB bandwidth of the transducer. Because the backscattered TMM signal was measured in water, the backscatter of the MBs suspension was compensated by the attenuation of the ultrasound (α) through the MBs suspension between the transducer and the upper surface of ROI (d_{up}).

$$CTR = 10\log_{10}\left(\frac{Powerbackscattered_{Bubble}}{Powerbackscattered_{TMM}}\right) + \alpha \cdot 2d_{up} \tag{5.4}$$

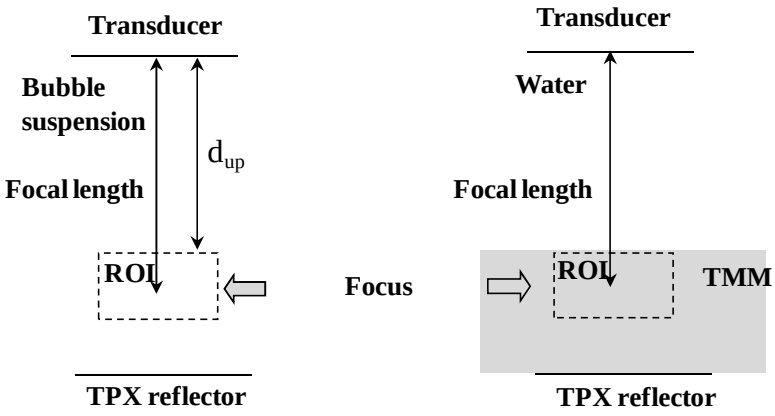

(a) Backscattered signal from MB suspension *(b) Backscattered signal from TMM*

Figure 5. 3: *Schematic of CTR experimental set-up*

Each experiment was repeated three times and 900 independent samples (300 consecutive frames on 3 lines) in ROI were colleted per experiment.

The power spectra of the backscattered signals from two TMM samples at three positions per TMM were measured and the averaged spectra over the 3dB bandwidth of each transducer were calculated and shown in Table 5.3. These values were used as the denominator for the CTR calculation in Equation 5.4.

Table 5. 3: *The mean backscatter value from TMM samples over the 3dB bandwidth of the four transducers*

Transducers	**710B**	**707B**	**704**	**711**
TMM BS (dB)	30.2068 ± 0.9915	31.9763 ± 0.9776	30.8297 ± 0.9928	28.9287 ± 0.9061

5.3.4 Determination of transmitting pressure

For the attenuation and CTR measurement, the transmitting peak negative pressures (PNP) were set at 0.56 MPa for transducer 710B and 707B (MI=0.16 at 12 MHz frequency). For transducers 704 and 711, the PNP was selected at 0.58 MPa

(MI=0.09 at 43 MHz frequency) to approximate a comparable PNP output similar to that exhibited by transducers 710B and 707B. The measurement of the acoustic pressure from the four transducers can be found in Chapter 2 and values listed in Table 5.4 are selected from Appendix 3.

Table 5. 4: *Characteristics of four high frequency transducers. The central frequency and focal length measurements are defined by manufacturer's literature. The PNP (measured by a membrane hydrophone) and 3dB bandwidth (measured from the frequency spectrum) in response to the specific output power setting of each transducer.*

Transducer model RMV	**710B**	**707B**	**704**	**711**
Central frequency (MHz)	25	30	40	55
Focal length (mm)	15	12.7	6	6
Power	3%	3%	13%	50%
PNP (MPa)	0.56	0.56	0.58	0.58
Measured 3dB band width (MHz)	12 - 25	17 - 31	18 - 32	24 - 43

5.4 RESULTS

5.4.1 Scattering cross-section of the three UCAs based on simulation results

Figure 5.4 shows the scattering cross-section of the three UCAs for different sizes in the vicinity of the estimated resonance diameters. In the frequency range 12- 43 MHz of this study, the peak of the scattering cross-section of the resonant Definity (0.7-1.7μm) and MicroMarker (1.3-3.1μm) MBs is comparable to that of the larger MBs (e.g. 8μm diameter MBs). The small MBs below the resonant diameter contribute negligibly to the scattering. The scattering cross-sections of the large MBs above the resonance diameter of these three UCAs are comparable at high frequency range.

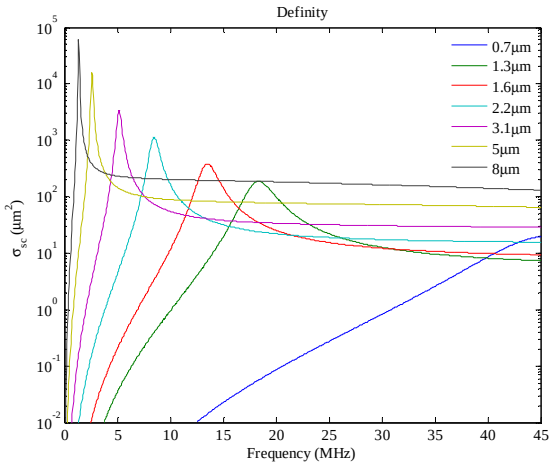

(a) Definity

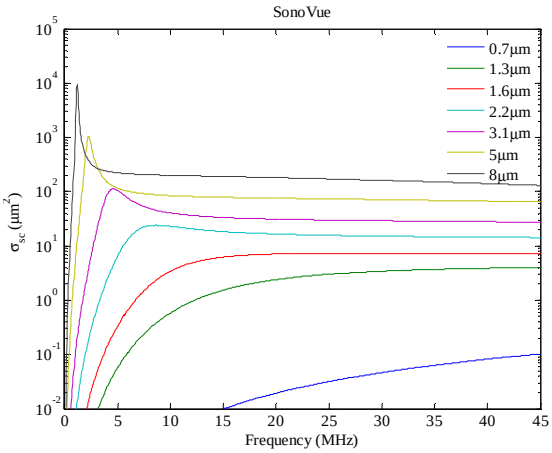

(b) SonoVue

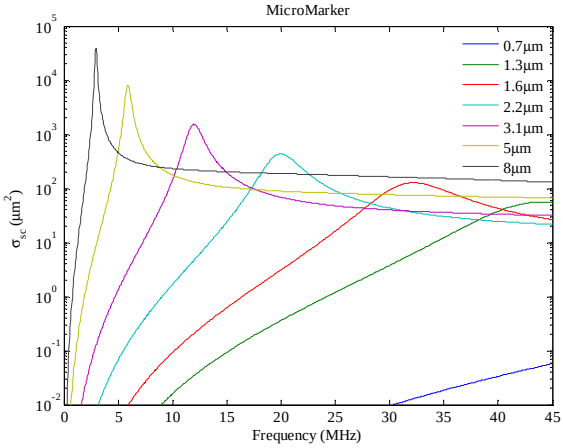

(c) MicroMarker

Figure 5. 4: *The simulation of scattering cross section σsc of (a) Defintiy, (b) SonoVue and (c) MicroMarker as a function of frequency at different diameters*

5.4.2 Size distribution of MBs and variation in concentration pre- and post- decantation

Figure 5.5 shows the volume based size distribution of Definity, SonoVue and MicroMarker. The two percentages in the legend of Definity and SonoVue are the percentages of the native population that lie below and above 2 μm (the boundary). It can be seen that the small MBs are successfully removed via decantation, however a certain number of small MBs still exist in the large MBs population. The reason for presenting volume based size distribution is because Gorce et al (2000) showed a good correlation between volume fraction and mean echogenicity efficacy of SonoVue rather than MB absolute number in the frequency range 1-10 MHz.

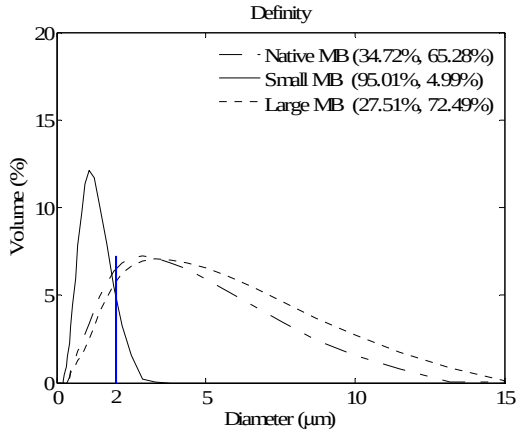

(a) Definity

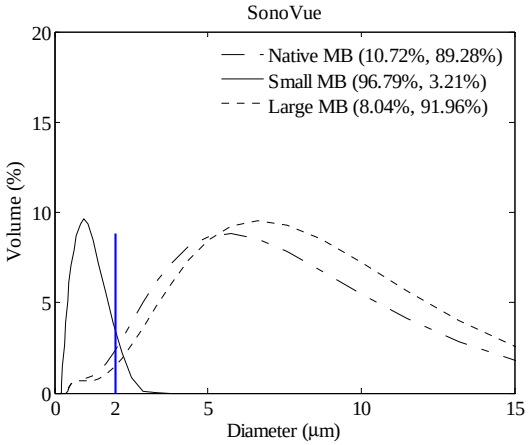

(b) SonoVue

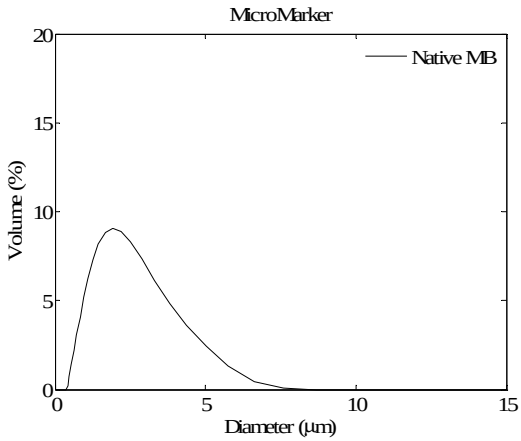

(c) MicroMarker

Figure 5. 5: *The volume based size distribution of 3 populations of (a) Definity, (b) SonoVue and 1 population of (c) MicroMarker. The 2 percentages in the legend of Definity and SonoVue are the percentages below and above 2 μm.*

Table 5.5 shows the variation in calculated concentration of the decanted two subpopulations compared with the native population. For both Definity and SonoVue, the concentration of small MBs population was found to decrease while the concentration of the large MBs was found to increase after decantation.

Table 5. 5: *The relative percentage of concentration of small and large MBs compared with the native population, where negative and positive numbers indicate decrease and increase in concentration respectively.*

	Small MBs (%)	Large MBs (%)
Definity	- 5.92 ± 0.74	8.12 ± 12.72
SonoVue	-23.05 ± 10.62	72.09 ± 11.74

5.4.3 The frequency-dependent attenuation of UCAs suspensions

Figure 5.6 shows the attenuation ($dB \cdot cm^{-1}$) as a function of frequency of the three UCAs. From the data collected in this study over the frequency range (12-43 MHz) the attenuation decreases with increasing frequency for native (a) Definity, (b)

SonoVue and (c) MicroMarker. The variation in attenuation from MicroMarker is the smallest and less than 2dB·cm^{-1} in amplitude over the frequency range of 12-43 MHz. The results are in good agreement with the published data of Definity (Goertz et al. 2007) and SonoVue (Gorce et al. 2000). The attenuation curve of MicroMarker has not previously been published. The attenuation curves focus on the comparison between the data acquired in this thesis and the published data at different frequencies. Thus, the attenuation results of the subpopulations are not presented in this thesis.

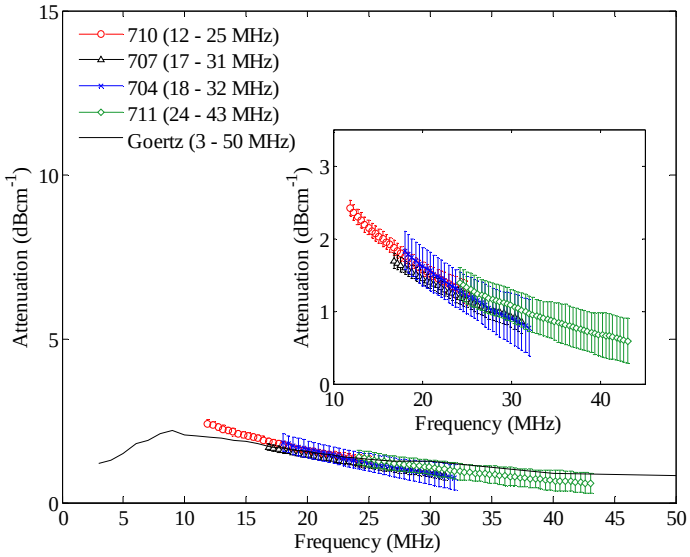

(a) Definity

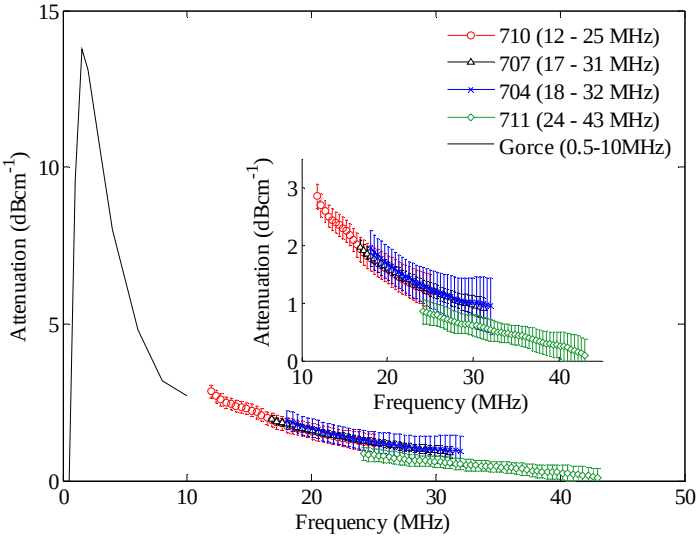

(b) SonoVue

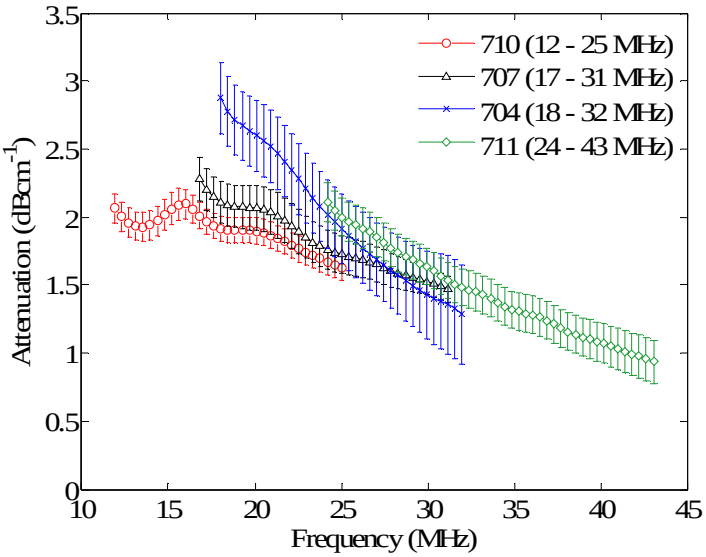

(c) MicroMarker

Figure 5. 6: *Frequency dependent attenuation of native UCAs measured by 4 transducers over their 3dB bandwidths. (a) The attenuation of Definity is compared with the experimental results of Goertz (2007); (b) the attenuation of SonoVue is compared with the results of Gorce (2000), the concentration of Gorce's experiment is 1:2000 therefore the attenuation is corrected by multiplying 3.2 as we use 1:625 dilution; (c) MicroMarker. Insets in (a) and (b) zoom in the attenuation at high frequencies and use to compare with (c).*

5.4.4 CTR

Figure 5.7 shows the CTR of SonoVue and Definity at the three populations and native MicroMarker measured by the four transducers. As the CTR is a normalized result to the backscattered TMM, a value of which closer to zero indicates a higher backscatter capability from MB suspension. The CTR of each UCA decreases more than 5dB from the result of transducer 710B (12-25 MHz) to 711 (24 - 43MHz). The CTR measured by transducer 707B and 704 is comparable due to their similar driving frequency range and PNP. For each subpopulation of Definity and SonoVue, the large MB population produces the highest CTR. Despite the differences in gases,

shells and size distributions between the agents, when measured using the same transducer the magnitude of the CTR of each of the three native UCAs is approximately the same.

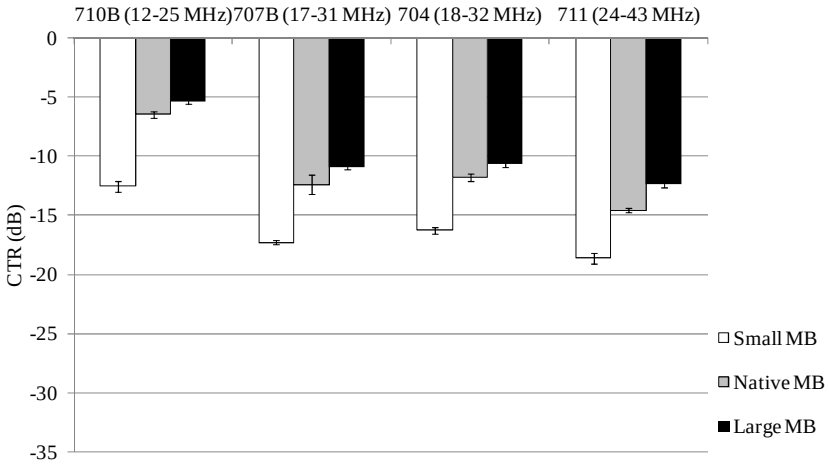

(a) Definity

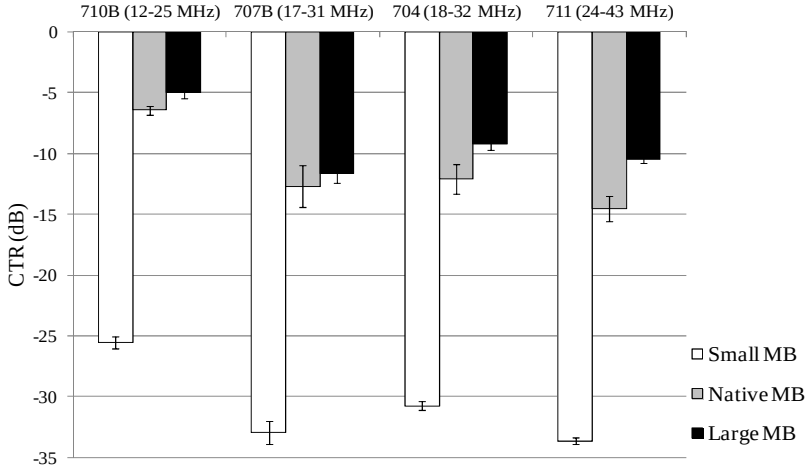

(b) SonoVue

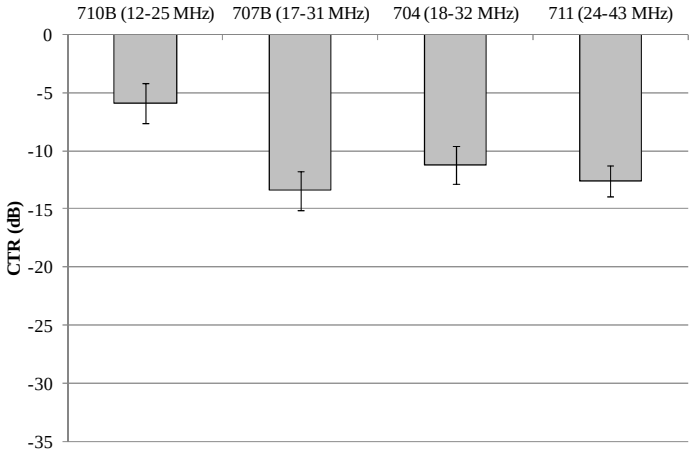

(c) MicroMarker

Figure 5. 7: *The CTR of small, native and large populations of Definity and SonoVue and of native MicroMarker measured by the 4 transducers over their 3dB bandwidths, the error bars were calculated from the three independent measurements*

5.5 DISCUSSION

5.5.1 The influence of decantation

In addition to the altered size distributions of Definity and SonoVue through decantation shown in Figure 5.5, in Table 5.5 it is shown that concentration decreases in the small MB population whereas increases in the large MB population compared with the native population. The resultant influence on CTR of subpopulations is discussed in the discussion of CTR in section 5.5.4.

In this study, decantation was chosen to alter the size distribution of MBs and its advantages over other methods such as filtration (Cheung et al. 2008, de Jong et al. 1992) or centrifugation (Feshitan et al. 2009) include 1) no compression force applied, 2) no limitation of size required during these processes and 3) simplified concentration variation for preclinical injections. Talu et al (Talu et al. 2008) and Barrack and Stride (Barrack and Stride 2009) have showed the destruction of MBs

using narrow gauged needles (0.241mm-diameter for 25G, 0.159mm-diameter for 30G needle). MBs which have either been passed through a filter of diameter generally ranging between 1 and 10 μm or experienced the centrifugal force are likely to be destroyed. Another drawback of using a filter is selection of MB size is directly restricted by the filter pore size from the manufacturer. Additionally, both filtration and centrifugation introduce pre-dilution before practical application. Specifically, MBs usually require high dilution (>1:1000), to allow sufficient space to isolate MBs in centrifugation, and to avoid clogging in filtration pores. However, *in vivo* applications especially small animal injections require limited injection volume (100μl for mice (Foster et al. 2011)) and higher concentration (e.g. MicroMarker 1×10^7 MBs in 50 μl per injection) than the physics experiment requirements *in vitro* (e.g., 0.8×10^6 MBs/ml applied in this study), the pre-dilution is irreversible and may hinder the underlying practical application. The only limitation of decantation is the time required to separate out the different sized MBs.

5.5.2 The influence of pressure on the attenuation measurement

Transmitting pressure for the acoustic measurement is set at 0.56 MPa (MI=0.16 at 12 MHz frequency) and 0.58 MPa (MI=0.09 at 43 MHz frequency). Small, individual Definity and MicroMarker MBs (< 2 μm) were found to be preferentially disrupted at 25MHz and acoustic PNP ranging from 0.2-1 MPa (Helfield et al. 2012), i.e., lower PNP than that used in this study. However, in this study the attenuation of ultrasound through the native Definity suspension did not vary with time over 15 minutes at 4% power (PNP=0.67 MPa) (Chapter 4.8). This indicates that the applied PNP does not destroy the MB suspension over the measurement period. Note that in the published attenuation experiments, Goertz (2007) used 25 kPa over the frequency range 12-29MHz (maximal MI = 0.007) and Gorce (2000) used 10 kPa over the frequency range 0.8-10MHz (maximal MI = 0.011) as transmitting pressure to approach a small oscillation of MBs. The attenuation acquired at higher PNP in this study shows similarity in magnitude with these published data. This implies that the attenuation of Definity and SonoVue display a low sensitivity to pressure at these

low non-destructive pressures over the frequency range of 12-43 MHz. However, further investigations of pressure dependence are required to prove this hypothesis.

5.5.3 The limitation of simulation of resonance frequency

The attenuation values of native Definity (Figure 5.6.a) and SonoVue (Figure 5.6.b) measured over 12 - 43MHz are consistent with published results at similar dilution ratios. The measurement of attenuation is used to determine the shell stiffness and friction (de Jong et al. 1992, Goertz et al. 2007), the good agreement of the measured attenuation at high frequencies with the published results indicates the shell properties in Table 5.2 are appropriate to be used in the simulation of resonance frequency in Figure 5.1. However, the equations for the calculation of resonance frequency are derived from small scale linear oscillations of encapsulated MBs, and the shell parameters in Table 5.2 are derived at different frequencies compared to the range of interest in this study, hence it is possible that the values of shell parameters may not be entirely accurate. For example, 1μm SonoVue was found to resonate at 21 MHz (Bouakaz and de Jong 2007) while in Figure 5.1, 1 μm SonoVue was even below the critical size. In addition, the literature is not conclusive on the MB theoretical behaviour at any frequency range. However, the accuracy of the calculation of the resonant frequency is not an absolute requirement for this work. An approximate figure for the sizes of resonating and non-resonating MBs is possible to attain using the existing theory, and as shown by the results we consider that this is an acceptable means of guiding size fractionation.

5.5.4 The impact of decantation on CTR

For each UCA, the CTR of the native population lay between the response from the small and large MB populations with the largest CTR measured in the large MB population. An *in vivo* study at 40 MHz showed that Definity (4-5 μm-diameter, 6-8 μm-diameter) had a higher mean video intensity than Definity (1-2 μm-diameter) indicating that large MBs contributed predominately to the fundamental response

(Sirsi et al. 2010). This can also be supported by Figure 5.4. For each UCA, MBs at resonance and of diameters larger than resonance contribute most to the scattering while small MBs below the resonant diameter are acoustically undetectable. However, it should be noted that in this study, the Definity MBs in the small subpopulation are resonant MBs (<1.7 μm-diameter) above 12MHz. The low CTR from the small resonant MBs suggests that at high frequency the large off-resonance MBs are more suitable for enhancing the fundamental acoustic response than small resonant MBs, although the influence of decreasing concentration of small Definity MBs after decantation cannot be completely excluded. An improvement of 20dB in CTR of SonoVue large MBs over small MBs also supports this conclusion. Hence decantation performs an effective method for CTR enhancement by increasing the absolute number of large MBs in a limited volume, which is particularly useful for practical *in vivo* preclinical injection regimes where the injected volume is often limited.

5.5.5 Comparison of three lipid UCAs and considerations of their preclinical applications

At the same concentration, the attenuation and CTR of the three native UCAs are found to be comparable measured by transducers 710B, 707B and 704 shown in Figure 5.6 and 5.7. From the results of transducer 711, MicroMarker presents 2dB increase in CTR and a large attenuation of approximate 0.5-1dB·cm^{-1} at 30-43 MHz in comparison to native Definity and SonoVue. This indicates an advantage of using MicroMarker at frequencies higher than 30MHz. From the practical application point of view, at frequencies below 30MHz not only Definity but also, SonoVue may also be used preclinically at similar MB concentrations as MicroMarker. For instance, the recommended bolus injection of MicroMarker is 1×10^7 mbs per 50μl (1:10 dilution) for mice cardiovascular, kidney and liver imaging and 1×10^8 mbs per 50μl for tumors, retina and hind limb imaging, respectively (Visualsonics, 2012). Assuming an injection of 50 μl UCAs of 1×10^7 mbs, the dilution changes to 1:60 for native Definity and 1:2.5 for native SonoVue UCAs. However, for 1×10^8 mbs per 50 μl, native SonoVue faces the dilemma of low concentration within limited injected

volume (100 μl). As discussed the advantages of decanted large MBs for CTR enhancement, the increasing concentration of large MBs may aid enhancement in preclinical injections. Using SonoVue for *in vivo* practical application requires further studies.

5.6 CONCLUSION

There are 2 main conclusions from this chapter

- From the measurement of attenuation and CTR of Definity, SonoVue and MicroMarker at high frequency from 12 to 43 MHz using a PNP of 0.56MPa/ 0.58MPa, the acoustic characterisation of the three native UCAs are comparable at same number concentration below 30MHz, though their size distributions and encapsulated gases and shells are significantly different. Above 30MHz, native MicroMarker produces higher values of attenuation and CTR compared with native Definity and SonoVue.

- From the CTR comparison of subpopulations of Definity and SonoVue, altering the size distribution and concentration through decantation enables further enhancement for specific applications and may take full advantage of the imaging capabilities of the scanner. In addition to Definity and MicroMarker, SonoVue may also be suitable for preclinical application using an appropriate dilution and using large decanted SonoVue at high frequencies.

Chapter 6

The subharmonic response of three phospholipid contrast agents

6.1 AIM

This chapter aims to investigate the subharmonic response of three lipid shelled ultrasound contrast agents (UCAs) Definity, SonoVue and MicroMarker by simulation in conjunction with experimental data. Firstly, simulations of subharmonic to fundamental ratio (SFR) of individual microbubble (MB) were performed and the influence of insonating parameters was studied. Secondly, the experimental data of the three UCAs were acquired using a 25-cycle, 668kPa peak negative pressure (PNP), 25MHz ultrasound pulse under Engineering mode. Thirdly, the discrepancy between the experimental data and the simulation result was discussed.

6.2 INTRODUCTION

Harmonic imaging exploits the nonlinear properties of UCAs and specifically the 2nd harmonic. However broadband transducers that can receive the 2nd harmonic signals at high frequencies remain a manufacturing challenge. Additionally, tissue itself displays the 2nd harmonic properties when driven at high power and high frequency reducing the contrast to tissue ratio at the second harmonic. The generation of subharmonic is a unique property of MBs as tissue emits no subharmonic signal. Thus detecting the subharmonic signal improves contrast enhancement although spatial resolution is compromised (de Jong et al. 2000, Shankar et al. 1998).

The onset pressure for subharmonic generation of a free bubble was previously found to be lowest at a driving frequency equal to twice the MB's resonance frequency (de Jong et al. 2000, Eller and Flynn 1969, Forsberg et al. 2000) and this threshold was shown to be lower than the MB destruction threshold (Chomas et al. 2002). For MB resonating at the insonation frequency, the pressure threshold for producing subharmonic was found to be higher than the destruction threshold from the optical experiment using a lipid MB MP1950 (Mallinckrodt, Inc., St. Louis, MO) at 2.25MHz (Chomas et al. 2002). An experiment using polymer shell MB SHU563A (Schering, Germany) also showed that the generation of sub- and ultra-harmonics linked to the destruction of MBs (Uhlendorf and Hoffmann 1994). However, subharmonic emissions have also been measured at low pressure, e.g., subharmonic threshold of SonoVue is 34.7kPa at 3.3MHz and 26.4kPa at 5MHz (Biagi et al. 2007), pressure for stable subharmonic response of albumin encapsulated Infoson (other name marketed in US is Albunex) is 50-100kPa at 2.25MHz (Lotsberg et al. 1996). The generation of subharmonic was shown to undergo three stages: occurrence, growth and saturation at 2 MHz (Shi et al. 1999). The subharmonic is insignificant at very low insonation pressures and starts to increase after the insonation pressure exceeds a certain threshold then gradually grows with increasing pressure. Within this growth stage before MBs are destroyed, the subharmonic signals may be extracted and useful for imaging purposes owing to the unique subharmonic generation by MBs and consequently high subharmonic signal to noise ratio. With a further elevation of the pressure, the subharmonic signals enter into the phase of saturation then the signal-to-noise ratio will be greatly reduced due to the destruction of MBs (Shi et al. 1999).

Cheung et al. (2008) compared the SFR of Definity in three populations (5 μm filtered, 1.2 μm filtered and native) in the frequency range 20-40MHz and validated the hypothesis that off-resonance MBs with diameters less than 5 μm were responsible for the subharmonic signal when insonated at their 2^{nd} harmonic frequency. Additionally, the diameters of MBs that generate subharmonic at driving frequencies of 20 MHz and 30 MHz were simulated and were shown to be larger than the diameter of MBs which generate 2^{nd} harmonic which is associated with the

resonant MBs (Goertz et al. 2003). In other words, at both high and low frequencies, not the resonant MBs, but larger MBs resonating at half of the driving frequency predominately produce subharmonic echoes.

For other *in vitro* studies of subharmonics conducted at high frequency, Helfield et al (2012a) showed a variation in subharmonic response of 5 types of individual phospholipid-encapsulated MBs (<3 μm) associated with different shell structures using an optical-acoustic setup operating at 25MHz and 0.02-1.2 MPa. Among the 5 types of MBs, MicroMarker was shown to produce the highest and most consistent subharmonic response. Although MBs of various micro-structural heterogeneities produce different nonlinear responses in terms of active size and amplitude, no clear relationship was indicated between these factors. The subharmonic of individual MicroMarker targeted MBs bound on gelatin were studied as a function of pressure and size at 30 MHz (Sprague et al. 2010). The pressure threshold for emitting subharmonics was found to be 110 kPa and MBs smaller than 1.7 μm in diameter were disrupted in the pressure range 0.4-1 MPa showing phenomena of rapid dissolving and/or detaching from the bounded surface.

In vivo subharmonic contrast intravascular ultrasound (IVUS) imaging (transmitted at 30 MHz and 40 MHz, received at 15MHz and 20MHz respectively) was found to be feasible using atherosclerotic rabbit aorta for improvement of vessel lumen boundary detection and *vasa vasorum* imaging (Goertz et al. 2006, Goertz et al. 2007). The subharmonic signature of MicroMarker (exposure to 30MHz signal of magnitude 1MPa, detection at 15MHz) in the mice renal cortex as a function of concentration was measured in the context of microvascular flow imaging (Stapleton et al. 2007). The recommended dose range was found to lie between 0 and 300μL $\cdot kg^{-1}$ (i.e., 0 to 10 million MBs per mL of blood), as in this concentration range the average enhancement and integrated enhancement of the agent increased linearly.

The above literature reviews the generation and properties of the subharmonic response of the UCAs at low frequencies and the limited signature of subharmonics (bulk Definity suspension (Cheung et al., 2008) and small individual Definity and

MicroMarker (<3μm) (Helfield et al, 2012a)) at high frequencies. The subharmonic studies of another common UCA SonoVue have not been published and its feasibility for subharmonic application remains unclear. As described in Chapter 5, altering the size distribution of commercially available UCAs enables further enhancement for fundamental applications. In a similar manner, the size distribution for improving high frequency subharmonic application is worthy of investigation. Additionally, to date no comparison has been made between the bulk experimental data and the suharmonic modelling of individual MB.

In this chapter, the simulation is firstly performed to analyse the impact of frequency, pressure and pulse length (number of cycle) on the subharmonic properties of individual MB. Secondly, the experimental subarmonic data of three native UCAs is discussed and the discrepancy with the simulation results is explored. Thirdly, the potential improvement of the subharmonic application by changing the size distribution of commercially UCAs is discussed using the subpopulations described in Chapter 5. All these are suggested to contribute to the benefit of using MB subharmonic technique at high frequencies than other harmonic alternatives owing to its advantage of minimal subharmonic generation from tissue.

6.3 METHOD AND MATERIALS

6.3.1 Simulation of the scattered signal of individual MB

The simulation uses an open source and free downloaded toolbox BUBBLESSIM in MATLAB developed by Lars Hoff from The Norwegian University of Science and Technology. This toolbox simulates the dynamic oscillation of MBs and outputs the scattered signal by inputting the parameters of model, MB, ultrasound and environment. Figure 6.1 shows the interface of the toolbox and Table 6.1 lists the main options employed in the simulation. The current version of the BUBBLESIM

toolbox is only capable of processing one simulation each time after inputting the parameters. The MATLAB codes developed by Dr. David Thomas and Dr. Padraig Looney (Medical Physics, The University of Edinburgh) (Looney 2011, Thomas 2009) were applied to allow multiple simulations automatically.

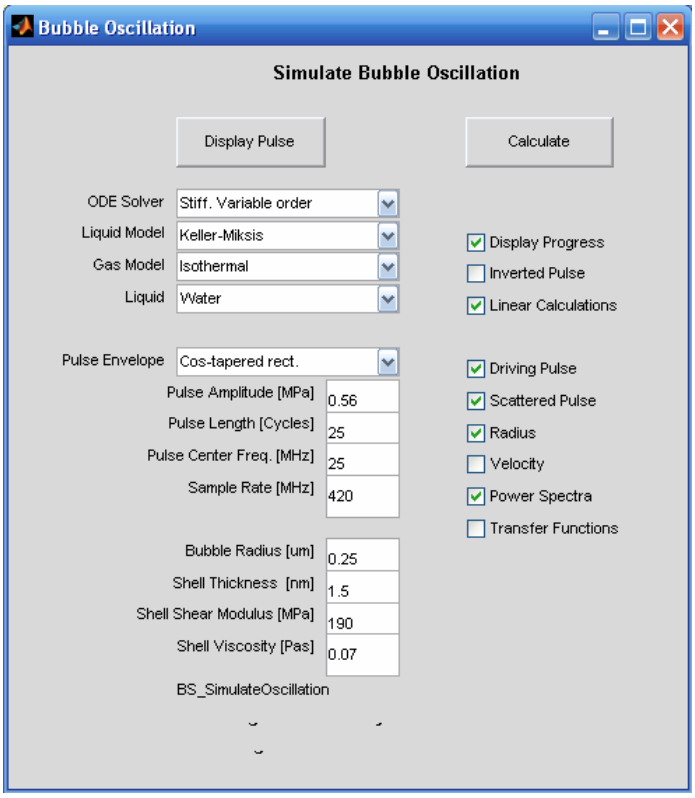

Figure 6. 1: *The interface of BUBBLESIM Toolbox providing the option of model and parameters of ultrasound and MBs*

Table 6. 1: *Selections of model and key parameters*

Catalogue	**Options available in BUBBLESIM toolbox**	**Applied option**
Simulation Model	1. Rayleigh-Plesset (R-P) 2. Trilling 3. Keller-Miksis (K-M) 4. Modified R-P with radiation damping	K-M
Thermal damping (Gas mode)	1. Isothermal 2. Adiabatic 3. Thermal damping pulse frequency 4. Thermal damping resonance frequency	Isothermal
Ordinary Differential equation (ODE) solver	1. Runge - Kutta 4-5 order (ODE45) 2. Stiff variable order (ODE 15s)	ODE 15s

Amongst the four models, the main reason for choosing the Keller–Miksis model is that this model takes into consideration radiation damping and large amplitude oscillations (Doinikov and Bouakaz 2011, Keller and Miksis 1980), despite this it suffers a risk of numerical instability (Andersen and Jensen 2009). The equation of Keller-Miksis model is:

$$\left(1-\frac{\dot{R}}{c}\right)R\ddot{R}+\frac{3}{2}\left(1-\frac{\dot{R}}{3c}\right)\dot{R}^2=\left(1+\frac{\dot{R}}{c}+\frac{R}{c}\frac{d}{dt}\right)G \tag{6.1}$$

where $G=\frac{1}{\rho_L}\left[P_{G0}\left(\frac{R_0}{R}\right)^{3\kappa}+P_v-\frac{2\sigma}{R}-4\eta_L\frac{\dot{R}}{R}-P_0-P_{ac}(t)\right]$,

Pressures:

$P_{G0}= P_0 - P_v + 2\sigma/R_0$ is the pressure of gas in the MB at equilibrium status, P_0 is the hydrostatic pressure at rest, P_v is the vapour pressure in the MB, $2\sigma/R_0$ is Laplace pressure and σ is the surface tension, P_{ac} (t) is the driving pressure.

Parameters of MBs:

R is the instantaneous radius of MB, $\dot{R}$ =dR/dt is the speed of MB wall, $\ddot{R} = d^2R/dt^2$, R_0 is the rest radius, κ is the polytropic exponent of gas also the ratio of specific heat of gas.

Parameters of liquid:

c is the speed of sound, η_L is the dynamic viscosity, ρ_L is the density

The determination of whether the thermal damping is considered isothermal or adiabatic is estimated by the Peclet number $P_e = R_0^2\omega/D_{th}$, where D_{th} is the thermal diffusivity of gas and ω is the angular frequency (Doinikov and Bouakaz 2011). If $P_e >>1$, $\kappa = \gamma$ and adiabatic is applied. If not, $\kappa =1$, i.e., the thermal damping is approximately isothermal (Doinikov and Bouakaz 2011). Note that the polytropic exponents of gas used in the published work are close to 1 (Definity: 1.06 (Goertz et al. 2007), SonoVue: 1.095 (Marmottant et al. 2005) and MicroMarker: 1.045 (Helfield et al. 2012)). Thus, isothermal was used as thermal damping.

ODE 15s and ODE 45 are two numerical solvers in MATLAB and are suitable for solving stiff and non-stiff ordinary differential equations, respectively. The solution deriving from stiff differential equation is numerically stable only within a small time-scale. The main principle in determining the type of equation is whether the equation includes certain terms resulting in a solution with rapid variation. Due to the consideration of rapid variation of the solution introduced by the large oscillation, the dynamic oscillation system may become stiff. Thus, ODE 15s was chosen.

The relevant parameters of the MBs are listed in Table 6.2. Although the shell parameters may be both frequency and size dependent (Faez et al. 2011), there is limited published data on this variation. However, such variation in shell parameters

is potentially one of the reasons in explaining the discrepancy between the experimental data and simulation results, but no further quantified explorations of their influence are discussed in this thesis.

Table 6. 2: *The shell elastic modulus Gs (MPa), viscosity ηs (Pa·S) and shell thickness ε (nm) of the three UCAs. Based on the parameters in Table 5.2, using* $G_s = \chi/3\varepsilon = S_p/6\varepsilon$, $\eta_s = \kappa_s/3\varepsilon = S_f/48\pi\varepsilon$ *, Gs and ηs can be converted from shell surface elasticity χ, stiffness S_p, surface viscosity κs and friction S_f (Doinikov and Bouakaz 2011).*

UCAs	**G_s (MPa)**	**η_s (Pa·S)**	**ε (nm)**
Definity	190	0.07	1.5
SonoVue	61	0.597	3
MicroMarker	572	0.33	3

The insonating parameters used in the simulations are listed in Table 6.3. The diameter of simulated individual MBs ranges from 0.5 to 8 μm.

Table 6. 3: *Parameters of ultrasound applied in the simulations, the selective values are based on the parameters of Vevo770 scanner except the pressures*

Frequency	**Pressure**	**Number of cycles**	**Pulse envelope**	**Sampling frequency**
25/30/40/55 MHz	0.05/0.35/0.65/0.95MPa	5/10/15/20/25	Cosine-tapered rectangle	420 MHz

6.3.2 Comparison of the measured data and the simulation results

Based on the simulation, the backscattered signal from specific sized MBs can be obtained at each diameter in response to the measured diameter from the Mastersizer data. This backscattered signal was filtered using an elliptic filter with 2MHz bandwidth in the fundamental and subharmonic frequency to form the fundamental and subharmonic components, respectively. The output volume based size distributions from the Mastersizer are presented in the format of a relative percentage at each diameter. Here the volume based size distribution curve is used because of its better correlation with the backscattered signal than number based size distribution curve (Gorce et al. 2000). These percentages are used as weighting factor and determine the various contributions of MBs at different diameters to the fundamental and subharmonic components of the backscattered signal. The SFR of a group of MBs from the simulation is calculated using Equation 6.2.

$$\mathrm{SFR} = 10\log_{10}\frac{\sum subharmonic_i \times weight_i \times number}{\sum fundamental_i \times weight_i \times number} \tag{6.2}$$

where $\mathrm{weight_i}$ is the weighting factor, $\mathrm{subharmonic_i}$ and $\mathrm{fundamental_i}$ are the components of the subharmonic and fundamental backscattered signal at each diameter i, respectively. These three variables of all the diameters compose three row vectors, whereas number is the total number of testing MBs, i.e., a scalar quantity and can be cancelled out from the numerator and denominator. The only assumption in this equation is that the concentration of the MBs suspension is sufficiently low and no multiple scattering occurs. Under this assumption of low concentration, the SFR becomes independent of concentration.

6.3.3 Experimental measurement of the SFR

The subharmonic components were extracted from the backscattered signal acquired in the same manner as shown in Figure 5.3.a in Chapter 5. The concentration and

acquisition of the different sized subpopulations is the same as described in Chapter 5. The calculation of the SFR uses Equation 6.3,

$$\mathrm{SFR} = 10\log_{10}\frac{\sum_{2\,MHzBW} Subharmonics}{\sum_{2\,MHzBW} Fundamentals} \tag{6.3}$$

where the numerator and denominator are the power spectra of backscattered signal integrated over the 2 MHz bandwidth of the transmitting frequency and subharmonic frequency, respectively. This calculation of SFR over the 2MHz bandwidth approximates the difference between the fundamental peak and subharmonic peak. For transducer 710B these values are 25MHz and 12.5MHz respectively.

In these experiments, the SFR was only measured using transducer 710B (transmitting signals: 25MHz frequency, 25 cycles, 668 kPa PNP). The reason is due to the following considerations:

- one PNP, the experiment used the lowest PNP 0.67MPa (lowest power), the other 15 discrete power outputs are have higher PNP and likely to increase MB destruction

- the subharmonic peak is discernible from the spectrum using 25 cycle signal, a 1-cycle pulse did not produce a subharmonic peak as shown in Figure 6.13. Only 25-cycle signal was applied in this study to present the SFR 'confidently'.

Another experiment was performed to test the concentration independence of SFR by measuring the SFR of SonoVue at a series of doubling dilutions: (1: 312.5/ 1:625/ 1:1250) at three populations (same dilutions as described in Chapter 5, the dilution of 1: 625 corresponds to 0.8×10^6 mbs/ml). For each concentration and subpopulation, measurement was completed only once.

6.4 RESULTS

6.4.1 The comparison of backscattered signal from TMM and UCAs

Figure 6.2 shows the backscattered signal from TMM in (a) B-mode images and in (b) frequency domain measured by transducer 710B (25-cycle, 25 MHz, 100% power in response to 2.77 MPa-PNP). There is no subharmonic peak at half the transmitting frequency 12.5MHz at 100% power. Because nonlinearity increases with increasing power, no backscattered response of TMM at 12.5MHz under low power is expected. In comparison with this response in the subharmonic frequency range, Figure 6.3 shows the spectrum of the backscattered signal from MicroMarker MBs using the same transmitting parameters except the power is set to 3% in response to a PNP of 0.67MPa. A peak can be seen at 12.5 MHz. The difference of the backscattered component at the subharmonic frequency from the TMM and MBs demonstrates the potential advantage of exploiting subharmonic response from MBs than fundamental or second harmonic components. However, in this study the numerator and denominator of the key parameters SFR in equation 6.2 are from the backscattered signal of MB suspension. The backscattered signal from TMM is not used for normalisation because of the following three reasons. 1) The comparison can be conducted between measured SFR and the simulation results without modelling the backscattered signal from TMM. 2) Backscattered signal from MB suspension travels through the same medium, while TMM is generally measured in water and the different mediums introduce variation in attenuation of ultrasound. If measuring TMM in MB suspension or attenuation of ultrasound at long cycle signal, this would extend the time length of experiment and restrict the number of experiments using one vial of contrast agent. Applying UCAs from different vials raises extra uncertainties. 3) SFR defined in equation 6.3 is a concentration independent parameter which aims to certify which diameter of MB dominates the subharmonic component without considering the influence of concentration in the experiment.

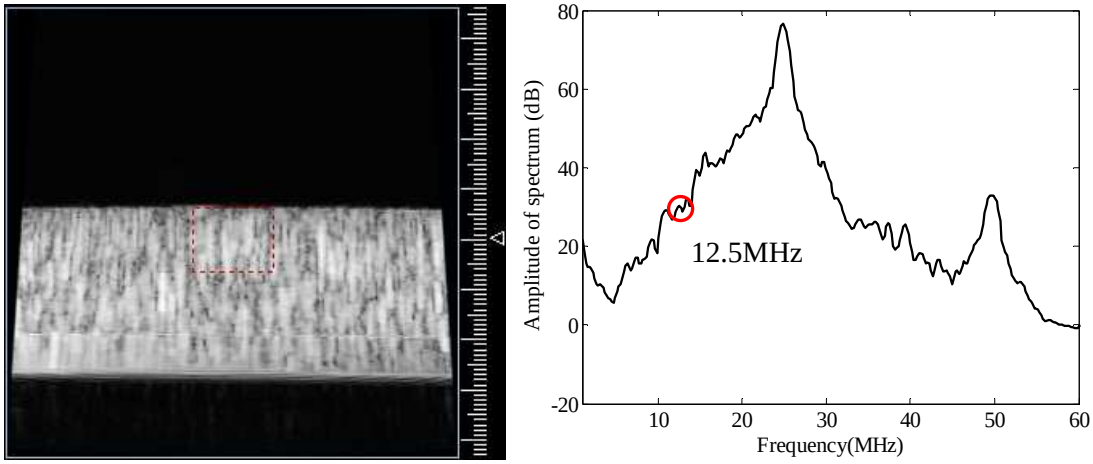

(a) *(b)*

Figure 6. 2: *(a) The B-mode image of TMM at 25MHz, 100% power, 25-cycle using transducer 710B (b) The averaged spectrum of 300 backscattered samplings in response to the backscattered signal from the TMM in (a), red circle in (b) marks the position of the half the driving frequency.*

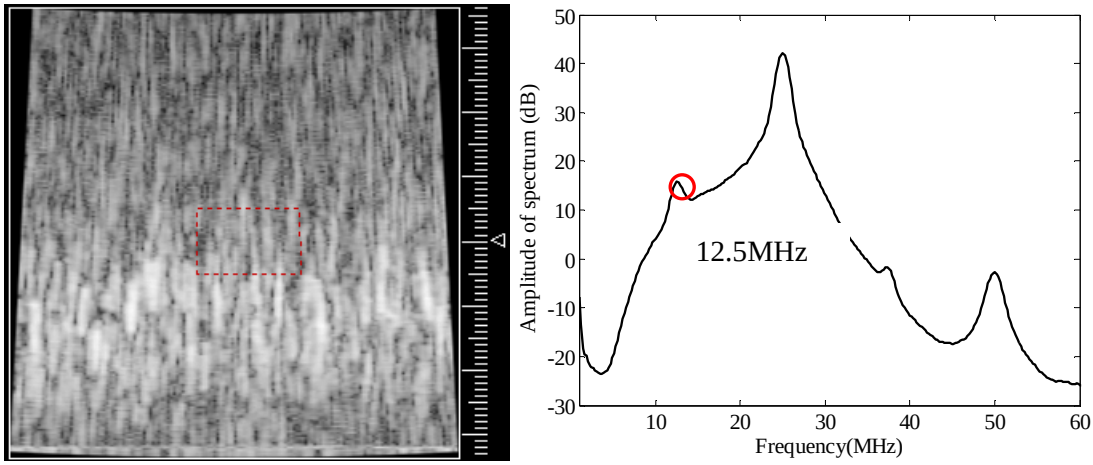

(a) *(b)*

Figure 6. 3: *(a) The backscattered signal from the suspension of MicroMarker MBs at 25MHz, 3% power, 25-cycle using transducer 710B. (b) The averaged spectrum of 300 backscattered samplings in response to the signal from MicroMarker MBs in (a), red circle in (b) marks the position of the half the driven frequency.*

6.4.2 The simulation of SFR as a function of *frequency* (25 - 55 MHz), *pressure* (0.05 – 0.95 MPa) and *number of cycles* (5/10/15/20/25)

Figure 6.4 shows the variation of fundamental, subharmonic and SFR of (a) Definity, (b) SonoVue and (c) MicroMarker in a diameter range of 0.5-8 μm at four frequencies 25MHz, 30MHz, 40MHz and 55MHz. The variation in the position of the peak of the fundamental and subharmonic reflects MBs of changing diameters resonating at the driving frequencies and half of the driving frequency, respectively. The SFR shows 1) a trough in the curve because of the low subharmonic component from small MBs, 2) a peak at the same position as the peak of subharmonic occurs. The possible reason explaining the occurrence of the high SFR of Definity at MB sizes less than 1μm may be due to the fact that both fundamental and subharmonic components are very small and the logarithm of the quotient of which (two infinitesimals) produces an unstable solution (definition of SFR shown in Equation 6.2). This value at small diameter would not interfere the experimental result as the transducer is not sufficiently sensitive to receiving the weak signal scattered from the small MBs.

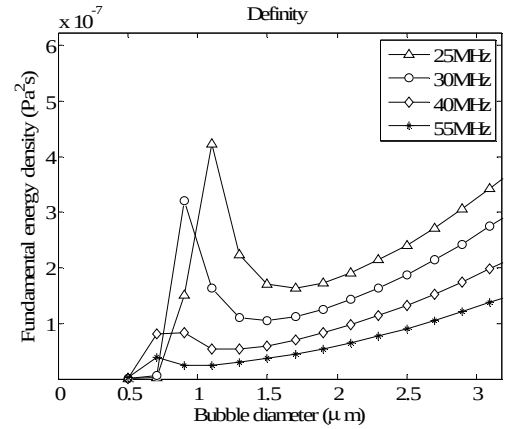

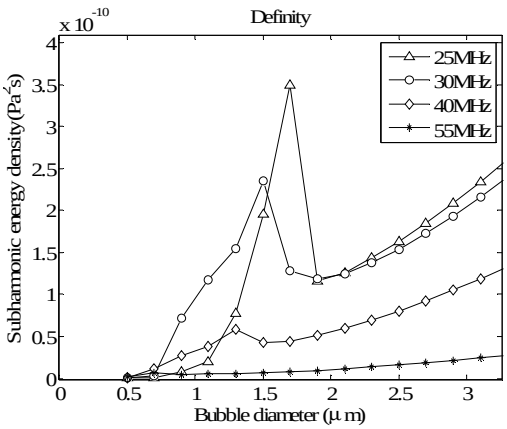

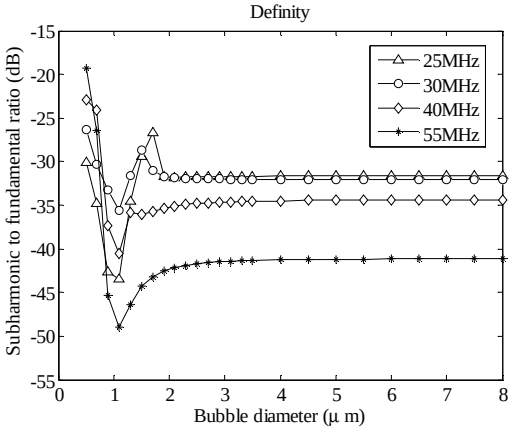

(a) Definity

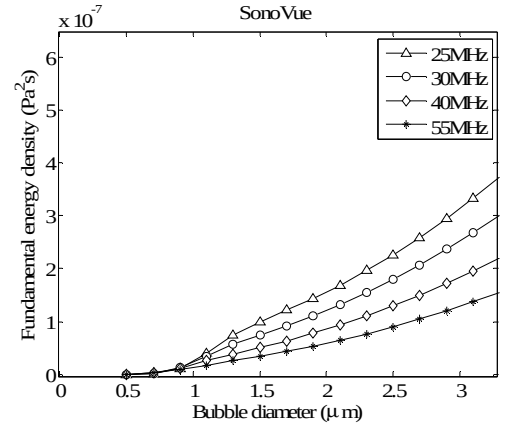

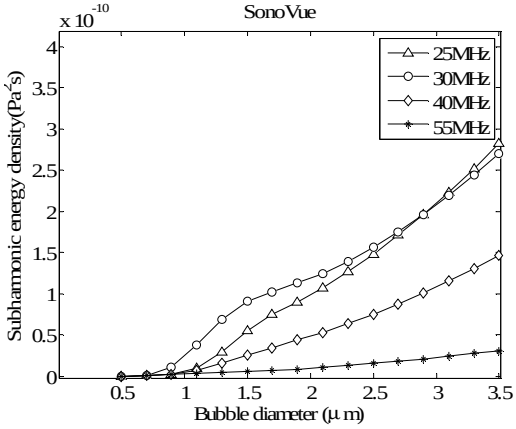

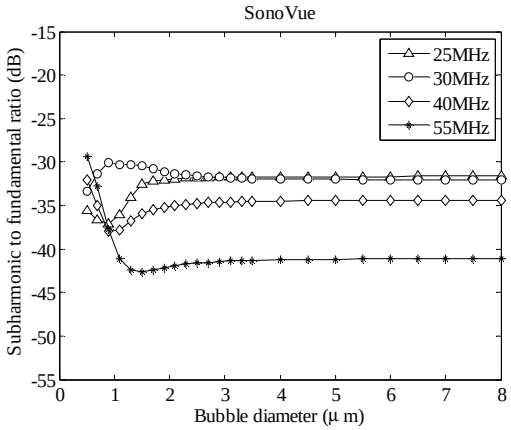

(b) SonoVue

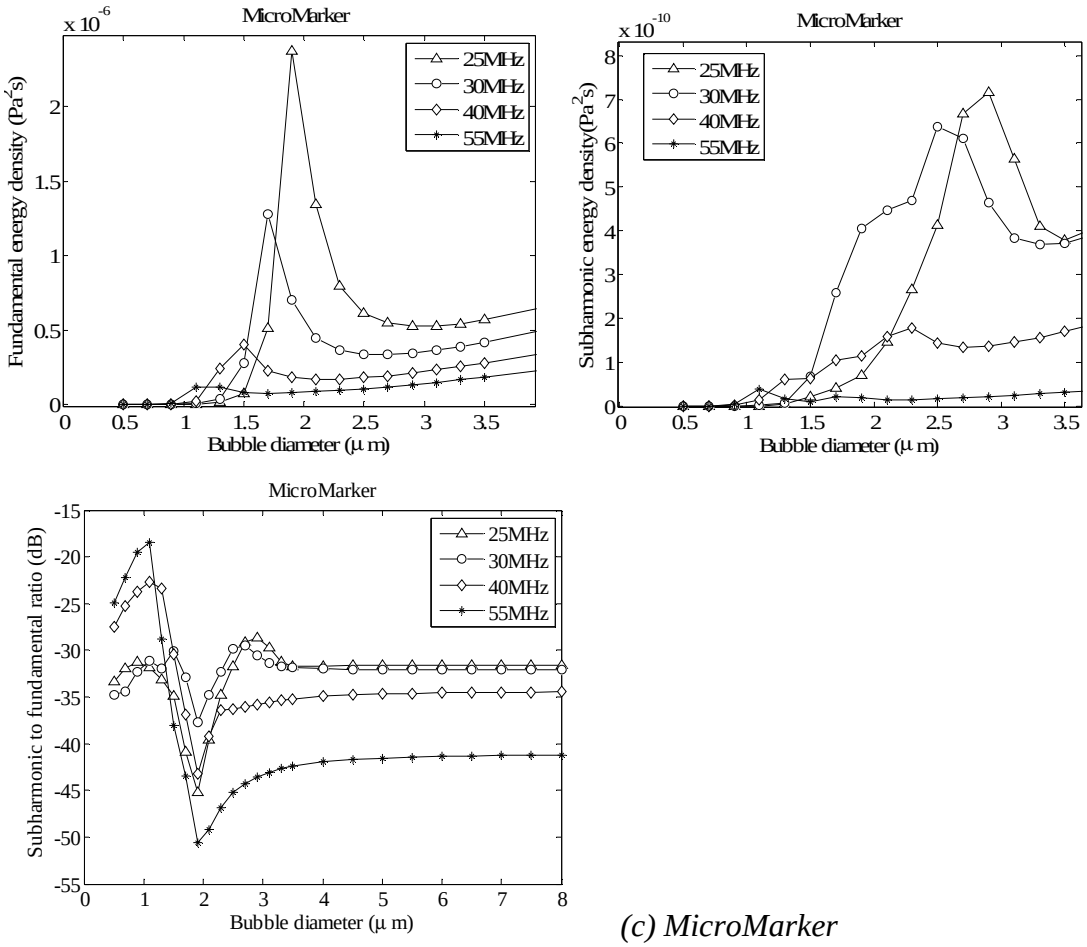

(c) MicroMarker

Figure 6. 4: *The simulated response of the fundamental, subharmonic and SFR of (a) Definity, (b) SonoVue and (c) MicroMarker to insonating frequencies at 25 MHz, 30 MHz, 40 MHz and 55 MHz, other insonating parameters fixed at 560 kPa-PNP and 25-cycle.*

Figure 6.5 shows the influence of pressure from 0.05 MPa to 0.95 MPa on the SFR of (a) Definity, (b) SonoVue and (c) MicroMarker in a diameter range 0.5-8 μm. Compared with SonoVue and MicroMarker, Definity presents the widest dynamic range of SFR with pressure variation.

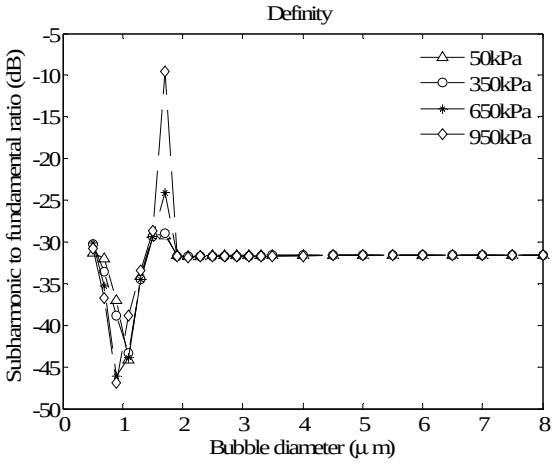

(a) Definity

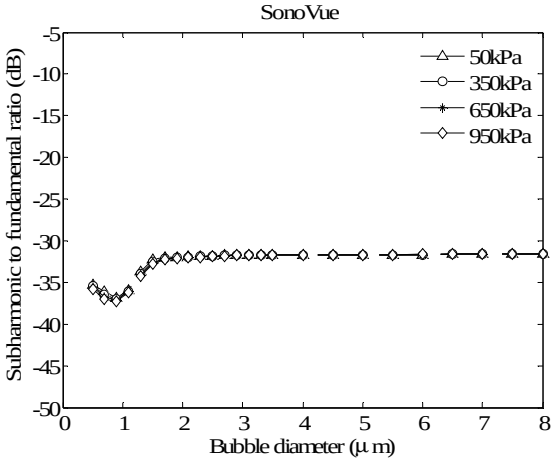

(b) SonoVue

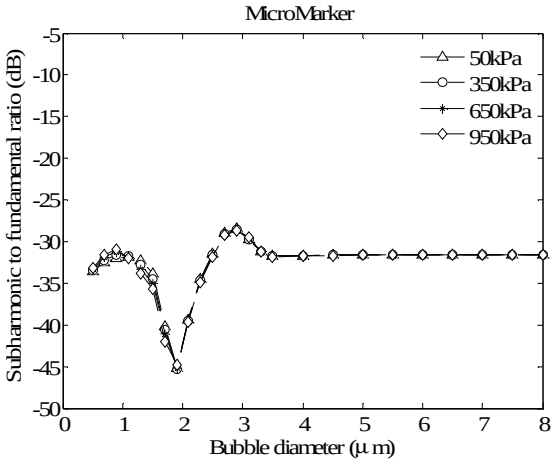

(c) MicroMarker

Figure 6. 5: *The simulated variation in the SFR of (a) Definity, (b) SonoVue and (c) MicroMarker with pressure from 0.05 MPa to 0.95 MPa, other insonating parameters fixed at 25MHz and 25 cycles*

The simulation of the SFR of (a) Definity, (b) SonoVue and (c) MicroMarker varied with number of cycles is shown in Figure 6.6 in a MB diameter of 0.5-8 μm. The peak of the SFR is from the insonating signal of 5 cycles. A shorter number of cycles is found to produce a greater SFR than using long number of cycles. However, the SFR for the MB larger than 4 μm from 10-cycle signal is higher than the value from 5-cycle signal.

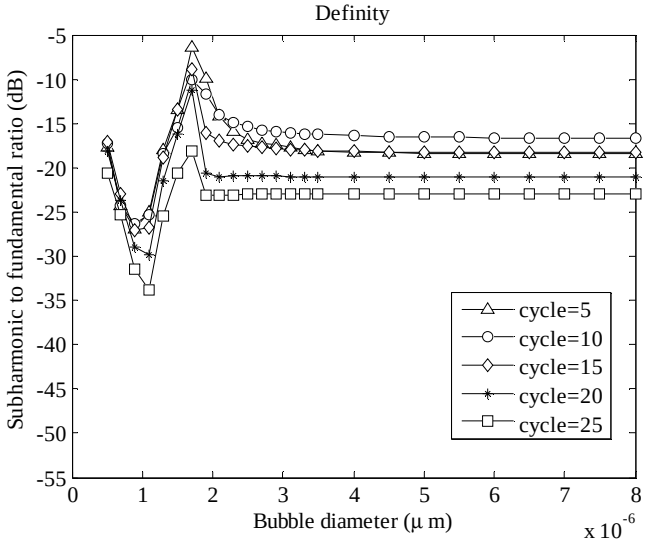

(a) Definity

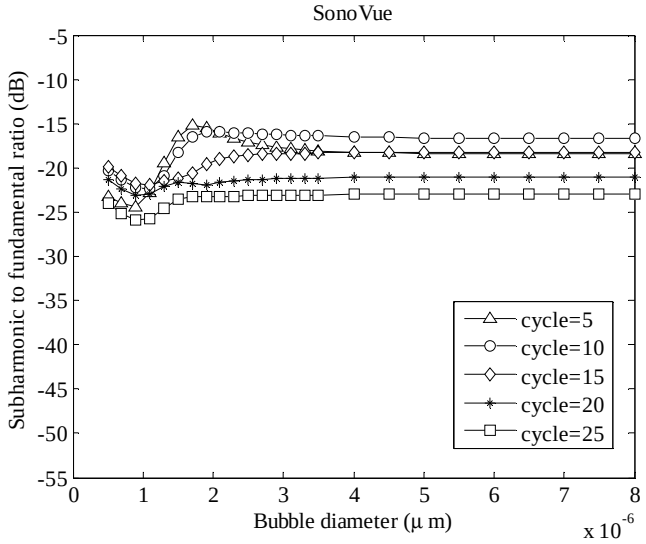

(b) SonoVue

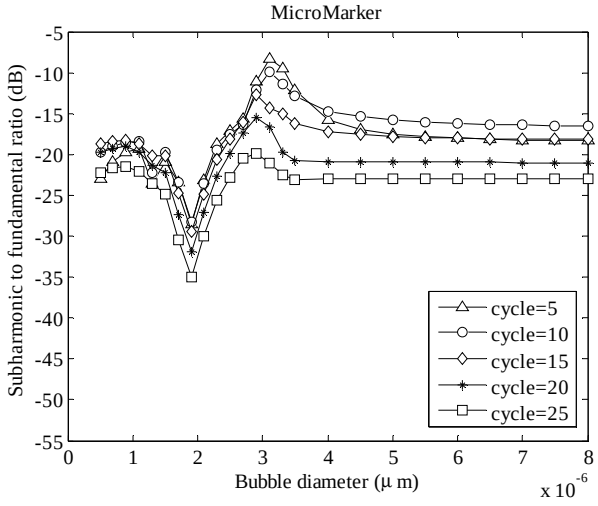

(c) MicroMarker

Figure 6. 6: *The simulated SFR of (a) Definity, (b) SonoVue and (c) MicroMarker varied with number of cycles from 5 to 25, other insonating parameters fixed at 560kPa and 25MHz*

6.4.3 The comparison of the measured data and the simulation results

Figure 6.7 - 6.9 show the simulation results of (a) energy density of RF data, fundamental and the subharmonic components and (b) the SFR as a function of bubble diameter for Definity, SonoVue and MicroMarker. The transmitting signal uses the parameters from transducer 710B applied in the experiment: 25MHz, 25 cycles and 0.67 MPa.

From the simulation of Definity in Figure 6.7.a and MicroMarker in Figure 6.9.a, it can be seen that the fundamental energy density is the largest part of the response as it almost overlaps with RF signal. The bubble diameter yielding the peak of fundamental is shifted to a smaller diameter from the diameter where the peak of subharmonic appears. As expected, in Figure 6.7.b and 6.9.b the bubble generating the highest subharmonic response produces the peak of the SFR. The trough of the SFR is located at the resonant diameter (peak of the fundamental component shown in Figure 6.7.a and 6.9.a). SonoVue in Figure 6.8 presents a different behaviour

compared with Definity and MicroMarker. Without a clear peak in the fundamental and subharmonic curves, both the energy density in Figure 6.8.a and SFR in Figure 6.8.b display a lower amplitude of 'oscillation' with a larger increase that then doesn't change with increasing diameter.

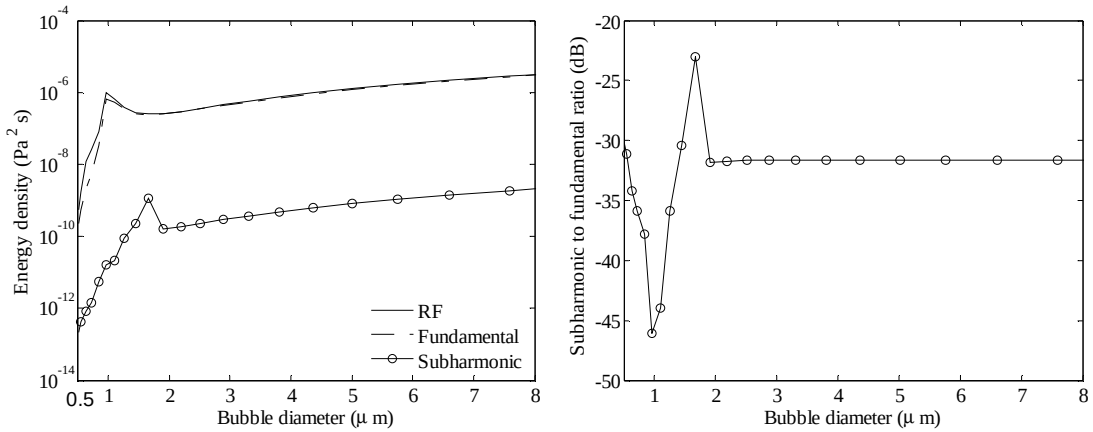

(a) *(b)*

Figure 6. 7: *The variation in (a) energy density of the simulated RF data, fundamental and subharmonic components as a function of bubble diameter (b) SFR of Definity MBs as a function of bubble diameter*

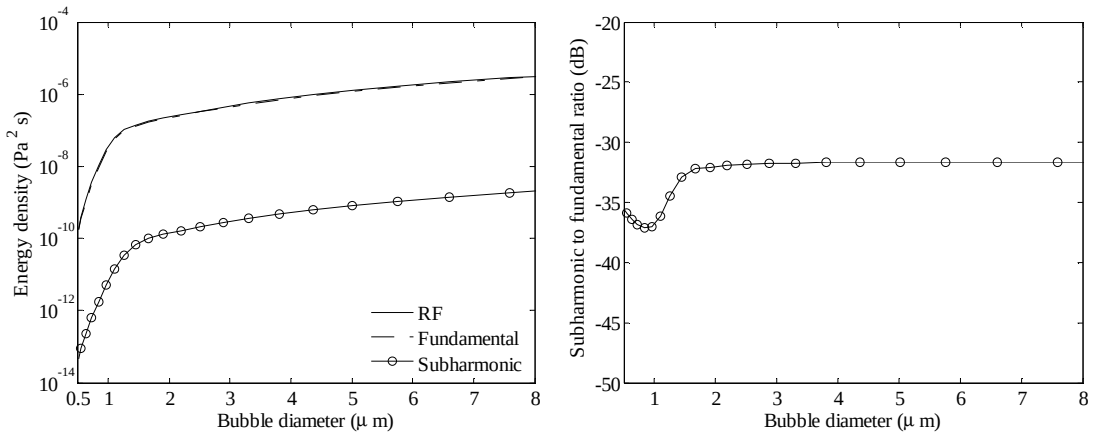

(a) *(b)*

Figure 6. 8: *The variation in (a) energy density of the simulated RF data, fundamental and subharmonic components (b) SFR of SonoVue MBs as a function of bubble diameter*

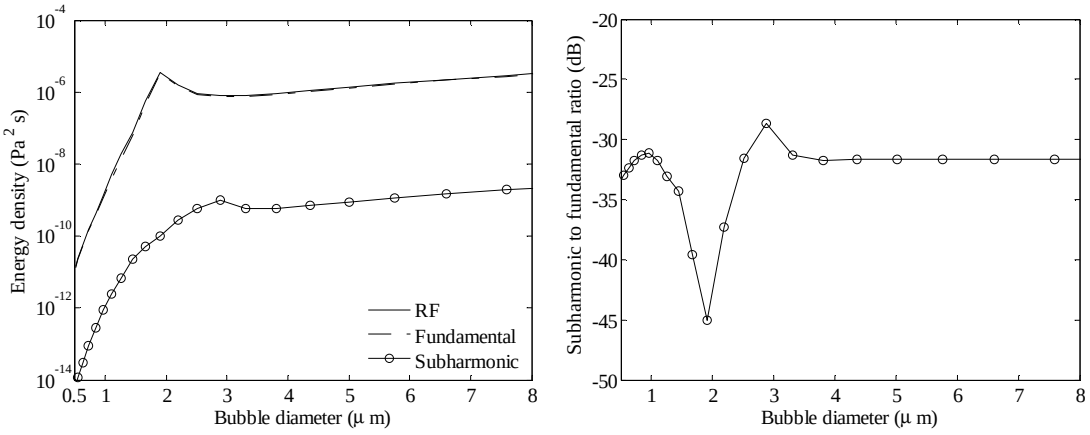

(a) *(b)*

Figure 6. 9: *The variation in (a) energy density of the simulated RF data, fundamental and subharmonic components (b) SFR of MicroMarker MBs as a function of bubble diameter*

Using the above simulated fundamental and subharmonic components at each diameter and incorporating the measured size distribution in Equation 6.3, Figure 6.10 shows the simulated SFR of Definity and SonoVue at three populations and native MicroMarker based on the volume based size distribution curve in Figure 5.5.

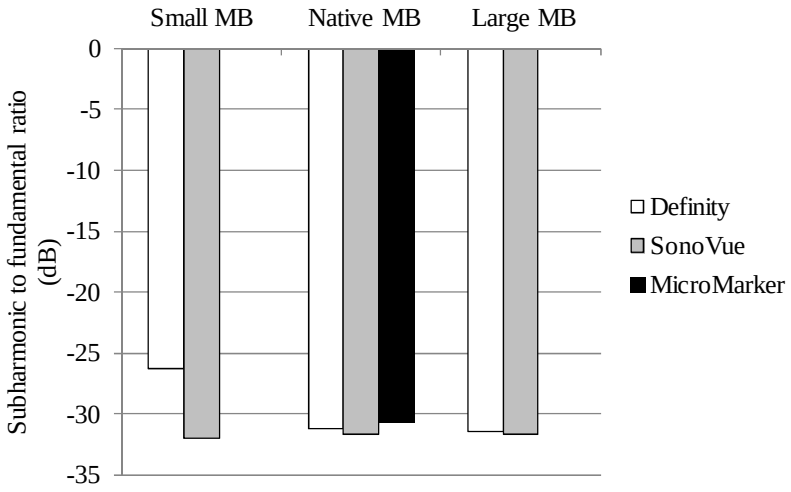

Figure 6. 10: *The simulated SFR of groups of MBs of Definity, SonoVue and MicroMarker using volume based size distribution curve based on the experimental parameters of transducer 710B (25-cycle 0.67 MPa-PNP, 25 MHz-transmitting frequency)*

6.4.4 The experimental data of the SFR

Figure 6.11 shows the measured SFR of SonoVue and Definity of three populations and the native MicroMarker using transducer 710B. The SFR of the decanted small MBs population is higher than their corresponding native and large MB population. In the comparison of the three native UCAs, MicroMarker shows a 3.2dB and 6.6dB higher SFR than SonoVue and Definity, respectively.

Compared with the experimental data, the simulated values in Figure 6.10 of Definity are close to the measured data and small MB population produces higher SFR than the native and large MB populations. But SonoVue and MicroMarker display an approximate 5dB difference in the SFR.

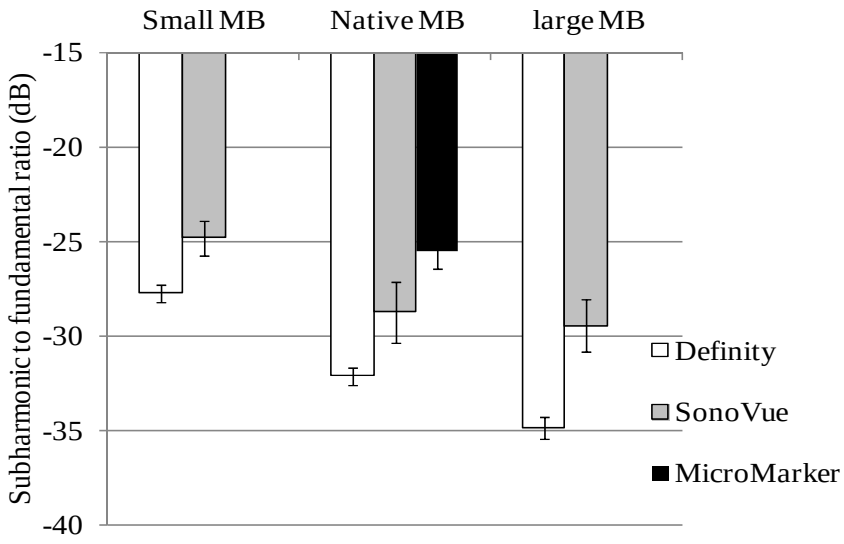

Figure 6. 11: *The SFR measured by transducer 710B at 25-cycle, 0.67 MPa-PNP, 25 MHz-transmitting frequency, 12.5MHz-receiving frequency, the error bars were calculated from the three independent measurements*

The measured SFR of SonoVue at three subpopulations in Table 6.4 shows good consistency at each dilution and supports hypothesis that SFR is independent with concentration from Equation 6.3.

Table 6. 4: *Measured SFR of SonoVue at three subpopulations and three dilution ratios using transducer 710B (25-cycle 0.67 MPa-PNP, 25 MHz-transmitting frequency)*

Dilution	Small MB	Native	Large
1:312.5	-23.59 ± 2.48	-27.22 ± 1.42	-26.45 ± 2.47
1:625	-23.38 ± 2.45	-26.75 ± 1.38	-26.64 ± 2.43
1:1250	-23.19 ± 2.50	-25.83 ± 1.37	-27.34 ± 2.37

6.5 DISCUSSION

6.5.1 The influence of pressure, frequency and number of cycles on subharmonic generation – simulation study

The **driving frequency** determined the diameter of the MBs producing the highest subharmonics, i.e., MBs resonate at half of the driving frequency shown in Figure 6.4. Additionally, subharmonic signals are known to be stimulated by narrow band signals (de Jong et al. 2009). The resonant MBs at the driving frequency reduce the SFR owing to its high fundamental component. Mono-disperse MBs resonating at half the driving frequency may optimize the subharmonic generation. To optimize the population for subharmonic generation the mono-disperse MBs resonating at half the driving frequency may be the ideal. This population is different from the MBs for the fundamental generation in Chapter 5, as both the resonant and large off-resonance MBs can be the main contributors.

The **pressure** shows its impact on the magnitude of the SFR of MBs in Figure 6.5. Only Definity displays a sensitive pressure dependence of SFR compared with SonoVue and MicroMarker. For SonoVue and MicroMarker their SFRs become approximate pressure independent. Possible reasons may be related to the current

published different shell parameters in Table 5.2. The shell stiffness of Definity and SonoVue are comparable but are only one tenth the magnitude of MicroMarker. The shell friction of MicroMarker and SonoVue are 10 and 20 times higher than Definity, respectively. The results of high shell stiffness and high friction impose strong resistance to the forced stress and may provide a transformation mechanism of the kinetic energy to heat dissipation. The nonlinear properties of Definity, such as the generation of subharmonics are more obvious due to its relative low shell stiffness and friction. The experimental subharmonic data of Definity from a previous study (Cheung et al. 2008) also showed this sensitive variation from rapid growth to steady state, then gradual reduction as a function of pressure in the range 0.13-1.3 MPa. SonoVue showed a very low pressure threshold (<100kPa) for the emission of subharmonics at low frequencies (3.3MHz, 5MHz) (Biagi et al. 2007). At 25MHz MicroMarker showed a subharmonic threshold of 89kPa (subharmonic power is 3dB higher than noise floor) and smaller than 2μm were observed to disrupt at 1.2 MPa, but most MBs larger than 2.6 μm were not disrupted (Helfield et al. 2012). As reviewed in the introduction to this chapter there are generally two cases of subharmonic emission at low frequencies: 1. stable subharmonic emission when pressure above subharmonic threshold, 2. subharmoic emission related to destruction. Assuming the SonoVue and MicroMarker MBs emit stable subharmonics but are not destroyed at the simulated pressure, the magnitude of the subharmonics may increase proportionally to fundamental components with increasing pressure for SonoVue and MicroMarker. The resultant SFR becomes a stable constant without a high sensitivity to pressure.

Shorter **number of cycles** produces a higher SFR of individual MBs in Figure 6.6. The experimental data of native Definity population also confirmed short 4-cycle signal generated high SFR which reduced in magnitude to a steady level of 13dB around 15 cycles (Cheung et al. 2008). The reason was attributed to narrower bandwidth at longer cycle increasing the fundamental and subharmonic logarithmically, which yielded decrease of the noise floor, the height of the side lobe and the adjacent fundamental signal. However, experimental results presented here give a limited experimental view at the subharmonic frequency using 25-cycle signal

in the frequency spectrum in Figure 6.12, while shorter number of cycles e.g., 4 or 10 actually do not produce any discernable enhancement at the subharmonic frequency. But calculation of SFR by filtering the signal in the fundamental and subharmonic frequency leads to the same conclusion, i.e., transmitting signal of shorter cycles give higher SFR than long cycles. The spectrum using shorter cycle pulse is broader than long cycle pulse shown in Figure 2.17-2.18. In particularly around subharmonic frequency, the spectral energy of short cycle pulse distributes in a wide range and no discernable peak does not mean none or low subharmonic energy. Thus, the bandwidth for filtering subharmonics from short cycle pulse requires to be carefully chosen.

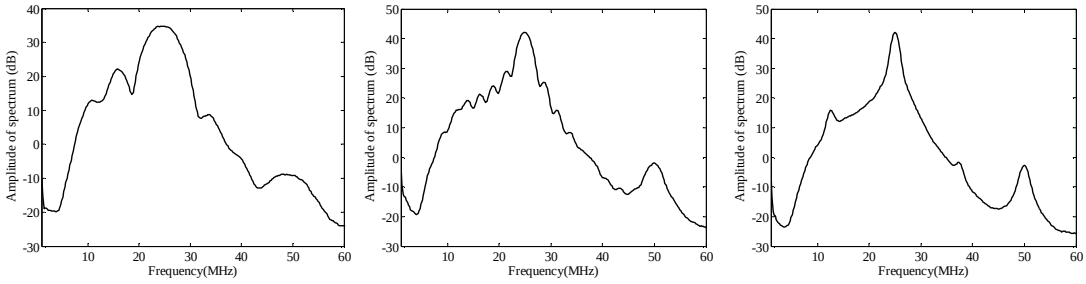

(a) cycle = 4 *(b) cycle = 10* *(c) cycle = 25*

Figure 6. 12: The measured SFR of MicroMarker insonating at 3% power and three cycle lengths (a) 4 cycles, (b) 10 cycles and (c) 25 cycles

6.5.2 The discrepancy between the experimental data and simulation results

Figure 6.11 shows that small Definity and SonoVue MBs produces higher SFR than the native and large MBs population, which indicates that small MBs are predominantly responsible for subharmonic response at the tested 25 MHz frequency. Considering the resonant diameter of MBs and size distribution, in Figure 6.7 Definity MBs of a diameter of 1.7 μm were found to resonate at 12.5 MHz (half of 25MHz). The volume percentage of this diameter is higher in small MBs

population than the native and large MBs population shown in Figure 5.5.a, thus small MBs population produces the highest SFR.

Among the three native UCA solutions, MicroMarker produced the highest SFR and the reason may be attributed to the diameter of its resonant MBs is the largest compared with Definity and SonoVue (resonant diameter at 12.5MHz: 1.7 μm for Definity and 3.1 μm for MicroMarker). Because the simulation results in Figure 5.1 show that SonoVue does not, whereas Definity does resonate above 10MHz, theoretically Definity MBs emit a higher SFR than SonoVue (Figure 6.10). However, from experimental data SonoVue demonstrated a higher SFR than Definity in each pair group of small, native and large population (Figure 6.11). Additionally, SonoVue of 1 μm was found to resonate at 21MHz (Bouakaz and de Jong 2007). From this point of view, the shell properties of SonoVue acquired at low frequencies (Gorce et al. 2000) may not be suitable for the simulation at high frequencies. Thus the shell properties of the small SonoVue MBs in particularly at higher frequencies are worth further investigating to fully understand the nonlinearity of SonoVue at high frequencies.

More than 5dB difference was found between the simulated and measured SFR of SonoVue and MicroMarker in Figure 6.10 and Figure 6.11. The potential of numerical instability of the Keller – Miksis model is not the only possibility explaining this discrepancy. At the tested ultrasound parameters (25MHz, 0.67MPa, 25-cycle signal), MBs may fragment or oscillate non-spherically which make the original simulated model lose stability and distract feasibility. For instance, expansion-dominated behaviour of MicroMarker was found in the rupturing regime at high frequency (Helfield et al. 2012). This behaviour of one bubble is defined as its ratio of absolute expansion $(R_{max}-R_0)/R_0$ to absolute compression $(R_0-R_{min})/R_0$ is larger than 1, where R_0, R_{max} and R_{min} are the equilibrium, maximum and minimum radii respectively. The shell properties may change during the oscillation as the shell of Definity was described as strain-softening material (Thomas et al. 2009). Additionally, non-spherical oscillation of MBs larger than 1.9 μm was investigated using a ultra-high-optical imaging and optical tweezers to produce the subharmonic

response at 1.7MHz at acoustic pressures up to 200 kPa (Dollet et al. 2008). Although this study was conducted at low frequency, a similar phenomenon can be expected for the small MBs resonating at half the driving frequency to emit the subharmonic response. As discussed above, the shell properties of SonoVue particularly may need further investigation because of the mismatch between the simulations and experimental results. In summary, the complexities of variation in MBs themselves during the oscillation and the limitation of the model cause the difference between the experimental data and simulation results. Thus the dynamic oscillation and shell properties of MBs may require further studies.

6.5.3 The limitation of comparison of subharmonic to fundamental ratio

SFR is a relative parameter based on its definition in Equation 6.3, and as such is dependent upon the magnitude and characteristics of both the fundamental and sub-harmonic components of the tested sample. Thus the ability to infer characteristics of the subharmonic from this parameter and to compare different contrast agents and subpopulations using this parameter may be undermined. However, CTR of the three native UCAs at 25MHz are comparable shown in Figure 5.7. Due to normalizing to the same backscattered signal from TMM, CTR reflects the comparable backscattered signal of the three UCAs in the fundamental frequency range. Note that CTR is calculated in the 3dB bandwidth of the transducer (transducers 710B, 707 and 704 all covering 25MHz which is used in the subharmonic experiments), so it is not strictly equivalent to the averaged spectra within 2MHz-bandwidth applied in the SFR calculation. Nevertheless, the above analysis of MicroMarker producing higher subharmonic components than native Definity and SonoVue populations is very likely to be correct. Additionally, the above discussions suggest the small microbubble subpopulation dominates in subharmonic production compared with native and large subpopulations. Figure 5.7 shows that the small subpopulation of Definity and SonoVue produces more than 5dB decrease in CTR than their native and large subpopulations. Thus, it is unlikely that the absolute magnitude of the subharmonic component from small subpopulation is greater than native and large subpopulations despite the small subpopulation shows the highest SFR. From the

practical subharmonic imaging point of view, SFR is a useful parameter as the core of imaging focuses on the difference between the signal and noise, i.e., a relatively high subharmonic value compared to its fundamental component would aid the subtraction of the subharmonics from the received signals. Further investigations are required to answer these questions.

6.6 CONCLUSION

The simulation results suggest the role of the insonating parameters on the SFR. Briefly, MBs resonating at half of the driving frequency predominately drive the subharmonics, i.e., the frequency determines MB of the most effective diameter. The pressure and number of cycles influence the magnitude of the oscillation. Although discrepancy between the experimental data and simulation exist, the main reasons for this discrepancy may be the shell properties of MB especially the small MBs at high frequencies are not well established and the actual MB oscillation and the assumption of the model are mismatched.

The experiments conducted in this chapter only show the global acoustic properties and provides insufficient evidence for the modelling results. However, from the experimental data three points can be concluded: 1. Native MicroMarker produced higher SFR at 25MHz compared with native Definity and SonoVue. 2. At low concentrations, SFR was a concentration independent parameter. 3. Changing size distribution altered the subharmonic response and at 25MHz the small population of Definity and SonoVue (diameter< 2μm) was found to be the most effective for the generation of subharmonic signals. From the designing and tailoring UCAs point of view, non-destructive SFR can be improved by selectively increasing the number of MBs resonating at half the driving frequency.

Chapter 7

Influence of temperature, needle gauge and injection rate on the size distribution and acoustic responses of ultrasound contrast agents at high frequency

7.1 AIM

This chapter investigated the influence of needle gauge, injection rate and temperature on the size distribution, acoustic attenuation, contrast to tissue ratio (CTR) and subharmonic to fundamental ratio (SFR) of solutions of Definity and SonoVue. The measurement of size distribution was performed by Ms Ioanna Panagakou as her Master Maxi-project (Centre for Cardiovascular Science, University of Edinburgh) under the supervision of the author of this thesis and the work of the acoustic measurement were completed by the author and Ms Ioanna Panagakou together.

7.2 INTRODUCTION

There is increasing application of UCAs in the preclinical field (Foster et al. 2011), and therefore *in vitro* studies using UCAs at high frequencies are of importance (Goertz et al. 2005, Helfield et al. 2012). However the difference between the administration of UCAs in an *in vivo* environment (small needle gauge and slow injection rate at body temperature) and the *in vitro* experiment (large needle gauge, fast injection rate and room temperature) need to be considered. Needle gauges selected for the *in vivo* small animals studies includes: 24G for rat tail vein injection (Miller et al. 2007) , 27G for mice tail vein injection (Howard et al. 2006) and 30G

for pig cervical region of nerve (Heaton et al. 2005) and dog lymphatic system (Wisner et al. 2002). The injection rates are set at 0.5 mL/kg/min for rat tail injection (Miller et al. 2007) and 1.2-2.4 ml/ml for mice tail injection (Browning et al. 2011). Generally *in vitro* experiments of UCAs are performed at room temperature using the needle gauges 18G-20G at a relatively fast injection rate that simulates the process of bolus intravenous injection for human.

7.2.1 The influence of temperature

Both Definity and SonoVue are lipid coated UCAs. The fluid-gel phase transition temperature of the lipid in bilayer state vary from -1 °C and 75 °C (Pu et al. 2006) and -1 °C and 55 °C (Zook and Vreeland 2010) depending on the phospholipids acyl chain length. Lipid molecules are limited on the plane of the membrane in the two phases (fluid: liquid phase, gel: solid phase), but liquid phase allows a freer diffusion of molecules than in solid phase (Berg 1993). For this reason, the viscosity, membrane elasticity, free energy and diffusion coefficient of the shell can be changed below, at or above the transition temperature (Zook and Vreeland 2010). The lipid shell of Definity consists of three phospholipids (DPPA, DPPC and MPEG 5000 DPPE) (Helfield et al. 2012). SonoVue possesses an amphiphilic phospholipid shell (a hydrophilic surface outside and a hydrophobic surface inside) (Greis 2004) and involves two lipids (DSPC and DPPG) (Mulvana et al. 2011). The shells of both UCAs are mono-layered and are a combination of lipids, thus a specific phase transition temperature is unknown and its resultant influence needs to be investigated.

Previously the thermal response of SonoVue was studied at 37-43 ^{o}C and its lipid transition temperature was measured to be 40^{o}C, which was derived from an observation of maximal diameter and backscattering intensity (ultrasound frequency: 2.5- 8MHz, low MI: 0.0081-0.113) at 40 ^{o}C and a rapid decrease afterwards (Guiot et al. 2006). Individual Definity and SonoVue MBs were measured at 21 ^{o}C – room temperature and 37 ^{o}C –body temperature using a high speed optical camera under an insonation of 1.7 MHz, 10-80 kPa pulse (Vos et al. 2008). Compared with the

performance at room temperature, Definity and SonoVue showed an increase in radical excursion (which equals to $\Delta D/D_0$, where ΔD is the maximum peak-zero amplitude of the linear oscillation, D_0 is the initial diameter of MBs) and a decrease in onset of acoustic oscillation at body temperature. Intensive temperature dependence studies of SonoVue were completed at 3.5 MHz-ultrasound (Mulvana et al. 2010, Mulvana et al. 2011). Due to the increasing temperature close to transition temperature, it was found that the resultant expanding MBs and rapid diffusion raised the mean diameter, attenuation, backscatter and nonlinear components.

7.2.2 The effect of needle size and injection rate

Talu (Talu et al. 2008) measured the variation in concentration and mean diameter of one in-house lipid-encapsulated UCA at 3 concentrations (1, 5, 10×10^8 MBs·ml^{-1}) using 3 needle gauges (23G, 27G and 30G) at 5 injection rates (0.01, 0.03, 0.1, 0.3 and 0.5 ml/sec). Due to the measured significantly declining concentration with increasing needle gauge (i.e., decreasing inner diameter), the main reason was inferred to be the destruction of MBs. The reduction in mean diameter was attributed to the decrease in the entire population due to diffusion by forced compression and possibly destruction of large MBs. A similar study investigating the influence of administration variables (2 needle gauges: 18G and 25G; 2 syringes: 5ml and 10ml; 5 discrete flow rates from 2 to 3.3 ml·min^{-1}; 2 suspending fluid: distilled water and 95% volume-glycerol) was performed using another in-house MB (Barrack and Stride 2009). The results from this study showed that in addition to the hydrostatic pressure, shear stress due to the increasing pressure and velocity gradient played a key role in destroying MBs. However, one difference was that the growing volume flow rate reduced the destruction of MBs, which is not in agreement with the study of Talu (2007). The discrepancy was blamed on the difference of initial diameter, size distribution, concentration and composition of MBs. An *in vivo* experiment improving the plasmid transfection and MBs-mediated gene transfection using SonoVue also supported the above findings by testing the effects of using 3 needle gauges (25G, 27G and 29G) (Browning et al. 2011).

From the above reviewed studies, temperature, needle gauge and injection rate have effects on the structure, size distribution and acoustic properties of UCAs. However, many questions remain unsolved. Firstly, the previous studies are limited to the ultrasound frequencies relevant for clinical applications and little research has been performed at high frequency. Secondly, the impact of temperature, needle gauges and injection rate were discussed separately and neither interactions between them nor their importance were compared and ranked. Thirdly, some in-house MBs have been studied while commercial UCAs are the products that are most commonly used preclinically and their characterisation is not clear.

In this chapter, the influence of needle gauges (19G, 27G and 30G), injection rate ($0.85ml{\cdot}min^{-1}$ and $3ml{\cdot}min^{-1}$) and temperature (room temperature $20\pm2^{o}C$ and body temperature $37\pm5^{o}C$) on the size distribution and acoustic properties of Definity and SonoVue have been measured in the frequency range of 17-31MHz. The experimental details are presented initially and selective results of measured parameters between *in vitro* (19G, 3ml/min at RT) and *in vivo* (27G/30G, 0.85ml/min at BT) are shown. Then differences between the *in vitro* and *in vivo* are summarized after discussing the impact of each factor.

7.3 METHOD AND MATERIALS

This experiment employed one transducer 707B (nominal centre frequency=30MHz, 3dB bandwidth=17-31MHz, 6dB bandwidth=13-35MHz at 3% transmitting power and the peak negative pressure (PNP) was measured to be -0.56 MPa). From the pressure experiments in Chapter 4, at this PNP MBs are not destroyed at room temperature. A full experimental procedure is described below after the description of the 3 needle gauges, 2 injection rates and temperature manipulation.

7.3.1 Needle gauge

Three needle gauges including 19G, 27G and 30G (Becton, Dickinson and Company (BD), USA) were employed. These needles are generally used in human intravenous injection but also *in vitro* experiments including the mice tail injection and mice heart injections. Table 7.1 listed the information of these needles including inner diameter and cross-sectional area.

Table 7. 1: *The inner diameter and cross-sectional area*

Needle Gauge	Inner Diameter (mm)	Area (mm^2)
19G	0.686	0.37
27G	0.21	0.03
30G	0.159	0.02

7.3.2 Injection rate

Two injection rates were applied 0.85 $ml \cdot min^{-1}$ and 3$ml \cdot min^{-1}$, where 0.85 $ml \cdot min^{-1}$ was generally used for bolus injection in mice vein tail and 3 $ml \cdot min^{-1}$ simulates the injection rate applied in *in vitro* experiments. The steady and reproducible injection rate was controlled using a syringe pump (Aladdin, World precision instruments Inc., USA) by connecting a tested needle with 1ml-syringe (ID = 4.78 mm) to reach an injection rate of 0.85 $ml \cdot min^{-1}$ and 2ml-syringe (ID=8.66 mm) for 3$ml \cdot min^{-1}$ injection rate.

7.3.3 Temperature control and the measurement of dissolved oxygen level

The experiments were undertaken in air saturated distilled water at both the room temperature (RT) $20 \pm 2^{o}C$ and body temperature (BT) $37 \pm 5^{o}C$ environment. A dissolved oxygen probe (Vernier Software & Technology, OR, USA) monitored

dissolved oxygen value in the water by assuming: 1. oxygen (O_2) and nitrogen (N_2) are the dominant gas in the water, 2. the dissolved O_2 is proportional to the N_2 at atmospheric pressure under Henry's law (Mulvana et al. 2012). Based on the theoretical 100% dissolved O_2 capacity in the water at the temperature from 0 ^oC to 35 ^oC at 760 mm Hg pressure provided by the manufacturer, an exponent curve was fitted to extrapolate the dissolved O_2 value up to 42 ^oC. Figure 7.1 shows the dissolved O_2 varying with temperature and its value is 6.49 $mg \cdot L^{-1}$ at 37 ^oC. The air-saturated water at RT was prepared by leaving the distilled water over 24 hours. The air-saturated water at BT was obtained by heating the water till 42 ^oC then degassing using a vacuum pump. The resultant air saturated water at BT was sealed in a bottle placed on a hotplate to maintain temperature of the water during the experiment.

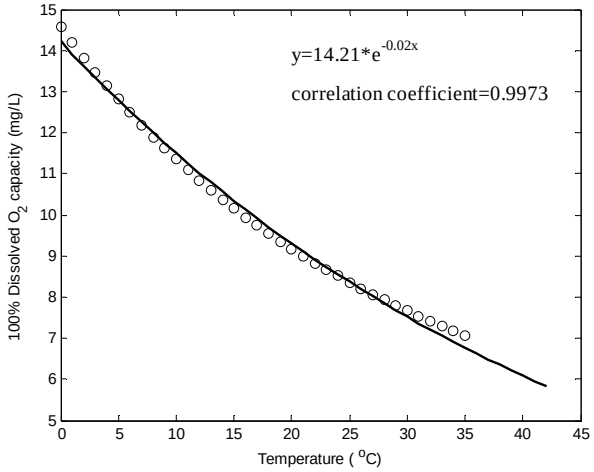

Figure 7. 1: *The 100% dissolved O_2 capacity varies with temperature in water*

7.3.4 Experimental arrangement

The method of UCAs reconstitution, sizing and measurement of attenuation (Chapter 4), CTR and SFR (Chapter 5 and 6) at RT were described in the previous chapters. SFR was measured using a 25-cycle signal. For the process of withdrawing UCAs, a 19G needle was inserted to a vial of activated Definity and a second 19G was

inserted for venting the gas. One of the 19G needles was connected to a syringe and the UCAs were withdrawn at a steady slow rate by hand. The activated SonoVue was withdrawn from the vial using the syringe incorporated in the SonoVue contrast reconstitution kit. The choice of connected syringe depends on the injection rate selected (1ml-syringe for 0.85 $ml \cdot min^{-1}$ and 2ml-syringe for 3$ml \cdot min^{-1}$). The syringe was then placed horizontally on a syringe pump and connected with one of the needles under test. At an injection rate setting, UCAs were pushed out into an Eppendorf PCR tube and were ready for sizing and acoustic measurement. The only difference for the experiments undertaken from BT to RT was replacing the water (solvent) at RT to the prepared air-saturated water at BT. The MB suspension was placed in an open tank and stirred continuously during the measurement. The water tank was placed on a hotplate setting at 42 ^{o}C to maintain the temperature at BT during the acoustic measurements. However, there was no temperature control for the MB sizing measurement using Mastersizer and the resultant variation in temperature during the experiment might potentially contribute to the uncertainties of the sizing results.

In addition to the different size distributions and capabilities of light scatter, the initial maximum concentration of reconstituted Definity (1.2×10^{10} $MBs \cdot ml^{-1}$) and SonoVue (5×10^{8} $MBs \cdot ml^{-1}$) varied in magnitude, thus different volumes of MBs (0.25 mL-Definity and 1.5 ml-SonoVue) were diluted in 240 ml-water for their individual MB sizing experiment to reach a obscuration above 5%, based on which Mastersizer generated a volume-based size distribution outcome.

Taking the above three factors into consideration: A: Needle Gauge (A1＝19G，A2=27G, A3=30G), B: injection rate (B1=3ml/min, B2=0.85ml/min) and C: Temperature (C1=RT, C2=BT), there are 12 combinations shown in Table 7.2. In this study, the setting of 19G, 3ml/min at RT (A1B1C1) is defined as ***'in vitro'*** representing a typical in vitro situation. Both 27G 0.85ml/min at BT (A2B2C2) and 30G 0.85ml/min at BT(A3B2C2) are defined as ***'in vivo'*** representing values typically used in an *in vivo* study. The size distribution, attenuation, CTR and SFRof the resultant 12 combinations were measured. Each experiment was repeated

three times and the measurements were acquired in 0.5-3 minutes after introducing MBs into water. After acquisition, the data were then downloaded to a local pc and analyzed using MATLAB.

Table 7. 2: *Experiment arrangement of the 12 combinations from 3 needle gauges, 2 injection rates and 2 temperatures*

	A(Gauge)	B(injection rate)	C(Temperature)	
1	19G	3ml/min	RT	19G_ RT3ml/min
2	19G	3ml/min	BT	19G_ BT3ml/min
3	19G	0.85ml/min	RT	19G_RT0.85 ml/min
4	19G	0.85ml/min	BT	19G_BT0.85 ml/min
5	27G	3ml/min	RT	27G_RT3ml/min
6	27G	3ml/min	BT	27G_BT3ml/min
7	27G	0.85ml/min	RT	27G_RT0.85 ml/min
8	27G	0.85ml/min	BT	27G_BT0.85 ml/min
9	30G	3ml/min	RT	30G_RT3ml/min
10	30G	3ml/min	BT	30G_BT3ml/min
11	30G	0.85ml/min	RT	30G_RT0.85 ml/min
12	30G	0.85ml/min	BT	30G_BT0.85 ml/min

Pressure drop and shear stress in the syringes and needles

The shear stress τ in the syringes and needle can be calculated using Equation 7.1 (Barrack and Stride 2009)

$$\tau_i = \frac{8 \ \mu \quad u_i}{D_i} \tag{7.1}$$

Where μ_i is viscosity of the suspending liquid (for water, μ_{water}=0.001 Pa·s), u_i is the velocity of the liquid, D_i is the inner diameter, i indicates either syringe or needle.

The pressure drop from the syringe to the needle is calculated using Equation 7.2 based on Bernoulli's equation (Barrack and Stride 2009)

$$P_s - P_n = \frac{1}{2}\rho\left(u_n^2 - u_s^2\right) \tag{7.2}$$

where P_s is the pressure near the piston in the syringe, P_n is the pressure at the outlet of the needle which equals atmospheric pressure, ρ is the density of the suspending liquid (for water, ρ_{water} =1000 kg·m^{-3}), u_n and u_s are the velocity of liquid in the needle and syringe respectively and are calculated Equation 7.3

$$u_i = \frac{4Q}{\pi D_i^2} \tag{7.3}$$

where Q is the flow rate of the liquid.

7.3.4 Statistics

The impact of needle gauge (19G, 27G and 30G) was determined by the groups with significant differences calculated using a one-way ANOVA. The influence of injection rate and temperature was determined by groups with significant difference from T test. T test was performed between the *in vivo* (27G/30G 0.85ml/min at BT) and *in vitro* (19G 3ml/min at RT) cases to understand the integrated effect of the needle gauges, injection rate and temperature on the size distribution and acoustic properties in the frequency range 17-31MHz.

The rescale range analysis determines the importance of each of the factors (Ziayoddin et al. 2012) and specifically in this study it ranks the influence of needle gauge, injection rate and temperature on the measured variables of mean diameter, attenuation, CTR and SFR. Compared to the general calculation based on an orthogonal array, the calculations in this study used an entire date set (complete combination of all possibilities) and the algorithm was listed in the Appendix 5 and 6. The orthogonal array design is proposed by Genichi Taguchi and aids to improve the efficiency of manufacture by reducing the variability (Montgomery 2008). The calculated R value represented the difference between the maximal and minimal results in each group of results (mean diameter, attenuation, CTR or SFR) and the

experimental factor in response to the largest R value is the one that has the most influence on the results (Di et al. 2003, Li et al. 2001).

7.4 RESULTS

The results of *in vitro* (RT 3ml/min) and *in vivo* (BT 0.85ml/min) measured by three needle gauges are selectively presented in this section and the remainder of the data in the Appendix 7 and 8. The results of T test were marked between *in vitro* (19G 3ml/min RT) and *in vivo* (27G/30G 0.85ml/min BT) on the Figure 7.3-7.6.

7.4.1 The size distribution and mean diameter of Definity and SonoVue

The volume based size distributions of Definity and SonoVue in the *in vitro* (19G 3ml/min RT) and *in vivo* (27G/30G 0.85ml/min BT) are shown in Figure 7.2. Compared with the size distribution curve from the RT measurements in each figure, the trend is that the size distribution made at BT measurement reduces in mean diameter and total gas volume compared to RT measurements.

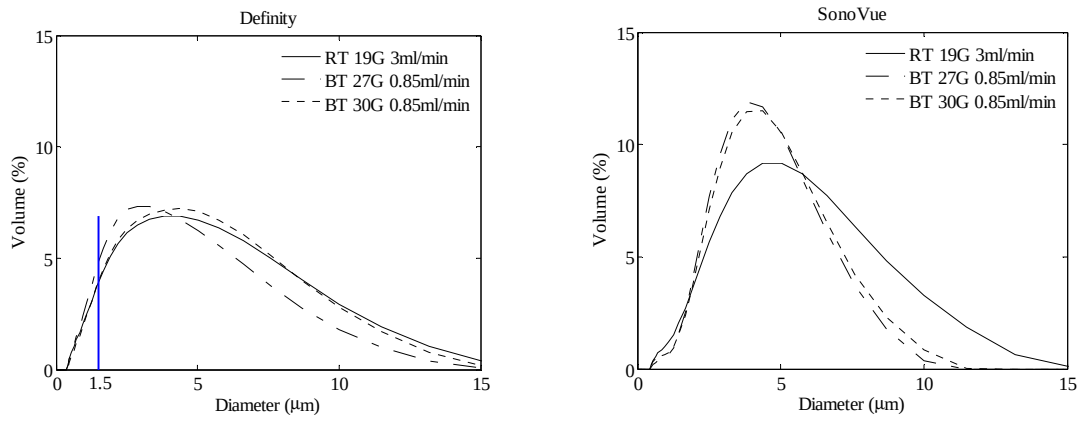

(a) Definity *(b) SonoVue*

Figure 7. 2: *The size distribution of (a) Definity and (b) SonoVue in the in vitro case (19G RT 3ml/min) and in vivo case (27G/30G BT 0.85ml/min). The line at 1.5 μm in (a) corresponds to the Definity MBs resonate at 15MHz based on the simulation of resonant frequency in Chapter 5*

Figure 7.3 shows the mean diameter of Definity and SonoVue. At RT, the mean diameter decreases with increasing needle gauge. There is no significant difference in mean diameter of Definity between in vitro and in vivo cases. For SonoVue, significant decrease of 0.7 μm in mean diameter is shown in Figure 7.3.b. For each pair (same needle gauge, different injection rates and temperatures) of both UCAs, the mean diameter decreases from RT to BT and from fast to low injection rate using 19G and 27G needle. However, the result using the smallest diameter needle (30G) needle does not follow this trend.

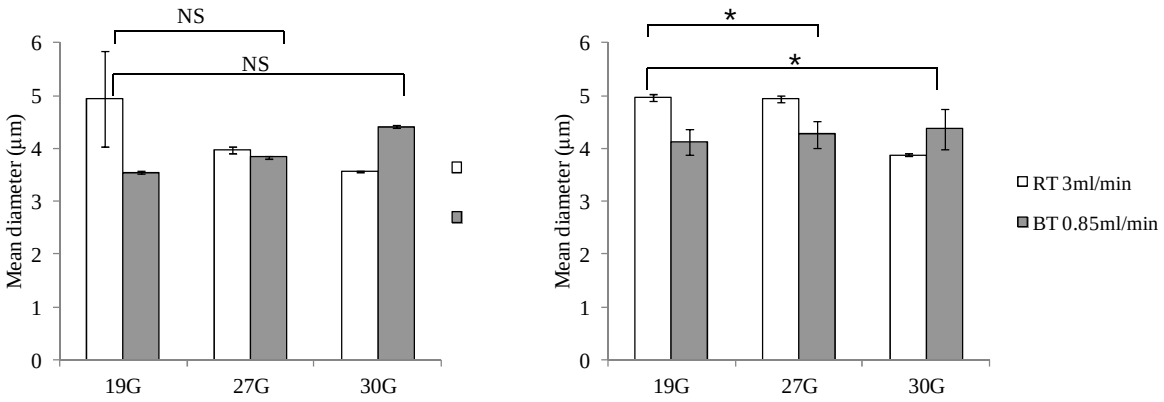

(a) Definity *(b) SonoVue*

Figure 7. 3: *The mean diameter comparison of (a) Definity and (b) SonoVue in the in vitro case (RT 3ml/min) (white bar) and in vivo case (BT 0.85ml/min) (shaded bar), NS: no significant difference, * P<0.05*

7.4.2 The acoustic properties comparison of Definity and SonoVue

Attenuation

The attenuation of Definity and SonoVue are presented in Figure 7.4. At RT, the attenuation decreases with increasing needle gauges. The attenuation of SonoVue in Figure 7.4.b shows extremely significant difference of 0.94dBcm^{-1} between the *in vitro* (RT) and *in vivo* (BT) cases. For each pair (same needle gauge, different injection rates and temperatures) of both UCAs, the attenuation of the two UCAs measured in the frequency range from 17-31 MHz decreases from RT to BT and

from high to low injection rate except the results of Definity measured at 27G needle. But the difference is not significant between the two settings (19G, 3ml/min, RT and 27G, 3ml/min, RT).

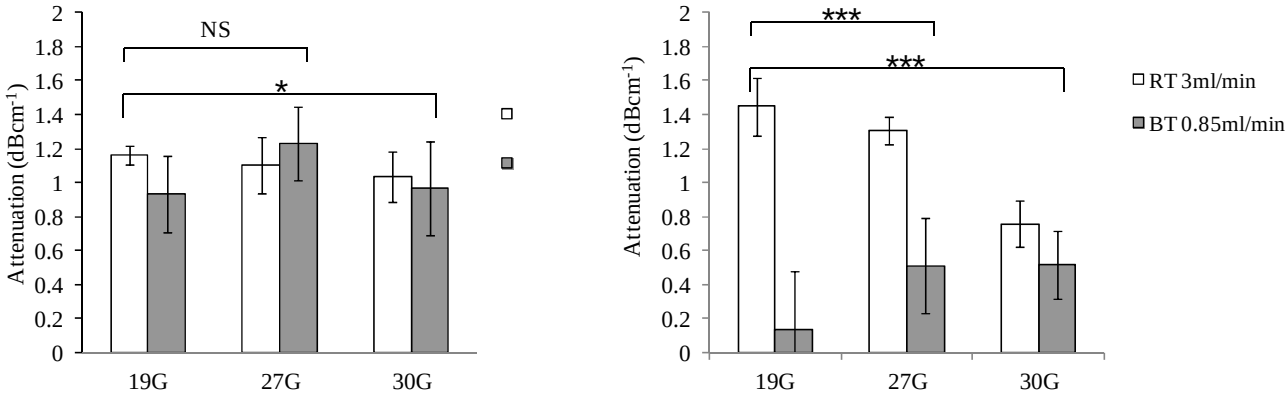

(a) Definity *(b) SonoVue*

Figure 7. 4: *The attenuation comparison of (a) Definity and (b) SonoVue in the in vitro case (RT 3ml/min) and in vivo case (BT 0.85ml/min), NS: no significant difference, * P<0.05, ***P<0.001*

CTR

Figure 7.5 shows little variation in CTR of Definity and SonoVue except for the result of SonoVue measured by 19G needle at BT over the frequency range 17-31 MHz. CTR of Definity increases significantly from 19G at RT to 27G at BT. CTR of SonoVue presents very significant difference of 1.70dB between *in vitro* and *in vivo* cases. In each pair group of the same needle gauge, the value of CTR decreases from RT to BT and from high to low injection rate measured at 19G and 27G and the contrary is true for the result of 30G needle. At RT, CTR decreases with increasing needle gauges for both UCAs.

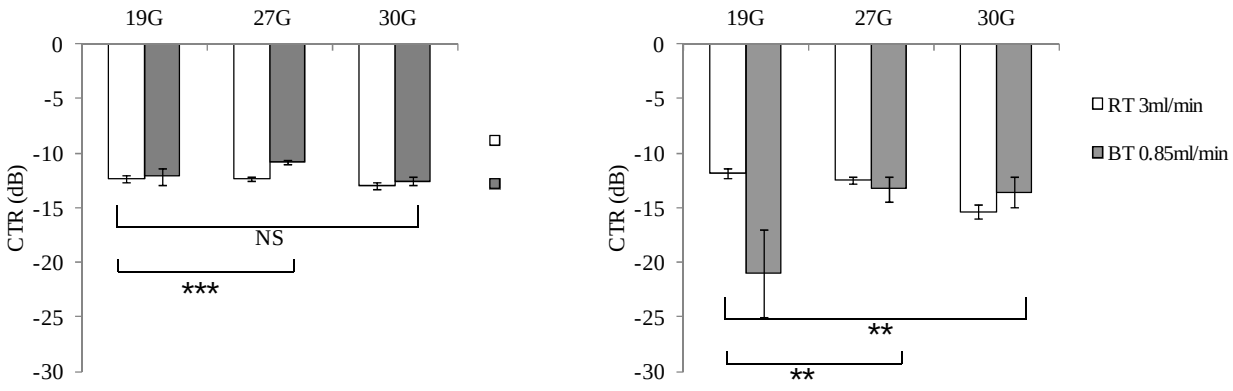

(a) Definity *(b) SonoVue*

Figure 7. 5: *The CTR comparison of (a) Definity and (b) SonoVue in the in vitro case (RT 3ml/min) and in vivo case (BT 0.85ml/min), NS: no significant difference, ** P<0.01, ***P<0.001*

Subharmonic to fundamental ratio

The SFR of Definity and SonoVue are shown in Figure 7.6. In Figure 7.6a, Definity demonstrates a significant difference of 0.96dB between 19G and 27G in SFR, but there is little variation between the groups of 19G and 30G. In Figure 7.6b, for SonoVue, there is a significant decrease in the SFR between the *in vitro* and *in vivo* setting. At RT for Definity and SonoVue, SFR increases with increasing needle gauges which is contrary to the results of CTR.

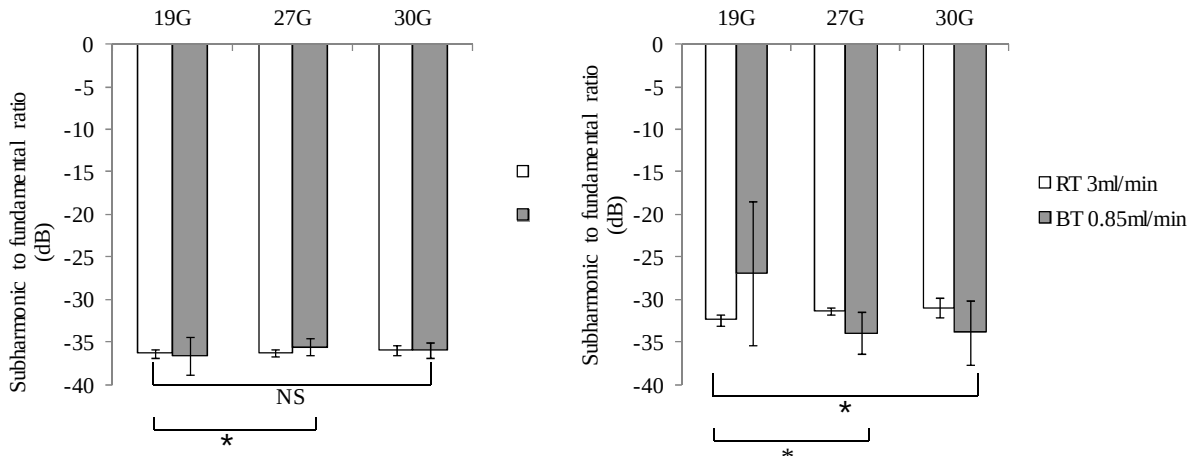

(a) Definity *(b) SonoVue*

Figure 7. 6: *The subharmonic to fundamental ratio comparison of (a) Definity and (b) SonoVue in the in vitro case (RT 3ml/min) and in vivo case (BT 0.85ml/min), NS: no significant difference, * P<0.05*

7.4.3 Pressure drop and shear stress in the syringes and needles

Table 7.3 lists the calculated shear stress in the syringes and needles and the pressure drop from the piston in the syringe to the outlet of the needle at different tested combinations. At certain injection rates (0.85 ml/min using 1ml-syringe, 3ml/min using 2ml-syringe), the pressure drop and the shear stress in the needle increase with the increasing needle gauge (i.e., decreasing I.D.). Applying the same needle, the fast injection rate (3ml/min) produces a higher pressure drop and shear stress in the needle than from the slow injection rate (0.85 ml/min), but the shear stress in the syringe decreases due to a wider inner diameter using a 2ml-syringe.

Table 7. 3: *The velocity, shear stress in the tested syringe (1ml I.D.: 4.78mm, 2ml I.D.: 8.66) and needles (19G, 27G, 30G) and the pressure drop (Ps-Pn) from syringe to needle*

Injection rate(ml/min)	Syringe ID (mm)	Mean velocity in syringe (mm/s)	Needle ID(mm)	Mean velocity in needle (mm/s)	Pressure drop Ps-Pn (Pa)	Shear stress in syringe (mPa)	Shear stress in needle (Pa)
0.85	4.78	0.79	0.686	38.35	0.73	1.32	0.45
0.85	4.78	0.79	0.21	409.22	83.73	1.32	15.59
0.85	4.78	0.79	0.159	713.84	254.79	1.32	35.92
3	8.66	0.85	0.686	135.35	9.16	0.78	1.58
3	8.66	0.85	0.21	1444.31	1043.02	0.78	55.02
3	8.66	0.85	0.159	2519.45	3173.82	0.78	126.76

7.4.4 Rescale range analysis

The impacts of needle gauge, injection rate and temperature rated from high to low on the mean diameter and acoustic properties of Definity and SonoVue are listed below:

Definity

Mean diameter: needle gauge > injection rate > temperature

Attenuation: needle gauge > temperature> injection rate

CTR: temperature > needle gauge > injection rate

Subharmonic to fundamental ratio: needle gauge > injection rate> temperature

SonoVue

Mean diameter: injection rate > needle gauge> temperature

Attenuation: temperature>needle gauge > injection rate

CTR: temperature > needle gauge >injection rate

Subharmonic to fundamental ratio: needle gauge > injection rate >temperature

7.5 DISCUSSION

The discussion of individual factors is based on the entire dataset including data presented in Appendix 7 and 8. Figures 7.2-7.6 only show the difference between selected typical *in vitro* and *in vivo* settings.

7.5.1 The impact of needle on the MBs

The results obtained from the study of needle gauges obtained at RT agree with the studies (Barrack and Stride 2009, Talu et al. 2008) that increasing needle gauges (i.e., narrower ID) reduces the mean MB diameter due to the aggravated diffusion of the MBs owing to an increase in the forced compression, shear stress (Table 7.3) and velocity gradient (Barrack and Stride 2009). From Chapter 5 it has been shown that both the resonant MBs and large off-resonance MBs contribute to the fundamental acoustic properties, consequently the attenuation (Figure 7.4) and CTR (Figure 7.5) decrease with increasing needle gauges at RT as expected. However, SFR (Figure 7.6) was found to increase. As shown in Chapter 6 subharmonic response was found to rely on the MBs that resonate at half the driven frequency. The driving frequency in this study was 30MHz, the diameter of Definity MBs that resonate at 15MHz is 1.5 μm shown in Figure 7.2a. The volume percentage of this diameter may increase at narrower needle size (size distribution curves not included) and may account for the increase in its SFR.

7.5.2 The impact of injection rate on the MBs

The increase in injection rate from 0.85 ml/min to 3ml/min at RT is found to increase the mean diameter of MBs which is not in agreement with the results from (Barrack and Stride 2009, Talu et al. 2008). Both Defintiy and SonoVue are poly-disperse large MBs (4-5μm) of a concentration 1.2×10^{10} MBs/ml (Lantheus Medical Imaging 2011) and $2\text{-}5\times10^{8}$ MBs/ml (Schneider 1999) respectively. The structure and the size

distribution of Definity and SonoVue are comparable to in-house MBs in Barrack's study and different from the mono-disperse small MB in Talu's experiment. However, the concentration of MBs is similar to Talu's study but not with Barrack's as the latter used a concentration around 10^7 MBs/ml. At RT, the reason for the increase in mean diameter from low to high injection rate may be because higher injection rate at 3ml/min using a 2ml-syringe introduces lower shear stress in the syringe shown in Table 7.3 compared with the low injection rate at 0.85ml/min using 1ml-syringe.

Although the mean diameter increased from low to high injection rates at RT, for Definity and SonoVue in the frequency range of 17-31MHz the measured attenuation was not found to vary significantly. However, a significant increase was found in CTR and a significant decrease in the SFR. Note that the only exception occurs in the result of SonoVue using 30G needle at RT, which shows a decrease in mean diameter and CTR and an increase in SFR. This trend may result from the interaction between the narrow needle gauge and high injection rate. In this setting, the shear stress is 126.76 Pa shown in Table 7.3 and the value is close to the threshold 150 Pa above which cell damage is predominately due to shear stress (Leverett et al. 1972). The shear resistance of the monolayer lipid MBs are not expected to be stronger than the bilayer, lipid and protein mixed membrane of the animal cells. Thus, this high shear stress by using 30G needle at high injection rate may cause destruction of most MBs and a decrease in the mean diameter of the entire MB population.

7.5.3 The impact of temperature on MBs

The mean diameter of Definity and SonoVue MBs increases from RT to BT based on the data of the same injection rate and needle gauge in Appendix 7 and 8, though in Figure 7.3 the measured diameter at BT is smaller than the diameter obtained at RT that may be influenced by the compression from increasing needle gauges and low injection rate. The process of MB dissolution was previously found to be in 3 phases: (1) an initially quick growth, (2) steady dissolution (Van Liew and Burkard 1995), (3) phase changes from low vapour pressure to vapour-to-liquid under Laplace

pressure (Kabalnov et al. 1998, Kwan and Borden 2010). In the first growth stage, the increasing temperature further enables MBs expansion by weakening the chemical bonds between lipid molecules and changing the shell elasticity and surface tension (Mulvana et al. 2011).

The attenuation of Definity and SonoVue MBs reduces at BT compared with the values at RT in the frequency range 17-31MHz. However, the attenuation of SonoVue measured at 3.5 MHz 100kPa pressure was found to increase with temperature below 40^{o}C (Mulvana et al. 2010). This finding also contradicts the results from Chapter 5 that MBs of large mean diameters correspond to large backscatter cross section leading to a higher attenuation and scattering energy. Taking into consideration the instability of MBs at BT, MBs may be disrupted under the insonating 0.56 MPa-PNP, despite this pressure proving to be non-destructive for MBs at RT shown in Chapter 4.

The CTR of Definity was found to increase at BT, but for SonoVue CTR decreases at BT compared with RT. On one side, the increased CTR may be attributed to the measured increase in mean diameter. On the other side, based on the assumption that MBs were destroyed in the analysis of attenuation, the diffused gas from MBs to the suspension becomes free MB then is dissolved gradually. The MBs with the gas of low Ostwald coefficient (Kabalnov et al. 1998) and low diffusivity and low solubility (Sarkar et al. 2009) will have a longer lifetime. In Table 7.4 it can be seen that C_3F_8 released from Definity processes a longer dissolution time compared the SF_6 gas from SonoVue. Consequently in the CTR measurement, the backscattered signal from the free SF_6 gas in the SonoVue suspension will have little effect on the acoustic measurements due to rapid dissolution. Thus the destruction of MBs and the difficultly in detecting free SF_6 gas contributes to the loss in CTR of SonoVue.

The SFR of Definity and SonoVue decreases from RT to BT. This indicates potential MB destruction during the subharmonic measurement due to the applied 25-cycle signal and the instability of MBs at BT.

Table 7. 4: *Parameters of gas of SonoVue and Definity (Sarkar et al. 2009)*

UCAs	Gas	Diffusivity coefficient in water	Ostwald coefficient	Permeability of gas through the encapsulation
SonoVue	SF_6	1.2×10^{-9} $m^2\cdot s^{-1}$	5.4×10^{-3}	8.7×10^{-6} $m\cdot s^{-1}$
Definity	C_3F_8	7.45×10^{-10} $m^2\cdot s^{-1}$	5.2×10^{-4}	1.2×10^{-6} $m\cdot s^{-1}$

7.5.4 The interaction between the needle gauge and injection rate with temperature

The influence of needle gauge and injection rate on the size distribution and acoustic characterisation of MBs at RT changes from the results acquired at BT. For instance, the mean diameter (Figure 7.3) and attenuation (Figure 7.4) of Definity and SonoVue were expected to reduce with increasing needle gauges but the contrary is true at the measurement of a 0.85ml/min-injection rate and BT. The interaction between the needle gauge, injection rate and temperature may occur. A narrower needle raises the shear stress to compress MBs and may force the MB to buckle (Barrack and Stride 2009), at which stage the surface tension (σ) equals to zero (Marmottant et al. 2005) leading to elimination of Laplace pressure ($P = 2\sigma/R$, R is the radius of MBs) (Van Liew and Burkard 1995). This makes the expansion of the MB at high temperature much easier compared with the MBs limited by the Laplace pressure. The potential change in the shell structure at BT on the other side promotes this process. Further investigations are required to validate these thoughts based on the optical observations.

From the rescale range analysis, the physical compression from the combination of needle gauge and injection rate predominately influences the mean diameter and SFR at 30MHz for both Definity and SonoVue. Temperature outperforms in the measurements of attenuation and CTR in the frequency range from 17-31MHz. SonoVue is sensitive to temperature while Definity is sensitive to needle gauge.

7.5.5 Consideration of the change in properties from *in vitro* to *in vivo* settings

Based on the above discussions of the impact of individual parameters and the interactions of needle gauge, injection and temperature, the variation of size distribution and the acoustic properties from the *in vitro* (19G, 3ml/min at RT) to in *vivo* (27G/30G, 0.85ml/min at BT) settings include: size distribution curves shift to the small diameter (Figure 7.2), mean diameters reduce accordingly (Figure 7.3), the attenuation (Figure 7.4) and CTR (Figure 7.5) decrease. The volume percentage of 1.5 μm-diameter MB (in response to the resonant diameter of Definity MBs at 15MHz) in Figure 7.2a increases at BT results in an increase in its SFR of Definity (Figure 7.6). However, the SFR of SonoVue decreases significantly at BT, which may be caused by instability and the destruction of MBs.

7.6 CONCLUSION

In this chapter, the influence between the *in vitro* (19G, 3ml/min at RT) and *in vivo* (27G/30G, 0.85ml/min at BT) experimental settings on the size distribution and acoustic properties of Definity and SonoVue in the frequency range of 17-31MHz was investigated. Specifically, for Definity from *in vitro* to *in vivo* setting, (1) there was no significant difference in mean diameter; (2) a significant decrease was found in attenuation and SFR; (3) an extremely significant increase occurs in CTR. For SonoVue, a significant decrease is observed in all the measured parameters including mean diameter, attenuation and CTR in the frequency range 17-31MHz and SFR at 30MHz. The reasons are from the combined effects of needle gauge and injection rate due to the physical compression and temperature due to the alteration of shell structure. From the rescale range analysis, SonoVue was found to be most sensitive to temperature while Definity was most sensitive to the needle gauges. Quantification of these parameters (needle gauge, injection rate and temperature) helps to explain quantitative differences in acoustic performance between *in vitro* and *in vivo* studies.

Chapter 8

Conclusions and future work

8.1 CONCLUSIONS

As outlined in Chapter 1, this thesis aimed to investigate the acoustic properties of ultrasound contrast agents (UCAs) at high ultrasound frequencies using a preclinical ultrasound scanner operating in RF mode. Briefly, Chapters 2 and 3 used an agar-based tissue mimicking material (TMM) to establish a platform for studying the essential acoustic parameters and developing the MATLAB codes necessary for this analysis, Chapters 4 to 6 focused on the comparative acoustic characterisation of three commercial lipid encapsulated UCAs using high frequency ultrasound. Before translation of the *in vitro* conclusions into explaining the future *in vivo* studies, an additional *in vitro* experiment using the practical *in vivo* administration process (thinner needle and slower injection rate at body temperature) was discussed in Chapter 7. Specific conclusions of each chapter are described below.

In Chapter 2 five high frequency transducers were characterised using a membrane hydrophone with an active element of 0.2 mm in diameter. Transmitting frequencies, pressures and spatial beam profiles were measured and provided quantitative information to support the studies of the following chapters.

Using these transducers and development of appropriate software, high frequency acoustical characterisation of TMM was performed in Chapter 3 using a broadband substitution technique. The speed of sound and attenuation were also acquired by a scanning acoustic macroscope (SAM) based in Dublin Institute of Technology. The results from the two independent systems were found to be comparable and showed that 1) the acoustical attenuation of TMM varied nonlinearly with frequency in a

format of 0.40 f + 0.0076 f^2 and 2) the speeds of sound in TMM measured by the Vevo 770 scanner and SAM system were found to be 1547.4 ± 1.4 $m \cdot s^{-1}$ and 1548.0 ± 6.1 $m \cdot s^{-1}$ in the frequency range 12-47MHz, respectively.

Chapter 4 described the extension of the experimental set-up and methods developed in chapter 3 to quantify the attenuation and normalized backscatter power (NBs) for UCAs. Through the concentration dependent experiments, a concentration of 0.8×10^6 mbs/ml was determined to be used in the following chapters. It was shown that for the three contrast agents that his value lay in the range in which the attenuation varied linearly with concentration and NBs varied linearly with the concentration. Additionally, for the non-destructive study of high frequency acoustic properties of Definity, SonoVue and MicroMarker in Chapters 5-7, the influence of the insonation pressure and time on the attenuation and NBs of microbubbles (MBs) was investigated. A power output of 3% on the Visualsonics scanner, corresponding to a PNP less than 0.56MPa was found not to destroy the MBs.

Based on the developed experimental methods and the determined ultrasound parameters (concentration and pressure), Chapter 5 and 6 focused on the comparison of acoustical properties of three lipid-encapsulated UCAs Definity, SonoVue and MicroMarker (untargeted) as a function of their frequency and size population. At the same number concentration below 30MHz, the acoustic characterisation of the three native UCAs are comparable, though their size distributions and encapsulated gases and shells are significantly different. Native MicroMarker produces higher values of attenuation and CTR compared with native Definity and SonoVue at frequencies above 30MHz and higher subharmonic to fundamental ratio at 25MHz. Altering the size distribution and concentration of Definity and SonoVue through decantation enables further enhancement for specific applications and may take full advantage of the imaging capabilities of the scanner. In Chapter 6, at 25MHz small Definity and SonoVue MBs (< 2μm in diameter) were predominantly responsible for the subharmonic response. Additionally, simulations were made using BUBBLESIM toolbox and showed that 1) MBs resonating at half of the driving frequency may predominately drive the subharmonics, 2) the pressure and number of cycle influence

the magnitude of the oscillation. It was suggested that the main reasons causing the discrepancy between the experimental data and simulation may be the complicated variation in MBs during the oscillation and the limitations of the model.

In Chapter 7, the influence between *in vitro* (19G needle, 3ml/min at RT) and *in vivo* (27G/30G needle, 0.85ml/min at BT) experimental settings on the size distribution and acoustic properties of Definity and SonoVue was investigated in the frequency range from 17 to 31MHz. Because of the physical compression and variation in the shell structure, all the measured parameters (mean diameter, attenuation, CTR, subharmonic to fundamental ratio) were found to be significantly altered except for the mean diameter of Definity. SonoVue is found to be most sensitive to temperature while Definity is most sensitive to the needle gauges.

8.2 FUTURE WORK

The high frequency ultrasound transducers have been characterised at room temperature in Chapter 2. Similar quantifications may be also required at body temperature for the following reasons. 1) The practical *in vivo* applications of UCAs are at body temperature and the results from Chapter 7 indicate a significant difference in the UCAs response between room temperature and body temperature. 2) The speed of sound in the water varies with temperature leading to the variation in the spatial distribution of beam profile and change of the focal position. 3) Nonlinear effects of ultrasound increase with temperature (Van Dongen and Verweij 2008).

In Chapter 3, the speed of sound and attenuation of ultrasound through TMM has been measured, further investigation of its backscatter properties and its frequency dependence remains to be studied. Note that the transmitting power applied in the study is at 10% for the tested transducers (transducer 710B: 1.06MPa, 707B: 1.05MPa, 704: 0.52MPa and 711: 0.23MPa), the occurrence of nonlinearity of ultrasound through TMM at these PNP is likely to be low. However, the nonlinear effects within TMM become more significant with increasing transmitting power at higher frequencies. Dong (Dong et al. 1999) measured the nonlinearity parameter

B/A of TMM (non-fat materials range from 5.6 to 6.6, fat materials are 9.8 and 11.1) at 2.25 MHz. Willams (Williams et al. 2006) found the B/A of a gelatine based TMM to be 7.4 ± 0.6. Thus it is of interest to study the relationship between the nonlinearity of TMM and transmitting power. Additionally, the previously published acoustic properties of biological tissue at high frequency are limited. Using the preclinical scanner it would be useful to acquire the speed of sound, acoustic attenuation and backscatter of biological tissue. The protocol of manufacturing TMM can be adjusted to match the measured acoustic parameters of the tissue at high frequencies. This developed TMM can be used as a specific phantom for assessing and evaluating the high frequency preclinical ultrasound devices.

A range of concentration within which a linear response of the attenuation and backscatter was confirmed in Chapter 4. The determination of this linear range of concentration can diminish the consideration of the multi-scattering between the MBs. But multi-scattering effects are likely to occur *in vivo* and introduce complicated interactions between the MBs thus further investigations at high frequencies under multi-scattering are necessary.

In the concentration dependent experiment, an interesting phenomenon of expansions and contractions of ‘MB’ were observed at low concentration in response to high insonation power shown in Figure 8.1. Theoretically, even at the applied ultrasound (12 – 47 MHz), spatial resolution is insufficient to observe the expansion and contraction of individual MB as well as the temporal resolution. But the oscillating particles look like the MBs. In Figure 8.1, the white line on the top of each oscillating particle may be the scatter from each MB under the sweeping of the single element transducer. The changing arc beneath the white line (the section in the highlighted yellow circle) may be attributed to the cavitation of the MB. Detailed explanations require further studies.

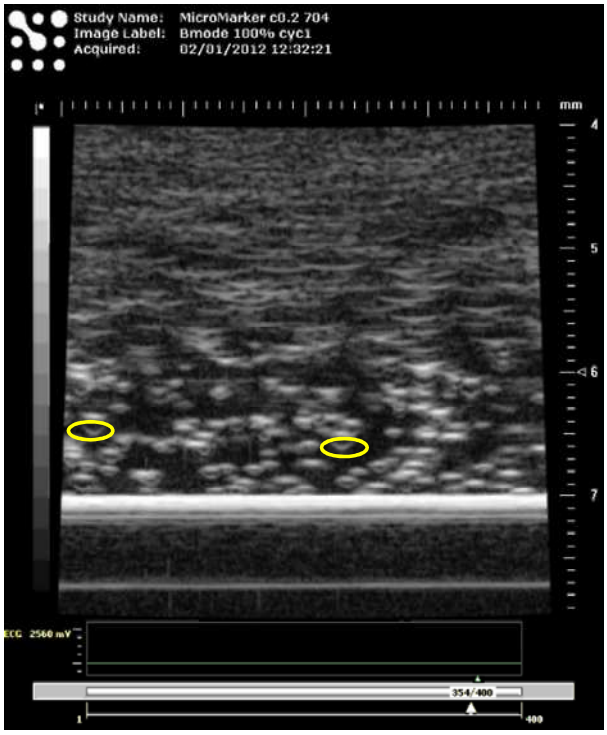

Figure 8. 1*: B-mode image of MicroMarker MBs suspension at 0.2×10^{6} mbs/ml concentration under 100% transmitting power, the section in the highlighted yellow circles are the contracting and expanding arcs during the MB oscillation*

The contrast to tissue ratio was measured in Chapter 5 as a signature of the fundamental response of the MBs suspension. Due to the limited acoustical data from soft tissue published at high frequency, choosing an independent quantity like backscatter coefficient may provide a more independent measure of different experimental modalities.

In Chapter 6, the subharmonic to fundamental ratio of SonoVue was found to be higher than Definity at 25MHz in each group of native, small and large population. However, the simulation results suggested that Definity MBs of a certain diameter resonated at 12.5 MHz but no SonoVue MBs resonated above 10MHz. One of the explanations is the shell properties of SonoVue acquired at the low frequency range might not accurately reflect its properties at high frequencies, despite the measured attenuation was found to be constant with the published data at lower frequency

range. For this reason, the shell properties in particular of SonoVue require further investigation. From the simulations in Chapter 6, discrepancies exist between simulation and experimental data that may be due to the mismatch between the experimental data and the model. The shell parameters are used in the model to simulate the oscillation of individual MB but they are acquired from a certain population of MB suspension. As known the shell properties vary with the diameter of the MBs. Thus, measuring the shell properties of a narrow range of bubble diameters (mono-disperse) would reduce the discrepancy between the simulation and experiment. This narrow range in diameter would be the most suitable to contribute to a targeted applications for specific frequency used for subhamonic study. From the simulation point of view, other models considering the diffusion in the insonating cycles and the variation in shell during the oscillation may be employed to study the subharmonic of MBs and further experimental data can be acquired to validate the efficacy of these models.

The influence of needle gauges, injection rate and temperature on the two clinical UCAs Definity and SonoVue was studied in Chapter 7. The preclinical UCAs MicroMarker study was not completed. From the discussion of the results at body temperature, the transmitting signal of long number of cycles and non-destructive pressure at room temperature may disrupt the MBs at body temperature, so future experiments using a lower pressure are necessary. Despite the published papers using high speed cameras showing a lower onset threshold of oscillation, larger radial oscillation and reduced stability of MBs at body temperature, explanations for this have centred almost solely around the proximity of body temperature to the transition phase temperature of lipids. How this process evolves and detailed explanations can be found through further research using a florescence microscope to capture the variation in the chemistry structure of lipid shell during the oscillation at body temperature. The experiments in this thesis are *in vitro* studies. The environment changes in this chapter already reveal the large distance from *in vitro* to *in vivo*. The complexities in the biological tissue are expected to introduce more uncertainties. The final goal is to successfully transfer the physics knowledge and understandings to applications *in vivo*.

The applications of MBs destruction plays an important role in perfusion, gene and drug delivery (Stride and Saffari 2003). Three main mechanisms of UCAs destruction have been identified to be fragmentation, acoustically driven diffusion, and static diffusion depending on the insonation pressure from high to low level (Chomas et al. 2001). The destruction of Definity was measured at 20 MHz and 25MHz using a flow phantom and the results indicated the destruction increased with the increasing pressure, number of cycles and frame rate (Cherin et al. 2005). The destruction of SonoVue was studied at 10MHz using a dual-high frequency ultrasound excitation (Chih-Kuang et al. 2009). Compared with single frequency-excitation signal, this method significantly reduced the pressure threshold for destroying the MBs by employing a transmitting signal consisting of two-frequency sinusoids and the difference between the two frequencies equalled the resonance frequency of tested MBs. Due to the limited publications in studying the destruction of UCAs at high frequency and these two papers reviewed only used the lipid encapsulated UCAs at a frequency lower than 30MHz, the corresponding research of hard shell (polymer or albumin) MBs remains to be explored.

The studies are based on a commercial ultrasound scanner allowing reproducible measurements but on other side use of this scanner limited the flexibilities of transmitting and receiving settings, in particular in RF data acquisition mode. Future work may include developing modules to connect with the scanners to facilitate functions for further research.

In summary, acoustic characterisations of both TMM and UCAs in this thesis extend our understanding from low frequency to high frequency ultrasound and will enable the further development of ultrasound imaging techniques and UCAs design specifically for high frequency ultrasound applications.

Appendices

Appendix 1 The sensitivity of the membrane hydrophone (certificate of calibration issued by National Physical Laboratory).

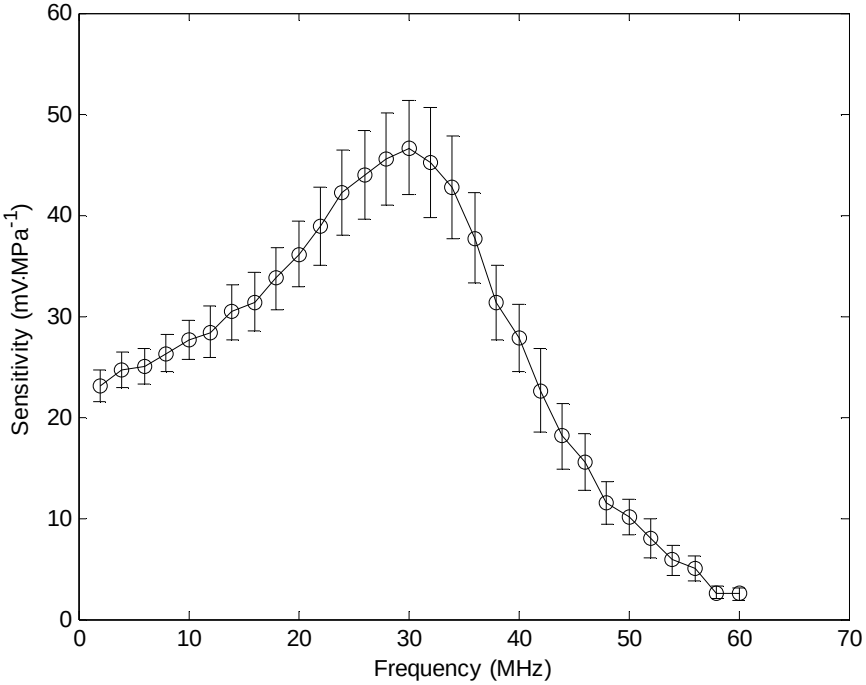

Appendix 2 The 3dB beamwidth (mm) of the transducers in M-mode (Table a - e) / PW-Doppler mode (Table f - j)

(a) 710B M mode

Transducer 710	f=20MHz, Power=100%	f=20MHz, Power=10%	f=25MHz, Power=100%	f=25MHz, Power=10%	f=30MHz, Power=100%	f=30MHz, Power=10%
Peak positive	0.15	0.16	0.15	0.15	0.14	0.15
Peak negative	0.19	0.16	0.17	0.15	0.16	0.14

(b) 707B M mode

Transducer 707	f=25MHz, Power=100%	f=25MHz, Power=10%	f=30MHz, Power=100%	f=30MHz, Power=10%	f=35MHz, Power=100%	f=35MHz, Power=10%
Peak positive	0.15	0.13	0.12	0.12	0.12	0.12
Peak negative	0.18	0.14	0.13	0.13	0.12	0.12

(c) 704 M mode

Transducer 704	f=35MHz, Power=100%	f=35MHz, Power=10%	f=40MHz, Power=100%	f=40MHz, Power=10%	f=45MHz, Power=100%	f=45MHz, Power=10%
Peak positive	0.14	0.14	0.14	0.14	0.16	0.13
Peak negative	0.15	0.15	0.15	0.13	0.14	0.13

(d) 711 M mode

Transducer 711	f=50MHz, Power=100%	f=50MHz, Power=10%	f=55MHz, Power=100%	f=55MHz, Power=10%	f=60MHz, Power=100%	f=60MHz, Power=10%
Peak positive	0.15	0.43	0.17	0.21	0.17	0.33
Peak negative	0.14	0.13	0.14	0.13	0.16	0.16

(e) 708 M mode, the bolded 3dB beamwidths are in particular broad because the variation of peak positive pressure is small (<0.5 MPa in 1mm distance)

Transducer 708	f=50MHz, Power=100%	f=50MHz, Power=10%	f=55MHz, Power=100%	f=55MHz, Power=10%	f=60MHz, Power=100%	f=60MHz, Power=10%
Peak positive	0.21	**0.83**	0.23	**0.84**	0.20	**0.66**
Peak negative	0.18	0.17	0.19	0.18	0.20	0.20

(f) 710B PW-Doppler mode at 100% power

Transducer 710	f=20MHz, SV=1	f=20MHz, SV=20	f=25MHz, SV=1	f=25MHz, SV=20
Peak positive	0.15	0.15	0.15	0.25
Peak negative	0.18	0.21	0.17	0.27

(g) 707B PW-Doppler mode at 100% power

Transducer 707	f=23MHz, SV=1	f=23MHz, SV=20	f=30MHz, SV=1	f=30MHz, SV=20
Peak positive	0.14	0.16	0.15	0.13
Peak negative	0.16	0.18	0.14	0.14

(h)704 PW-Doppler mode at 100% power

Transducer 704	f=30MHz, SV=1	f=30MHz, SV=20	f=40MHz, SV=1	f=40MHz, SV=20
Peak positive	0.17	0.16	0.15	0.14
Peak negative	0.17	0.16	0.16	0.16

(i) 711 PW-Doppler mode at 100% power

Transducer 711	f=40MHz, SV=1	f=40MHz, SV=20	f=55MHz, SV=1	f=55MHz, SV=20
Peak positive	0.14	0.13	0.15	0.30
Peak negative	0.14	0.15	0.15	0.24

(j) 708 PW-Doppler mode at 100% power

Transducer 708	f=40MHz, SV=1	f=40MHz, SV=20	f=55MHz, SV=1	f=55MHz, SV=20
Peak positive	0.15	0.15	0.15	0.25
Peak negative	0.18	0.18	0.18	0.30

Appendix 3 The amplitude of signal measured by membrane hydrophone for four transducers (a) 710B, (b)707B, (c) 704 and (d) 711.

(a) 710B

710B Power	Amplitude of Peak Positive (mV)	Amplitude of Peak Negative (mV)	Measured Central Frequency (MHz)	Sensitivity of Membrane Hydrophone	Peak negative pressure (MPa)	MI
100%	104.0	100.0	20	36.1	2.77	0.62
79%	94.0	94.0	22	38.9	2.42	0.52
63%	86.0	88.0	22	38.9	2.26	0.48
50%	78.0	84.0	22	38.9	2.16	0.46
40%	72.0	78.0	22	38.9	2.01	0.43
32%	64.8	68.0	22	38.9	1.75	0.37
25%	58.4	64.8	24	42.2	1.54	0.31
20%	53.6	59.2	24	42.2	1.40	0.29
16%	48.8	54.4	24	42.2	1.29	0.26
13%	44.0	48.8	24	42.2	1.16	0.24
10%	40.8	44.8	24	42.2	1.06	0.22
8%	34.4	38.4	24	42.2	0.91	0.19
6%	29.2	32.8	24	42.2	0.78	0.16
5%	27.6	32.0	24	42.2	0.76	0.15
4%	24.4	27.6	24	42.2	0.65	0.13
3%	20.4	23.6	24	42.2	0.56	0.11

(b) 707B

707B Power	Amplitude of Peak Positive (mV)	Amplitude of Peak Negative (mV)	Measured Central Frequency (MHz)	Sensitivity of Membrane Hydrophone	Peak negative pressure (MPa)	MI
100%	90	120	24	42.2	2.84	0.58
79%	86	110	24	42.2	2.61	0.53
63%	76	102	24	42.2	2.41	0.49
50%	68	94	24	42.2	2.23	0.45
40%	64	88	24	42.2	2.09	0.43
32%	58	82	24	42.2	1.94	0.40
25%	53.6	73.6	24	42.2	1.74	0.36
20%	47.2	64	24	42.2	1.52	0.31
16%	42.4	57.6	24	42.2	1.36	0.28
13%	38.4	51.2	24	42.2	1.21	0.25
10%	34.4	46.4	26	44	1.05	0.21
8%	30.4	41.6	26	44	0.95	0.19
6%	27.6	37.2	26	44	0.85	0.17
5%	24.4	32.8	26	44	0.75	0.15
4%	22.0	29.6	26	44	0.67	0.13
3%	18.8	24.8	26	44	0.56	0.11

(c) *704*

704 Power	Amplitude of Peak Positive (mV)	Amplitude of Peak Negative (mV)	Measured Central Frequency (MHz)	Sensitivity of Membrane Hydrophone	Peak negative pressure (MPa)	MI
100%	55.2	77.6	26	44	1.76	0.35
79%	46.6	64.8	26	44	1.47	0.29
63%	40.8	57.6	26	44	1.31	0.26
50%	38.4	52.0	28	45.5	1.141	0.22
40%	32.8	44.8	28	45.5	0.98	0.19
32%	28.8	38.8	28	45.5	0.85	0.16
25%	26.4	34.8	28	45.5	0.76	0.14
20%	23.2	30.8	28	45.5	0.68	0.13
16%	20.4	27.2	28	45.5	0.60	0.11
13%	19.6	25.6	26	44	0.58	0.11
10%	17.6	22.8	26	44	0.52	0.10
8%	15.8	19.4	28	45.5	0.43	0.08
6%	14.0	17.2	26	44	0.39	0.08
5%	12.4	14.8	28	45.5	0.33	0.06
4%	11.0	12.6	30	46.6	0.27	0.05
3%	10.0	11.2	26	44	0.25	0.05

(d) ***711***

711 Power	Amplitude of Peak Positive (mV)	Amplitude of Peak Negative (mV)	Measured Central Frequency (MHz)	Sensitivity of Membrane Hydrophone	Peak negative pressure (MPa)	MI
100%	25.2	41.2	28	45.5	0.91	0.17
79%	21.6	33.2	32	45.2	0.73	0.13
63%	18.8	29.6	32	45.2	0.65	0.12
50%	16.8	26	32	45.2	0.58	0.10
40%	14.8	22.8	32	45.2	0.50	0.09
32%	14.0	20.8	32	45.2	0.461	0.08
25%	12.4	17.6	32	45.2	0.39	0.07
20%	11.0	15.4	32	45.2	0.34	0.06
16%	10.6	14.2	32	45.2	0.31	0.06
13%	9.2	12.6	32	45.2	0.28	0.05
10%	8.4	10.6	32	45.2	0.23	0.04
8%	7.6	9.6	32	45.2	0.21	0.04
6%	6.8	8.4	32	45.2	0.19	0.03
5%	6.6	6.8	32	45.2	0.15	0.03
4%	6.2	6.2	32	45.2	0.14	0.02
3%	5.8	5.2	32	45.2	0.12	0.02

Appendix 4 Performance verification certificate of Mastersize 2000 optical unit

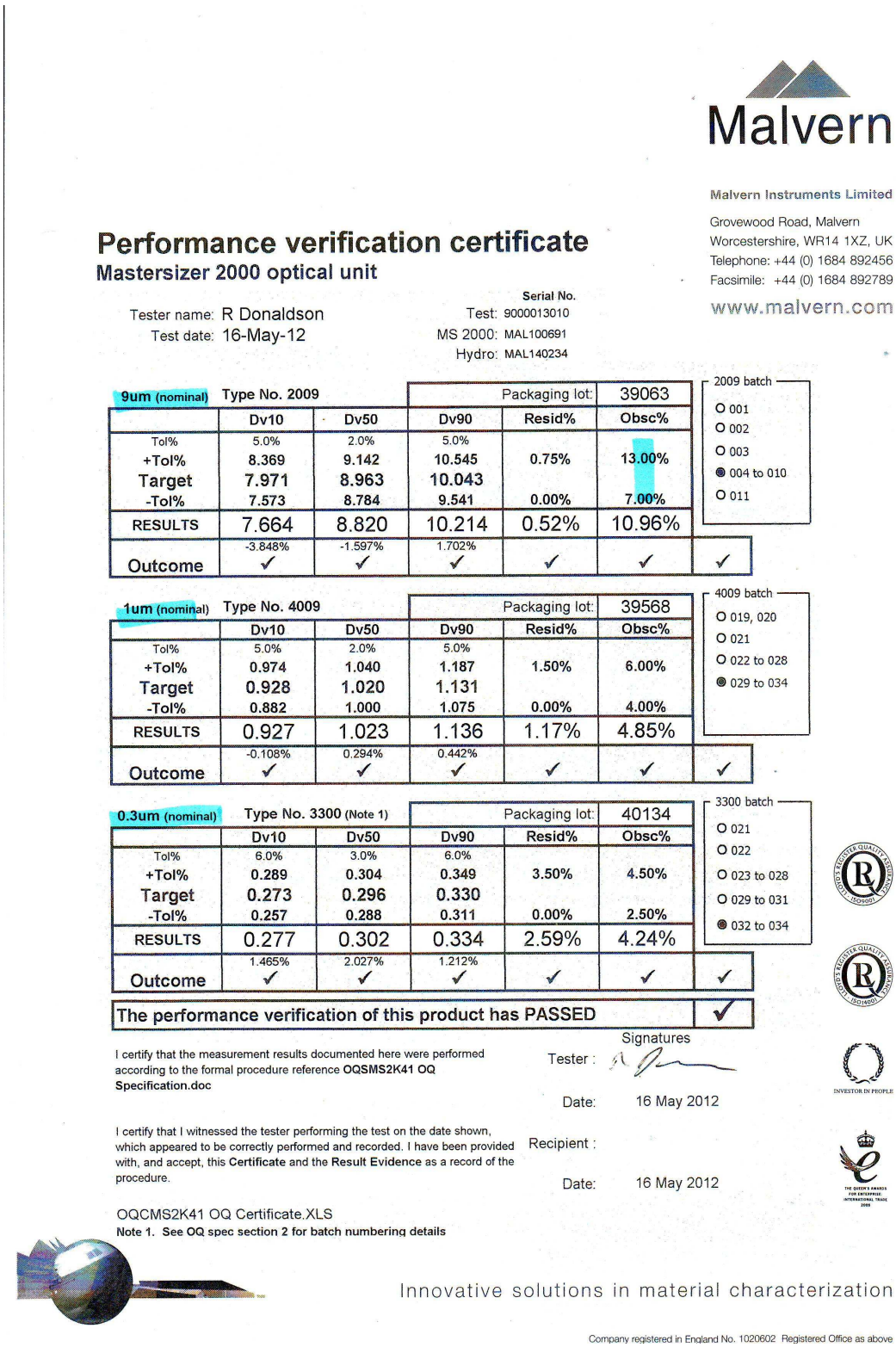

Malvern

Malvern Instruments Limited
Grovewood Road, Malvern
Worcestershire, WR14 1XZ, UK
Telephone: +44 (0) 1684 892456
Facsimile: +44 (0) 1684 892789
www.malvern.com

Performance verification certificate

Mastersizer 2000 optical unit

Tester name: R Donaldson
Test date: 16-May-12

Serial No.
Test: 9000013010
MS 2000: MAL100691
Hydro: MAL140234

9um (nominal) Type No. 2009 — Packaging lot: 39063

	Dv10	Dv50	Dv90	Resid%	Obsc%
Tol%	5.0%	2.0%	5.0%		
+Tol%	8.369	9.142	10.545	0.75%	13.00%
Target	7.971	8.963	10.043		
-Tol%	7.573	8.784	9.541	0.00%	7.00%
RESULTS	7.664	8.820	10.214	0.52%	10.96%
Outcome	-3.848% ✓	-1.597% ✓	1.702% ✓	✓	✓	✓

2009 batch: ○ 001 ○ 002 ○ 003 ◉ 004 to 010 ○ 011

1um (nominal) Type No. 4009 — Packaging lot: 39568

	Dv10	Dv50	Dv90	Resid%	Obsc%
Tol%	5.0%	2.0%	5.0%		
+Tol%	0.974	1.040	1.187	1.50%	6.00%
Target	0.928	1.020	1.131		
-Tol%	0.882	1.000	1.075	0.00%	4.00%
RESULTS	0.927	1.023	1.136	1.17%	4.85%
Outcome	-0.108% ✓	0.294% ✓	0.442% ✓	✓	✓	✓

4009 batch: ○ 019, 020 ○ 021 ○ 022 to 028 ◉ 029 to 034

0.3um (nominal) Type No. 3300 (Note 1) — Packaging lot: 40134

	Dv10	Dv50	Dv90	Resid%	Obsc%
Tol%	6.0%	3.0%	6.0%		
+Tol%	0.289	0.304	0.349	3.50%	4.50%
Target	0.273	0.296	0.330		
-Tol%	0.257	0.288	0.311	0.00%	2.50%
RESULTS	0.277	0.302	0.334	2.59%	4.24%
Outcome	1.465% ✓	2.027% ✓	1.212% ✓	✓	✓	✓

3300 batch: ○ 021 ○ 022 ○ 023 to 028 ○ 029 to 031 ◉ 032 to 034

The performance verification of this product has PASSED ✓

Signatures

I certify that the measurement results documented here were performed according to the formal procedure reference **OQSMS2K41 OQ Specification.doc**

Tester : [signature]
Date: 16 May 2012

I certify that I witnessed the tester performing the test on the date shown, which appeared to be correctly performed and recorded. I have been provided with, and accept, this **Certificate** and the **Result Evidence** as a record of the procedure.

Recipient :
Date: 16 May 2012

OQCMS2K41 OQ Certificate.XLS
Note 1. See OQ spec section 2 for batch numbering details

Innovative solutions in material characterization

Appendix 5 The algorithms of the rescale range analysis

A: Needle Gauge (A1＝19G，A2=27G, A3=30G), B: injection rate (B1=3ml/min, B2=0.85ml/min) and C: Temperature (C1=RT, C2=BT)

	A (Gauge)	B(injection rate)	C (Temp)			∑Ai	∑Bi	∑Ci
1	1	1	1	19G_ RT3ml	K1	i = 1:4	i=1,2,5,6,9,10	i=2n-1 (n=1-6)
2	1	1	2	19G_ BT3ml	K2	i = 5:8	i=3,4,7,8,11,12	i=2n (n=1-6)
3	1	2	1	19G_RT0.85	K3	i= 9:12		
4	1	2	2	19G_BT0.85	k1	K1A/4	K1B/6	K1C/6
5	2	1	1	27G_RT3ml	k2	K2A/4	K2B/6	K2C/6
6	2	1	2	27G_BT3ml	k3	K3A/4		
7	2	2	1	27G_RT0.85	R	max(ki)- min(ki), (i =1,2,3)		
8	2	2	2	27G_BT0.85	R’	$R\times0.52\times\sqrt{4}$	$R\times0.71\times\sqrt{6}$	
9	3	1	1	30G_RT3ml	rank			
10	3	1	2	30G_BT3ml				
11	3	2	1	30G_RT0.85				
12	3	2	2	30G_BT0.85				

Appendix 6 Table of correction coefficient for uneven number of levels in the rescale range analysis

Number of Levels	***m***	2	3	4	5	6	7	8	9	10
Correction coefficient	***d***	0.71	0.52	0.45	0.4	0.37	0.35	0.34	0.32	0.31

Appendix 7 The mean diameter, attenuation, CTR and subharmonic to fundamental ratio of Definity

Definity	Mean diameter	Attenuation ($dB \cdot cm^{-1}$)	CTR (dB)	Subharmonic to fundamental ratio (dB)
19G_ RT3ml	4.94 ± 0.90	1.16 ± 0.06	-12.34 ± 0.31	-36.36 ± 0.45
19G_ BT3ml	3.41 ± 0.04	1.15 ± 0.13	-11.26 ± 0.49	-35.94 ± 0.65
19G_RT0.85	3.59 ± 0.03	1.22 ± 0.12	-12.96 ± 0.41	-35.46 ± 0.38
19G_BT0.85	3.55 ± 0.03	0.93 ± 0.22	-12.12 ± 0.76	-36.59 ± 2.20
27G_RT3ml	3.97 ± 0.06	1.10 ± 0.16	-12.33 ± 0.21	-35.36 ± 0.41
27G_BT3ml	3.89 ± 0.03	1.13 ± 0.29	-11.28 ± 0.57	-35.30 ± 2.21
27G_RT0.85	3.51 ± 0.02	1.20 ± 0.07	-12.96 ± 0.30	-35.23 ± 0.40
27G_BT0.85	3.84 ± 0.03	1.23 ± 0.22	-10.85 ± 0.20	- 35.56 ± 0.97
30G_RT3ml	3.57 ± 0.02	1.04 ± 0.15	-13.00 ± 0.35	-35.95 ± 0.54
30G_BT3ml	3.25 ± 0.51	0.87 ± 0.45	-12.80 ± 0.37	-35.43 ± 1.65
30G_RT0.85	3.17 ± 0.01	1.06 ± 0.31	-13.39 ± 0.50	-35.47 ± 0.57
30G_BT0.85	4.41 ± 0.03	0.97 ± 0.27	-12.54 ± 0.41	-35.97 ± 0.94

Appendix 8 The mean diameter, attenuation, CTR and subharmonic to fundamental ratio of SonoVue

SonoVue	Mean diameter	Attenuation ($dB \cdot cm^{-1}$)	CTR (dB)	Subharmonic to fundamental ratio (dB)
19G_ RT3ml	4.97 ± 0.06	1.45 ± 0.17	-11.86 ± 0.45	- 32.41 ± 0.69
19G_ BT3ml	5.87 ± 0.31	0.83 ± 0.17	-10.44 ± 0.98	-35.47 ± 1.64
19G_RT0.85	3.82 ± 0.26	1.28 ± 0.05	-12.74 ± 0.23	-32.36 ± 0.55
19G_BT0.85	4.12 ± 0.24	0.13 ± 0.35	-23.18 ± 4.03	-26.94 ± 8.46
27G_RT3ml	4.94 ± 0.07	1.31 ± 0.08	-12.49 ± 0.30	-31.34 ± 0.40
27G_BT3ml	3.93 ± 0.23	0.37 ± 0.16	-15.24 ± 2.29	-32.97 ± 2.26
27G_RT0.85	3.80 ± 0.05	1.27 ± 0.03	-13.00 ± 0.32	-32.37 ± 0.62
27G_BT0.85	4.27 ± 0.25	0.51 ± 0.28	-13.26 ± 1.15	-33.92 ± 2.40
30G_RT3ml	3.88 ± 0.02	0.76 ± 0.14	-15.35 ± 0.65	-30.96 ± 1.12
30G_BT3ml	4.53 ± 0.28	0.00 ± 0.13	-27.30 ± 2.48	-20.78 ± 2.25
30G_RT0.85	4.40 ± 0.11	0.91 ± 0.20	-14.32 ± 0.94	-32.62 ± 1.02
30G_BT0.85	4.37 ± 0.38	0.52 ± 0.20	-13.56 ± 1.45	-33.90 ± 3.70

List of publications

Journal Publications

- **C. Sun**, S. Pye, J. Browne, A. Janeczko, B. Ellis, M. Butler, V. Sboros, A. Thomson, M. Brewin, C. Earnshaw, C.M. Moran. The Speed of Sound and Attenuation of an IEC Agar-Based Tissue-Mimicking Material for High Frequency Ultrasound Applications. *Ultrasound in Medicine & Biology* 2012;38:1262-70.
- X.Yang, **C. Sun**, T. Anderson, C. M. Moran, P.W. Hadoke, G.A. Gray, P.R. Hoskins. Assessment of spectral Doppler in preclinical ultrasound using a small-size rotating phantom, *Ultrasound in Medicine & Biology*, in press, 2013

Proceeding papers

- **C. Sun**, V. Sboros, M. Butler, C.M. Moran. The acoustic properties comparison of lipid microbubbles at high ultrasound frequencies, *In Proceedings of IEEE International Ultrasonics Symposium*, poster presentation by Dr. V. Sboros, Dresden, October, 2012.
- **C. Sun**, S. Pye, A. Janeczko, B. Ellis, M. Brewin, M. Butler, V. Sboros, A. Thomson, J. Browne, C.M. Moran. The acoustic attenuation of an IEC agar-based tissue-mimicking material measured at 12 - 47 MHz, *In Proceedings of IEEE International Ultrasonics Symposium*, poster presentation, Orlando, October, 2011.

Conference presentations

- **C. Sun**, V. Sboros, M. Butler, C.M. Moran. The acoustic properties of different size-populations of microbubbles from 12 - 43 MHz, *2013 Rotterdam contrast symposium*, poster presentation by Dr. C.M. Moran, Rotterdam, January, 2013.
- **C. Sun**, I. Panagakou and C.M. Moran. Influence of temperature, needle gauge and injection rate on the size distribution and acoustic properties of UCAs at high frequency, *2012 British Medical Ultrasound Society (BMUS) annual meeting*, poster presentation by Ms. I. Panagakou, Telfold, December, 2012.
- **C. Sun**, V. Sboros, M. Butler, C.M. Moran. The acoustic properties of microbubbles and their concentration dependence at 12 - 45 MHz, *2012 the first meeting of Scottish Ultrasound*, poster presentation, Glasgow, February, 2012.
- **C. Sun**, V. Sboros, M. Butler, C.M. Moran. The acoustic properties of microbubbles and their concentration dependence at 12 - 45 MHz, *2012 Rotterdam contrast symposium*, poster presentation, Rotterdam, January, 2012.
- **C. Sun**, S. Pye, J. Browne, A. Janeczko, B. Ellis, M.B. Butler, V. Sboros, C.M. Moran. Measurement of the acoustic attenuation of IEC agar-based tissue-mimicking material from 10 - 33 MHz, *2011 British Medical Ultrasound Society (BMUS) annual meeting*, poster presentation, Brighton, October, 2011.
- **C. Sun**, S. Pye, A. Janeczko, B. Ellis, M. Brewin, M. Butler, V. Sboros, C. Earnshaw, A. Thomson, J. Browne, C.M. Moran. The acoustic speed and attenuation in an IEC agar-based tissue-mimicking material measured at 14 - 46 MHz, *2011 Institute of Physics and Engineering in Medicine (IPEM) Physics & Technology of Medical Ultrasound conference*, oral presentation, York, March 2011.

Courses attended

- Fourth preclinical ultrasound imaging day, November, 2012, Edinburgh
- Leeds Microbubble Symposium, July, 2011, Leeds
- BMUS preclinical ultrasound study day, October, 2010, London
- BMUS clinical contrast meeting, May 2010, Dublin

References

AIUM. Methods for specifying acoustic properties of tissue mimicking phantoms and objects, Stage I. American Institute of Ultrasound in Medicine Technical Standards Committee Laurel, Maryland, 1995.

Ali M, Magee D, Dasgupta U, Signal Processing Overview of Ultrasound Systems for Medical Imaging. Texas Instruments White Paper 2008:1–26.

Andersen KS, Jensen JA, Ambient pressure sensitivity of microbubbles investigated through a parameter study. The Journal of the Acoustical Society of America 2009;126:3350.

Apfel RE, Holland CK, Gauging the likelihood of cavitation from short-pulse, low-duty cycle diagnostic ultrasound. Ultrasound Med. Biol. 1991;17:179-85.

Badea R, Seicean A, Diaconu B, Stan-Iuga R, Sparchez Z, Tantau M, Socaciu M, Contrast-enhanced ultrasound of the pancreas--a method beyond its potential or a new diagnostic standard. J Gastrointestin Liver Dis 2009;18:237-42.

Barnett S, Nonthermal issues: Cavitation--Its nature, detection and measurement. Ultrasound Med. Biol. 1998;24:S11-S21.

Barrack T, Stride E, Microbubble Destruction During Intravenous Administration: A Preliminary Study. Ultrasound Med. Biol. 2009;35:515-22.

Berg HC. Random walks in biology: Princeton Univ Pr, 1993.

Bertolotto M, Martegani A, Aiani L, Zappetti R, Cernic S, Cova M, Value of contrast-enhanced ultrasonography for detecting renal infarcts proven by contrast enhanced CT. A feasibility study. European Radiology 2008;18:376-83.

Biagi E, Breschi L, Vannacci E, Masotti L, Stable and transient subharmonic emissions from isolated contrast agent microbubbles. Ultrasonics, Ferroelectrics and Frequency Control, IEEE Transactions on 2007;54:480-97.

Bideau-Mehu A, Abjean R, Guern Y, Refractive index of octofluoropropane (C3F8) in the 300-150 nm wavelength range. Nuclear Instruments and Methods in

Physics Research Section A: Accelerators, Spectrometers, Detectors and Associated Equipment 1996;381:576-77.

Bilaniuk N, Wong GSK, Speed of sound in pure water as a function of temperature. The Journal of the Acoustical Society of America 1993;93:2306.

BMUS, Guidelines for the safe use of diagnostic ultrasound equipment. The British Medical Ultrasound Society 2009.

Boliren CF, Huffman DR, Absorption and scattering of light by small particles. J Wiley & Sons, New York 1983.

Bouakaz A, de Jong N, WFUMB safety symposium on echo-contrast agents: Nature and types of ultrasound contrast agents. Ultrasound Med. Biol. 2007;33:187-96.

Bouakaz A, Versluis M, de Jong N, High-speed optical observations of contrast agent destruction. Ultrasound Med. Biol. 2005;31:391-99.

Bracco, SonoVue package leaflet: information for the user 2011.

Brewin MP, Pike LC, Rowland DE, Birch MJ, The Acoustic Properties, Centered on 20 MHz, of an IEC Agar-Based Tissue-Mimicking Material and its Temperature, Frequency and Age Dependence. Ultrasound Med. Biol. 2008;34:1292-306.

Bridal SL, Roberjot V, Laugier P, Berger G. Attenuation and backscatter coefficient measurements from 2 to 60 MHz using backscattered RF signals from a tissue-mimicking phantom. Ultrasonics Symposium, 1996. Proceedings., 1996 IEEE, 1996. pp. 1151-54 vol.2.

Bristol-MyersSquibb. Luminity Summary of the European Public Assessment Report (EPAR) 2006.

Browne JE, Ramnarine KV, Watson AJ, Hoskins PR, Assessment of the acoustic properties of common tissue-mimicking test phantoms. Ultrasound Med. Biol. 2003;29:1053-60.

Browne JE, Watson AJ, Gibson NM, Dudley NJ, Elliott AT, Objective measurements of image quality. Ultrasound Med. Biol. 2004;30:229.

Browning RJ, Mulvana H, Tang M, Hajnal JV, Wells DJ, Eckersley RJ, Influence of Needle Gauge On In Vivo Ultrasound and Microbubble-Mediated Gene Transfection. Ultrasound Med. Biol. 2011;37:1531-37.

Bruce M, Averkiou M, Tiemann K, Lohmaier S, Powers J, Beach K, Vascular flow and perfusion imaging with ultrasound contrast agents. Ultrasound Med. Biol. 2004;30:735-43.

Burns PN, Becher H. Handbook of contrast echocardiography: Frankfurt: Springer Verlag, 2000.

Burns PN, Wilson SR, Simpson DH, Pulse inversion imaging of liver blood flow: improved method for characterizing focal masses with microbubble contrast. Investigative radiology 2000;35:58.

Butler M, B. , Thomas D, H. , Pye S, D. , Moran C, M. , McDicken WN, Sboros V, The acoustic response from individual attached and unattached rigid shelled microbubbles. Applied Physics Letters 2008;93:223906.

Cannon LM, Fagan AJ, Browne JE, Novel Tissue Mimicking Materials for High Frequency Breast Ultrasound Phantoms. Ultrasound Med. Biol. 2011;37:122-35.

Catalano O, Aiani L, Barozzi L, Bokor D, De Marchi A, Faletti C, Maggioni F, Montanari N, Orlandi P, Siani A, Sidhu P, Thompson P, Valentino M, Ziosi A, Martegani A, CEUS in abdominal trauma: multi-center study. Abdom. Imaging 2009;34:225-34.

Chen X, Wang J, Villanueva FS. Ultra fast brightfield and fluorescence imaging. 17th EUROPEAN SYMPOSIUM ON ULTRASOUND CONTRAST IMAGING. Rotterdam,Netherland, 2012.

Cherin E, Needles A, Stapleton S, Williams R, Foster FS, Tavakkoli J, Mehi J. Microbubble contrast agent destruction using 20-25 MHz ultrasound. Ultrasonics Symposium, 2005 IEEE, 2005. pp. 751-54.

Chetty K, Stride E, Sennoga CA, Hajnal JV, Eckersley RJ, High-speed optical observations and simulation results of SonoVue microbubbles at low-pressure insonation. Ultrasonics, Ferroelectrics and Frequency Control, IEEE Transactions on 2008;55:1333-42.

Cheung K, Couture O, Bevan PD, Cherin E, Williams R, Burns PN, Foster FS, In vitro characterization of the subharmonic ultrasound signal from Definity microbubbles at high frequencies. Physics in medicine and biology 2008;53:1209.

Chih-Kuang Y, Shin-yuan S, Che-chou S, Microbubble destruction by dual-high-frequency ultrasound excitation. Ultrasonics, Ferroelectrics and Frequency Control, IEEE Transactions on 2009;56:1113-18.

Chin CT, Lancee C, Borsboom J, Mastik F, Frijlink ME, de Jong N, Versluis M, Lohse D, Brandaris 128: A digital 25 million frames per second camera with 128 highly sensitive frames. Rev. Sci. Instrum. 2003;74:5026-34.

Chomas J, Dayton P, May D, Ferrara K, Nondestructive subharmonic imaging. Ultrasonics, Ferroelectrics and Frequency Control, IEEE Transactions on 2002;49:883-92.

Chomas JE, Dayton P, Allen J, Morgan K, Ferrara KW, Mechanisms of contrast agent destruction. Ultrasonics, Ferroelectrics and Frequency Control, IEEE Transactions on 2001;48:232-48.

Claudon M, Cosgrove D, Albrecht T, Bolondi L, Bosio M, Calliada F, Correas JM, Darge K, Dietrich C, D'Onofrio M, Evans DH, Filice C, Greiner L, Jager K, Jong Nd, Leen E, Lencioni R, Lindsell D, Martegani A, Meairs S, Nolsoe C, Piscaglia F, Ricci P, Seidel G, Skjoldbye B, Solbiati L, Thorelius L, Tranquart F, Weskott HP, Whittingham T, Guidelines and Good Clinical Practice Recommendations for Contrast Enhanced Ultrasound (CEUS) - Update 2008. Ultraschall in Med 2008;29:28-44.

Claudon M, Dietrich CF, Choi BI, Cosgrove DO, Kudo M, Nolsoe CP, Piscaglia F, Wilson SR, Barr RG, Chammas MC, Chaubal NG, Chen M-H, Clevert DA, Correas JM, Ding H, Forsberg F, Fowlkes JB, Gibson RN, Goldberg BB, Lassau N, Leen ELS, Mattrey RF, Moriyasu F, Solbiati L, Weskott H-P, Xu H-X, Guidelines and Good Clinical Practice Recommendations for Contrast Enhanced Ultrasound (CEUS) in the Liver-Update 2012: A WFUMB-EFSUMB Initiative in Cooperation With Representatives of AFSUMB, AIUM, ASUM, FLAUS and ICUS. Ultrasound Med. Biol. 2012.

Correas J-M, Bridal L, Lesavre A, Méjean A, Claudon M, Hélénon O, Ultrasound contrast agents: properties, principles of action, tolerance, and artifacts. European Radiology 2001;11:1316-28.

Cosgrove D, Ultrasound contrast agents: An overview. European Journal of Radiology 2006;60:324-30.

Culjat MO, Goldenberg D, Tewari P, Singh RS, A Review of Tissue Substitutes for Ultrasound Imaging. Ultrasound Med. Biol. 2010;36:861-73.

De Jong N, Acoustic properties of ultrasound contrast agents. Ph.D thesis. Rotterdam: Erasmus University 1993.

de Jong N, Emmer M, van Wamel A, Versluis M, Ultrasonic characterization of ultrasound contrast agents. Medical and Biological Engineering and Computing 2009;47:861-73.

de Jong N, Frinking PJA, Bouakaz A, Ten Cate FJ, Detection procedures of ultrasound contrast agents. Ultrasonics 2000;38:87-92.

de Jong N, Hoff L, Skotland T, Bom N, Absorption and scatter of encapsulated gas filled microspheres: Theoretical considerations and some measurements. Ultrasonics 1992;30:95-103.

Del Grosso VA, Mader CW, Speed of sound in pure water. The Journal of the Acoustical Society of America 1972;52:1442.

Di X, Chan KKC, Leung HW, Huie CW, Fingerprint profiling of acid hydrolyzates of polysaccharides extracted from the fruiting bodies and spores of Lingzhi by high-performance thin-layer chromatography. J. Chromatogr. A 2003;1018:85-95.

Dobrucki LW, Sinusas AJ. Cardiovascular molecular imaging. Semin. Nucl. Med., 2005. p. 73.

Doinikov AA, Bouakaz A, Review of shell models for contrast agent microbubbles. Ultrasonics, Ferroelectrics and Frequency Control, IEEE Transactions on 2011;58:981-93.

Dollet B, van der Meer SM, Garbin V, de Jong N, Lohse D, Versluis M, Nonspherical Oscillations of Ultrasound Contrast Agent Microbubbles. Ultrasound Med. Biol. 2008;34:1465-73.

Dong F, Madsen EL, MacDonald MC, Zagzebski JA, Nonlinearity parameter for tissue-mimicking materials. Ultrasound Med. Biol. 1999;25:831-38.

Duck FA. Physical properties of tissue: a comprehensive reference book. London: Academic Press, 1990.

Duck FA, Nonlinear acoustics in diagnostic ultrasound. Ultrasound Med. Biol. 2002;28:1-18.

Duck FA, Baker AC, Starritt HC. Ultrasound in medicine: Taylor & Francis, 1998.

Duineveld PC, Bouncing and Coalescence of Bubble Pairs Rising at High Reynolds Number in Pure Water or Aqueous Surfactant Solutions. Applied Scientific Research 1997;58:409-39.

Edler I, Lindström K, The history of echocardiography. Ultrasound Med. Biol. 2004;30:1565-644.

Eller A, Flynn HG, Generation of Subharmonics of Order One-Half by Bubbles in a Sound Field. The Journal of the Acoustical Society of America 1969;46:722.

Faez T, Goertz D, De Jong N, Characterization of Definity(TM) Ultrasound Contrast Agent at Frequency Range of 5-15 MHz. Ultrasound Med. Biol. 2011;37:338-42.

Feshitan JA, Chen CC, Kwan JJ, Borden MA, Microbubble size isolation by differential centrifugation. Journal of Colloid and Interface Science 2009;329:316-24.

Fish P. Physics and instrumentation of diagnostic medical ultrasound: John Wiley & Sons Inc, 1990.

Forsberg F, Liu JB, Burns PN, Merton DA, Goldberg BB, Artifacts in ultrasonic contrast agent studies. Journal of ultrasound in medicine 1994;13:357-65.

Forsberg F, Shi WT, Goldberg BB, Subharmonic imaging of contrast agents. Ultrasonics 2000;38:93-98.

Foster FS, Hossack J, Adamson SL, Micro-ultrasound for preclinical imaging. Interface Focus 2011;1:576-601.

Foster FS, Pavlin CJ, Harasiewicz KA, Christopher DA, Turnbull DH, Advances in ultrasound biomicroscopy. Ultrasound Med. Biol. 2000;26:1-27.

Frenkel V, Ultrasound mediated delivery of drugs and genes to solid tumors. Advanced Drug Delivery Reviews 2008;60:1193-208.

Fry WJ, Dunn F, Ultrasonic intensity gain by composite transducers. The Journal of the Acoustical Society of America 1962;34:188-92.

Goertz DE. High frequency flow imaging of the microcirculation. Toronto: University of Toronto, 2002.

Goertz DE, Cherin E, Needles A, Karshafian R, Brown AS, Burns PN, Foster FS, High frequency nonlinear B-scan imaging of microbubble contrast agents.

Ultrasonics, Ferroelectrics and Frequency Control, IEEE Transactions on 2005;52:65-79.

Goertz DE, de Jong N, van der Steen AFW, Attenuation and Size Distribution Measurements of Definity(TM) and Manipulated Definity(TM) Populations. Ultrasound Med. Biol. 2007;33:1376-88.

Goertz DE, Frijlink M, Bouakaz A, Chin CT, de Jong N, van der Steen AWF. The effects of bubble size on nonlinear scattering from microbubbles. Ultrasonics, 2003 IEEE Symposium on, 2003. pp. 1503-06 Vol.2.

Goertz DE, Frijlink ME, de Jong N, van der Steen AFW, Nonlinear intravascular ultrasound contrast imaging. Ultrasound Med. Biol. 2006;32:491-502.

Goertz DE, Frijlink ME, Tempel D, Bhagwandas V, Gisolf A, Krams R, de Jong N, van der Steen AFW, Subharmonic Contrast Intravascular Ultrasound for Vasa Vasorum Imaging. Ultrasound Med. Biol. 2007;33:1859-72.

Goertz DE, Needles A, Burns PN, Foster FS, High-frequency, nonlinear flow imaging of microbubble contrast agents. Ultrasonics, Ferroelectrics and Frequency Control, IEEE Transactions on 2005;52:495-502.

González RC, Woods RE. Digital Image Processing: Prentice Hall, 2001.

Gorce J, Arditi M, Schneider M, Influence of Bubble Size Distribution on the Echogenicity of Ultrasound Contrast Agents: A Study of SonoVue (TM). Investigative radiology 2000;35:661.

Gramiak R, Shah PM, Echocardiography of the Aortic Root. Investigative Radiology 1968;3:356-66.

Greis C, Technology overview: SonoVue (Bracco, Milan). European Radiology Supplements 2004;14:P11-P15.

Guan J, Matula TJ, Using light scattering to measure the response of individual ultrasound contrast microbubbles subjected to pulsed ultrasound in vitro. The Journal of the Acoustical Society of America 2004;116:2832.

Guiot C, Pastore G, Napoleone M, Gabriele P, Trotta M, Cavalli R, Thermal response of contrast agent microbubbles: Preliminary results from physico-chemical and US-imaging characterization. Ultrasonics 2006;44, Supplement:e127-e30.

Hall TJ, Bilgen M, Insana MF, Krouskop TA, Phantom materials for elastography. Ultrasonics, Ferroelectrics and Frequency Control, IEEE Transactions on 1997;44:1355-65.

Harvey CJ, Blomley MJK, Eckersley RJ, Cosgrove DO, Developments in ultrasound contrast media. European Radiology 2001;11:675-89.

Harvey CJ, Blomley MKJ, Eckersley RJ, Cosgrove DO, Developments in ultrasound contrast media. European Journal of Radiology 2000;11:675-89.

Heaton DA, Golding S, Bradley CP, Dawson TA, Cai S, Channon KM, Paterson DJ, Targeted nNOS gene transfer into the cardiac vagus rapidly increases parasympathetic function in the pig. J. Mol. Cell. Cardiol. 2005;39:159-64.

Helfield BL, Cherin E, Foster FS, Goertz DE, Investigating the Subharmonic Response of Individual Phospholipid Encapsulated Microbubbles at High Frequencies: A Comparative Study of Five Agents. Ultrasound Med. Biol. 2012;38:846-63.

Helfield BL, Huo X, Williams R, Goertz DE, The Effect of Preactivation Vial Temperature on the Acoustic Properties of DefinityTM. Ultrasound Med. Biol. 2012.

Hill CR. Physical Principles of Medical Ultrasonics. 1st edn: Ellis Horwood, 1986.

Hoff L. Acoustic characterization of contrast agents for medical ultrasound imaging: Kluwer Academic Publishers, 2001.

Hoskins P. Diagnostic ultrasound: physics and equipment: Cambridge Univ Pr, 2002.

Hoskins PR, Martin K, Thrush A. Diagnostic ultrasound: physics and equipment: Cambridge University Press, 2010.

Howard CM, Forsberg F, Minimo C, Liu JB, Merton DA, Claudio PP, Ultrasound guided site specific gene delivery system using adenoviral vectors and commercial ultrasound contrast agents. J. Cell. Physiol. 2006;209:413-21.

Huang YP, Zheng YP, Leung SF, Choi APC, High Frequency Ultrasound Assessment of Skin Fibrosis: Clinical Results. Ultrasound Med. Biol. 2007;33:1191-98.

Humphrey VF, Nonlinear propagation in ultrasonic fields: measurements, modelling and harmonic imaging. Ultrasonics 2000;38:267-72.

Huo E, Helfield B, Goertz D, Scaling of viscoelastic shell properties of lipid encapsulated microbubbles with frequency. The Journal of the Acoustical Society of America 2010;128:2280.

IEC. Ultrasonics – Flow measurement systems – Flow test object. Standard 61685. London: International Electrotechnical Commission 2001.

Inglis S, Ramnarine KV, Plevris JN, McDicken WN, An anthropomorphic tissue-mimicking phantom of the oesophagus for endoscopic ultrasound. Ultrasound Med. Biol. 2006;32:249-59.

Insana M, Wagner RF, Brown DG, Hall TJ, Describing small-scale structure in random media using pulse-echo ultrasound. Journal of the Acoustical Society of America 1990;87.

Janssen BJA, Smits JFM, Autonomic control of blood pressure in mice: basic physiology and effects of genetic modification. American Journal of Physiology - Regulatory, Integrative and Comparative Physiology 2002;282:R1545-R64.

Kabalnov A, Klein D, Pelura T, Schutt E, Weers J, Dissolution of multicomponent microbubbles in the bloodstream: 1. theory. Ultrasound Med. Biol. 1998;24:739-49.

Kagadis GC, Loudos G, Katsanos K, Langer SG, Nikiforidis GC, In vivo small animal imaging: current status and future prospects. Med. Phys. 2010;37:6421.

Kaufmann BA, Wei K, Lindner JR, Contrast Echocardiography. Curr. Probl. Cardiol. 2007;32:51-96.

Kaye GWC, Laby TH. Tables of Physical and Chemical Constants 16th edition. Essex, England: Longman, 1995.

Keller JB, Miksis M, Bubble oscillations of large amplitude. The Journal of the Acoustical Society of America 1980;68:628.

Kennedy JE, High-intensity focused ultrasound in the treatment of solid tumours. Nature Reviews Cancer 2005;5:321-27.

Kennedy JE, Ter Haar GR, Cranston D, High intensity focused ultrasound: surgery of the future? Br. J. Radiol. 2003;76:590-99.

Khismatullin DB, Resonance frequency of microbubbles: Effect of viscosity. Journal of the Acoustical Society of America 2004;116:1463-73.

King RL, Herman BA, Maruvada S, Wear KA, Harris GR. Development of a HIFU phantom, 2007. pp. 351-56.

Kips JG, Segers P, Van Bortel LM, Identifying the vulnerable plaque: A review of invasive and non-invasive imaging modalities. Artery Research 2008;2:21-34.

Kofler JM, Madsen EL, Improved method for determining resolution zones in ultrasound phantoms with spherical simulated lesions. Ultrasound Med. Biol. 2001;27:1667-76.

Kwan JJ, Borden MA, Microbubble Dissolution in a Multigas Environment. Langmuir 2010;26:6542-48.

Lantheus Medical Imaging. Prescribing Information of Definity vial for (perflutren lipid microsphere) injectable suspension, In: Inc LMI, ed: Lantheus Medical Imaging Inc, 2011.

Leen E. Ultrasound contrast harmonic imaging of abdominal organs. Seminars in Ultrasound, CT, and MRI: Elsevier, 2001. pp. 11-24.

Leen E, Ceccotti P, Kalogeropoulou C, Angerson WJ, Moug SJ, Horgan PG, Prospective multicenter trial evaluating a novel method of characterizing focal liver lesions using contrast-enhanced sonography. Am. J. Roentgenol. 2006;186:1551-59.

Leighton TG. The acoustic bubble: Academic Press, 1997.

Leighton TG, Dumbrell HA, New approaches to contrast agent modelling. Journal of Physics: Conference Series 2004;1:91.

Leverett LB, Hellums JD, Alfrey CP, Lynch EC, Red blood cell damage by shear stress. Biophys. J. 1972;12:257-73.

Li Y, Chen J, Lun SY, Rui XS, Efficient pyruvate production by a multi-vitamin auxotroph of Torulopsis glabrata: key role and optimization of vitamin levels. Appl. Microbiol. Biotechnol. 2001;55:680-85.

Lindner JR, Evolving applications for contrast ultrasound. The American Journal of Cardiology 2002;90:72-80.

Liu Y, Miyoshi H, Nakamura M, Encapsulated ultrasound microbubbles: Therapeutic application in drug/gene delivery. J. Controlled Release 2006;114:89-99.

Lizzi FL, Greenebaum M, Feleppa EJ, Elbaum M, Coleman DJ, Theoretical framework for spectrum analysis in ultrasonic tissue characterization. The Journal of the Acoustical Society of America 1983;73:1366.

Lockwood GR, Ryan LK, Hunt JW, Foster FS, Measurement of the ultrasonic properties of vascular tissues and blood from 35-65 MHz. Ultrasound Med. Biol. 1991;17:653.

Looney P. Theoretical modelling of ultrasound contrast agents. Edinburgh: The University of Edinburgh, 2011.

Lotsberg O, Hovem JM, Aksum B, Experimental observation of subharmonic oscillations in Infoson bubbles. The Journal of the Acoustical Society of America 1996;99:1366.

Lubbers J, Graaff R, A simple and accurate formula for the sound velocity in water. Ultrasound Med. Biol. 1998;24:1065-68.

MacGillivray TJ, Ellis W, Pye SD, The resolution integral: visual and computational approaches to characterizing ultrasound images. Physics in Medicine and Biology 2010;55:5067.

Madsen EL, Deaner ME, Mehi J, Properties of Phantom Tissuelike Polymethylpentene in the Frequency Range 20-70 MHz. Ultrasound Med. Biol. 2011;37:1327-39.

Malvern Instruments Ltd., Operators Guide. 1999.

Marmottant P, Van Der Meer S, Emmer M, Versluis M, De Jong N, Hilgenfeldt S, Lohse D, A model for large amplitude oscillations of coated bubbles accounting for buckling and rupture. The Journal of the Acoustical Society of America 2005;118:3499.

Marsh J, N. , Hughes M, S. , Hall C, S. , Lewis S, H. , Trousil R, L., Brandenburger G, H. , Levene H, Miller J, G. , Frequency and concentration dependence of the backscatter coefficient of the ultrasound contrast agent Albunex. The Journal of the Acoustical Society of America 1998;104:1654-66.

Martinoli C, Pretolesi F, Crespi G, Bianchi S, Gandolfo N, Valle M, Derchi LE, Power Doppler sonography: clinical applications. European Journal of Radiology 1998;27:S133-S40.

Maruvada S, Shung KK, Wang S-H, High-frequency backscatter and attenuation measurements of selected bovine tissues between 10 and 30 MHz. Ultrasound Med. Biol. 2000;26:1043-49.

McDicken WN. Diagnostic ultrasonics: principles and use of instruments: WB Saunders Company, 1991.

Miller DL, Dou C, Wiggins RC, Wharram BL, Goyal M, Williams AR, An in vivo rat model simulating imaging of human kidney by diagnostic ultrasound with gas-body contrast agent. Ultrasound Med. Biol. 2007;33:129-35.

Montgomery DC. Design and analysis of experiments: Wiley, 2008.

Moran CM, Bush NL, Bamber JC, Ultrasonic propagation properties of excised human skin. Ultrasound Med. Biol. 1995;21:1177-90.

Moran CM, Butler MB, Sboros V, Anderson T, Anderson D, McDicken WN. High frequency characterisation of commercial contrast agents. Ultrasonics Symposium, 2005 IEEE, 2005. pp. 1996-98.

Moran CM, Pye SD, Ellis W, Janeczko A, Morris KD, McNeilly AS, Fraser HM, A Comparison of the Imaging Performance of High Resolution Ultrasound Scanners for Preclinical Imaging. Ultrasound Med. Biol. 2011;37:493-501.

Moran CM, Thomson AJW, Rog-Zielinska E, Gray GA, High resolution echocardiography in the assessment of cardiac physiology and disease in preclinical models. Exp. Physiol. 2012.

Moran CM, Watson RJ, Fox KAA, McDicken WN, In vitro acoustic characterisation of four intravenous ultrasonic contrast agents at 30 MHz. Ultrasound Med. Biol. 2002;28:785-91.

Morse PMC, Ingard KU. Theoretical acoustics: Princeton Univ Pr, 1986.

Mulvana H, Stride E, Hajnal JV, Eckersley RJ, Temperature Dependent Behavior of Ultrasound Contrast Agents. Ultrasound Med. Biol. 2010;36:925-34.

Mulvana H, Stride E, Tang M-X, Hajnal JV, Eckersley RJ, The Influence of Gas Saturation on Microbubble Stability. Ultrasound Med. Biol. 2012;38:1097-100.

Mulvana H, Stride E, Tang M, Hajnal JV, Eckersley R, Temperature-Dependent Differences in the Nonlinear Acoustic Behavior of Ultrasound Contrast Agents Revealed by High-Speed Imaging and Bulk Acoustics. Ultrasound Med. Biol. 2011;37:1509-17.

Narayana PA, Ophir J, The measurement of attenuation in nonlinearly attenuating media by the zero crossing method. Ultrasound Med. Biol. 1984;10:715-18.

Needles A, Arditi M, Rognin NG, Mehi J, Coulthard T, Bilan-Tracey C, Gaud E, Frinking P, Hirson D, Foster FS, Nonlinear Contrast Imaging with an Array-Based Micro-Ultrasound System. Ultrasound Med. Biol. 2011;36:2097-106.

O'Neil HT, Theory of focusing radiators. The Journal of the Acoustical Society of America 1949;21:516.

Obriot J, Ge J, Bose TK, St-Arnaud JM, Determination of the density from simultaneous measurements of the refractive index and the dielectric constant of gaseous CH4, SF6, and CO2. Fluid Phase Equilibria 1993;86:314-50.

Ophir J, Alam SK, Garra BS, Kallel F, Konofagou EE, Krousko T, Merritt CRB, Righett R, Souchon R, Srinivasan S, Elastography: imaging the elastic properties of soft tissues with ultrasound. Journal of Medical Ultrasonics 2002;29:156.

Ophir J, Parker KJ, Contrast agents in diagnostic ultrasound. Ultrasound Med. Biol. 1989;15:319-33.

Patton CA, Harris GR, Phillips RA, Output levels and bioeffects indices from diagnostic ultrasound exposure data reported to the FDA. IEEE Transactions on Ultrasonics Ferroelectrics and Frequency Control 1994;41:353-59.

Pinkerton JMM, The absorption of ultrasonic waves in liquids and its relation to molecular constitution. Proceedings of the Physical Society. Section B 1949;62:129.

Piscaglia F, Nolsoe C, Dietrich CF, Cosgrove DO, Gilja OH, Bachmann Nielsen M, Albrecht T, Barozzi L, Bertolotto M, Catalano O, The EFSUMB Guidelines and Recommendations on the Clinical Practice of Contrast Enhanced Ultrasound (CEUS): update 2011 on non-hepatic applications. Ultraschall Med. 2011;33:33.

Porter TM, Smith DAB, Holland CK, Acoustic techniques for assessing the Optison destruction threshold. Journal of ultrasound in medicine 2006;25:1519-29.

Postema M. Medical Bubbles Veenendaal, Nertherland, 2004.

Postema M, Marmottant P, Lancee CT, Hilgenfeldt S, Jong Nd, Ultrasound-induced microbubble coalescence. Ultrasound in Medicine & Biology 2004;30:1337-44.

Postema M, Van Wamel A, Lancee CT, De Jong N, Ultrasound-induced encapsulated microbubble phenomena. Ultrasound Med. Biol. 2004;30:827-40.

Preston RC. Output Measurements for Medical Ultrasound. Teddington, UK: Springer-Verlag, 1991.

Pu G, Borden MA, Longo ML, Collapse and Shedding Transitions in Binary Lipid Monolayers Coating Microbubbles. Langmuir 2006;22:2993-99.

Qin S, Caskey C, F. , Ferrara K, W. , Ultrasound contrast microbubbles in imaging and therapy: physical principles and engineering. Physics in Medicine and Biology 2009:R27.

Quaia E, Microbubble ultrasound contrast agents: an update. European Radiology 2007;17:1995-2008.

Quaia E, Whittingham T. Contrast-Specific Imaging Techniques: Technical Perspective. Contrast Media in Ultrasonography: Springer Berlin Heidelberg, 2005. pp. 43-70.

Ramnarine KV, Anderson T, Hoskins PR, Construction and geometric stability of physiological flow rate wall-less stenosis phantoms. Ultrasound Med. Biol. 2001;27:245-50.

Rhee S. High frequency (IVUS) ultrasound transducer technology - applications and challenges. Applications of Ferroelectrics, 2007 ISAF 2007 Sixteenth IEEE International Symposium, 2007. pp. 856-57.

Rijsterborgh H, Mastik F, Lancee CT, Verdouw P, Roelandt J, Bom N, Ultrasound myocardial integrated backscatter signal processing: Frequency domain versus time domain. Ultrasound Med. Biol. 1993;19:211-19.

Saijo Y, Sasaki H, Okawai H, Nitta S-i, Tanaka M, Acoustic properties of atherosclerosis of human aorta obtained with high-frequency ultrasound. Ultrasound Med. Biol. 1998;24:1061-64.

Sarkar K, Katiyar A, Jain P, Growth and Dissolution of an Encapsulated Contrast Microbubble: Effects of Encapsulation Permeability. Ultrasound Med. Biol. 2009;35:1385-96.

Sboros V, Response of contrast agents to ultrasound. Advanced Drug Delivery Reviews 2008;60:1117-36.

Schneider M, SonoVue, a new ultrasound contrast agent. European Radiology 1999;9:S347-S48.

Sennoga CA, Yeh JSM, Alter J, Stride E, Nihoyannopoulos P, Seddon JM, Haskard DO, Hajnal JV, Tang M-X, Eckersley RJ, Evaluation of Methods for Sizing and Counting of Ultrasound Contrast Agents. Ultrasound Med. Biol. 2012.

Shankar PM, Krishna PD, Newhouse VL, Advantages of Subharmonic Over Second Harmonic Backscatter for Contrast-To-Tissue Echo Enhancement. Ultrasound Med. Biol. 1998;24:395-99.

Shaw A, Hekkenberg R. Standards to support performance evaluation for diagnostic ultrasound imaging equipment. NPL Report AC 2. Teddington, Middlesex, UK: National Physical Laboratory, 2007.

Shi W, Forsberg F, Raichlen J, Needleman L, Goldberg B, Pressure dependence of subharmonic signals from contrast microbubbles. Ultrasound Med. Biol. 1999;25:275-83.

Sidhu PS, Allan PL, Cattin F, Cosgrove DO, Davies AH, Do DD, Karakagil S, Langholz J, Legemate DA, Martegani A, Diagnostic efficacy of SonoVue, a second generation contrast agent, in the assessment of extracranial carotid or peripheral arteries using colour and spectral Doppler ultrasound: a multicentre study. Br. J. Radiol. 2006;79:44-51.

Silverman RH, High-resolution ultrasound imaging of the eye – a review. Clinical & Experimental Ophthalmology 2009;37:54-67.

Silverman RH, Ketterling JA, Mamou J, Coleman DJ, Improved high-resolution ultrasonic imaging of the eye. Archives of ophthalmology 2008;126:94.

Sirsi S, Feshitan J, Kwan J, Homma S, Borden M, Effect of Microbubble Size on Fundamental Mode High Frequency Ultrasound Imaging in Mice. Ultrasound Med. Biol. 2010;36:935-48.

Smith DAB, Porter TM, Martinez J, Huang S, MacDonald RC, McPherson DD, Holland CK, Destruction Thresholds of Echogenic Liposomes with Clinical Diagnostic Ultrasound. Ultrasound Med. Biol. 2007;33:797-809.

Sprague MR, Cherin E, Foster FS, A new transducer receive transfer function calibration method: application to microbubble backscattering cross-section measurements at high frequency. Ultrasonics, Ferroelectrics and Frequency Control, IEEE Transactions on 2011;58:1159-68.

Sprague MR, Chérin E, Goertz DE, Foster FS, Nonlinear Emission from Individual Bound Microbubbles at High Frequencies. Ultrasound Med. Biol. 2010;36:313-24.

Stapleton S, Goodman H, Zhou Y-Q, Cherin E, Henkelman RM, Burns PN, Foster FS, Acoustic and Kinetic Behaviour of Definity in Mice Exposed to High Frequency Ultrasound. Ultrasound Med. Biol. 2009;35:296-307.

Stapleton SA, Needles A, Henderson E, Foster FS. Concentration Requirements for Subharmonic Quantitative Contrast Enhanced High Frequency Ultrasound Flow Studies. Ultrasonics Symposium, 2007. IEEE, 2007. pp. 1061-64.

Stride E, Saffari N, On the destruction of microbubble ultrasound contrast agents. Ultrasound Med. Biol. 2003;29:563-73.

Stride E, Saffari N, Investigating the significance of multiple scattering in ultrasound contrast agent particle populations. IEEE Transactions on Ultrasonics Ferroelectrics and Frequency Control 2005;52:2332-45.

Sun C, Pye SD, Browne JE, Janeczko A, Ellis B, Butler MB, Sboros V, Thomson AJW, Brewin MP, Earnshaw CH, Moran CM, The Speed of Sound and Attenuation of an IEC Agar-Based Tissue-Mimicking Material for High Frequency Ultrasound Applications. Ultrasound Med. Biol. 2012;38:1262-70.

Takeuchi M, Ogunyankin K, Pandian NG, McCreery TP, Sweitzer RH, Caldwell VE, Unger EC, Avelar E, Sheahan M, Connolly R, Enhanced visualization of intravascular and left atrial appendage thrombus with the use of a thrombus-targeting ultrasonographic contrast agent (MRX-408A1): In vivo experimental echocardiographic studies. J. Am. Soc. Echocardiogr. 1999;12:1015-21.

Talu E, Powell RL, Longo ML, Dayton PA, Needle Size and Injection Rate Impact Microbubble Contrast Agent Population. Ultrasound Med. Biol. 2008;34:1182-85.

Tang M-X, Eckersley RJ, Noble JA, Pressure-dependent attenuation with microbubbles at low mechanical index. Ultrasound Med. Biol. 2005;31:377-84.

Teirlinck CJPM, Bezemer RA, Kollmann C, Lubbers J, Hoskins PR, Fish P, Fredfeldt K-E, Schaarschmidt UG, Development of an example flow test object and comparison of five of these test objects, constructed in various laboratories. Ultrasonics 1998;36:653-60.

Teirlinck ICJPM, Validation of a flow Doppler test object for diagnostic ultrasound scanners. 1997.

ter Haar G, Therapeutic applications of ultrasound. Progress in Biophysics and Molecular Biology 2007;93:111-29.

ter Haar G, Harnessing the interaction of ultrasound with tissue for therapeutic benefit: high-intensity focused ultrasound. Ultrasound Obstet. Gynecol. 2008;32:601-04.

Thomas DH. Acoustic investigation of microbubble response to medical imaging ultrasound pulses. The University of Edinburgh: The University of Edinburgh, 2009.

Thomas DH, Looney P, Steel R, Pelekasis N, McDicken WN, Anderson T, Sboros V, Acoustic detection of microbubble resonance. Applied Physics Letters 2009;94:243902.

Treeby BE, Zhang EZ, Thomas AS, Cox BT, Measurement of the Ultrasound Attenuation and Dispersion in Whole Human Blood and its Components From 0-70 MHz. Ultrasound Med. Biol. 2011;37:289-300.

Uhlendorf V, Hoffmann C. Nonlinear acoustical response of coated microbubbles in diagnostic ultrasound. Ultrasonics Symposium, 1994. Proceedings., 1994 IEEE: IEEE, 1994. pp. 1559-62.

Unger EC, Hersh E, Vannan M, Matsunaga TO, McCreery T, Local drug and gene delivery through microbubbles. Progress in Cardiovascular Diseases 2001;44:45-54.

Unger EC, Matsunaga TO, McCreery T, Schumann P, Sweitzer R, Quigley R, Therapeutic applications of microbubbles. European Journal of Radiology 2002;42:160-68.

Van Dongen KW, Verweij MD, Sensitivity study of the acoustic nonlinearity parameter for measuring temperatures during High Intensity Focused

Ultrasound treatment. Journal of the Acoustical Society of America 2008;123:3225.

Van Liew HD, Burkard ME, Behavior of bubbles of slowly permeating gas used for ultrasonic imaging contrast. Investigative radiology 1995;30:315.

Van Trees HL. Optimum array processing: Wiley NY, 2002.

VisualSonics, VisualSonics® Vevo 770® Digital RF Option Operator Manual. 2006.

VisualSonics, VisualSonics® Vevo 770® High-Resolution Imaging System Operator Manual. 2006.

Visualsonics, Vevo MicroMarker™ Non-Targeted Contrast Agent Kit: Instructions and Protocols Rev1.4. 2012.

Vogt M, Scharenberg R, Moussa G, Sand M, Hoffmann K, Altmeyer P, Ermert H, A New High Frequency Ultrasound Skin Imaging System: Imaging Properties and Clinical in Vivo Results. Acoustical Imaging 2007:137-44.

Vokurka K, On Rayleigh's model of a freely oscillating bubble. I. Basic relations. Czechoslovak Journal of Physics 1985;35:28-40.

Vos HJ, Emmer M, de Jong N. Oscillation of single microbubbles at room versus body temperature. Ultrasonics Symposium, 2008. IUS 2008. IEEE, 2008. pp. 982-84.

Wei K, Jayaweera AR, Firoozan S, Linka A, Skyba DM, Kaul S, Quantification of Myocardial Blood Flow With Ultrasound-Induced Destruction of Microbubbles Administered as a Constant Venous Infusion. Circulation 1998;97:473-83.

Wells PNT. Biomedical ultrasonics: Academic Press New York, 1977.

Whittingham TA, WFUMB safety symposium on echo-contrast agents: Exposure from diagnostic ultrasound equipment relating to cavitation risk. Ultrasound Med. Biol. 2007;33:214-23.

Williams R, Cherin.Emmanuel, Lam.Toby YJ, Tavakkoli J, Zemp RJ, Stuart FF, Nonlinear ultrasound propagation through layered liquid and tissue-equivalent media: computational and experimental results at high frequency. Physics in Medicine and Biology 2006;51:5809.

Wisner ER, Ferrara K, Gabe JD, Patel D, Nyland TG, Short RE, Ottoboni TB, Contrast enhanced intermittent power Doppler ultrasound with sub-micron bubbles for sentinel node detection. Acad. Radiol. 2002;9:S389-S91.

Zagzebski JA. Essentials of ultrasound physics: Mosby, 1996.

Zeqiri B, Hodnett M, Measurements, phantoms, and standardization. Proceedings of the Institution of Mechanical Engineers, Part H: Journal of Engineering in Medicine 2010;224:375-91.

Ziayoddin M, Shinde M, Lalitha J, Orthogonal Array Approach for Optimization of Carrageenase Production by Solid State Fermentation of Pseudomonas aeruginosa ZSL-2. J Microb Biochem Technol 2012;4:096-95.

Zook JM, Vreeland WN, Effects of temperature, acyl chain length, and flow-rate ratio on liposome formation and size in a microfluidic hydrodynamic focusing device. Soft Matter 2010;6:1352-60.